

**NEAR INFRARED FLUORESCENT OPTICAL LYMPHOGRAPHY
FOR CANCER DIAGNOSTICS**

A Dissertation

by

JESSICA PEREA HOUSTON

Submitted to the Office of Graduate Studies of
Texas A&M University
in partial fulfillment of the requirements for the degree of

DOCTOR OF PHILOSOPHY

December 2005

Major Subject: Chemical Engineering

**NEAR INFRARED FLUORESCENT OPTICAL LYMPHOGRAPHY
FOR CANCER DIAGNOSTICS**

A Dissertation

by

JESSICA PEREA HOUSTON

Submitted to the Office of Graduate Studies of
Texas A&M University
in partial fulfillment of the requirements for the degree of

DOCTOR OF PHILOSOPHY

Approved by:

Chair of Committee,
Committee Members,

Head of Department,

Eva M. Sevick-Muraca
Mark T. Holtzapple
Chun Li
Gerard L. Coté
Kenneth R. Hall

December 2005

Major Subject: Chemical Engineering

ABSTRACT

Near Infrared Fluorescent Optical Lymphography

for Cancer Diagnostics. (December 2005)

Jessica Perea Houston, B.S., New Mexico State University;

M.S., Texas A&M University

Chair of Advisory Committee: Dr. Eva M. Sevick-Muraca

A new molecular imaging modality has been developed to detect and locate positive axillary and sentinel lymph nodes non-invasively in breast cancer patients undergoing lymphoscintigraphy. The modality is based on fluorescent photon detection to locate the presence of indocyanine green (ICG) in the lymph subsequent to peritumoral injection of ICG into the breast. The imaging system consists of a gain-modulated intensified charge-coupled device (ICCD) camera, which captures low-intensity, near-infrared, and frequency-modulated photons. A four-fold ‘optical lymphography’ study was conducted to (1) examine fluorescence depth penetration and ICCD system accuracy at clinically relevant depths, (2) compare image quality of the ICCD system vs. conventional gamma imaging, (3) measure ICG pharmacokinetics *in vivo*, and (4) develop a clinical protocol while examining pre-clinical factors such as the outcome of combining ICG with sulfur colloids used in lymphoscintigraphy.

The frequency-domain ICCD system was found to precisely detect modulation amplitude, I_{AC} , and phase, θ , at depths up to 9 cm and with I_{AC} accuracy less than 20% and θ less than 2° using an 80-mW laser incident on phantoms having ranging tissue

optical properties. Significant differences in the mean depth of penetration owing to 0.62-ns lifetime and 100-MHz frequency increases were detected.

An *in vivo* optical vs. nuclear image quality comparison demonstrated statistically similar ($\alpha=0.05$) target-to-background ratios for optical (1.4 \pm 0.3) and nuclear (1.5 \pm 0.2). Alternatively, resulting image signal-to-noise ratios (SNR) from the ICCD system were greater than that achieved with a conventional gamma camera ($p_{\text{value}} \ll 0.01$). Analysis of SNR versus contrast showed greater sensitivity of optical over nuclear imaging for subcutaneous tumors.

In vivo and rapid detection of ICG in the blood-stream of nude mice was accomplished with a home-built avalanche photodiode dynamic fluorescence measurement system. Intensity data upon i.v. injection were regressed with a pharmacokinetic model describing the partitioning of ICG from the blood to the surrounding tissues. ICG blood-clearance was detected approximately 15 min after injection.

Lastly, a human subject protocol was written, practiced, and federally approved for the application of optical lymphography. Furthermore, ICG was unaffected when mixed with sulfur colloids thus supporting the feasibility for combining fluorescence imaging with lymphoscintigraphy in breast cancer patients.

DEDICATION

*To my husband, Kevin,
for always being by my side.*

ACKNOWLEDGEMENTS

I would like to pay tribute to several people, all of whom have greatly impacted the content of this dissertation and my tenure at the Photon Migration Laboratories. I would first like to acknowledge with utmost sincerity and appreciation my advisor, Dr. Eva M. Sevick-Muraca; her support is paramount to the success of optical imaging of sentinel lymph nodes in breast cancer patients. I am grateful to Eva as well as her husband, Paul Muraca, for providing a temporary home so that I could complete research both in Houston and College Station. Secondly, I thank my committee member Dr. Chun Li, whom is nearly my co-advisor and has allowed me to be a member of his research group for the latter 1.5 years of my project; he supported my U. T. M. D. Anderson Cancer Center studies and enabled a successful and collaborative research project. I acknowledge also my committee members, Dr. Mark Holtzapple and Dr. Gerard Cote, who helped challenge me and shape the success of my dissertation. I am very appreciative of the NSF Luis Stokes Alliance for Minority Participation Bridge-to-Doctorate Program, directed at TAMU by Dr. Karen Butler-Purry and Dr. Rita Caso; the NSF funding provided me with a noteworthy graduate stipend for 2 years.

My former and present colleagues who have become good friends deserve major recognition because without their support many projects would be incomplete or simply not possible; thank you very, very much to Dr. Alan Thompson, Dr. Mike Gurfinkel, Dr. Shi Ke, Dr. Anu Godavarty, Dr. Tianshu Pan, John Rasmussen, Dr. Wei Wang, Sunkuk Kwon, and Kildong Hwang. Also I would like to acknowledge other PML and MDACC colleagues whose advice was valued: Dr. Ranadhir Roy, Marites Pasuelo, Xiaxiao Wen,

Feng Liang, Dr. Amit Joshi and Sarabjyot Dali. I would like to thank other folks at TAMU and UTMDACC who played key roles in the clinical study and the successful component of its development including Dr. Gary Whitman, Anne-Marie Stachowiack, and Randy Marek.

My family has forever been my inspiration, my support, my role models, and without *every* single member, my success would have been completely stifled. Thank you to my husband, Kevin Houston, my mother, Francella Manzanares, my father, Jacob A. Perea, my sisters Gwendolyn Warniment and Olivia Treasure, and their husbands, Adam Warniment and Morgan Treasure. Thank you also to my second family, Richard, Susan, and Rick Houston, and Julie Lunsford.

NOMENCLATURE

Abbreviations:

1-D	one-dimensional
3-D	three-dimensional
a.u.	arbitrary unit
AC	alternating current
A/D	analog-to-digital
APD	avalanche photodiode
car	carotene
CCD	charge-coupled device
CT	computed tomography
CW	continuous wave
Cy	Cyanine
DAQ	data acquisition
DC	direct current
DIUF	deionized ultrafiltered
DLS	dynamic light scattering
DTTCI	3,3'-diethylthiatricarbocyanine iodide
FACS	fluorescence activated cell sorting
FAD	flavin adenine dinucleotide
FDA	Food and Drug Administration
FDPM	frequency-domain photon migration
FFT	fast Fourier transform
GPIB	general purpose interface bus
HPPH	hexylpyropheophorbide
HSA	human serum albumin
ICCD	intensified charge-coupled device
ICG	indocyanine green
IDE	investigational device exemption
IMAG	imaginary
IND	investigational new drug
IR	infrared
kRGDf	lysine-arginine-glycine-aspartic acid-lysine
M21	melanoma tumor cells with a high expression of $\alpha V\beta 3$ integrin membrane receptors
M21-L	melanoma tumor cells with a low expression of $\alpha V\beta 3$ integrin membrane receptors
Mab	monoclonal antibody
MCAM	Siemens gamma camera
MCP	multi-channel plate
MDACC	M. D. Anderson Cancer Center

Abbreviations continued:

MR	magnetic resonance
NADH	nicotinamide adenine dinucleotide
NIR	near-infrared
NT	normal tissue
OD	optical density
PASP	sodium polyaspartate
PET	positron emission tomography
PML	Photon Migration Laboratories
RF	radio frequency
REAL	real component of imaginary function
ROI	region of interest
ROIs	regions of interest
SLN	sentinel lymph node
SLNM	sentinel lymph node mapping
SNR	signal-to-noise ratio
SPECT	single photon emission computed tomography
TBR	target-to-background ratio
TD	time domain
TPSF	time point spread function
WB	whole body
WW317	cyclic peptide conjugated to ¹¹¹ Indium and IRDye800
WW307	cyclic peptide conjugated to IRDye800
WW396	two cyclic peptides (dimer) conjugated to IRDye800

English symbols:

<i>c</i>	speed of light [m/sec]
<i>C</i>	contrast
<i>DS</i>	detector signal
<i>D</i>	diffusion coefficient [cm]
<i>f</i>	Fourier transform spectrum
<i>FS</i>	fluorescent signal
<i>g</i>	mean cosine of scattering angle
<i>h</i>	Planck's constant [J*s]
<i>i</i>	imaginary number
<i>I</i>	attenuated light intensity [a.u.]
<i>I₀</i>	incident light intensity [a.u.]
<i>I_{AC}</i>	amplitude of intensity-modulated light [a.u.]
<i>I_{DC}</i>	mean intensity of modulated light [a.u.]
<i>k</i>	non-radiative relaxation rate [s ⁻¹]
<i>MS</i>	mixed signal
<i>n</i>	refractive index

English symbols continued:

N	number of samples in Fourier transform
PS	projected signal
P	probability
r	position
t	time [sec]
z	depth position [cm]

Greek symbols:

α	subunit of the membrane protein, integrin
β	subunit of the membrane protein, integrin
ε	Beer-Lambert extinction coefficient
ϕ	fluorescence quantum yield
Φ	photon fluence rate [W/cm^2]
Γ	radiative relaxation rate [sec^{-1}]
λ	wavelength of light [nm]
μ_a	absorption coefficient [cm^{-1}]
μ_{amf}	absorption coefficient due to fluorophores at fluorescent emission wavelength [cm^{-1}]
μ_{axf}	absorption coefficient due to fluorophores at excitation wavelength [cm^{-1}]
μ_s	scattering coefficient [cm^{-1}]
μ_s'	reduced scattering coefficient [cm^{-1}]
ν	frequency of light: speed of light divided by the wavelength of light [sec^{-1}]
θ	phase of intensity-modulated light [$^\circ$] or [rad]
σ	standard deviation
τ	average fluorophore lifetime [ns]
ω	angular frequency of intensity modulation [rad/sec]

Subscripts:

AC	alternating current
DC	direct current
inst	instrument
m	fluorescent emission
nr	non-radiative
x	excitation

Superscripts:

t	target
b	background

TABLE OF CONTENTS

	Page
ABSTRACT	iii
DEDICATION	v
ACKNOWLEDGEMENTS	vi
NOMENCLATURE	viii
TABLE OF CONTENTS	xi
LIST OF TABLES	xiv
LIST OF FIGURES	xvi
1. INTRODUCTION	1
1.1 Near-infrared Optical Imaging as a Molecular Imaging Tool	2
1.2 Significance for Cancer Staging by Sentinel Lymph Node Mapping in Breast Cancer Patients	4
1.3 Organization of Dissertation	9
2. BACKGROUND	11
2.1 Fluorescence Photon Migration Theory	11
2.2 Fluorescence Measurement Methods	15
2.3 Fluorescence Photon Migration Model	17
2.4 Fluorescence Measurement Geometries	19
2.5 Contrast Agents for Fluorescence FDPM Imaging	21
2.5.1 Exogenous Non-Specific and Disease-Specific Fluorophores	38
2.5.2 Non-Specific or Disease-Specific Nano-particles	43
2.5.3 Endogenous Fluorophores	44
2.5.4 Fluorescent Proteins	45
2.5.5 Bioluminescent Enzymes	45
2.5.6 Dual-Modality Nuclear and Optical Imaging	46
3. INSTRUMENTATION, MATERIALS, AND FLUORESCENCE MEASUREMENT METHODS	48
3.1 ICCD Camera System	49
3.1.1 CCD Camera	50

	Page
3.1.2 Image Intensifier.....	52
3.1.3 Modulation Instruments	54
3.1.4 Laser Components	55
3.1.5 Clinical Accessories	56
3.1.6 Optical Components and Accessories That Minimize Image Artifacts	58
3.2 FDPM Data Acquisition Methods.....	59
3.3 Phantom and Target Materials	63
3.4 Optical and Gamma Imaging Instrumentation.....	70
3.4.3 Small Animal Optical Imaging System.....	71
3.4.4 Small Animal Gamma Camera.....	72
3.5 Fluorescence Point Detection Measurement System	74
3.5.1 Avalanche Photodiode.....	76
3.5.2 DAQ Instruments	77
3.5.3 Fiber Optic Probe	77
3.5.4 Other Optic Accessories.....	78
4. PHASE 1: IMAGING PHANTOMS	80
4.1 Probablistic Model of Penetration Depth.....	80
4.2 Probability Distributions in the Frequency Domain for a Homogeneously Distributed Fluorophore Excited by a Planar Wave	85
4.3 Analytical Predictions for Comparison to Phantom Experiments	87
4.5 Experimental Design.....	88
4.5.1 Homogeneous Experiment	89
4.5.2 Heterogeneous Experiment	90
4.6 Results and Discussion on Probability Analysis Predictions.....	91
4.7 Results and Discussion on Homogeneous Phantom Experiments vs. Analytical Predictions.....	99
4.8 Results and Discussion on Heterogeneous Phantom Experiments	116
5. PHASE 2: IMAGING SMALL ANIMALS.....	136
5.1 Optical Imaging vs. Conventional Nuclear Imaging.....	136
5.1.1 Dual-labeled Contrast-agent.....	137
5.1.2 Animal Studies	139
5.1.3 Image Processing.....	140
5.1.4 Calculation of Nuclear vs. Optical	141
5.1.5 Results of Nuclear and Optical Image Comparison	144
5.1.6 Discussion of Nuclear and Optical Imaging Comparison.....	153
5.2 Single-point Fluorescence Detection in the Mouse Ear.....	160
5.2.1 Pharmacokinetic Model of Contrast Agent Uptake in Small Animals	161
5.2.2 Animal Studies	165

	Page
5.2.3 Results of Pharmacokinetic Mapping using the Fiber Optic Fluorescence Measurement System.....	167
5.2.4 Discussion on Single Point Fluorescence Measurements <i>in vivo</i>	171
6. PHASE 3: IMAGING PATIENTS	173
6.1 Stability of ICG and Sulfur Colloid	173
6.1.1 Fluorescence Spectra.....	174
6.1.2 Particle Sizing.....	179
6.2 Protocol	187
6.2.1 Objectives.....	187
6.2.2 Background	187
6.2.3 Procedural Steps.....	188
6.3 Standard Operating Procedure for Clinical ICCD Imager	191
6.4 Statistical Considerations and Data Management.....	192
7. SUMMARY AND CONCLUSIONS.....	194
REFERENCES.....	198
APPENDIX I CALCULATION OF ATTENUATED EXCITATION AND EMISSION WAVE	220
VITA	223

LIST OF TABLES

		Page
Table 1.1	Lists of different imaging modalities that have been developed to visualize the lymphatic system for cancer staging.....	7
Table 2.1	Chronological listing of fluorescent contrast agent studies on small animals <i>in vivo</i>	23
Table 3.1	Summary of phantoms investigated with the resulting optical properties measured using FDPH heterodyne instrumentation at the PML. The summary includes the concentration of Liposyn® and absorbing ink used, type of fluorophore employed and resulting optical properties.....	68
Table 4.1	Matrix of experiments performed for homogeneous phantom measurements in which either ICG or DTTCI was used. The frequency was varied in increments of 30 MHz starting from 30 MHz to 130 MHz, and the scattering solution was either a 1% (vol/vol) solution of Liposyn® in water or a 0.5 % solution.....	90
Table 4.2	Matrix of experiments performed for heterogeneous phantom measurements in which either ICG or DTTCI was used. The frequency was varied in increments of 30 MHz starting from 30 MHz to 130 MHz, and the scattering solution was a 0.5 % (vol/vol) solution of Liposyn® in DIUF water.....	91
Table 5.1	Specifications of the parameters used to collect images using the intensified CCD camera system and the M.CAM small animal gamma imager. All images were obtained under the instrumentation parameters outlined, with the exception of one M.CAM image that was arbitrarily cropped to 648 × 900 pixels (resolution unchanged) and three animals that were imaged with a smaller field of view during the optical imaging study (values in parentheses).....	143
Table 5.2	Summary of the mean projected signals for the M21 tumor ROI, the whole body (WB) ROI, the M21-L ROI and the normal tissue (NT) ROI. All mean intensity values listed in the table were computed following Equation 5.1. The resulting ROI data are from the ICCD imaging system and M.CAM system's measured 16-bit intensities [a.u.]. The error bar values are standard deviations computed on the mean projected signal.....	149

Table 5.3	Target to background ratios, signal to noise ratios, and contrast values computed following Equations 5.2, 5.3, and 5.4. The SNR value is from the M21 target and M21-L background. The resulting TBR values for the (i) M21 target with M21-L background, the (ii) M21 target with NT background, and the (iii) M21 target with WB background are outlined. The contrast results were computed using the target M21 tumor and the background M21-L tumor. The error bars are relative standard deviation values propagated for the computed ratios.	150
Table 6.1	The University of Texas M. D. Anderson Cancer Center Nuclear Medicine sentinel lymph node mapping general procedure combined with fluorescence-enhanced optical imaging as described in the ID01-512 protocol	189
Table 6.2	The step-by-step operation of frequency-domain optical imaging to be undertaken on human subjects undergoing sentinel lymph node mapping in the nuclear imaging suite. The steps are part of the optical lymphography protocol.	191

LIST OF FIGURES

		Page
Figure 1.1	Organization of dissertation.....	10
Figure 2.1	Absorbance spectra of tissue with a shaded region to indicate the wavelength range of the NIR imaging window. Adapted from Lim and Soter. ⁶⁰	12
Figure 2.2	Jablonski diagram illustrating radiative and non-radiative photon relaxation. Adapted from Lakowicz. ⁷⁹	15
Figure 2.3	Illustration of frequency domain photon migration. The red emission wave is dampened in amplitude and shifted in phase relative to the blue excitation wave.....	16
Figure 2.4	Illustration of reflectance (top) and trans-illumination imaging (bottom) geometries. In reflectance imaging the laser is incident on the same tissue surface that detection occurs and in trans-illumination imaging the detector is on a different tissue surface than the incident laser beam.....	21
Figure 2.5	Chemical structure (top) and normalized fluorescence spectrum (bottom) of indocyanine green fluorescent dye. The excitation spectrum is taken with the emission monochromator at 830 nm and the emission spectrum is taken with the excitation monochromator at 785 nm. Indocyanine green was dissolved in DIUF water.....	39
Figure 3.1	Illustration of the intensified charge-coupled device camera system components, which includes the image intensifier circuitry and modulation instruments.....	50
Figure 3.2	The 16-bit CCD camera head with fiber taper. Illustration reproduced from Roper Scientific, Tucson, AZ.....	52
Figure 3.3	Illustration of how the ICCD system is housed within the mobile cart and how the CCD head is mounted onto an articulating arm.....	57
Figure 3.4	Photograph of the clinical ICCD camera system. Instrumentation resides in the interior of the cart, which is on casters for mobility around the nuclear imaging suite.	57

	Page
Figure 3.5	Dimensions of the Vertica-L Pendant Strong Arm® used to mount the CCD camera head. Reproduced from design specifications provided by Strong Arm Designs, Inc.....58
Figure 3.6	Illustration of phantom and fiber optic imaging system for detection of the depth of fluorescence penetration in a homogenous scattering solution. The fibers are inserted into the center of the phantom for detection of fluorescence and relayed to an "interfacing plate" which the ICCD camera system images.65
Figure 3.7	Photograph of cylindrical phantom with fiber optics inserted into the center for fluorescence depth measurements.....66
Figure 3.8	Illustration of heterogeneous phantom containing a fluorescent target.....69
Figure 3.9	Photograph of the fluorescent target used in the heterogeneous phantom study.69
Figure 3.10	Small animal gamma camera (photograph on left) and illustration of the components of a conventional gamma camera (on right).74
Figure 3.11	Illustration of fluorescence point detection measurement system for detecting dynamic fluorescence changes in the blood of a live nude mouse.75
Figure 3.12	Hamamatsu APD module used for cw fluorescence detection <i>in vivo</i>76
Figure 3.13	Drawing of the bifurcated fiber bundle used for fluorescence measurements on the mouse ear reproduced with permission from RoMack Inc.79
Figure 4.1	Illustration of photon propagation through a scattering solution. Illumination with an expanded beam at time $t=0$, creates the planar propagation of excitation light. The excitation light is absorbed by a fluorophore at time t' and spherical fluorescence emission is emitted at time t^* . The fluorescent or phosphorescent photon travels to the surface to be detected at time, t . The transit time from emission to the surface is described by time $t-t^*$82

Figure 4.2	The phantom on the left contains a homogeneous distribution of optical properties having a uniform distribution of fluorophore, which is depicted by the green shaded area. The phantom on the right contains a cubic fluorescent target with optical properties different from its homogeneous surroundings, which is illustrated by the difference in color between the target and background. As depicted in the homogeneous phantom, a planar wave propagates through the medium and upon reaching a fluorophore at any location a spherical emission photon density wave is produced. Alternatively, with a phantom containing a fluorescent target, the propagating photon density wave reaches the target region, which is the only location where spherical emission waves are produced.	89
Figure 4.3	Normalized probability distribution of fluorescence spontaneously re-emitted over the depth, z , and for varying times, t . The reduced scattering and absorption coefficients are equivalent to $\mu_s' = 10 \text{ cm}^{-1}$ and $\mu_{\text{axf}} = 0.02 \text{ cm}^{-1}$, respectively.	92
Figure 4.4	Normalized probability distribution of fluorescence from a fluorophore with a lifetime of 10 ns distributed over the dimensionless depth, z , and for varying times, t . The reduced scattering and absorption coefficients are equivalent to $\mu_s' = 10 \text{ cm}^{-1}$ and $\mu_{\text{axf}} = 0.02 \text{ cm}^{-1}$, respectively.	93
Figure 4.5	Normalized probability distribution of fluorescence spontaneously re-emitted over the depth, z and for varying frequencies, ω . The reduced scattering and absorption coefficients are equivalent to $\mu_s' = 10 \text{ cm}^{-1}$ and $\mu_{\text{axf}} = 0.02 \text{ cm}^{-1}$, respectively.	95
Figure 4.6	Normalized probability distribution of fluorescence from a fluorophore with a lifetime of 10 ns distributed over the depth, z and for varying frequencies, ω . The reduced scattering and absorption coefficients are: $\mu_s' = 10 \text{ cm}^{-1}$, $\mu_{\text{axf}} = 0.02 \text{ cm}^{-1}$	96
Figure 4.7	Mean depth, $\langle z \rangle$, versus detection time, t , (a), and mean depth, $\langle z \rangle$, versus modulation frequency, ω , (b) calculated from a PDF analysis on a fluorescent solution with uniform concentration of fluorophore at lifetimes of 0, 1, and 10 ns.	98

- Figure 4.8 I_{AC} (top left), θ (top right), I_{AC} relative error (bottom left) and absolute θ error (bottom right) vs. depth measured at 30 MHz. Experimental data (dotted points) are plotted with predictions (solid line) for a phantom in which $\mu_a = 0.063 \text{ cm}^{-1}$, $\mu_s' = 17 \text{ cm}^{-1}$, and $\tau = 1.18 \text{ ns}$. The error bars on the phase plot represent the standard deviation in the pixel region of interest selected. 101
- Figure 4.9 I_{AC} (top left), θ (top right), I_{AC} relative error (bottom left) and absolute θ error (bottom right) vs. depth measured at 60 MHz. Experimental data (dotted points) are plotted with predictions (solid line) for a phantom in which $\mu_a = 0.063 \text{ cm}^{-1}$, $\mu_s' = 17 \text{ cm}^{-1}$, and $\tau = 1.18 \text{ ns}$. The error bars on the phase plot represent the standard deviation in the pixel region of interest selected. 102
- Figure 4.10 I_{AC} (top left), θ (top right), I_{AC} relative error (bottom left) and absolute θ error (bottom right) vs. depth measured at 90 MHz. Experimental data (dotted points) are plotted with predictions (solid line) for a phantom in which $\mu_a = 0.18 \text{ cm}^{-1}$, $\mu_s' = 10 \text{ cm}^{-1}$, and $\tau = 0.56 \text{ ns}$. The error bars on the phase plot represent the standard deviation in the pixel region of interest selected. 103
- Figure 4.11 I_{AC} (top left), θ (top right), I_{AC} relative error (bottom left) and absolute θ error (bottom right) vs. depth measured at 100 MHz. Experimental data (dotted points) are plotted with predictions (solid line) for a phantom in which $\mu_a = 0.1 \text{ cm}^{-1}$, $\mu_s' = 5 \text{ cm}^{-1}$, and $\tau = 0.56 \text{ ns}$. The error bars on the phase plot represent the standard deviation in the pixel region of interest selected. 104
- Figure 4.12 I_{AC} (top left), θ (top right), I_{AC} relative error (bottom left) and absolute θ error (bottom right) vs. depth measured at 130 MHz. Experimental data (dotted points) are plotted with predictions (solid line) for a phantom in which $\mu_a = 0.0063 \text{ cm}^{-1}$, $\mu_s' = 17 \text{ cm}^{-1}$, and $\tau = 1.18 \text{ ns}$. The error bars on the phase plot represent the standard deviation in the pixel region of interest selected. 105

- Figure 4.13 Experiments (dotted line) vs. predictions (solid line) for a highly absorbing (blue color, $\mu_a = 0.12 \text{ cm}^{-1}$) and low absorbing (red color, $\mu_a = 0.03 \text{ cm}^{-1}$) phantom ($\mu_s' = 10 \text{ cm}^{-1}$). The amplitude (top left), phase (top right), amplitude relative error (bottom left) and absolute phase error (bottom right) are plotted versus depth. The error bars on the phase plot represent the standard deviation in the pixel region of interest selected..... 108
- Figure 4.14 Experiments (dotted line) vs. predictions (solid line) for a highly scattering (red color, $\mu_s' = 10 \text{ cm}^{-1}$) and low scattering (blue color, $\mu_s' = 20 \text{ cm}^{-1}$) phantom ($\mu_a = 0.1 \text{ cm}^{-1}$). The amplitude (top left), phase (top right), amplitude relative error (bottom left) and absolute phase error (bottom right) are plotted versus depth. The error bars on the phase plot represent the standard deviation in the pixel region of interest selected..... 109
- Figure 4.15 Experiments (dotted line) vs. predictions (solid line) for high frequency (red color) and low frequency (blue color) measurements on a homogeneous phantom with optical properties: $\mu_a = 0.04 \text{ cm}^{-1}$ and $\mu_s' = 10 \text{ cm}^{-1}$. The amplitude (top left), phase (top right), amplitude relative error (bottom left) and absolute phase error (bottom right) are plotted versus depth. The error bars on the phase plot represent the standard deviation in the pixel region of interest selected..... 110
- Figure 4.16 Experiments (dotted line) vs. predictions (solid line) for a large lifetime (red color, $\tau = 1.18 \text{ ns}$) and small lifetime (red color, $\tau = 0.56 \text{ ns}$) phantom ($\mu_a = 0.04 \text{ cm}^{-1}$, $\mu_s' = 10 \text{ cm}^{-1}$). The amplitude (top left), phase (top right), amplitude relative error (bottom left) and absolute phase error (bottom right) are plotted versus depth. The error bars on the phase plot represent the standard deviation in the pixel region of interest selected..... 112
- Figure 4.17 Mean depth experimental results for 30, 60, 90, 100, and 130 MHz. Data were acquired from a phantom with a fluorophore lifetime of 1.18 ns (blue) and a fluorophore lifetime equal to 0.56 ns (red). The error bars represent the standard deviation computed on the mean value. 114

- Figure 4.18 Mean depth experimental results (solid bars) as well as predictions (striped bars) for 30, 60, 90, 100, and 130 MHz. Data were acquired from a phantom with a fluorophore lifetime of 1.18 ns (blue) and a fluorophore lifetime equal to 0.56 ns (red). The error bars represent the standard deviation computed on the mean value. 115
- Figure 4.19 Normalized I_{DC} (top left), I_{AC} (top right), θ (bottom left), I_{AC}/I_{DC} (bottom right) versus tissue depth for a 1 μM fluorescent ICG target immersed 1.5 cm below the surface of a non-fluorescing phantom. The target optical properties were: $\mu_a = 0.12 \text{ cm}^{-1}$, and $\mu_s' = 10 \text{ cm}^{-1}$, and the background optical properties were: $\mu_a = 0.1 \text{ cm}^{-1}$ and $\mu_s' = 10 \text{ cm}^{-1}$. Measurements were acquired at 30 (red points), 60 (yellow points), 90 (green points), 100 (blue points), and 130 MHz (magenta points)..... 117
- Figure 4.20 Normalized I_{DC} (top left), I_{AC} (top right), θ (bottom left), I_{AC}/I_{DC} (bottom right) versus tissue depth for a 1 μM fluorescent ICG target immersed 3.5 cm below the surface of a non-fluorescing phantom. The target optical properties were: $\mu_a = 0.12 \text{ cm}^{-1}$, and $\mu_s' = 10 \text{ cm}^{-1}$, and the background optical properties were: $\mu_a = 0.1 \text{ cm}^{-1}$ and $\mu_s' = 10 \text{ cm}^{-1}$. Measurements were acquired at 30 (red points), 60 (yellow points), 90 (green points), 100 (blue points), and 130 MHz (magenta points)..... 118
- Figure 4.21 Normalized I_{DC} (top left), I_{AC} (top right), θ (bottom left), I_{AC}/I_{DC} (bottom right) versus tissue depth for a 1 μM fluorescent ICG target immersed 5.5 cm below the surface of a non-fluorescing phantom. The target optical properties were: $\mu_a = 0.12 \text{ cm}^{-1}$, and $\mu_s' = 10 \text{ cm}^{-1}$, and the background optical properties were: $\mu_a = 0.1 \text{ cm}^{-1}$ and $\mu_s' = 10 \text{ cm}^{-1}$. Measurements were acquired at 30 (red points), 60 (yellow points), 90 (green points), 100 (blue points), and 130 MHz (magenta points)..... 119

- Figure 4.22 Normalized I_{DC} (top left), I_{AC} (top right), θ (bottom left), I_{AC}/I_{DC} (bottom right) versus tissue depth for a 1 μM fluorescent DTTCI target immersed 1.5 cm below the surface of a non-fluorescing phantom. The target optical properties were: $\mu_a = 0.063 \text{ cm}^{-1}$, and $\mu_s' = 10 \text{ cm}^{-1}$, and the background optical properties were: $\mu_a = 0.01 \text{ cm}^{-1}$ and $\mu_s' = 10 \text{ cm}^{-1}$. Measurements were acquired at 30 (red points), 60 (yellow points), 90 (green points), 100 (blue points), and 130 MHz (magenta points)..... 120
- Figure 4.23 Normalized I_{DC} (top left), I_{AC} (top right), θ (bottom left), I_{AC}/I_{DC} (bottom right) versus tissue depth for a 1 μM fluorescent DTTCI target immersed 3.5 cm below the surface of a non-fluorescing phantom. The target optical properties were: $\mu_a = 0.063 \text{ cm}^{-1}$, and $\mu_s' = 10 \text{ cm}^{-1}$, and the background optical properties were: $\mu_a = 0.01 \text{ cm}^{-1}$ and $\mu_s' = 10 \text{ cm}^{-1}$. Measurements were acquired at 30 (red points), 60 (yellow points), 90 (green points), 100 (blue points), and 130 MHz (magenta points)..... 121
- Figure 4.24 Normalized I_{DC} (top left), I_{AC} (top right), θ (bottom left), I_{AC}/I_{DC} (bottom right) versus tissue depth for a 1 μM fluorescent DTTCI target immersed 5.5 cm below the surface of a non-fluorescing phantom. The target optical properties were: $\mu_a = 0.063 \text{ cm}^{-1}$, and $\mu_s' = 10 \text{ cm}^{-1}$, and the background optical properties were: $\mu_a = 0.01 \text{ cm}^{-1}$ and $\mu_s' = 10 \text{ cm}^{-1}$. Measurements were acquired at 30 (red points), 60 (yellow points), 90 (green points), 100 (blue points), and 130 MHz (magenta points)..... 122
- Figure 4.25 Normalized I_{DC} (top left), I_{AC} (top right), θ (bottom left), I_{AC}/I_{DC} (bottom right) versus tissue depth for a 1 μM fluorescent ICG target immersed 1.5 cm below the surface of a phantom with a 10^{-8} M uniform concentration of ICG. The target optical properties were: $\mu_a = 0.12 \text{ cm}^{-1}$, and $\mu_s' = 10 \text{ cm}^{-1}$, and the background optical properties were: $\mu_a = 0.1 \text{ cm}^{-1}$ and $\mu_s' = 10 \text{ cm}^{-1}$. Measurements were acquired at 30 (red points), 60 (yellow points), 90 (green points), 100 (blue points), and 130 MHz (magenta points). 124

- Figure 4.26 Normalized I_{DC} (top left), I_{AC} (top right), θ (bottom left), I_{AC}/I_{DC} (bottom right) versus tissue depth for a 1 μM fluorescent ICG target immersed 3.5 cm below the surface of a phantom with a 10^{-8} M uniform concentration of ICG. The target optical properties were: $\mu_a = 0.12 \text{ cm}^{-1}$, and $\mu_s' = 10 \text{ cm}^{-1}$, and the background optical properties were: $\mu_a = 0.1 \text{ cm}^{-1}$ and $\mu_s' = 10 \text{ cm}^{-1}$. Measurements were acquired at 30 (red points), 60 (yellow points), 90 (green points), 100 (blue points), and 130 MHz (magenta points). 125
- Figure 4.27 Normalized I_{DC} (top left), I_{AC} (top right), θ (bottom left), I_{AC}/I_{DC} (bottom right) versus tissue depth for a 1 μM fluorescent ICG target immersed 5.5 cm below the surface of a phantom with a 10^{-8} M uniform concentration of ICG. The target optical properties were: $\mu_a = 0.12 \text{ cm}^{-1}$, and $\mu_s' = 10 \text{ cm}^{-1}$, and the background optical properties were: $\mu_a = 0.1 \text{ cm}^{-1}$ and $\mu_s' = 10 \text{ cm}^{-1}$. Measurements were acquired at 30 (red points), 60 (yellow points), 90 (green points), 100 (blue points), and 130 MHz (magenta points). 126
- Figure 4.28 Normalized I_{DC} (top left), I_{AC} (top right), θ (bottom left), I_{AC}/I_{DC} (bottom right) versus tissue depth for a 1 μM fluorescent DTTCl target immersed 1.5 cm below the surface of a phantom with a 10^{-8} M uniform concentration of DTTCl. The target optical properties were: $\mu_a = 0.063 \text{ cm}^{-1}$, and $\mu_s' = 10 \text{ cm}^{-1}$, and the background optical properties were: $\mu_a = 0.01 \text{ cm}^{-1}$ and $\mu_s' = 10 \text{ cm}^{-1}$. Measurements were acquired at 30 (red points), 60 (yellow points), 90 (green points), 100 (blue points), and 130 MHz (magenta points). 128
- Figure 4.29 Normalized I_{DC} (top left), I_{AC} (top right), θ (bottom left), I_{AC}/I_{DC} (bottom right) versus tissue depth for a 1 μM fluorescent DTTCl target immersed 3.5 cm below the surface of a phantom with a 10^{-8} M uniform concentration of DTTCl. The target optical properties were: $\tau = 1.18 \text{ ns}$, $\mu_a = 0.063 \text{ cm}^{-1}$, and $\mu_s' = 10 \text{ cm}^{-1}$, and the background optical properties were: $\mu_a = 0.1 \text{ cm}^{-1}$ and $\mu_s' = 10 \text{ cm}^{-1}$. Measurements were acquired at 30 (red points), 60 (yellow points), 90 (green points), 100 (blue points), and 130 MHz (magenta points). 129

- Figure 4.30 Normalized I_{DC} (top left), I_{AC} (top right), θ (bottom left), I_{AC}/I_{DC} (bottom right) versus tissue depth for a 1 μM fluorescent DTTCl target immersed 5.5 cm below the surface of a phantom with a 10^{-8} M uniform concentration of DTTCl. The target optical properties were: $\tau = 1.18$ ns, $\mu_a = 0.063$ cm^{-1} , and $\mu_s' = 10$ cm^{-1} , and the background optical properties were: $\mu_a = 0.1$ cm^{-1} and $\mu_s' = 10$ cm^{-1} . Measurements were acquired at 30 (red points), 60 (yellow points), 90 (green points), 100 (blue points), and 130 MHz (magenta points)..... 130
- Figure 4.31 I_{DC} area measurement acquired at the surface of a phantom with a 1 μM fluorescent target ($\tau = 1.18$ ns, $\mu_a = 0.063$ cm^{-1} , $\mu_s' = 10$ cm^{-1}) immersed 1.5 cm (top), 3.5 cm (middle), and 5.5 cm (bottom) below the surface of a non-fluorescing Liposyn® scattering solution ($\tau = 1.18$ ns, $\mu_a = 0.01$ cm^{-1} , $\mu_s' = 10$ cm^{-1}). The color bars represent the arbitrary intensity levels of DC..... 132
- Figure 4.32 I_{AC} area measurement acquired at the surface of a phantom with a 1 μM fluorescent target ($\tau = 1.18$ ns, $\mu_a = 0.063$ cm^{-1} , $\mu_s' = 10$ cm^{-1}) immersed 1.5 cm (top), 3.5 cm (middle), and 5.5 cm (bottom) below the surface of a non-fluorescing Liposyn® scattering solution ($\tau = 1.18$ ns, $\mu_a = 0.01$ cm^{-1} , $\mu_s' = 10$ cm^{-1}). The color bars represent the arbitrary intensity levels of I_{AC} 133
- Figure 4.33 I_{DC} area measurement acquired at the surface of a phantom with a 1 μM fluorescent target ($\tau = 1.18$ ns, $\mu_a = 0.063$ cm^{-1} , $\mu_s' = 10$ cm^{-1}) immersed 1.5 cm (top), 3.5 cm (middle), and 5.5 cm (bottom) below the surface of a fluorescing Liposyn® scattering solution ($\tau = 1.18$ ns, $\mu_a = 0.01$ cm^{-1} , $\mu_s' = 10$ cm^{-1}). The color bars represent the arbitrary intensity levels of I_{AC} 134
- Figure 4.34 I_{AC} area measurement acquired at the surface of a phantom with a 1 μM fluorescent target ($\tau = 1.18$ ns, $\mu_a = 0.063$ cm^{-1} , $\mu_s' = 10$ cm^{-1}) immersed 1.5 cm (top), 3.5 cm (middle), and 5.5 cm (bottom) below the surface of a fluorescing Liposyn® scattering solution ($\tau = 1.18$ ns, $\mu_a = 0.01$ cm^{-1} , $\mu_s' = 10$ cm^{-1}). The color bars represent the arbitrary intensity levels of I_{AC} 135

Figure 5.1	Chemical structure of cyclic RGD peptide (courtesy of Dr. Wei Wang) dual-labeled with IRDye800 and a derivative of diethylenetriaminepenta-acetic acid.....	138
Figure 5.2	White light (left), nuclear scintigram (center), and fluorescence-enhanced optical image (right) of a typical nude mouse xenograph bearing an integrin-positive (M21) tumor in the left thigh (right side: anterior view is displayed by figure) and an integrin-negative (M21-L) tumor in the right thigh (left side: anterior view is displayed by figure). The digital photo of the animal depicts the regions of interest (ROIs) selected for the collection of intensity signals either in the positive tumor, negative tumor, or normal tissue regions. The nuclear and optical images show a low signal in the negative (M21-L) tumor (left side), a high signal in the bladder indicating wash-out of the dye, and a high signal in the integrin positive (M21) tumor (right side). The optical image was plotted in a pseudo-color format for enhancement of the intensity scale in the tumor and background. The nuclear image was also adjusted with the same color scale for better discrimination between the several levels of gray provided by the 16-bit image. The nuclear image was acquired after 15 minutes of integration whereas the optical image was acquired for a total exposure time of 800 ms.	146
Figure 5.3	White light (left), nuclear scintigram (center), and fluorescence-enhanced optical image (right) of the remaining five nude mice xenografts (a - e).	147
Figure 5.4	Bar plots of target to background ratios (top) and signal to noise ratios (bottom) of the M21 tumor region of interest to the M21-L tumor background region of interest computed from NIR (dark-shaded) and gamma (light-shaded) images for all six animals studied. Error bars represent the relative standard deviation.	151
Figure 5.5	SNR vs. contrast calculated using Equations 5.3 and 5.4 using optical and nuclear image intensity data [a.u.]. The expected linear relationship between the SNR and contrast are different between optical and nuclear. That is, the optical imaging SNR vs. contrast slope is dramatically increased over the nuclear imaging SNR vs. contrast.	152

Figure 5.6	Two (top) and three (bottom) compartment generic pharmacokinetic models used to describe the uptake of a fluorescent contrast agent by either (i) the blood and tissue; (ii) the blood, extravascular, extracellular space and the cell membrane; (ii) the extravascular endothelium, vascular endothelium and cell membrane; or (iii) the vascular endothelium, extravascular endothelium and the cell membrane.....	163
Figure 5.7	APD fluorescence intensity [a.u.] data acquired from the tail veins of three normal nude mice. Data from animal #1 are plotted in blue, data from animal #2 are plotted in red and data from animal #3 are plotted in black. The intensity measurements are plotted versus data acquisition time [s] and were acquired upon a bolus intravenous injection of 1 μ M of indocyanine green.	168
Figure 5.8	ICCD images of three nude mice before indocyanine green injection (left), upon injection (middle) and 15 min after injection (right). Data from animal #1 are plotted in figure 5.7 (a), data from animal #2 are plotted in figure 5.7 (b) and data from animal #3 are plotted in figure 5.7 (c). The images are plotted in a monochrome pseudocolor scheme.	169
Figure 5.9	Fluorescence ROI ICCD intensity [a.u.] data acquired from the right flanks of three normal nude mice. Data from animal #1 are plotted in blue, data from animal #2 are plotted in red and data from animal #3 are plotted in black. The intensity measurements are plotted versus data acquisition time [sec] and were acquired upon a bolus intravenous injection of 1 μ M of indocyanine green. Error bars represent the standard deviation in the pixel intensity values for each ROI drawn.....	170
Figure 5.10	APD fluorescence intensity [a.u.] vs. time and with a corresponding non-linear regression. Data from animal #1 are plotted in blue, data from animal #2 are plotted in red and data from animal #3 are plotted in black. The intensity measurements were acquired upon a bolus intravenous injection of 1 μ M of indocyanine green.	172

Figure 6.1	Normalized excitation and emission spectral data of a 1- μ M concentration of ICG in DIUF water (blue excitation and pink emission lines), a 0.5- μ M concentration of ICG in DIUF water (yellow excitation and cyan emission lines), and DIUF water (orange excitation and purple emission lines).....	176
Figure 6.2	Normalized excitation and emission spectral data of a 1- μ M concentration of ICG in DIUF water (blue excitation and pink emission lines) and sulfur colloid suspension (yellow excitation and cyan emission lines).	177
Figure 6.3	Normalized excitation and emission spectra of a 1- μ M concentration of ICG in DIUF water (blue excitation and pink emission lines), and a 1- μ M concentration of ICG in a sulfur colloid suspension (orange excitation and green emission lines).	179
Figure 6.4(a)	Dynamic light scattering size report of the filtered sulfur colloid used for SLNM. The average diameter of the particle was measured using a Zetasizer (Malvern Instruments Ltd, Malvern UK).....	181
Figure 6.4(b)	Second page of the dynamic light scattering size report of the filtered sulfur colloid used for SLNM.....	182
Figure 6.5(a)	Dynamic light scattering size report of a mixture of 1- μ M of indocyanine green and filtered sulfur colloid used for SLNM. The average diameter of the particle was measured using a Zetasizer (Malvern Instruments Ltd, Malvern UK).....	183
Figure 6.5(b)	Second page of the dynamic light scattering size report of a mixture of 1- μ M indocyanine green and filtered sulfur colloid used for SLNM.....	184
Figure 6.6(a)	Dynamic light scattering size report of 1- μ M of indocyanine green in DIUF water. The size report was obtained from a Zetasizer (Malvern Instruments Ltd, Malvern UK).....	185
Figure 6.6(b)	Second page of the dynamic light scattering size report of 1- μ M indocyanine green in DIUF water.	186

1. INTRODUCTION

While present medical imaging modalities assess anatomical and morphological changes of cancer due to tumor growth and regression, only nuclear medicine offers a means for *molecular imaging* of cancer. Nuclear medicine is a non-invasive diagnostic imaging tool which enables oncologists and researchers to not only identify the presence of a tumor but also detect molecular signatures of cancer such as tumor metabolism, hypoxia, proliferation, apoptosis, vasculature, and angiogenesis.¹ Nuclear medicine is the gold standard for molecular imaging of cancer and is achieved by injecting a decaying radionuclide into the body. The radionuclide to be injected is typically bound to a biological moiety that will have affinity toward or interaction with a molecular target distinctly present at the disease site or abnormality that is to be detected. The accumulation of the radionuclide permits the detection of localized radioactive decay and projection of the detected signal into two-dimensional pictures portraying the location of the cancer-specific radionuclide.

Nuclear medicine is clinically robust and involves sophisticated modalities such as single photon emission computed tomography (SPECT) and positron emission tomography (PET), yet there are several factors that limit its practicability. Nuclear imaging requires injection of an ionizing form of radiation, gamma emissions, directly into the body and the resulting slow extravasation of that radionuclide as it homes in on the cancerous tissue. Moreover, the instrumentation sensitively detects decaying

This dissertation follows the style of *Journal of Biomedical Optics*.

radionuclides that are deeply seated within the body yet unfortunately, it is costly, requires long integration times, has limited resolution, and suffers from poor signal-to-noise and target-to-background ratios when compared to the fastest growing radiative emission and molecular imaging technique, optical imaging.

1.1 Near-infrared Optical Imaging as a Molecular Imaging Tool

Optical imaging measures photon migration, the time-dependent transport of near infrared (NIR) light within the body. Detection of NIR photons by optical techniques is non-invasive and non-radiative dependent. That is, NIR photons are non-ionizing falling within a much lower energy window (~ 0.001 to 10 eV) on the electromagnetic spectrum than gamma emissions ($\sim 10^3$ to 10^7 eV). Except for the difference in radiation type, optical imaging is similar to nuclear imaging because it relies on the injection of a disease-specific moiety into the body for cancer localization and imaging. Typically, optical imaging involves the injection of molecules that fluoresce in response to excitation by an external light source. The fluorescent molecule is tagged with a biological moiety that facilitates accumulation into the diseased tissue at the cancer cell surface or interior. Upon externally exposing the tissue to an excitation light source which penetrates the body and reaches the embedded fluorophore, fluorescence emission occurs. In turn, the emitted light is externally detected by sensitive photon detectors, and an image is produced portraying the location of the disease-specific fluorescent molecule.

In some instances, optical imaging may provide an improved means of molecular imaging in relation to nuclear medicine. Optical imaging sensitivity is promising, evidenced mainly by the fact that fluorescence is a repeatable process unlike radioactive

decay. Furthermore, optical imaging has a theoretical sensitivity that exceeds nuclear imaging by several orders of magnitude; the number of radiative events per second emitted by optical techniques is 10^{19} times more abundant than the total emitted by radionuclides. Section 5 discusses the comparison of radionuclide emissions and fluorescence emission in more detail. Additionally, fluorescence-enhanced optical imaging is able to detect femtomole² (10^{-15}) quantities of fluorescent molecules, which can lead to the detection of single clusters of cancer cells, unlike nuclear imaging, which is limited by the quantity of contrast agent injected.

Currently, NIR fluorescence-enhanced optical imaging is under development for the detection of breast cancer. With cancer-targeting fluorescent molecules, optical techniques, like nuclear techniques, have the potential to identify breast tumors and precancerous lesions for delineation and resection as well as detect cellular functions that are important to the detection of breast cancer and assessment of breast cancer therapies. Fluorescence-enhanced imaging of the breast with disease-specific fluorescent molecules is in its infancy having yet to be clinically translated. At the Photon Migration Laboratories however, work toward fluorescence-enhanced imaging of the breast has been heavily developing. Promising studies include tomographic reconstructions of large breast-shaped phantoms³ and molecular *in vivo* imaging on breast cancer xenografts.⁴ Thus, following the continued development of fluorescence-enhanced photon migration for breast cancer detection, this thesis presents a human subjects study to translate to the clinic fluorescence-enhanced optical imaging for detection of breast cancer metastases. Accordingly, the aims are (i) the development of

a clinically robust fluorescence-enhanced optical imaging detection system, (ii) the evaluation of imaging sensitivity in phantom models in comparison to simulations, (iii) the assessment of optical imaging in relation to nuclear imaging using *in vivo* models, (iv) the development of a measurement system to measure the kinetics of fluorophore in the blood, and (v) the potential to detect fluorescence in breast cancer patients undergoing a nuclear medicine procedure for the detection of cancer metastases in the lymph.

1.2 Significance for Cancer Staging by Sentinel Lymph Node Mapping in Breast Cancer Patients

One of the current standards of care for determining metastasis of cancer is the staging of the lymph nodes that surround the primary tumor. Because tumors lack lymphatics, during growth drainage from the tumor occurs through the extravascular space and into the regional lymph nodes, potentially enabling metastases. As a prognostic indicator of metastases, the lymph nodes are resected and a histological analysis can indicate if cancer cells have spread by lymphatic drainage. The sentinel lymph node is the first lymph node to harbor tumor metastases. If the sentinel lymph node is not positive, then it is unlikely that the downstream axillary nodes are positive. Therefore, resection of the sentinel lymph node prevents morbidity associated with resection of the axillary and surrounding lymph nodes, the previously accepted and widely used method for cancer prognosis. Sentinel lymph node mapping (SLNM) has been 91 to 100% effective in greater than 95% of patients,⁵⁻⁸ and has shown to accurately predict axillary node status in 98% of all cases.^{9, 10} Sentinel lymph node

mapping is currently used for esophageal, lung, skin, endometrial, thyroid, and colorectal cancers.¹¹⁻¹⁷

Prior to extracting the sentinel lymph node, a majority of centers use a nuclear medicine technique known as lymphoscintigraphy. Lymphoscintigraphy involves injection of a radionuclide subcutaneously into the tumor-bearing breast. For SLNM the radionuclide most often employed is technetium 99m, a gamma emitter with a 6-hour half life. The technetium 99m is tagged with a filtered sulfur colloid, which aids accumulation of the gamma-emitter into the lymphatic system and lymph nodes. Once the sulfur-tagged radionuclide, or radiopharmaceutical, fully diffuses into the lymph channels and lymph nodes, imaging is performed with a gamma camera. Based on the lymphoscintigram, or nuclear image of the lymph, the surgeon may locate the sentinel lymph node for resection the next day.

The surgical procedure generally involves two additional sentinel lymph node-localization steps to identify where the node resides. Immediately before surgery, the surgeon locates the source of radiation with a hand held gamma probe to detect "hot-spots" over the skin. Additionally before surgery, a blue dye, isosulfan blue, which quickly extravasates to the sentinel node, is peritumorally injected to help the surgeon visually mark and locate the blue-colored node during surgical resection. The sentinel lymph node is located with an increased accuracy when all three localization methods (i.e., imaging, gamma probe, and blue-dye) are used.¹⁸⁻²⁰

Yet the preoperative lymphoscintigraphy step, which should provide the location of the sentinel lymph node, may instead provide false-negative results. It has been reported that between 3 to 30% of sentinel lymph nodes are not detected by lymphoscintigraphy but are detected surgically with the gamma probe, or blue dye.²¹⁻²³ Several factors influencing this non-visualization are related to the inadequate drainage of the radiopharmaceutical to the sentinel lymph node. The cause for poor drainage may be due to (i) the age of the cancer patient and size of the breast--the sentinel node may reside at depths >4 cm below the tissue surface, (ii) slow drainage of the technetium 99m colloid through the lymphatic channels, (iii) disruption of drainage due to the presence of scar tissue, (iv) low uptake of the technetium 99m colloid due to hyperplasia, (v) fatty degeneration and gross metastasis, and (vi) changes in the physiologic integrity of the lymph node.²¹⁻³² In addition, factors such as the size of colloid, injection site, injection volume, and timing of the imaging scans are not standardized thus contribute to failed SLNM procedures.^{22, 28, 33, 34} In fact, a few studies suggest that due to the overall failure to detect the sentinel lymph node, weighted by the cost and time required to perform the procedure, lymphoscintigraphy may not be required altogether.^{20, 35}

In light of the difficulties of nuclear techniques, many imaging modalities are developing to map the lymph channels. Table 1.1 outlines the current modalities studied for lymphatic mapping in addition to nuclear medicine techniques. The imaging systems loosely include: (i) magnetic resonance imaging (MRI) with gadolinium or iron oxide particle enhancement, (ii) x-ray imaging and x-ray computed tomography (CT) with iodine enhancement, (iii) acoustic imaging with gas-filled microsphere enhancement,

and (iv) optical imaging with endogenous chromophores, fluorescent molecules or inorganic quantum dot particles. Some of the recent examples using magnetic resonance imaging include visualization of lymphatic drainage in dog legs based on a gadopentetate dimeglumine contrast agent³⁶ and visualization of the entire mouse lymphatic system using dendrimer-tagged PAMAM-G8 gadolinium.³⁷ X-ray imaging examples with contrast enhancement are less common, however recent studies have involved radiograph lymphography for the mapping of the lymph in rabbits with iodine-based contrast enhancement³⁸ and computed tomography of the sentinel node in the breast with an iodinated contrast agent.³⁹ A recent study involving acoustic techniques employed sub-micron microspheres containing gas to detect sentinel lymph nodes *in vivo* using a canine model.⁴⁰ Because contrast agents for ultrasound imaging are still developing, acoustic applications for lymphatic imaging are limited to invasive laparoscopic ultrasound procedures as in the gastrointestinal tumor staging study by Gretschel *et al.*⁴¹

Table 1.1 Lists of different imaging modalities that have been developed to visualize the lymphatic system for cancer staging.

Imaging Modality for Lymphatic Mapping
Nuclear Lymphoscintigraphy:
Gamma camera, SPECT, or PET imaging with radiopharmaceuticals tagged with colloid.
MR Lymphography:
Magnetic resonance imaging with gadolinium contrast enhancement.
CT Lymphography:
X-ray computed tomography images with enhancement typically with iodine.
Lymphangiography:
Simple radiograph images are obtained with iodine-based enhancement.
Acoustical Lymphography:
Ultrasound-based imaging using gas-filled microspheres or invasive laparoscopes.
Optical Lymphography:
Fluorescence optical imaging with chromophores, fluorophores or quantum dots.

Among these various lymphography studies, "optical lymphography" has emerged promisingly. Optical imaging of the lymphatics involves the visualization of the lymph channels and sentinel lymph nodes with optical photon detectors and visible-to-infrared light sources. Some examples of lymph node detection using optical imaging involve contrast enhancement with endogenous chromophores as well as fluorescent agents such as indocyanine green (ICG), fluorescein isothiocyanate (FITC), Cyanine 5.5 (Cy5.5) and quantum dots. Recent examples of metastatic sentinel lymph node detection with ICG involve invasive fluorescence detection with electronic endoscopes, which were used on gastric cancer patients.^{42, 43} ICG has also been employed as a dye for visual demarcation of the sentinel node, similar to isosulfan blue.^{44, 45} FITC has been used *in vivo* for fluorescence microlymphography on systemic sclerosis patients; FITC was injected into the hand to image the skin's lymphatic capillaries.^{46, 47} Microlymphography has also been performed in mice for intra-tumor lymph imaging and detection of lymphangiogenesis and hyperplasia.⁴⁸⁻⁵⁰ In a separate *ex vivo* study, fluorescence from endogenous chromophores in colorectal cancer specimens permitted differentiation between metastatic and normal lymph nodes.⁵¹ Otherwise, most larger-area non-invasive optical imaging contrast-enhanced studies have been performed in small or large animals. Reynolds *et al.*⁵² and Gurfinkel *et al.*⁵³ were first to image cancer progression *in vivo* from canine mammary tumors with hexylpyropheophorbide-carotene and indocyanine green enhancement. Frangioni and coworkers have performed several studies involving ICG or quantum dots to image the lymph nodes intraoperatively or

prior to surgery in pigs, rats, and mice.⁵⁴⁻⁵⁸ A more recent study injected a protected graft copolymer-Cyanine 5.5 into nude mice for axillary lymph node detection.⁵⁹

1.3 Organization of Dissertation

It is apparent by the several studies performed in animals as well as the limited studies in humans, that optical lymphography may greatly enhance lymph node visualization. In light of those promising results, this work aims to develop a robust fluorescence imaging system for sentinel lymph node mapping and thus close the bench-to-bedside gap that exists for fluorescence-enhanced optical imaging systems. Therefore, this dissertation provides the framework required to accomplish a federally approved clinical trial in which sentinel lymph node mapping is to be performed using an injected fluorescent contrast agent. The organization of this dissertation thus falls into three central phases to accomplish this goal: (i) imaging in phantoms, (ii) imaging in small animals with nuclear and optical comparison, and (iii) the development for imaging in patients. Figure 1.1 provides a flow chart of the organization.

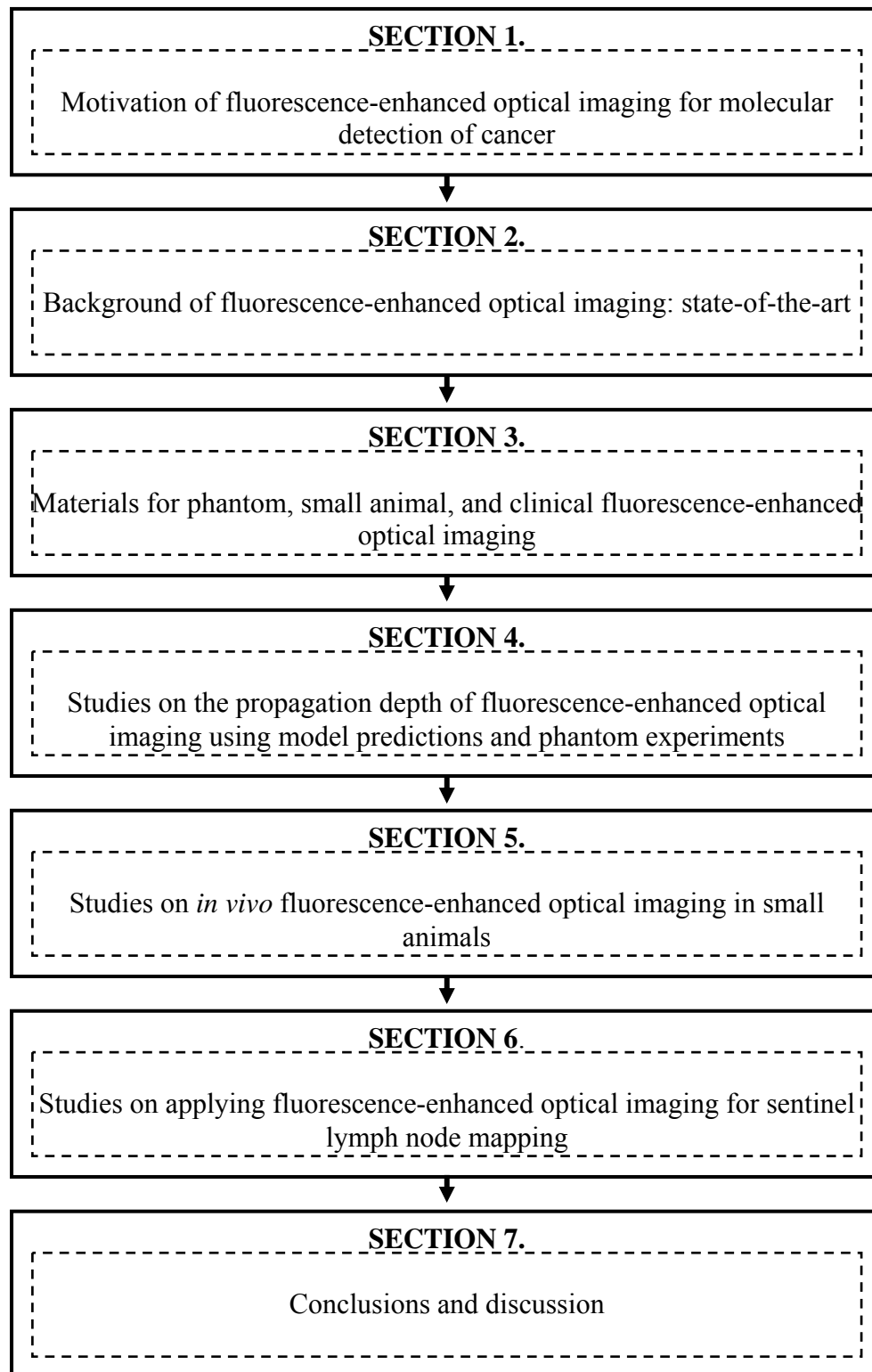


Figure 1.1 Organization of dissertation.

2. BACKGROUND

To preface the importance of the translation of optical imaging to the clinic, a complete summary is provided below describing fluorescence-enhanced optical imaging development to-date. Section 2 provides an overview on the development of optical contrast agents, a general description of fluorescence-enhanced photon migration, time-resolved imaging, optical imaging measurement methods and geometries, and models which describe the propagation of fluorescent light within scattering media.

2.1 Fluorescence Photon Migration Theory

Photon migration relies on the deep penetration of near-infrared light within the optical wavelength window of approximately 700–900 nm. Within the NIR wavelength range, blood, melanin, and water have minimal absorption. Figure 2.1 is a reproduction⁶⁰ of the absorbance spectra for oxy- and deoxy-hemoglobin, melanin, and water, showing absorption changes across the visible and infrared spectrum. Owing to the low absorption by blood, melanin, and water, NIR light has the potential to penetrate the skin deeply and scatter several centimeters into tissues. The application of photon migration involves penetrating the NIR light source onto the tissue surface for propagation within the body. The NIR light multiply scatters and minimally absorbs, and upon re-emission at the tissue surface is collected for measurements of intensity and time of NIR light propagation.

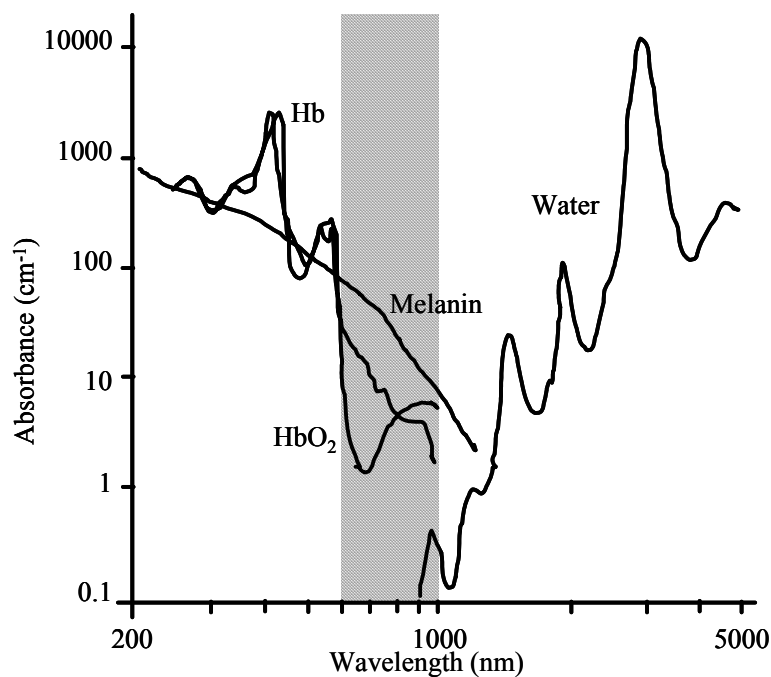


Figure 2.1 Absorbance spectra of tissue with a shaded region to indicate the wavelength range of the NIR imaging window. Adapted from Lim and Soter.⁶⁰

Tissue absorption and scattering properties, or tissue *optical properties*, are ultimately extracted from NIR photon migration measurements for the discrimination between normal and diseased tissue. The optical properties of tissue are characterized in terms of scattering and absorption probabilities. The probability for NIR light absorption is defined as the absorption coefficient, μ_a [cm^{-1}]. Similarly, the probability for diffuse NIR light scattering is defined as the reduced scattering coefficient, μ_s' [cm^{-1}]. The absorption coefficient and reduced scattering coefficient are proportional to hemoglobin concentrations, water, and fat content, thus tissue heterogeneity caused by spatial changes in blood, water, and fat content cause perturbations in μ_a and μ_s' values.

Photon migration measurements that exploit changes in μ_a and μ_s' due to blood, fat, and water content utilize endogenous chromophore contrast within the tissue. Endogenous photon migration measurements are widely studied for breast cancer. Recent work involves studies on the intact breast for the delineation of tumors,⁶¹⁻⁶³ determination of tumor and normal tissue oxygenation levels,⁶⁴⁻⁶⁹ and tomographic reconstruction of ≥ 1 -cm-sized tumors.⁷⁰⁻⁷⁵

Alternatively, exogenous fluorophores that fluoresce in the NIR provide greater contrast than is possible with endogenous contrast or with exogenously elevated levels of absorption and scattering when time-dependent methods are employed.^{76, 77} Exogenous fluorophores may be introduced into the tissue by injection, and accordingly the NIR light incident on the tissue surface will scatter and absorb until reaching the NIR fluorophore embedded within. Upon absorption of the NIR light, the fluorophore will become excited and in turn, radiatively relax. The fluorescence process occurs with molecules having several conjugated double bonds allowing for free excitation of the delocalized electrons. The fluorescence process is best described in terms of the electronic and vibrational state of the fluorescing molecule. The simplest fluorescence process occurs when light of a specific energy, $h\nu_1$ [eV], is absorbed by a molecule residing at equilibrium in a ground state, S_0 . The molecule, upon absorption of the photon's energy, is subsequently excited to a higher electronic energy level. Fluorescence occurs when the molecule radiatively relaxes, releasing the energy, $h\nu_2$ [eV], required for it to return back to its ground state. The energy of a photon is described by Planck's constant, $h=4.13\times 10^{-15}$ [eV·s], and by the photon's speed and wavelength whereby

$\nu = \frac{3 \times 10^8 \text{ m/s}}{\text{wavelength of light [m]}}$. The energy released is lower than the energy absorbed;

therefore the emitted photon wavelength is longer than the excitation photon wavelength.

In addition to radiative emission, the molecule's return to the ground state can occur in a non-irradiative manner through the release of thermal energy. Figure 2.2 is a Jablonski diagram that illustrates the process of excitation and relaxation. The ratio of the number of photons emitted to the number absorbed is the fluorescence quantum yield, ϕ , which is governed by the rate constants, Γ and k . The rate constants, Γ and k refer to the rate of radiative and non-radiative relaxation, respectively.

$$\phi = \frac{\Gamma}{\Gamma + k} \quad (2.1)$$

Similarly, the fluorophore lifetime, τ , which is typically on the order of 10^{-8} seconds, is described by the average time the molecule spends in its excited state and is mathematically shown as:

$$\tau = \frac{1}{\Gamma + k} \quad (2.2)$$

The lifetime of the fluorophore, as will be presented later in Section 4, is significant to photon migration measurements of light that has scattered greater than 1 cm, and like the optical properties, μ_a and μ_s' , lifetime can be the parameter on which tomographic reconstruction is based.⁷⁸

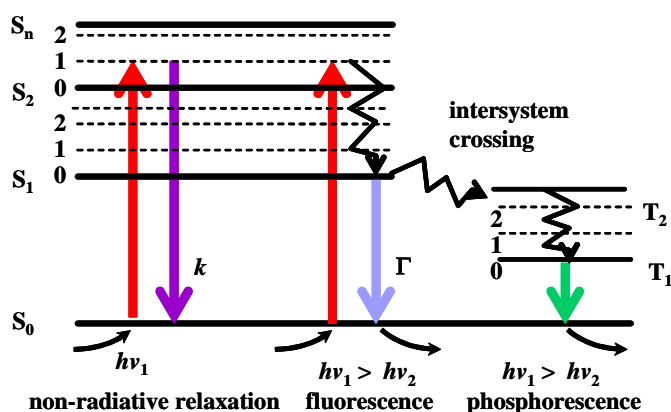


Figure 2.2 Jablonski diagram illustrating radiative and non-radiative photon relaxation. Adapted from Lakowicz.⁷⁹

2.2 Fluorescence Measurement Methods

Methods of measuring fluorescence-enhanced photon migration include both steady-state and time-resolved techniques. Steady-state, or continuous wave (CW) imaging involves capturing the fluorescent signal after excitation by a steady and continuous source of NIR light. CW imaging is a time-invariant method of photon migration in that the measurements at the tissue surface provide no information regarding how long the photons have migrated and what path-lengths they have taken as they randomly scatter within tissue. Time-domain and frequency-domain measurements not only collect the magnitude of the emitted fluorescent wave, but also photon time-of-flight characteristics which relate to both the tissue optical properties and decay kinetics of the fluorophore (τ and ϕ). Time-domain methods are typically performed by exciting the tissue with picosecond pulses of light and gating the detector to capture early

arriving photons that travel to the tissue surface within short windows of time, or performing single photon counting or streak camera measurements. Frequency-domain techniques include modulating the excitation light at a radio frequency (RF) and collecting the emitted and modulated fluorescent light at the tissue surface. The emitted light is a photon density wave that is modulated at the same frequency of the excitation wave, however dampened in amplitude, I_{AC} , and shifted in phase, θ , owing to optical property changes and fluorescence decay kinetics. Figure 2.3 illustrates the frequency-domain concept in which a modulated emission photon density wave is plotted to demonstrate its attenuation relative to a modulated excitation photon density wave.

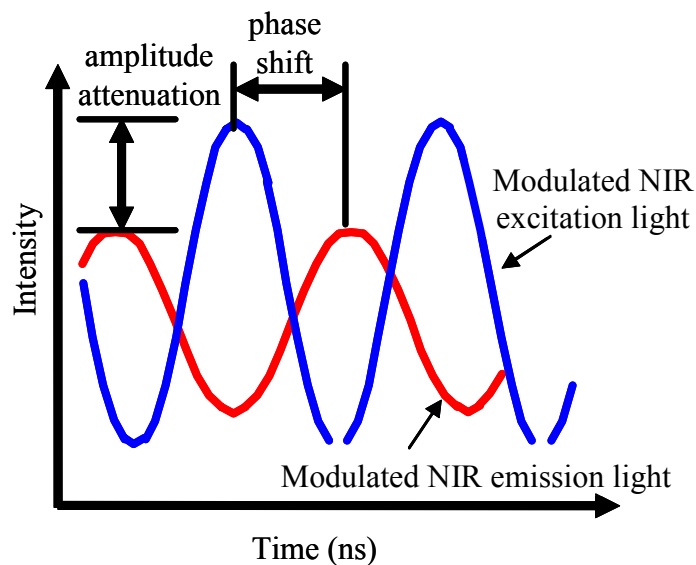


Figure 2.3 Illustration of frequency domain photon migration. The red emission wave is dampened in amplitude and shifted in phase relative to the blue excitation wave.

2.3 Fluorescence Photon Migration Model

Fluorescence-enhanced frequency-domain photon migration can be mathematically described using a first-order approximation to the radiative transport equation, the diffusion equation:

$$D\nabla^2\Phi(\mathbf{r},\omega)+\left(-\mu_a+\frac{i\omega}{c}\right)\Phi(\mathbf{r},\omega)=-S(\mathbf{r},\omega) \quad (2.3)$$

The diffusion equation describes the fluence, Φ [W/cm^2], or angle integrated flux, of photons at a position, \mathbf{r} , and modulating at a frequency, ω . Other diffusion dependent terms in this equation are D , the diffusion coefficient, $D=[3(\mu_a+\mu_s')]^{-1}$ [cm]; μ_a , the absorption coefficient [cm^{-1}]; μ_s' [cm^{-1}], the reduced scattering coefficient; c , the speed of light [cm/s]; the imaginary unit $i, \sqrt{-1}$; and S , the total power of the incident photons [W/cm^2]. This equation can be likened to an energy balance of photons in which the first term represents the diffusive flow of photons in and out of the volume, the second term represents the dampening of the diffuse photon density wave due to absorption, and the source term at the right side of the equation is a generation term. Solutions to this equation can either be obtained using appropriate analytical approximations, or numerically through finite-element or finite-difference schemes. Solving the diffusion equation with known optical properties to obtain the fluence is typically referred to as forward modeling; this is in opposition to tomographic reconstructions, which are inversion schemes that use the value of Φ , to iteratively obtain values of τ , μ_a , or μ_s' .

For a fluorescing system, photon migration occurs at two separate wavelengths, the excitation and emission wavelength. Therefore the diffusion equation can be

described for the propagation of photons at a unique wavelength. The equations below are modified with nomenclature identifying photon diffusion at the excitation and emission wavelength:

$$D_x \nabla^2 \Phi_x(\mathbf{r}, \omega) + \left(\mu_{ax} + \frac{i\omega}{c} \right) \Phi_x(\mathbf{r}, \omega) = -S_x(\mathbf{r}, \omega) \quad (2.4)$$

$$D_m \nabla^2 \Phi_m(\mathbf{r}, \omega) + \left(\mu_{am} + \frac{i\omega}{c} \right) \Phi_m(\mathbf{r}, \omega) = -S_m(\mathbf{r}, \omega) \quad (2.5)$$

where the subscript x represents photons at the excitation wavelength and the subscript m represents photons at the emission wavelength. Accordingly μ_{ax} [cm^{-1}] represents the absorption coefficient at the excitation wavelength, which is the sum of μ_{axi} [cm^{-1}] and μ_{axf} [cm^{-1}], the absorption coefficients owing to non-fluorescing chromophores and fluorophores, respectively. Conversely, μ_{am} [cm^{-1}] represents the total photon absorption at the emission wavelength. The diffusion coefficient, which was defined previously also depends on the excitation wavelength denoted by D_x and the emission wavelength denoted by D_m . $S_x(\mathbf{r}, \omega)$ is the excitation source term, which is equivalent to 1, for a sinusoidally modulated wave at frequency ω , and $S_m(\mathbf{r}, \omega)$ is the emission source term due to the generation of fluorescent photons based on the excitation fluence weighted by single exponential fluorescence decay. The emission source term is given in Equation 2.6.

$$-S_m(\mathbf{r}, \omega) = \frac{-\phi \mu_{axf}}{1 - i\omega\tau} \Phi_x(\mathbf{r}, \omega) \quad (2.6)$$

Single exponential fluorescence decay, which is incorporated into the emission source term above is obtained via a Fourier transform of the time-dependent first-order

decay kinetic expression,⁷⁹ $\frac{\phi\mu_a}{\tau}\exp\left(-\frac{t}{\tau}\right)$, describing emitted light intensity following an incident pulse of excitation light at time, t .

In addition to the frequency-domain diffusion equation, a time-domain representation can be described at the excitation and emission wavelengths. Equation 2.7 represents the general time domain diffusion equation with the photon fluence, Φ [W/cm²], expressed at position, \mathbf{r} , and time, t .

$$\frac{1}{c} \frac{\partial \Phi(\mathbf{r}, t)}{\partial t} - D \nabla^2 \Phi(\mathbf{r}, t) + \mu_a \Phi(\mathbf{r}, t) = S(\mathbf{r}, t) \quad (2.7)$$

2.4 Fluorescence Measurement Geometries

Fluorescence-enhanced photon migration measurements can be accomplished by either of two measurement geometries and through a combination of data collection schemes. The geometries include reflectance imaging, which is the penetration of light and collection of light over the same surface, or trans-illumination imaging, which is the penetration of light and collection of light over different surfaces. Figure 2.4 is an illustration of the two imaging geometries. Clinically, the most feasible geometry for optical lymphography in the breast region is reflectance imaging. Reflectance imaging can be accomplished by data collection at a single point^{78, 80} or over a large surface area.^{81, 82} Optical imaging studies that involve small animals generally employ partial or whole-body illumination of planar excitation light whereas tomographic studies involve sequential excitation illumination from single point sources with fiber optic probes. Regardless of the method employed, the complexity of adapting point illumination and

point collection measurements over large areas associated with clinically relevant volumes restricts the translation to *in vivo* measurements. For example, Culver *et al.* recently demonstrated tomographic reconstruction of μ_a from *in vivo* transmission measurements acquired on a human breast.⁸³ Yet to obtain adequate signal the breast was not only physically compressed between two parallel plates to 10 cm in width but also held for long times so that source illumination could occur in tandem through a series of 45 fibers arranged 9 fibers \times 5 fibers on an illumination lattice. To prevent the collection of sparse data sets across a spatially large area, photon migration measurements with fiber optic point illumination such as that designed by Culver *et al.*, must be raster scanned across the tissue surface. Planar illumination in a reflectance geometry does not require contact with the tissue surface nor breast compression. Additionally, planar illumination covers a much larger area such as several centimeters as opposed to point illumination which is limited to several millimeters.

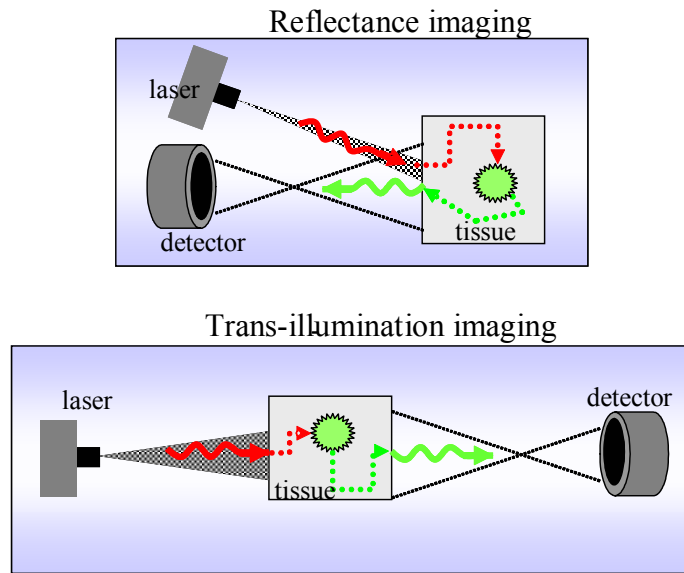


Figure 2.4 Illustration of reflectance (top) and trans-illumination imaging (bottom) geometries. In reflectance imaging the laser is incident on the same tissue surface that detection occurs and in trans-illumination imaging the detector is on a different tissue surface than the incident laser beam.

2.5 Contrast Agents for Fluorescence FDPM Imaging

Design and synthesis of fluorescent and other optical contrast agents has rapidly grown over the past several years. Fluorophores, quantum dots, nanoparticles, proteins, and bioluminescent enzymes are four of the common optical contrast agents exploited for *in vivo* optical imaging. Although any contrast agent that emits photons is promising because of the simplicity in the detection system, fluorophores are the closest to clinical translation; they have organic chemical structures that are versatile, enabling conjugation

to a number of delivery vehicles, are small enough to rapidly wash through the bloodstream, and may be detected at extremely low concentrations.

Overall, the recent flood of optical imaging studies exemplifies the ease with which optical imaging can be applied using fluorophores or other contrast agents. In general, contrast agent studies may be categorized into the following methods: (i) injection of an exogenous fluorophore molecule into the body that is non-specific or disease-specific; (ii) injection of an inorganic nano-particle into the body that is non-specific or disease-specific; (iii) detection of endogenous fluorophores in the body that are non-specific or disease-specific; (iv) creation of disease-specific “endogenous” fluorophores by transforming the body's diseased cells, or cells on which imaging is desired, with a gene that translates into an fluorescent protein; and (v) creation of disease-specific luminescence by transforming the body's diseased cells, or cells on which imaging is desired, with a gene that translates into a enzyme that catalyzes an oxidation reaction of an injected substrate to produce photons. Although not comprehensive to all five aforementioned mechanisms, Table 2.1 provides a cumulative summary of fluorescence-enhanced optical imaging studies based on *in vivo* imaging in small animals with optical systems that are continuous wave, time-resolved, or intensity-based. The following sections provide examples of the six mechanisms for contrast-enhanced imaging.

Table 2.1 Chronological listing of fluorescent contrast agent studies on small animals *in vivo*.

Author	Imaging system (incident fluence)	Animal Model	Dose	Contrast Agent	Excitation/ Emission λ	Overview
Biolo <i>et al.</i> (1991) ⁸⁴	Spectrograph for point detection of fluorescence following surface illumination	Mouse	0.12 mg/kg bw ~0.24 μ mol/ kg bw	ZnPc (Zinc Phthalocyanine) in liposomes, spectral detection of fluorescence at λ	600 nm	Study was to provide measurements for assessing pharmacokinetics of photo dynamic therapy (PDT) agent.
Pelegrin <i>et al.</i> (1991) ⁸⁵	Area illumination with area (133 mW/cm ²) detection using photography	Mouse, deceased	100 μ g/ animal ~600 pmol/ kg bw	Fluorescein isothiocyanate (FITC) coupled to monoclonal antibody (MAb)	488 nm Kodak Wratten filter #12 for excitation light rejection	Study the localization of dye targeted to human colon carconoma in mice after coupling to MAb.
Straight <i>et al.</i> (1991) ⁸⁶	Interstitial illumination (20 mW) with area detection using charge-coupled device (CCD) camera	Mouse	20 mg/kg bw ~70 μ mol/ kg bw	Photofrin II	514.5/, spectral discrimination 585-730 nm	This study validated the CCD technology for imaging drug distribution in tumors.
Folli <i>et al.</i> (1992) ⁸⁷	Fiber through endoscope illumination (10 mW/cm ²) with area detection using photography	Human	0.1-0.28 mg/ patient ~0.1nmol to 0.28 nmol/ patient	Fluorescein isothiocyanate (FITC) coupled to M Ab	488 nm Kodak Wratten filter #12 for excitation light rejection	Study immunophotodiagnosis in colon carcinoma patients.
Cubeddu <i>et al.</i> (1993,1997) ^{88, 89}	Area illumination (75 μ W/cm ²) with pulsed dye laser with gated CCD video camera	Mouse	5-25 mg/kg bw ~17-87 μ mol/ kg bw and 0.1 mg/kg ~0.35 μ mol/ kg bw	HpD (hematoporphyrin derivative)	405nm/>560 nm	Demonstrated the use of time-dependent measurements to identify HpD distinct from native fluorescence based upon long fluorescent lifetimes.
Kohl <i>et al.</i> (1993) ⁹⁰	Area detection with gated intensified CCD and area illumination with pulsed Nd:YAG laser at 60-80mJ	Mouse	0.2-1 mg/kg bw 0.7-.5 μ mol/	Porphyrin-based photosensitizers	405 nm-650 nm excitation spectra	Measured fluorescence contrast changes between tumor and normal tissue with delayed laser pulse relative to a gated image intensifier.

Table 2.1 Continued.

Author	Imaging system (incident fluence)	Animal Model	Dose	Contrast Agent	Excitation/ Emission λ	Overview
Folli <i>et al.</i> (1994) ⁹¹	Area illumination with area (13 mW/cm ²) detection using photography	Mouse, deceased	100 μ g/ animal ~600 pmol/ kg bw*	Indopentamethine-cyanine coupled to MAb directed against squamous cell carcinoma;	640 nm Kodak Wratten filter 70 for excitation light rejection	Showed the ability to detect indocyanine dye targeted to squamous cell carcinoma in the upper respiratory tract through MAb E48 without the need to remove skin as was necessary when fluorescein was employed.
Haglund <i>et al.</i> (1994) ⁹²	Area illumination (100-W tungsten-halogen bulb) and area detection with CCD.	Rat	1.0 mg/kg bw 1.3 μ mol/kg bw	Indocyanine green	780 nm / 830nm	Distinguish rat gliomas from normal brain tissue through free-agent fluorophore imaging with CCD camera.
Mordon <i>et al.</i> (1994) ⁹³	Area illumination (150W Xenon lamp, 2.5 mW/cm ²) with area detection using intensified CCD	Mouse	5 mg/kg bw (~13 μ mol)	5,6-CF carboxyfluorescein (BCECF)	465 nm/490 and 515 nm	This study showed the use of dual wavelength measurements of a ratiometric dye to provide a two-dimensional pH image of tumor tissues.
Ballou <i>et al.</i> (1995) ⁹⁴	Area illumination with area detection using intensified video camera, or cooled CCD	Mouse	10-100 μ g/ animal ~40 pmol to 6 nmol/ animal	Cyanine fluorochromes coupled to MAb	550-674 nm/565-694 nm	Demonstrated the use of tumor-targeting antibodies using Cy 3.18, Cy 5.18, and Cy 5.5.18 cyanine fluorochromes.
Devoisselle <i>et al.</i> (1995) ⁹⁵	Area (50mm ²) illumination (Xe lamp) with point detection using fiber to spectrograph	Mouse	7.5 mg/kg bw ~10 μ mol/ kg bw	Indocyanine green emulsion	720 nm/ spectra discrimination of fluorescence	Demonstrated the use of emulsion preparation to alter the pharmacokinetics of ICG.
Rokahr <i>et al.</i> (1995) ⁹⁶	N ₂ laser pulsed through fiber and detected with fiber to spectrometer	Human (urinary bladder cytoscopy)	50 mg/ patient	Protoporphyrin IX (Aminolaevulinic acid, ALA, induces fluorescence)	337 and 405/ 380 through 685 spectral discrimination	Descriminate malignant and normal bladder tissue with ALA induced protoporphyrin imaging.

Table 2.1 Continued.

Author	Imaging system (incident fluence)	Animal Model	Dose	Contrast Agent	Excitation/ Emission λ	Overview
Haglund <i>et al.</i> (1996) ⁹⁷	Area illumination with photography lights and area detection with CCD camera	Human (open brain)	1 mg/ kg bw ~1.3mmol / kg bw	Indocyanine green	790/805 nm	Study detection of human glioma with ICG imaging.
Sakatani, <i>et al.</i> (1997) ⁹⁸	Cooled CCD camera, 100 mW laser diode	Rat	554 picomoles/rat	ICG-lipoprotein	790 nm/840 nm	Cerebrospinal imaging with ICG bound to lipoprotein, injected intra-cranially.
Neri (1997) ⁹⁹	100W Tungsten lamp for area illumination with detection via an 8-bit CCD in a light tight box.	Mouse	100 μ l/mouse of a concentrated antibody solution of 1 mg/ml with 1:1 dye:Mab ratio	Fragments of human antibodies directed against oncofetal fibronectin (B-FN) and labeled with CY-7	673-748 nm/765-855 nm	Demonstrated the use of B-FN targeting for providing diagnostic imaging and therapy of cancer targeting angiogenic vessels.
Ballou <i>et al.</i> (1998) ¹⁰⁰	Area illumination and area detection via CCD	Mouse	50 μ g /animal Mab:dye (1:2) ~600 pmol/ animal	Cy3, Cy5, Cy5.5, Cy7 labeled Ab against human nucleolin and stage-specific embryonic antigen-1		Results demonstrated the ability to penetrate more deeply with Cy 7 dye.
Eker <i>et al.</i> (1999) ¹⁰¹	Fiber for excitation and collection in a colonoscope for detection via a spectrometer	Human	5 mg/kg bw ~30 nmol/ kg bw	Protoporphyrin IX, as a metabolized product of ALA (photosensitizer)	337, 405, 436 nm excitation	Demonstrated ALA as a contrast agent for detecting adenomatous polyps of the colon with promise for distinguishing adenomatous from hyperplastic polyps.
Reynolds <i>et al.</i> (1999) ⁵²	Laser area illumination (1 mW/ cm ²); intensified CCD	Canine	1.0 mg/kg bw ~1.3 μ mol/ kg bw	Indocyanine green	780 nm/830 nm	Demonstrated the ability to detect spontaneous disease of the canine mammary chain as well as reactive lymph nodes.

Table 2.1 Continued.

Author	Imaging system (incident fluence)	Animal Model	Dose	Contrast Agent	Excitation/ Emission λ	Overview
Becker <i>et al.</i> (1999) ¹⁰²	Area illumination and area detection with CCD and magnetic resonance imaging (MRI)	Mouse	2 $\mu\text{mol/kg}$ bw (1:2.4 or 2 for transferrin or HSA)	Indotricarbocyanine and ultrasmall superparamagnetic iron oxide particles coupled to transferrin or HSA		Demonstrated targeting of tumors which express the transferrin receptor using an optical agent as well as an MRI agent.
Weissleder <i>et al.</i> (1999); ¹⁰³ Mahmood <i>et al.</i> (1999) ¹⁰⁴ Tung <i>et al.</i> (2000) ¹⁰⁵	Area illumination and area detection using CCD in a light tight chamber; illumination with 150 W halogen lamp with interference filters, 10-100 $\mu\text{W}/\text{cm}^2$	Mouse	10 $\mu\text{mol/}$ animal (92 methoxypolyethyleneglycol (MPEG), 11 dye molecules); 2.5 nmol and 250 picomoles/ animal	Cy 5.5. loaded onto a polylysine and methoxypolyethylene glycol polymer backbone with cathepsin B, D, and H-cleavage sites.	610-650 nm/>700 nm	Demonstrated that tumor proteases can be used as molecular targets SNR for 30 second exposure 173 for 200 pmol in phantom.
Becker <i>et al.</i> (2000) ¹⁰⁶	Area illumination and area detection with CCD	Mouse	2 $\mu\text{mol/kg}$ bw	Transferrin and human serum albumin coupled with indotricarbocyanine dye	740 nm/ 780-900 nm	Demonstrating targeting to the tumors expressing transferrin receptor.
Gurfinkel <i>et al.</i> (2000) ⁵³	Area illumination (1.98 and 5.5 mW/cm^2) and area detection using intensified FDPM CCD system	Canine	1.1 and 1.0 mg/ kg bw ~ 1.3 $\mu\text{mol/kg}$ bw	ICG and carotene-modified PDT agent (hexylpyropheophorbide conjugated with carotene moiety) for reduction of phototoxicity	780 nm/830 nm (ICG) 660 nm/ 710 nm (HPPH-car)	Demonstrated the use of temporal AC measurements to image pharmacokinetic parameters in order to discern diseased tissues.
Licha <i>et al.</i> (2000) ¹⁰⁷	Single point detection and point illumination (5 mW) using FDPM	Rat	0.5 $\mu\text{mol/kg}$ bw	Derivatives of ICG (unclear whether fluorescence was detected in vivo).	746-780 nm/ 780-830 nm	Provided measurements of absorption at the excitation wavelength as a function of time to provide pharmacokinetic evaluation of ICG and its hydrophilic derivatives.

Table 2.1 Continued.

Author	Imaging system (incident fluence)	Animal Model	Dose	Contrast Agent	Excitation/ Emission λ	Overview
Yang <i>et al.</i> (2000) ¹⁰⁸ Hoffman <i>et al.</i> (2001)	Area illumination and detection using CCD camera	Mouse	-	Green fluorescent protein (GFP) expressed in vivo		Demonstrated visualization of tumors and tumor metastasis by whole body fluorescence imaging.
Ntzachristos <i>et al.</i> (2000) ⁷⁴	Fiber bundle to PMT using time-domain photon migration, point illumination and point detection	Human (breast)	0.25 mg/ kg bw ~0.32 μ mol/ kg bw	Indocyanine green		Fluorescence was not used, but absorption provided contrast which was validated by simultaneous MRI images obtained with gadolinium contrast.
Cubeddu <i>et al.</i> (2000) ¹⁰⁹	Area illumination (50 μ W/cm ²) and area detection using CCD camera	Mouse	2.5 and 5 mg/kg bw	Aluminum phthalocyanine	660-690 nm/720 nm	Measuring photodynamic therapy effects with fluorescence images through intensity changes.
Bugaj <i>et al.</i> (2001); ¹¹⁰ Achilefu <i>et al.</i> (2000 and 2001) ^{111, 112}	Area illumination (40 mW) and area detection using CCD camera	Rat	5.2-6.0 mg/ kg bw ~6.7-7.7 μ mol/ kg bw	ICG, ICG-small peptide conjugates cytate and cybesin	780 nm/830 nm	Targeting to rat tumor lines expressing the somatostatin and bombesin receptors.
Becker <i>et al.</i> (2000 and 2001) ^{113, 114} Licha <i>et al.</i> (2001) ¹¹⁵	Area illumination and detection using CCD camera	Mouse	0.02 μ mol/kg bw	Peptide-cyanine dye indodicarbocyanine (IDCC) and indotricarbocyanine (ITCC) conjugated to octreotate & octreotide	740nm/780-900 nm	Targeting to mouse tumor lines expressing the somatostatin receptor and /or vasoactive intestinal peptide (VIP); and the description of synthesis of the dye to the peptide, octreotide.

Table 2.1 Continued.

Author	Imaging system (incident fluence)	Animal Model	Dose	Contrast Agent	Excitation/ Emission λ	Overview
Balas (2001) ¹¹⁶	Multispectral imaging system 250-W halogen illumination by a fiberoptic bundle ring and area detection with a CCD camera	Human	unknown dose	Acetic acid	multi-spectral/ 525-nm	Imaging the cervix by measuring the reflection using cross-polarizers on the source and detector. Discrimination between cancer and normal tissue is observed after topical application of acetic acid on the tissue
Bremer. <i>et al.</i> (2001) ¹¹⁷	Area illumination and area detection using CCD in a light tight chamber; illumination with 150 W halogen lamp with interference filters, 10-100 $\mu\text{W}/\text{cm}^2$	Mouse	167 pmol/ animal, i.v.	Polylysine polymer coupled with matrix metalloproteinase (MMP)-2 peptide substrates holding Cy5.5	610-650 nm/>700 nm	Measure matrix metalloproteinase activity in vivo for directing the therapeutic use of proteinase inhibitors.
Ebert <i>et al.</i> (2001) ¹¹⁸	Area illumination with pulsed laser and detection using CCD camera (ambient light rejection)	Rat	2 $\mu\text{mol}/\text{kg}$ bw, i.v.	SIDAG (hydrophilic cyanine dye derivative), 1-1'-bis-(4-sulfbutyl) indotricarbocyanine 5,5'-dicarboxylic acid digluconate monosodium salt; Nd:Yag,	740 nm, 3 ns FWHM, 50Hz/750-800 nm	Demonstrated localization of tumor and presented phantom data using FDPM with contrast ratios of 6:1.
Finlay <i>et al.</i> (2001) ¹¹⁹	Fiber probe point illumination, point detection with fibers directed to CCD spectrograph	Rat	200 mg/ kg bw (ALA injected)	ALA induced porphyrin	514 nm /676 nm emission	Photobleaching kinetics of ALA induced protoporphyrin measured.

Table 2.1 Continued.

Author	Imaging system (incident fluence)	Animal Model	Dose	Contrast Agent	Excitation/ Emission λ	Overview
Rice <i>et al.</i> (2001) ¹²⁰	Area detection of light-emitting probes with CCD	Mouse	Bioluminescence of fluorescent proteins	Firefly luciferase	>600 nm emission	Imaging light emitting probes.
Soukous <i>et al.</i> (2001) ¹²¹	Area illumination using pumped dye laser (15 mW/cm ²) and detection using room temperature CCD camera	Hamster	670 μ g /animal ~3.3 nmol/ kg bw*	Anti-epidermal growth factor receptor (EGFR) MAb (C225) coupled to Cy 5.5 (1:2.1) IgG-Cy5.5 (1:2.3)	670 nm/ >700 nm	Demonstrated the targeted Mab-dye complex in cheek pouch tumor could be used to provide immunophotodiagnostic information thereby guiding therapeutic intervention.
Yang <i>et al.</i> (2001) ¹²²	Single pixel FDPM using point source and point detector	Rat	1.5 mg/ kg bw ~2 μ mol/ kg bw	Indocyanine green and diethyltricarbocyanine iodide (DTTCl)		Work towards demonstration of fluorescence imaging in vivo.
Boehm <i>et al.</i> (2001) ¹²³	Single pixel using multiple point and multiple detector with fiber to Siemens prototype laser mammography scanner spectrometer	Mouse	2 mmol/kg bw	Near infrared (NIR) 96010 ICG derivative; bis-1,1'-(4-sulfobutyl)-indotricarbocyanin)	775 nm/ 790 nm	Measure absorption profile in whole mouse to delineate tumor and test the prototype mammography scanner. ICG derivative used for optimum photophysical and pharmacological properties.
Zaheer <i>et al.</i> (2001) ¹²⁴	150-W halogen area illumination [18mW/cm ²] with band pass filters and area collection by Roper CCD Camera	Mouse	2.6 nanomoles/ animal	IR Dye78 conjugated to pamidronate	771 nm/ 796 nm	A comparison of MRI and nuclear imaging to optical fluorescence imaging through the detection of osteoblastic activity in vivo by conjugation of a bisphosphonate to a radionucleotide and fluorophore.

Table 2.1 Continued.

Author	Imaging system (incident fluence)	Animal Model	Dose	Contrast Agent	Excitation/ Emission λ	Overview
Chen <i>et al.</i> (2002) ¹²⁵	Imaging system similar to Ntziachristos (2001) using “fluorescence-mediated tomography”	Mouse	5 nmol/ animal	Cy 5.5. loaded onto a polylysine and methoxypolyethylene glycol polymer backbone with cathepsin B cleavage sites.	610-650 nm/ >700 nm	Imaging of atherosclerosis protease activity with “activatable fluorescent probe.”
Nakayama <i>et al.</i> (2002) ¹²⁶	250 mW laser diode area excitation and area detection with Orca-ER digital camera and a color video camera	Rat	50 nanomoles/ animal	Infrared (IR)-786 and IRDye78	771 nm/810 nm	Blood-based screening of fluorescent pathways during myocardial flow. Visualization of the heart anatomy and function was realized intra-operatively.
Ntziachristos <i>et al.</i> (2002) ¹²⁷	Point illumination with 200 mW laser diode and point detection to area detection (via interfacing plate) with 12-bit CCD	Mouse	100 nanomoles/ kg bw	Cyanine 5.5-tagged with a graft copolymer with a poly-lysine backbone and methoxypolyethylene glycol side chain to target cancer and fluoresce upon cleavage by tumor protease	670 nm/ 710 nm	Demonstrated in vivo tomographic imaging of tumor protease activity in small animals using a mouse immobilized within a cylinder filled with scattering solution.
Bremer <i>et al.</i> (2002) ¹²⁸	Area illumination and area detection using CCD in a light tight chamber; illumination with 150 W halogen lamp with interference filters	Mouse	2 nmol/ animal	Cyanine 5.5-tagged with graft co-polymer with poly-lysine backbone and methoxypolyethylene glycol side chain (cleavage sites for protease recognition)	675 nm/ 694 nm	Similar to Weissleder and Mahmood studies (1999) with the additional goal to determine expression levels of tumoral cathepsin-B activity in differentiated and undifferentiated breast cancers.

Table 2.1 Continued.

Author	Imaging system (incident fluence)	Animal Model	Dose	Contrast Agent	Excitation/ Emission λ	Overview
Solonenko <i>et al.</i> (2002) ¹²⁹	150 W mercury arc lamp delivered point source light through 640 mm fibers and point detection delivered to CCD camera	Canine	None	None	460 to 960 nm detected	Measured optical properties for blood oxygenation and motexafin lutetium uptake measurements in vivo
Ke <i>et al.</i> (2003) ¹³⁰ Gurfinkel <i>et al.</i> (2003) ¹³¹	Area illumination and detection with intensified CCD camera	Mouse	17 nanomoles/ mouse or 830 picomoles/ mouse	Cy 5.5, Indocyanine green Cy5.5 coupled to epidermal growth factor	660 nm/710 for Cy5.5 and 785nm/830nm for ICG	Studied fluorescence targeting to tumors overexpressing EGFR in vivo; presented pharmacokinetics of dye uptake into tumors and normal tissue.
Cuccia <i>et al.</i> (2003) ¹³²	Point source point detection with fibers to avalanche photodiode and network analyzer for frequency-domain measurements	Rat		Indocyanine green	785nm / 830nm	Coregistration of MRI and optical imaging in the rat combined with a pharmacokinetic model of contrast agent wash-out.
Petrovsky <i>et al.</i> (2003) ¹³³ and Schellenberger <i>et al.</i> (2003) ¹³⁴	Light-tight box with area illumination by 150-W halogen lamp and area detection with 12-bit CCD camera	Mouse	3.1 mg/kg animal	Cy5.5 coupled to Annexin	630nm/>670 nm	Studied a fluorescent probe for imaging tumor apoptosis, the principle being to couple C5.5 with annexin V, a protein with a high affinity to certain phospholipids, which are released from the cytoplasm during cell death.

Table 2.1 Continued.

Author	Imaging system (incident fluence)	Animal Model	Dose	Contrast Agent	Excitation/ Emission λ	Overview
Gannot <i>et al.</i> (2003) ¹³⁵	Area illumination and area detection with argon laser (200 MW) directed through mirrors, bandpass filters and CCD camera; continuous wave measurements	Mouse	50 μ L injected into mouse tongue and unclear what concentration of dye	Fluorescein isothiocyanate tagged with CD3 and CD19 antibodies. Targeting to lymphocytes that infiltrate tumor and tumor border	488 nm/ 520-550 nm	Demarcation of subcutaneously injected squamous cell carcinoma in mouse tongue with three-dimensional reconstruction of targeted fluorophore location. Depth of targeted fluorophore is simulated with layers of agarose gel placed over tongue.
Sokolov <i>et al.</i> (2003) ¹³⁶	Endoscope-compatible fiber optic optical coherence tomography and reflectance coherence tomography system	Human (ex vivo)		Gold nanoparticles conjugated to monoclonal antibody against epidermal growth factor receptor		Imaged cervical biopsies to screen for cancer by detecting gold nanoparticles that are targeted to EGFR.
Graves <i>et al.</i> (2003) ¹³⁷	Point source at multiple points with laser diode and optical switch and area detection with CCD	Mouse	2 nanomoles/ animal	Cyanine 5.5-tagged with a graft copolymer with a poly-lysine backbone and methoxypolyethylene glycol side chain to target cancer and fluoresce upon cleavage by tumor protease	672 nm/710 nm	Demonstrated tomographic imaging of tumor protease activity in small animals by using a parallel plate chamber with the animal immobilized within.
Intes <i>et al.</i> (2003) ¹³⁸	Point illumination and point detection to photodiodes	Human	0.25 mg/kg bw	Indocyanine green	785 nm/ 805 nm	2-D tomographic reconstructions of μ_a after injection of non-targeted ICG into the breast of cancer patients.

Table 2.1 Continued.

Author	Imaging system (incident fluence)	Animal Model	Dose	Contrast Agent	Excitation/ Emission λ	Overview
McGreevy <i>et al.</i> (2003) ¹³⁹	Endoscopic point source and detector to a CCD video camera	Porcine	1.5 mg/animal	Cyanine 5 conjugated to cobalimin, which is required by tumors to carry out one-carbon metabolism for deoxy-ribonucleic acid (DNA) synthesis	632 nm/ 668 nm	Lymphatic mapping using a fluorophore-protein (Vitamin B12) conjugate in a semi-invasive manner using endoscope. Work towards the development of lymph staging for cancer
Josephson <i>et al.</i> (2003) ⁵⁹	Halogen lamp area excitation (with bandpass filter to select the excitation wavelength between (610-650 nm) CCD detection	Mouse	2 nmoles (for subcutaneous injection) or 10 nanomoles (for intravenous injection)	Cyanine 5.5 conjugated to graft copolymer for pooling in the blood and lymph nodes	610-650 nm excitation/ 680-720 nm emission	Lymphatic mapping with fluorophore-polymer conjugate. Work towards the development of lymph staging for cancer.
Kennedy <i>et al.</i> (2003) ¹⁴⁰	200-mW laser expanded over 2-cm field of view and area detection with CCD camera	Mouse	10 nmol/ animal	Folate-fluorescein conjugate	488 m/515-585 nm	Imaging lung carcinoma tumors that over-express the folate receptor using the ligand, folic acid, bound to the fluorophore.
Lenkinski <i>et al.</i> (2003) ¹⁴¹	Area illumination and area detection with 50 mW/cm ² NIR laser diode, bandpass filters and orca-ER camera	Rat	0.1 μ mol/kg bw	Pam78, a derivative of pamidronate which binds to hydroxyapatite	770 nm/ 790-830 nm	Imaging microcalcifications from breast tumors in an animal model through the specificity of the contrast agent to hydroxiapatite calcification.
Moon <i>et al.</i> (2003) ¹⁴² Chen <i>et al.</i> (2005) ¹⁴³	Area illumination and light tight detection using CCD and 150 W halogen lamp with interference filters	Mouse	2 nmol/ animal	NIR2-folate, a near infrared fluorochrome conjugated to folate for targeting to the folate receptor	665 nm/ 686 nm	Studied fluorescence targeting to tumors over-expressing the folate receptor and arthritis <i>in vivo</i> .

Table 2.1 Continued.

Author	Imaging system (incident fluence)	Animal Model	Dose	Contrast Agent	Excitation/ Emission λ	Overview
Nakayama <i>et al.</i> (2003) ¹⁴⁴	150-mW halogen light area illumination at 50 mW/cm ² and area detection with a color video camera	Mouse	1 nmol/ animal	IR-786	760-780 nm/ 795-815 nm	Imaged brown adipose tissue perfusion by detecting intensity levels of the dye, which tends to accumulate in the mitochondria.
Chen <i>et al.</i> (2003) ¹⁴⁵	Point source and point detection with a FDPM “phase cancellation” system.	Mouse	0.2 mg/animal	Cypate-mono-2-deoxyglucose	780 nm/ 830 nm	2-D image construction of a fluorescent probe injected in a human hepatoblastoma mouse model to target glucose transporters over-expressed during tumor malignancy. Reconstruction was performed with a FDPM imaging system that uses dual sources 180° out of phase.
Citrin <i>et al.</i> (2004) ^{146, 147}	Area illumination by xenon source area detection with a Retiga camera	Mouse	0.01 mg/ animal	Cy5.5 conjugated to endostatin	675 nm/ 694 nm	Imaging lung carcinoma and determining binding efficacy of Cy5.5-labeled endostatin
Gondi <i>et al.</i> (2004) ¹⁴⁸	Area illumination and area detection using CCD in a light tight chamber; illumination with 150 W halogen lamp with interference filters, 10-100 μ W/cm ²	Mouse	10 nmol/ animal (92 methoxypoly-ethyleneglycol (MPEG), 11 dye molecules).	Cy 5.5. loaded onto a polylysine and methoxypolyethylene glycol polymer backbone with cathepsin B cleavage sites.	610-650 nm/>700 nm	Demonstrated that tumor proteases can be used as molecular targets for imaging inhibition of tumor growth with treatment of antisense urokinase plasminogen activator receptor.

Table 2.1 Continued.

Author	Imaging system (incident fluence)	Animal Model	Dose	Contrast Agent	Excitation/ Emission λ	Overview
Kircher <i>et al.</i> (2004) ¹⁴⁹	Area illumination and area detection using CCD in a light tight chamber; illumination with 150 W halogen lamp with interference filters, 10-100 $\mu\text{W}/\text{cm}^2$	Mouse	10 $\mu\text{mol}/$ animal (92 methoxypoly-ethyleneglycol (MPEG), 11 dye molecules); 2.5 nmol and 250 picomoles/ animal	Cy 5.5. and Cy 7 both dual-labeled to polylysine and methoxypolyethylene glycol polymer backbone with cathepsin B, D, and H-cleavage sites.	630 nm/700 nm, 736 nm/ 800 nm,	Demonstrated that tumor proteases can be used as molecular targets SNR for 30 second exposure 173 for 200 pmol in phantom.
Kelly <i>et al.</i> (2004) ¹⁵⁰	Endoscopy system using two channel fiber optic microendoscope	Mouse	Unknown	Cy5.5 or FITC bound to the peptide sequence, 'CPIEDRPMC', a colon cancer-specific peptide	Not specified	Demonstrated colon cancer detection with a library-derived peptide for proof of principle in developing high-throughput disease-specific fluorescent probes.
Moore <i>et al.</i> (2004) ¹⁵¹	Area illumination and area detection with Kodak CCD imaging system	Mouse		Cy5.5 conjugated to the peptide, EPPT1, as well as CLIO (cross-linked iron oxide) for MR imaging	630 nm/ >700 nm	Imaging early tumorigenesis through the targeting of the peptide to underglycosylated mucin-1 antigen
Shah <i>et al.</i> (2004) ¹⁵²	150-W halogen area illumination and area detection with a CCD camera in a light-tight chamber	Mouse	2.5 nmol/ animal	Cy5.5 bound to graft copolymer (similar to Weissleder studies)	610-650 nm/>700 nm	Imaging HIV protease activity in gliomas by detecting the fluorescence emitted after protease cleavage.
Ballou <i>et al.</i> (2004) ¹⁵³	Area illumination with four 250-W halogen lamp and area detection with Photometrics CCD	Mouse	20 pmol quantum dot/g bw	Quantum dots coated with poly(acrylic acid) polymer	450 nm/ 606, 635, 645, 655 nm	Imaged quantum dots coated with polymer to enhance biostability in mice.

Table 2.1 Continued.

Author	Imaging system (incident fluence)	Animal Model	Dose	Contrast Agent	Excitation/ Emission λ	Overview
Tigani <i>et al.</i> (2004) ¹⁵⁴	Area illumination with 3 laser diodes at 10 mW/cm ² and detection with CCD camera	Rat	20 μ L/ animal	Cy5.5 (non-specific) administered intratracheally	660 nm/ 700 nm	Imaged lobular distribution in the lung of rats and correlated to MRI.
Li <i>et al.</i> (2004) ¹⁵⁵	Raster scanned point source and point detection across tissue surface to a spectrofluorometer	Mouse (ex vivo)	54 nmol/animal	1,1'-dioctadecyl-3,3,3',3'-tetramethylindocarbocyanine perchlorate (DiI) labeled with low-density lipoprotein (LDL)	549 nm/ 564 nm	Imaged the binding of LDL to LDL receptors over-expressed in melanoma and hepatoblastoma tumors. The samples were snap-frozen from xenograft mice three hours after i.v. injection of the DiI-LDL.
Pogue <i>et al.</i> (2004)	Area and point illumination and detection using laser diode, fiber optics, PMT, and CCD	Mouse	5 mg/kg bw	aluminum phthalocyanine disulphonated (AlPcS ₂)	670 nm/ >685 nm for area detection and 633 nm/ >685 nm for raster scan	Compared raster scanned fluorescence imaging with reflectance geometry imaging in nude mice with fibrosarcoma tumors to detect the pharmacokinetics of the injected photodynamic agent.
Chen <i>et al.</i> (2004) ¹⁵⁶	Area illumination and area detection with broadband source and CCD	Mouse	0.1 to 3 nmol/animal	Cy5.5 conjugated to arginine-glycine-aspartic acid (RGD)	660 nm/ 710 nm	Imaged U87 glioblastoma tumors in xenografts by detecting fluorescence from Cy5.5 conjugated to RGD which binds to the α v β 3 integrin receptor over-expressed in the tumor.
Ghoroghchian <i>et al.</i> (2005) ¹⁵⁷	Area illumination and detection with Xenogen system	Rat	500 pmol/ animal	oligo(porphyrin) polymersome	705-765 nm/ 805-880 nm	Imaged polymersomes that fluoresce in the NIR by injecting agent into the center of a rat tumor.

Table 2.1 Continued.

Author	Imaging system (incident fluence)	Animal Model	Dose	Contrast Agent	Excitation/ Emission λ	Overview
Kwon <i>et al.</i> (2005) ¹⁵⁸	Area illumination and detection with laser diode (80 mW) and ICCD camera system	Mouse	3-10 nmol/animal	Cy5.5 labeled with RGD (arginine-glycine-aspartic acid) ligand	660 nm/ 710 nm	Measured the difference in pharmacokinetics of two tumor types. Binding rates of RGD ligands to high and low vascular tumors over-expressing the integrin receptor were evaluated.
Hwang <i>et al.</i> (2005) ¹⁵⁹	Area illumination and area detection with laser diode (80 mW) and ICCD camera system fitted with collimating optics	Mouse	3-9 nmol/ animal	Indocyanine green derivative (synthesized by Wei Wang, UTMDACC) conjugated to RGD peptide	785 nm/ 830 nm	Detected the binding of the RGD to melanoma tumors expressing integrin in order to improve the rejection of excitation light by implementing collimating lenses in front of standard fluorescence filters.
Ke <i>et al.</i> (2005) ¹⁶⁰	Area illumination and area detection with laser diode (80 mW) and ICCD camera system	Mouse	6 nmol/animal	IRDye800 conjugated to ¹¹¹ Indium and cyclic RGD peptide sequence	780 nm/ 830 nm	Demonstrated dual-modality imaging with a dual-labeled optical and nuclear imaging agent.
Hintersteiner <i>et al.</i> (2005)	Area illumination with 3 laser diodes (10 mw/cm ²) and area detection with Siemens CCD camera system	Mouse	0.01 to 3 mg/kg bw	AOI987, fluorescence oxazine dye that binds to amyloid plaques	660 nm/ 700 nm	Demonstrated <i>in vivo</i> NIR imaging of beta amyloid plaques in the brain of a mouse after i.v. injection of a plaque-targeting dye. Application for diagnostics of Alzheimer's.

2.5.1 Exogenous Non-Specific and Disease-Specific Fluorophores

When not bound to specific moieties which bind to or target diseased cells, fluorophores are characterized as non-specific. Non-specific dyes are generally washed out through the body's renal system accumulating in the kidneys and bladder within several minutes. Upon injection into the blood stream, the contrast agent will reach highly vascularized regions and may facilitate detection of abnormalities such as highly angiogenic tumors. The injection of non-specific agents remains limited because of the inability of the dye to selectively bind to diseased cells for discrimination against normal cells. Some common non-specific and exogenous fluorophores used for optical imaging include: fluorescein isothiocyanate (FITC), indocyanine green (ICG), derivatives of the cyanine dye (e.g. Cy3, Cy5, Cy5.5, Cy 7), photosensitizers (e.g. oligo-porphyrins, photoporphyrin IV, hexylpyropheophorbide-carotene), and dyes manufactured proprietarily (e.g. Licor's IRDye800).^{52, 53, 92, 132, 154} Photosensitizers have NIR emission and are thus favorable for deep tissue imaging as in the study by Reynolds *et al.*⁵² Most photosensitizers are used for photodynamic therapy however, and involve the production of porphyrin via the heme cell cycle, which requires introducing exogenous aminolaevulinic acid (ALA) into the body. Indocyanine green is particularly common because of the favorable NIR excitation and emission spectra as well as its characteristic binding to albumin in blood,⁹⁵ which enables imaging of vascularized areas more efficiently. The chemical structure and excitation and emission spectra of ICG are shown in Figure 2.5. ICG is the only federally approved dye for human subjects therefore is the exogenous contrast agent (Akorn Inc., Buffalo Grove, IL) proposed for

use in the optical lymphography for sentinel lymph node mapping studies described herein.

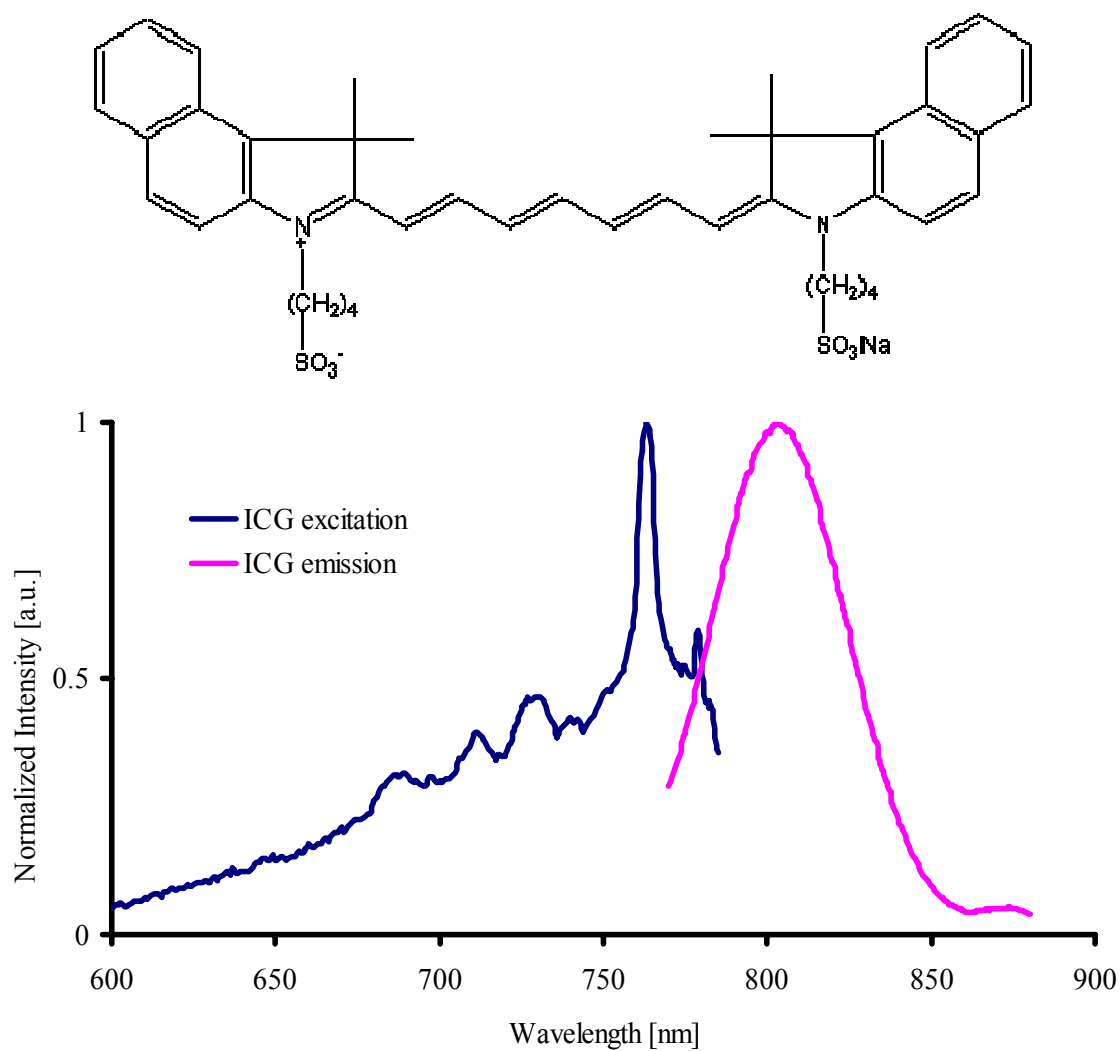


Figure 2.5 Chemical structure (top) and normalized fluorescence spectrum (bottom) of indocyanine green fluorescent dye. The excitation spectrum is taken with the emission monochromator at 830 nm and the emission spectrum is taken with the excitation monochromator at 785 nm. Indocyanine green was dissolved in DIUF water.

Fluorophores that are disease-specific may be bound to several biological moieties; one type is the fluorophore-antibody (Ab) conjugate. Fluorophore-Ab conjugates are among the earliest targeting agents and have been studied *in vivo* as early as 1991.⁸⁵ Fluorophore-Ab conjugates bind to cancer cells through an Ab-antigen mechanism in which proteins (antigens) that are specific to a cancer cell are bound by the Ab that is injected. Pelegrin *et al.* first studied this ability in mice by coupling FITC, which fluoresces at 530 nm, to a monoclonal antibody human colon carcinoma.⁸⁵ More recently, Soukos *et al.* bound an anti-epidermal growth factor receptor (anti-EGFR) monoclonal antibody to Cy 5.5 to image fluorescence from oral cancer cells, which over-express the receptor.¹²¹ There are few antibody-fluorophore conjugate studies provided in recent literature owing to the bulkiness of antibody molecules as well as their tendency to have a long blood half-life, which contributes to an elevated fluorescence background. Additionally, Ab conjugates may cause adverse immunogenic reactions in living subjects.¹⁶¹

The bulk of research on disease-specific agents involves a second type of conjugate, fluorophore-protein conjugates. Generally these fluorophore conjugates are injected into the animal body and by a simple binding mechanism will localize within or on the surface of the diseased cell. Binding of the fluorophore conjugate to the cell may occur within several minutes and continue for up to 48 hours after injection leading to high specificity of the fluorophore to the disease. The binding mechanism for the fluorophore-peptide conjugates follows a simple receptor-ligand interaction. Several cancers have well-characterized cellular compositions and are thus known to over-

express certain cell-surface receptors. Accordingly, these receptors play roles in signal transduction, proliferation, angiogenesis, and other cancer-related pathways. Ligands are typically small proteins and small amino acid sequences therefore can be synthesized and conjugated to fluorophores for fluorescence imaging of the cancer cell. Some common receptor-targeting schemes include (i) epidermal growth factor to epidermal growth factor receptor,¹³⁰ (ii) Arg-Gly-Asp (RGD) peptide to $\alpha_v\beta_3$ integrin receptor,^{156, 158, 160, 162, 163} (iii) cytate to somatostatin receptor,^{110, 164} (iv) cybesin to bombesin receptor,^{111, 165} (v) octreotate to the somatostatin receptor,¹¹⁴ (vi) folate to folate receptor,^{142, 143} (vii) low-density lipoprotein to LDL receptor,¹⁵⁵ and (viii) peripheral benzodiazepine ligand synthetically constructed in various forms to peripheral benzodiazepine receptor.¹⁶⁶

Unlike the peptide-receptor targeted mechanisms, fluorophores that are conjugated to various proteins enable molecular imaging of cell death or cancer cell metastasis. For example, the Cy5.5 fluorophore was recently tagged with annexin V¹³⁴, a protein with an affinity to phospholipid cell death byproducts, and upon injection of the contrast agent and subsequent induction of cell death, NIR fluorescence imaging of apoptosis was achieved. In another study, McGreevy *et al.* constructed a fluorophore-protein construct, ICG-cobalimin,¹³⁹ to image the accumulation of cobalimin near the tumor. Cobalimin, vitamin B₁₂, is required by tumors to carry out one-carbon metabolism for DNA synthesis. Because it is also a large protein, injection of this construct into the body enabled imaging of the lymph, albeit with invasive imaging technologies.

The fluorophore-polymer contrast agent is not as widely employed because of the large molecular weight of polymers, however has shown promise for various types of cancer imaging. For example, Weissleder *et al.*¹⁰³ designed bulky copolymers and attached them to fluorophore-peptide constructs. The constructs, which slowly extravasate through the bloodstream, do not fluoresce because the fluorophore is in a quenched state. The quenching of fluorescence occurs because excitation light energy absorbed by the fluorophore is transferred to the dominating polymer block. However upon undergoing phagocytosis by a cancerous cell expressing high levels of cancer-specific enzymes (e.g. cathepsin D, B, and matrix metalloproteinase), the fluorophore is cleaved from the bulky copolymer. Cleavage occurs by the cancer enzyme which recognizes the fluorophore-conjugated peptide sequence. Cleavage allows the now free dye to radiatively relax thus indirectly reporting levels of enzyme activity in the cancer cell. Another application using polymers for delivery to cancerous cells showed *in vivo* mapping of the lymphatics in nude mice with a graft copolymer-Cy5.5 fluorophore.⁵⁹ The removal of the copolymer-Cy5.5 construct from the body was slow because the polymer has a long blood half life, therefore as the conjugate localized in the lymph nodes, it could be imaged. Lastly, Ghoroghchian *et al.* have designed NIR emissive polymersomes, or spherical copolymers with a membrane bi-layer composed of hydrophilic heads groups and hydrophobic tails groups.¹⁵⁷ Introducing oligo-porphyrins that assimilate into the hydrophilic component enables also NIR imaging.

2.5.2 Non-Specific or Disease-Specific Nano-particles

Recently there has been a rapid increase in the development of non-organic agents for contrast-enhanced optical imaging. The synthesis of these nanoparticles includes development of quantum dots, gold nanoshells, and iron oxide and gold nanoparticles. Nanoparticles have been studied because they can be finely tuned to exhibit favorable excitation and emission properties, or other light emitting characteristics. Quantum dots, in particular, have very narrow excitation and emission spectra, thus can be imaged with high specificity. Recently Ballou *et al.* designed quantum dots and coated them with polymers to enhance their biostability in nude mice.¹⁵³ Quantum dots have also been coated with bovine serum albumin,¹⁶⁷ labeled with antibodies for prostate cancer specificity,¹⁶⁸ as well as have been designed for imaging of the lymphatics.⁵⁷ Alternatively, nanoparticles that are not fluorescent in nature, but can be optically imaged may also be designed for cancer specificity. For example, Sokolov *et al.* conjugated gold nanoparticles to monoclonal antibodies against epidermal growth factor receptor and demonstrated scattered light imaging *ex vivo* with human tissue samples.¹³⁶ Alternatively, nanoparticles can be combined with fluorescent contrast agents for multi-modality studies such as that performed by Kircher *et al.*, who conjugated Cy5.5 to an iron oxide particle, which enhances MRI images, for intraoperative brain tumor delineation.¹⁶⁹ Unfortunately, the single drawback of nanoparticles for clinical translation is their unknown fate upon injection into the body. Thus extensive testing and approvals are required to monitor and determine safe ingestion limits.

2.5.3 Endogenous Fluorophores

Exploiting the natural fluorescent contrast in tissues for optical imaging is not common in whole-body cancer or disease detection, however has been performed for several years. Natural tissue fluorescence is also known as autofluorescence. Endogenous fluorophores are used to distinguish small fluorescence spectra perturbations across a tissue sample to reflect the presence of disease, or cancer. The fluorescent signature of tissues will change with differing concentrations of endogenous fluorophores, which inevitably occurs due to changes in the pathological state of the tissue. The most common tissue fluorophores detected are NADH, FAD, collagen and elastin which excite and emit in the range: 290 nm to 520 nm.¹⁷⁰ Additionally, other obscure tissue components such as the amino acids tryptophan, tyrosine, phenylalanine, as well as the endogenous molecules pyridoxine, lipofuscin, and eosinophils can be excited for detection between 300 nm and 500 nm.¹⁷¹ Because endogenous fluorescence is not NIR, it is generally used with invasive endoscopic evaluations for internal cancers such as cervical, stomach, bladder, colon, etc. or for superficial topical measurements. Although, recently Demos *et al.* explored tissue autofluorescence in the NIR to discriminate between normal and cancerous bladder tissue *ex vivo* and reduce background fluorescence.^{172, 173} The use of endogenous fluorophores is not described in great detail because it is not within the scope of fluorescence-enhanced imaging for sentinel lymph node mapping.

2.5.4 Fluorescent Proteins

Genetically engineered endogenous fluorophores are, on the other hand, more popular for whole body optical imaging. Although these contrast agents are generally not reliable optical imaging probes because their fluorescence signals are emitted at higher energies than the NIR and they require translation of a genotype, they are nonetheless significant for small animal imaging studies. Fluorescent proteins have been widely used in biochemical assays to indicate some phenotypic expression. A gene that encodes for the fluorescent protein is introduced by a vector, or other translational method, into a diseased cell. Upon transcription into the protein, imaging can either identify the expression of some genotype, or simply the presence of a diseased cell in the body transfected with the fluorescent protein gene. The various proteins that have been studied for whole-body small animal imaging include green fluorescent protein, red fluorescent protein (RFP), and yellow fluorescent protein (YFP). More interesting work involving GFP include the detection of metastatic events and progression of cancer in nude mice with orthotopic tumors.¹⁷⁴⁻¹⁷⁷ For brevity, Table 2.1 does not include all studies to-date with GFP, YFP, and RFP.

2.5.5 Bioluminescent Enzymes

Bioluminescence is an optical imaging method that has gained immense popularity because it does not require an excitation source, or other complex optical equipment for imaging. A commercial camera system is in fact available for this application. Bioluminescence is the process in which photons are produced by a simple oxidation reaction in the cell and are captured by a CCD camera using a light-tight box

and very lengthy integration times. The production of photons occurs with the aid of a substrate that is injected into the body. The substrate however, only undergoes an oxidation reaction to produce photons if there is an enzyme present to catalyze the reaction. Thus, in order to have this enzyme present in the diseased cell, the gene encoding for the enzyme is stably transfected into the cell or diseased cells. Thus, upon injection of the substrate, photons will be produced at the disease site if there is continuous or controlled expression of the enzyme. The most common enzyme and its corresponding substrate that produce bioluminescence are luciferase and luciferin. Again, Table 2.1 does not provide a review of all bioluminescent studies, however some examples are provided below to preface the use of dual-modality imaging for the comparison of optical with gold-standard methods, which is described in Section 5.

2.5.6 Dual-Modality Nuclear and Optical Imaging

Dual-modality imaging is increasingly popular, particularly with optical contrast agents owing to the high resolution and photograph-quality images that optical systems provide. Optical imaging can easily provide a picture of the disease site in small animals for comparison to other modalities such as nuclear imaging and MRI. This thesis considers the comparison of nuclear imaging to optical imaging, therefore only studies involving gamma emission and photon emission are reviewed in this section. There are a handful of studies in the literature that combine optical and nuclear imaging. The most common examples involve bioluminescence. This combination is popular because a gene can be constructed to hold both an optical and nuclear vector. Studies by Blasberg *et al.* and Gambhir *et al.* are the most prominent and employ small animals that either (i)

express Renilla or firefly luciferase, which in the presence of ATP, oxygen, and its exogenous substrate, coelenterazine or D-luciferin, provides visible light (bioluminescence); and/or (ii) express the wild type or mutant herpes simplex virus type 1 thymidine kinase (genotype: HSV1-tk and HSV1-sr39tk, respectively), which phosphorylates PET labeled substrates such as FIAU (2'-fluoro-2'-deoxy-1- β -arabino-fluranosyl - 5 - iodouracil), FHBG (9- (4 - [18F] fluoro-3-hydroxymethylbutyl) guanine), and FPCV (8 - [18F] fluoropenciclovir).¹⁷⁸⁻¹⁸² Other non-bioluminescent studies include work by Zaheer *et al.* who injected separate optical and nuclear contrast agents to image osteoblastic activity.¹²⁴ This thesis presents work in which a dual-labeled optical and nuclear probe was injected into nude mice for direct *in vivo* comparison of optical and nuclear (see Section 5.1).^{160, 183}

Although the rapid development of contrast agents promises *in vivo* optical imaging of many different cancers, the actual clinical use of the aforementioned dye constructs, with the exception of free indocyanine green, is currently not possible. More specifically, the Food and Drug Administration (FDA) has not yet endorsed the optical contrast agents, or investigational new drugs (IND), for human subject use. As described previously, this project aims at developing an ICCD system that can easily image human subjects and detect fluorescence emission of the FDA approved contrast agent, indocyanine green. Before progressing to the results of this thesis, instrumentation, materials, and data acquisition methods for the detection of fluorescence are presented to foreshadow the resulting phantom and animal model work.

3. INSTRUMENTATION, MATERIALS, AND FLUORESCENCE

MEASUREMENT METHODS

The methodology for developing a clinical fluorescence-enhanced optical imaging system involves many contributions; research efforts include simulating photon diffusion, imaging fluorescence in tissue phantoms, imaging tumors in small animals, developing clinical protocols, and federal approval of the investigational device and imaging agent. As the aims of this work are to bridge the bench top-to-bedside gap, several research materials and methods were finely tuned for the use and/or development of three major instrumentation types: (i) an intensified charge-coupled device (ICCD) camera system for phantom and clinical imaging, (ii) nuclear and optical imaging systems for whole-body imaging in nude mice, and (iii) an avalanche photodiode (APD) detection system for single point fluorescence measurements for elucidating agent pharmacokinetics in nude mice. With these three base projects in mind, this thesis section is divided into five segments that describe: (1) the materials required for the development of an ICCD imaging system that can be used for phantom and patient studies, (2) the data acquisition procedures pertinent for ICCD imaging, (3) the materials and methods used for phantom measurements, (4) the materials and methods used for whole-body small animal nuclear and optical imaging, and (5) the materials and methods used for single-point fluorescence measurements in small animals.

3.1 ICCD Camera System

Fluorescence-enhanced ICCD camera instrumentation has long been studied and described in works from the Photon Migration Laboratories. This technology is never stagnant, and the latest generation ICCD camera system, which is modeled after prior art, includes advances in the CCD camera, the design of imaging suite mounts and support structures, addition of optical components based on functionality in small animal imaging, and optimized image acquisition methods based on previously reported FDPM measurement precision and accuracy. The main FDPM ICCD components are (1) a charge-coupled device camera, CCD cooling unit, and CCD controller, (2) an image intensifier, (3) a laser diode, diode mount, temperature controller, and laser controller, (4) two frequency signal generators and a radio-frequency amplifier, (5) a central processing unit (CPU) with a processor speed of 2.6 GHz, and (6) other mounting and optical accessories (e.g., lenses, filters, etc). An illustration of the instrumentation is provided in Figure 3.1.

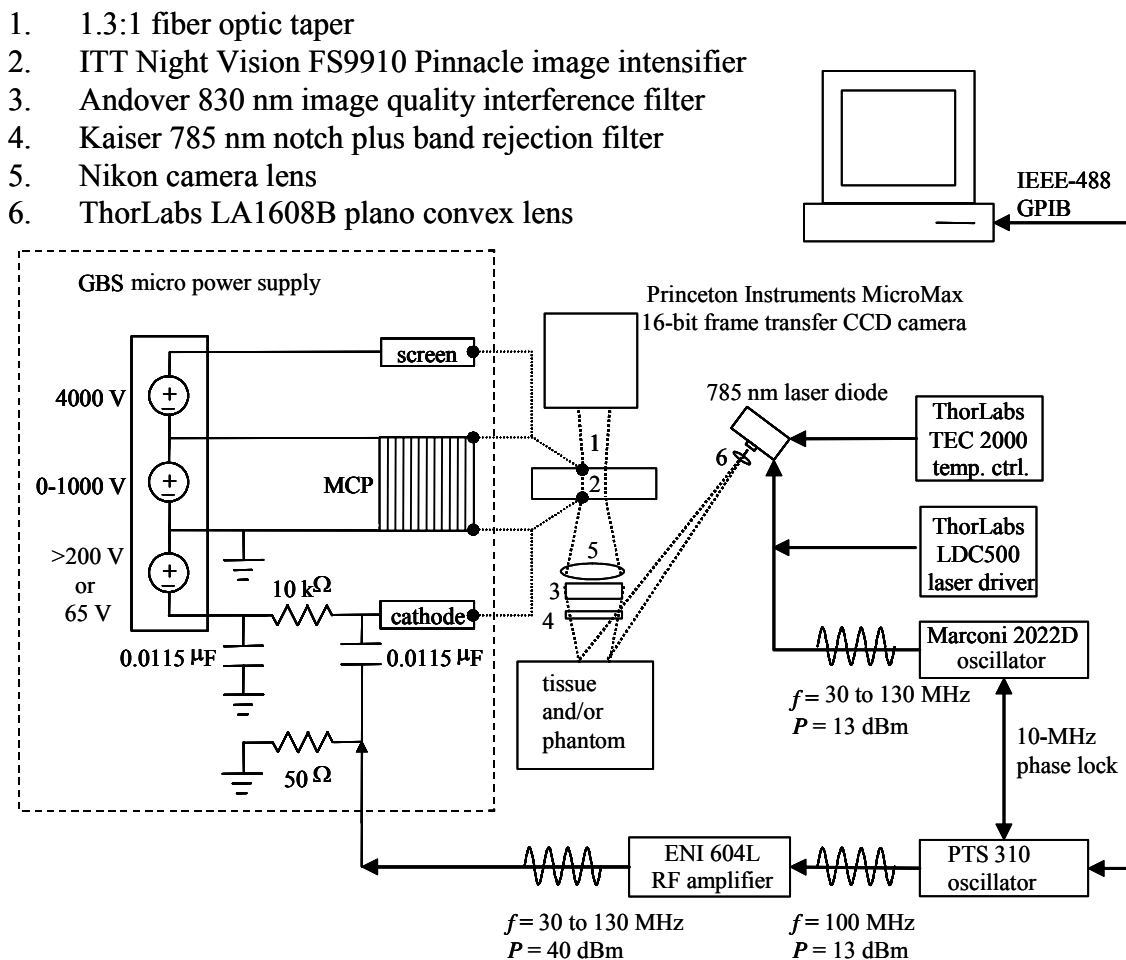


Figure 3.1 Illustration of the intensified charge-coupled device camera system components, which includes the image intensifier circuitry and modulation instruments.

3.1.1 CCD Camera

The charge-coupled device camera includes an E2V 47-20 Grade 1, 16-bit, frame transfer CCD chip with an active imaging area of 1024 x 1024 pixels; each pixel is 13 μm in length making the total active chip size approximately 13 x 13 mm^2 . The camera head displayed in Figure 3.2, controller and cooling unit are Princeton Instruments

(model: PI-SCX) and assembled by Roper Scientific in Tucson, AZ. An optimum 16-bit dynamic range where 2^{16} is equivalent to 65,536 gray levels was chosen to maximize the CCD performance. The 16 bits of data per pixel optimizes the CCD capacity to detect very dim and very bright parts of the fluorescence image under inspection. Additionally the CCD has a frame-transfer architecture with a maximum digitization frequency of 5 MHz. Separate image and storage arrays for image read-out promote rapid FDPM data collection; the integration time is approximately 5 min for acquisition of 320 images at 1000 ms exposure. The Princeton Instruments CCD camera was also designed to have a fiber bundle directly laminated to the square CCD chip with Roper Scientific's patented fiberoptic-coupling technology (US Patent 5,134,680). The fiber bundle effectively enlarges the size of the CCD so that the CCD can be directly interfaced with an 18-mm diameter, circular image intensifier, which is described below. This is the first custom-built Roper Scientific design of this type with specifications solely for this thesis to enable the circular image intensifier to be "tapered" down to the size of the CCD permitting photons to be relayed without loss of resolution. This fiber coupling "circle in a square" method involves a taper ratio of 1.3:1 which is approximately equivalent to the ratio of the image intensifier diameter to the square CCD chip length (18 mm : 13 mm). The CCD has optimum quantum efficiency within the bandwidth of approximately 200 nm to 900 nm. The increased dynamic range, fiber taper, and combined frame-transfer architecture make this system unique among all ICCD systems.

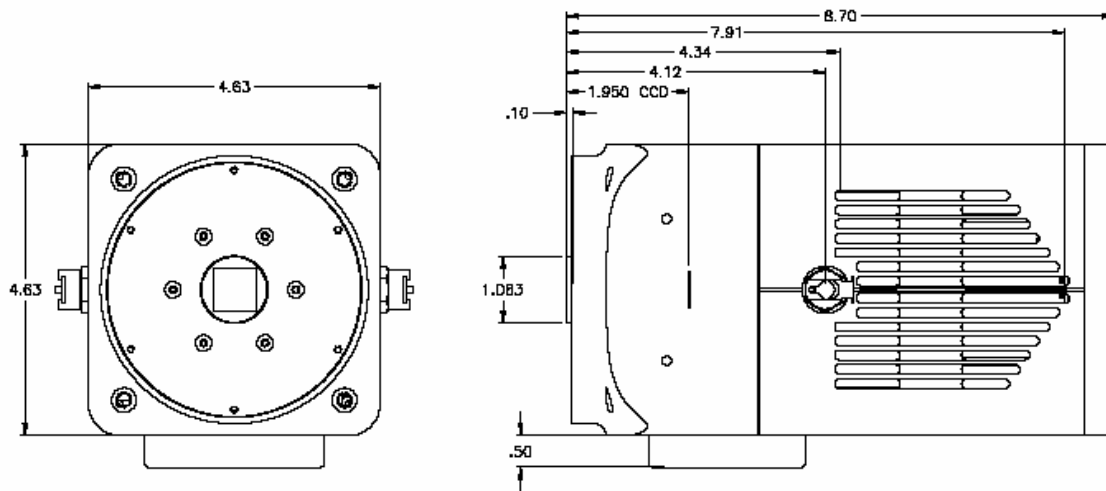


Figure 3.2 The 16-bit CCD camera head with fiber taper. Illustration reproduced from Roper Scientific, Tucson, AZ.

3.1.2 Image Intensifier

In combination with the CCD, an image intensifier promotes NIR photon detection. Used traditionally in night vision goggles for military purposes, an image intensifier is used to amplify low level light signals. For this study, the image intensifier is a Generation 3 Pinnacle™ “tube” that is 18 mm in diameter (model: FS9910, ITT NightVision, Roanoke, VA).

The image intensifier not only promotes light amplification but also permits time-resolved photon migration measurements and is composed of a photocathode, multi-channel plate (MCP), and phosphor screen. All three components work in sync whereby photons travel first into the photocathode. The photocathode collects incident photons and converts them to electrons for amplification. When a voltage potential is

created between the photocathode and the second stage, which is the MCP, the generated electrons will flow across a film barrier for amplification. An adjustable MCP gain can control the amount of light augmented. From the MCP, the amplified electrons flow to a phosphor screen. At the phosphor screen, the electrons are converted to photons and an amplified light signal is created. A 10-V fixed power supply (9 to 11 V narrow slot output with 1 A rating, model: Gold Box B10G100, Acopian, Easton, PA) in combination with a 0-10 V variable power supply (0 to 15 V output range with 1 A rating, model: Gold Box A015MX100, Acopian, Easton, PA) provide the adjustable MCP gain and power to the intensifier. The specifications for the Generation 3 Pinnacle™ image intensifier include a gain maximized at 2300 $\mu\text{A}/\text{lumen}$ in the NIR and signal to noise ratio of 25. Additionally, for imaging purposes, the Generation 3 Pinnacle™ tube was specified to have radiant uniformity throughout the screen at 830 nm, where ICG, the predominant fluorophore used herein emits photons.

The image intensifier is operated for continuous wave or frequency domain measurements. During continuous wave measurements the voltage potential of the photocathode-to-MCP is set to a direct current of >200 V, which is powered by a GBS Micro Power Supply (San Jose, CA, model: HVPS 20065400-003) via a home-built resistor-capacitor circuit. Figure 3.1 is an illustration that depicts the intensifier circuitry. Image intensifiers require a minimum “clamping” voltage to enable electrons to cross the MCP film barrier, therefore a large ($\gg 20$ V) cathode-MCP voltage potential enables better signal response and greater amplification for *in vivo* measurements, which are done in continuous wave mode. During modulation for FDPM phantom measurements,

the cathode-MCP voltage potential is reduced to 65 V dc and radio-frequency (30 to 130 MHz) modulated amplitude of 22 V ac is delivered onto the photocathode steady bias to modulate the photocathode response to input photons and create a frequency-dependent detection at a modulation depth (ac/dc) of approximately 40%.

3.1.3 Modulation Instruments

Frequency domain measurements are acquired using two phase-locked oscillators. Both frequency generators send modulated signals to the laser and image intensifier. The first oscillator, a Programmed Test Sources (PTS-310 frequency synthesizer, Programmed Test Sources, Inc., Littleton, MA, model 310M201GYX-53) instrument generates a 13-dBm RF signal which is directed to the image intensifier circuitry. In combination with a 47-dBm amplifier (ENI Technology, Inc., Rochester, NY, model 604L) and 20-dBm attenuator, the total RF signal sent to the image intensifier is approximately 40-dBm, which is equivalent to 22-V. The second oscillator, a Marconi signal generator (Marconi Instrument Ltd. Hertfordshire, England, model 2022D) creates a radio frequency signal at 13-dBm that is used to modulate the intensity output of the laser diode. The two modulators are phase locked with the PTS being the "slave" oscillator clocked by a 10-MHz external standard "master," which is the Marconi 2022D. A National Instruments IEEE-488 general purpose interface bus (AT-GPIB/TNT model: 778036-51, Austin, TX) configured for plug-n-play (TNT) into a PCI slot within a Dell Dimension 8300 Desktop personal computer enables computer programmed communication between the two oscillators. The desktop computer with 100 GB of disk

space for image storage, and with a Pentium[®] 4 processor is adequate for ICCD image acquisition.

3.1.4 Laser Components

In addition to the fluorescence detectors the optical imaging system requires an NIR light source for fluorophore excitation. Here, we employ a Thorlabs laser diode (785 nm, Sanyo DL7140-201, Thorlabs, Inc, NJ or DL-4140-001S, Power Technology) operating at a dc power of either 80 mW or 25 mW and lasing at 785 nm, the peak wavelength for ICG light absorption. The beam is expanded with a plano-convex lens to any desired circumference for area illumination and a holographic optical diffuser placed after the lens provides a uniform output light field. The diode current is kept constant by a driver (Thorlabs Inc. Newton, NJ, model LDC500) and temperature controller (Thorlabs, Inc. Newton, NJ, model TEC 2000). Similar to the image intensifier, the diode is modulated for the experiments herein over the frequency range from 30 to 130 MHz. The Marconi 2022D signal generator, which provides an RF modulated signal to the laser bias T, is adjusted at a power equivalent to 13 dBm. At 13 dBm, the laser modulation depth, $\frac{I_{AC}}{I_{AC} + I_{DC} - I_{th}}$, is approximately 30% when operating an 80-mW laser diode with a threshold current (I_{th}) rating equivalent to 30 mA. In the modulation depth equation above I_{AC} [mA] is the alternating current amplitude of the laser, which depends on the RF power, and I_{DC} [mA] is the mean laser current value, which is set by the user.

3.1.5 Clinical Accessories

The ICCD camera system was designed for mobility and to maneuver within the nuclear medicine suite at the University of Texas M. D. Anderson Cancer Center hospital. Accordingly, mounts and ICCD support structures include an articulating arm and a mobile heavy-duty cabinet. The dimensions of the cabinet, or mobile cart, are: 2' (w) x 4' (l) x 4' (h), and all instrumentation described previously fit comfortably within the cart. Figure 3.3 is an illustration of the cart with all ICCD components and Figure 3.4 is a photograph of the system. The cabinet (model: JJ245-U7, D.C. Graves, Wakefield, MA) has four polyurethane swivel casters with wheel brakes, lockable doors and drawers, a floor lock, and blue enamel finish over 14-gauge steel. On top of the cart, an articulating arm is mounted to hold the approximately 12-lb CCD camera head. The arm was manufactured by Strong Arm[®] Designs Inc., Horsham, PA (model: 501-LU3M16-38731 Vertica-L Pendant Arm) with dimensions provided in Figure 3.5. All cables (e.g., cooling tubes and power cords) that run from the CCD, monitor, and laser pass through the interior of the articulating arm.

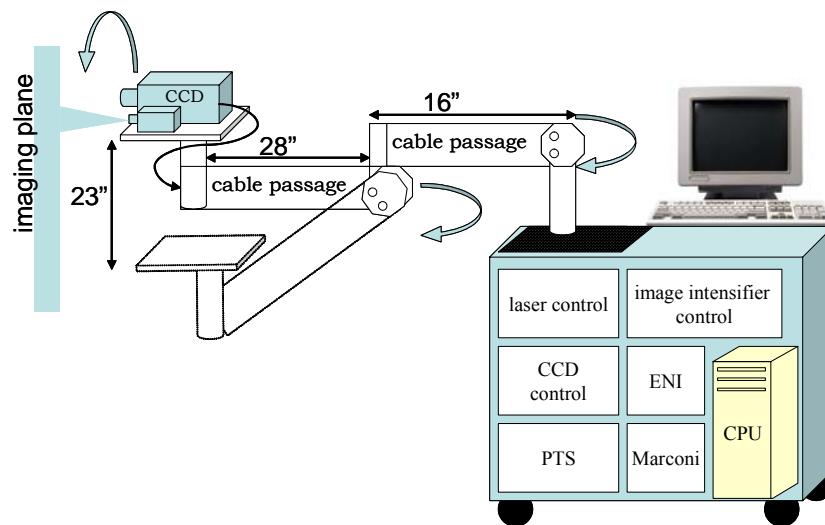


Figure 3.3 Illustration of how the ICCD system is housed within the mobile cart and how the CCD head is mounted onto an articulating arm.



Figure 3.4 Photograph of the clinical ICCD camera system. Instrumentation resides in the interior of the cart, which is on casters for mobility around the nuclear imaging suite.

3.1.6 Optical Components and Accessories That Minimize Image Artifacts

The tools which complete the ICCD camera system include optical accessories that permit optimum fluorescence signal acquisition. First, a 50-mm Nikkon Lens (Nikor, Tokyo, Japan) is used to focus the area light signal at the tissue or phantom surface onto the image intensifier. A 785-nm holographic notch band rejection filter (Kaiser Optical Systems Inc., Ann Arbor, MI, model HNPF-785.0-2.0) is placed in front of the Nikkor lens to selectively block the excitation wavelength. Additionally, an 830-nm band pass filter (Image quality, Andover Corp., Salem, NH, model 830.0-2.0) is stacked with the band rejection filter to selectively pass the emission signal (± 10 nm).

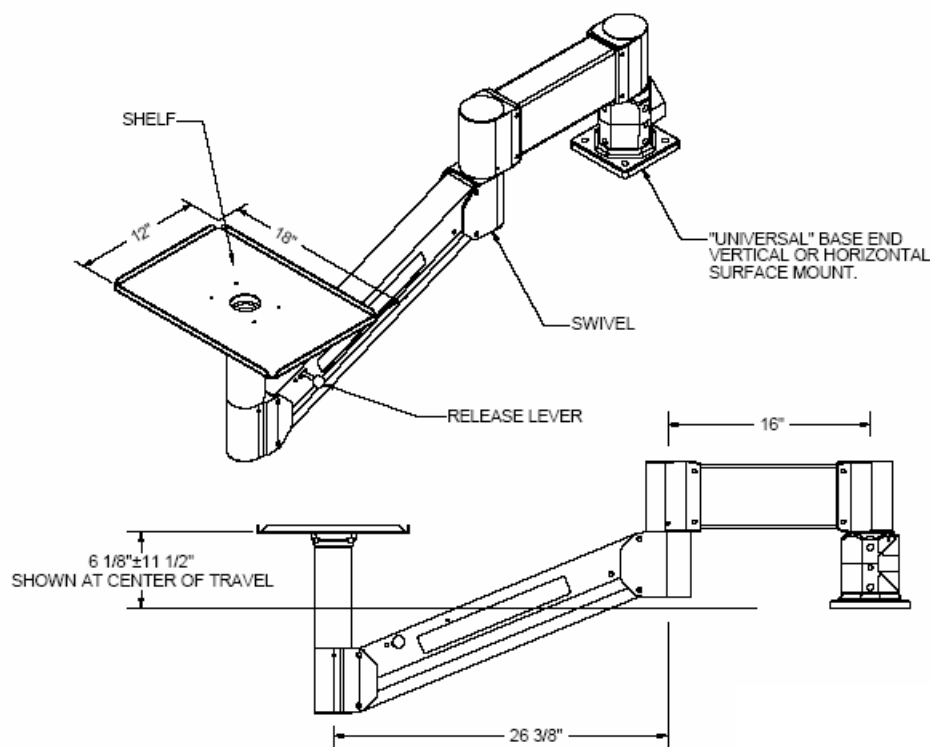


Figure 3.5 Dimensions of the Vertica-L Pendant Strong Arm® used to mount the CCD camera head. Reproduced from design specifications provided by Strong Arm Designs, Inc.

Quantification of the fluorescent events that occur *in vivo* with ICCD camera systems may be limited by the presence excitation light noise. During collection of fluorescence signals, excitation wavelengths are blocked with optical filters, yet despite blocking efforts, 19% of the total signal passed to the detector contains excitation light.² Presently, excitation noise limits the depth resolution of fluorescence in optical images to 3 centimeters and 2 centimeters for tomography.^{2, 184} The best rejection published in the literature is achieved by stacking two filters, an excitation rejection filter and a band-pass filter.² However simply stacking filters to add greater optical density and less transmittance may not be the solution. Recent work from the Photon Migration Laboratories demonstrates improved rejection upon collimation of the imaged photons prior to optical filtering.¹⁵⁹ Collimation optics may be essential for standard fluorescence ICCD imaging techniques particularly when the propagated excitation light fluence is up to four orders of magnitude or more greater than the fluence of the generated emission light. Appendix I outlines the calculation which compares the magnitude of attenuated excitation and emission light. Because it is known that the central wavelength of optical filters shifts with the angle of light incidence, ICCD systems must be tailored with collimating lenses.

3.2 FDPM Data Acquisition Methods

In addition to a description of the instrumentation, data acquisition procedures for measuring fluorescence signals are described. I_{AC} and θ are obtained with the ICCD camera system through a homodyne data acquisition (DAQ) procedure.¹⁸⁵ The principal behind homodyne data collection is simply the mixing of two frequency modulated

elements: (1) the fluorescent photon signal, FS, and (2) the RF modulated detector, DS, for demodulation of the desired fluorescence density wave. The fluorescent signal is a wave comprised of an average intensity (I_{DC}), amplitude (I_{AC}), and phase (θ). The phase of FS depends on the radio frequency (ω) of the laser and on a delay of propagation of the wave due to scattering and fluorescence decay kinetics (θ). The signal is mathematically defined as:

$$FS = F_{DC} + F_{AC} \cos(\omega t + \theta) \quad (3.1)$$

Similarly, the detector signal, DS, has a gain at a steady, I_{DC} , with amplitude, I_{AC} , and is modulated at an RF frequency of, ω , with an additional delay, θ_{inst} , that is introduced during the homodyne DAQ procedure. The detector signal is defined as:

$$DS = DS_{DC} + DS_{AC} \cos(\omega t + \theta_{inst}) \quad (3.2)$$

When the signals of FS and DS are mixed, the output is:

$$\begin{aligned} MS &= FS \times DS = \\ &FS_{DC}DS_{DC} + FS_{DC}DS_{AC} \cos(\omega t + \theta_{inst}) + FS_{AC}DS_{AC} \cos(\omega t + \theta) + \\ &\frac{FS_{AC}DS_{AC}}{2} \cos(\theta_{inst} - \theta) + \frac{FS_{AC}DS_{AC}}{2} \cos(2\omega t + \theta_{inst} + \theta) \end{aligned} \quad (3.3)$$

The mixing of FS and DS form a signal, MS, which has a high frequency component (ωt) as well as a phase contribution that varies in magnitude depending on the transit time of the detected wave (θ) and the instrument delay that is imposed during the DAQ procedure (θ_{inst}). The image intensifier does not read, amplify, and pass the signal at the phosphor screen at a rate that matches the frequency at which the signal is received. The

phosphor decay and recovery rate is limited. Therefore, only the low frequency components are passed; the remaining signal is time independent:

$$MS_{final} = FS_{DC} DS_{DC} \frac{FS_{AC} DS_{AC}}{2} \cos(\theta_{inst} - \theta) \quad (3.4)$$

The final signal obtained is the measured fluorescence photon density wave, which is output in a 2D image, that is, each pixel has a final I_{AC} , I_{DC} , and θ value.

The ICCD camera system homodyning method is enumerated below.

1. The phase-locked Marconi and PTS send equivalent radio-frequencies to the laser diode and image intensifier, respectively. The specific frequencies used were 30, 60, 90, 100, and 130 MHz.
2. The CCD camera acquires 10 frames, or images, of the image intensifier phosphor output during continuous modulation.
3. After acquiring 10 images, the phase of the PTS is delayed relative to the Marconi by a factor of $2\pi/32$.
4. The CCD captures a series of 10 images again.
5. Step 3 is repeated 32 times until a total phase change of 2π has been achieved and a “stack” of 32×10 images are collected.

The homodyne process is controlled using V++ Image Acquisition software (Digital Optics, Auckland, New Zealand) with pre-programmed scripts to direct the oscillators which communicate via the National Instruments IEEE-488 GPIB. The Pascal V++ scripts were modified for this work to collect frame-transfer CCD images. The 10 images collected at one phase-delay are averaged to obtain a single multi-pixel image for

each phase-delay, therefore a 32×1 multi-pixel image array is obtained. At each phase-delay, the image intensifier output intensity changes. The change is sinusoidal across all phase delays so that after a total of 32 phase delays an intensity-based sine wave is obtained from the stack of 32 images. Due to the sinusoidal intensity change, the I_{AC} and θ can be obtained using Fourier transform fit. With 32 discrete values at each pixel (i,j) , a fast Fourier transform is computed. The angle and modulus of the FFT result are simply the θ and I_{AC} of the final fluorescent signal:

$$\theta(i, j) = \tan^{-1} \left\{ \frac{\text{IMAG} \left[F(I_{ij})_{\max} \right]}{\text{REAL} \left[F(I_{ij})_{\max} \right]} \right\} \quad (3.5)$$

$$I_{AC}(i, j) = \frac{\sqrt{\text{IMAG} \left[F(I_{ij})_{\max} \right]^2 + \text{REAL} \left[F(I_{ij})_{\max} \right]^2}}{N/2} \quad (3.6)$$

$F(I_{ij})_{\max}$ represents the maximum output of the Fourier transform spectrum, which has real and imaginary components, of the steady state intensity at each pixel (i,j) and phase delay. N is the total number of phase delays. DC can be determined by simply averaging the intensity of each pixel for 32 phase-shifts in modulation. A Matlab routine provides the I_{AC} and θ , while V++ imaging software drives the homodyne data acquisition scheme.

It is notable to add that randomizing the 32×10 multi-pixel arrays before computing the FFT provides a statistically improved computation method.¹⁸⁶ Therefore a procedure has been developed in which the total number of frames, n , and phase delays, N , can be combined in a random manner to create a single array of 32×1 images. The randomization is done by randomly selecting a frame for each phase delay and then computing the FFT. This random selection is repeated in an iterative manner so that the phase-sensitive intensity data is combined in a multitude of combinations. Using 100 iterations, this data acquisition procedure reduces the noise in the final FFT data. A MatLab routine was used to compute the FFT following this randomization method for all the data calculated in this project.

3.3 Phantom and Target Materials

Following the instrumentation description and the DAQ procedures for FDPM measurements, this section describes the materials used in phantom experiments for Phase 1 of the thesis. The results from Phase 1 are described in Section 4. A phantom is a tissue-mimicking container, and for this study, two different phantom types were constructed at the Photon Migration Laboratories. The phantoms modeled a semi-infinite tissue slab to simulate the non-invasive clinical application of FDPM measurements in which the planar source is incident on the same surface over which fluorescence is detected. Hence the geometry to be constructed is semi-infinite with a planar boundary. The computations for comparing experimental data are then subject to extrapolated or zero fluence boundary conditions at the planar surface ($\Phi=0$ at an

extrapolated boundary or $\Phi=0$ at $z=0$) while the fluence, Φ , becomes small at the large distances ($z \rightarrow \infty$).

The first phantom constructed consisted of a $30 \times 10 \times 10 \text{ cm}^3$ (length \times width \times height) open box with a black acrylic bottom and clear Plexi-glass sides. The center point of one of the long sides of the rectangular phantom was identified at which a series of 10 holes, 1 mm in diameter with 1-mm drill bit, were there drilled in a single line starting 1 cm below the phantom top edge. The holes were drilled approximately 1 cm apart with hand-held accuracy. Within each hole, a fiber optic was inserted so that it reached the center of the phantom. The fibers were fastened with Mr. Sticky's water Glue®. The role of each evenly distributed fiber was to permit collection of fluorescence signals from varying depths thus providing fluorescence data in the z direction. Figure 3.6 is an illustration of the phantom system.

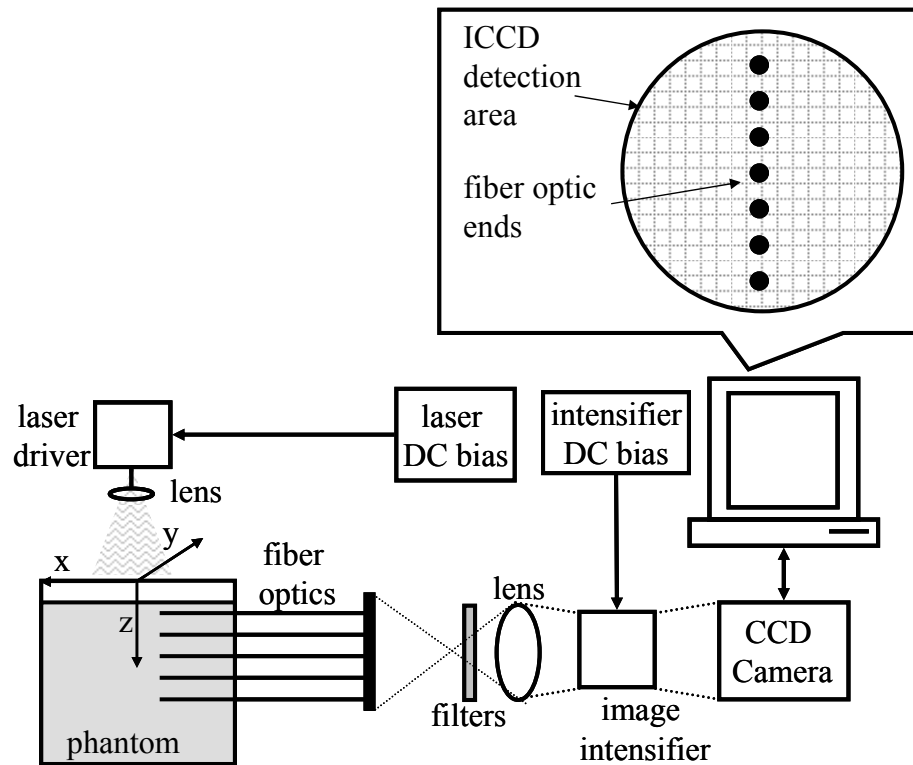


Figure 3.6 Illustration of phantom and fiber optic imaging system for detection of the depth of fluorescence penetration in a homogenous scattering solution. The fibers are inserted into the center of the phantom for detection of fluorescence and relayed to an "interfacing plate" which the ICCD camera system images.

The second phantom constructed was a transparent and sturdy Plexi-glass cylindrical container with a 22-cm diameter and 11-cm height. Similarly, a series of 9 holes, 1 mm in diameter with 1 mm drill bit, were drilled in a single line starting 1 cm below the phantom top edge to 1 cm from the phantom bottom edge. The holes were drilled with a drill machine to an exact interval distance of 1 cm. The 10 fiber optics were inserted all the way into the phantom center through these holes and fastened with Mr. Sticky's water Glue®. Figure 3.7 is a photograph of the cylindrical phantom.

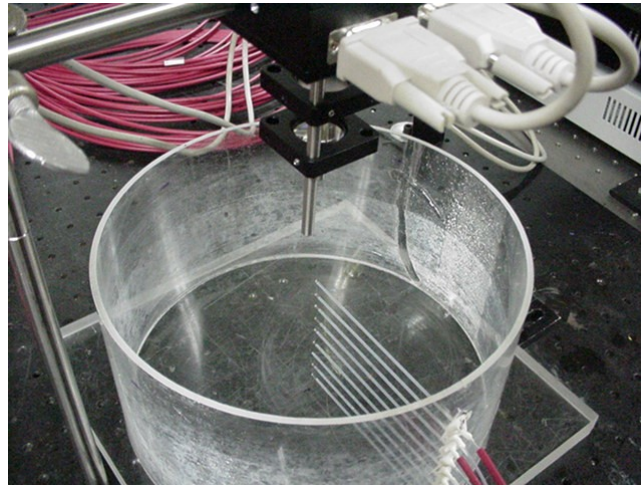


Figure 3.7 Photograph of cylindrical phantom with fiber optics inserted into the center for fluorescence depth measurements.

The opposite fiber optic ends which were not inserted in the phantom were arranged in a single line and inserted into a black interfacing plate which can be imaged by the ICCD camera system. The point-source point-ICCD detection method was previously developed at the Photon Migration Laboratories for tomography studies.¹⁸⁷

The phantom was filled with a scattering solution, Liposyn® (Abbott Laboratories, North Chicago, IL 60064) at either 0.5 or 1% v/v water. Liposyn® is a milky colored, intravenous fat emulsion commonly used for scattering measurements but traditionally used as a nutritional supplement in animals and primarily made of soybean and safflower oil. In addition to the Liposyn®, India ink was added at either 0.02 or 0.04 vol% to increase the absorption optical properties of the system. The Liposyn® emulsion chosen for the imaging study herein is a surrogate to true tissue because its scattering properties (μ_a and μ_s') are similar to that of breast tissue. For fluorescence measurements, either indocyanine green stabilized with a molar excess of

polyaspartate¹⁸⁸ or DTTCl, 3,3'-diethylthiatricarbocyanine iodide, (Sigma Aldrich) was uniformly mixed into the Liposyn® solution at a concentration of 1.0 μM . Indocyanine green and DTTCl have lifetimes of 0.56 ns and 1.18 ns, respectively. Both dyes absorb at 785 nm and emit fluorescence at 830 nm, so that similar optical filtering and excitation light can be used to compare fluorescence depth detection at different fluorophore lifetimes. Optical properties (μ_a and μ_s') were independently measured at the Photon Migration Laboratories^{189, 190} using a photo-multiplier tube detector, 785-nm laser diode point source, and frequency-domain instrumentation that through a heterodyne detection scheme provided measurements of I_{AC} and θ , at different source detector separation distances and modulation frequencies. A MatLab code developed by Dr. Tianshu Pan¹⁹¹ of the PML was used for a regression of the FDPM data to obtain the reduced scattering coefficient and absorption coefficient. Table 3.1 provides a summary of the phantoms studied and their computed optical properties.

Table 3.1 Summary of phantoms investigated with the resulting optical properties measured using FDPM heterodyne instrumentation at the PML. The summary includes the concentration of Liposyn® and absorbing ink used, type of fluorophore employed and resulting optical properties.

Solution, phantom I or II (date_experiment #)	Liposyn® concentration (vol %)	India ink concentration (vol %)	Dye and concentration (μM)	Optical properties (\pm std. dev.)	
				μ_a (cm^{-1})	μ_s' (cm^{-1})
1, I (042304)	0.5	0	ICG 0.098	0.1	5
II (042505)	0.5	0.02	ICG 1.0	0.18 (\pm 0.012)	10.2 (\pm 0.53)
2, II (031805_3)	0.5	0.02	DTTCI 1.0	0.047 (\pm 0.0117)	15.6 (\pm 16.7)
II (042505)	0.5	0.02	DTTCI 1.0	0.062 (\pm 0.008)	7 (\pm 0.6)
3, I (042904)	1.0	0	ICG 1.0	0.1	10
4, II (022805)	1.0	0	ICG 1.0	0.12 (\pm 0.001)	21.6 (\pm 0.19)
5, II (030105)	1.0	0	ICG 1.0	0.12 (\pm 0.0016)	21 (\pm 0.24)
6, II (031705_2)	1.0	0	DTTCI 1.0	0.043 (\pm 5.7e-004)	21.5 (\pm 0.19)
7, II (022805)	1.0	0.04	ICG 1.0	0.32 (\pm 0.0129)	20.9 (\pm 0.4)
II (042605)	1.0	0.02	ICG 1.0	0.17 (\pm 0.005)	9.6 (\pm 0.45)
8, II (031705_1)	1.0	0.02	DTTCI 1.0	0.063 (\pm 5e-004)	17.3 (\pm 0.2)
9, II (031805_1)	1.0	0.02	DTTCI 1.0	0.072 (\pm 0.0013)	18.8 (\pm 0.64)
10, II (031805_2)	1.0	0.02	DTTCI 1.0	0.063 (\pm 3.5e-004)	28.7 (\pm 0.46)

In addition to homogeneous phantom measurements, a fluorescent target was constructed to mimic the heterogeneous nature of breast tissue with lymph nodes. The fluorescent target was a $1 \times 1 \times 1 \text{ cm}^3$ clear plexi-glass cube filled with the $1 \mu\text{M}$ of the fluorescing Liposyn® solution. The target was immersed in a phantom at a fixed (x,y,z) location with either no fluorescence in the background or a fluorescence background:target concentration ratio of 100:1. Figure 3.8 is an illustration of the experimental set-up for the phantom containing a target and Figure 3.9 is a photograph of the target.

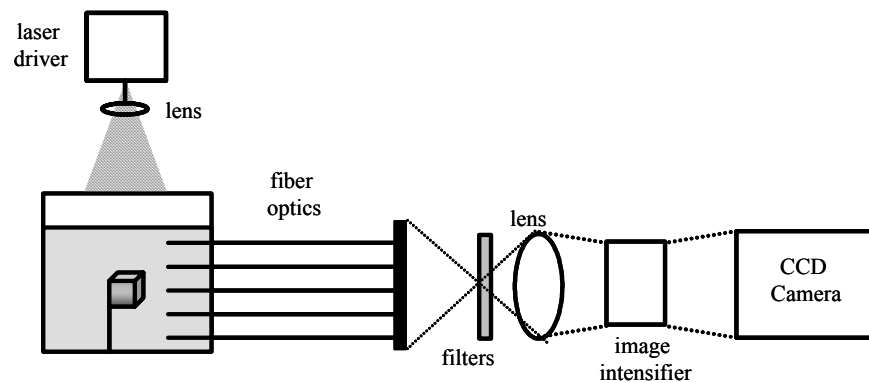


Figure 3.8 Illustration of heterogeneous phantom containing a fluorescent target.



Figure 3.9 Photograph of the fluorescent target used in the heterogeneous phantom study.

For fluorescence measurements, a planar 785-nm modulated laser source illuminated the Liposyn® surface. The laser power was adjusted at 70 mW for maximum modulation depth and expanded to 5 cm in diameter. For each experiment data was collected at a range of modulation frequencies (0 to 130 MHz) in increments of 30 MHz so that the total number of experiments conducted was the number of dyes time the number of modulation frequencies. Imaging was accomplished by focusing a standard Nikon camera lens at two different surfaces. For the phantom containing a fluorescent target, fluorescent light was collected both at the scattering surface where the planar beam is incident and at the fiber points via the interfacing plate. Recall, the interfacing plate holds the fibers, which carry fluorescence signals from directly within the semi-infinite medium. For the homogeneous phantom studies, only the interfacing plate was imaged. For all experiments to be compared, the exposure time, image intensifier dc voltage setting, focusing distance, number of phase delays for homodyne acquisition, $f/\#$ on the Nikon lens, and laser beam power were kept constant. Multi-pixel CCD images of I_{AC} , I_{DC} , and θ were collected for each experiment following the DAQ procedure discussed previously.

3.4 Optical and Gamma Imaging Instrumentation

In addition to phantom studies, the second phase of this thesis is the acquisition of *in vivo* data from small animals, namely nude mice. Small animal imaging has been developed by the Photon Migration Laboratories in collaboration with the University of Texas M. D. Anderson Cancer Center under the direction of Dr. Chun Li. Accordingly, a NIR fluorescence imaging system has been designed, constructed, and validated in

several previous works. Therefore to avoid redundancy this sub-section provides an overview of the materials used for the small animal ICCD imaging. Yet in addition to optical ICCD imaging, nuclear imaging studies were performed on nude mice for the first time at the Photon Migration Laboratories, thus a description of nuclear imaging instrumentation is provided with greater detail. Excerpts from Section 3.4 follow work described in the Houston *et al.* manuscript to be published in the *Journal of Biomedical Optics*, (2005).

3.4.3 Small Animal Optical Imaging System

Continuous wave optical imaging of fluorescent NIR photons was performed with an ICCD system similar to the phantom/clinical imaging system described previously.¹³⁰ The system consists of two complementary detectors, a NIR sensitive image intensifier (model FS9910C ITT Night Vision, Roanoke, VA) and a 16-bit dynamic range full frame Photometrics (model CH350, Roper Scientific, Trenton, NJ) charge-coupled device camera. The CCD camera does not have the fast frame transfer architecture as the camera described previously, therefore requires a shutter to prevent smearing during image readout. Additionally, the image intensifier was lens-coupled to the CCD camera as opposed to the fiber coupled system developed for the clinic. The full frame CCD camera imaged the 550-nm amplified light signal output at the intensifier's phosphor screen via a 40-mm Nikkor lens (Nikon, Japan). A 28- to 80-mm zoom Nikkor lens (Nikon, Japan) facilitated the focusing of the whole-body of a nude mouse on to the photocathode. For the small animal imaging studies presented herein,

an equivalent field of view detection diameter of 11.5 cm (or 8.1 cm for three animals) was used.

Fluorescence imaging on small animals was performed using similar laser and optical accessories including: a 785-nm laser diode (80-mW 785-nm, model Sanyo DL7140-201, ThorLabs, Newton, NJ), a plano-convex lens for beam expansion, a holographic optical diffuser to provide a uniform excitation light field, a 785-nm holographic notch band rejection filter (Kaiser Optical Systems Inc., Ann Arbor, MI, model HNPF-785.0-2.0), and an 830-nm band pass filter (Image quality, Andover Corp., Salem, NH, model 830.0-2.0). In addition to fluorescence images, white-light images of the nude mice were acquired by the CCD system, with no optical filtering and with a low power lamp.

3.4.4 Small Animal Gamma Camera

Following the aims to translate optical imaging to the clinic, it is logical to contrast optical imaging capabilities with the gold standard of molecular imaging, nuclear gamma scintigraphy. Therefore for the animal studies herein, conventional gamma imaging was accomplished with tools described below. Briefly, gamma imaging follows the following steps: (1) upon ^{111}In decay gamma photons are emitted isotropically from within the animal, (2) the emitted gamma photons are collimated, (3) the collimated gamma photons strike a scintillation crystal where visible photons (scintillation light) are produced, and (4) the photons are then guided towards a photomultiplier tube (PMT), which collects a ray sum of scintillation light used to generate the projection image.

Conventional gamma imaging involved an M.CAM small animal gamma camera (Siemens, Hoffman Estates, IL). Figure 3.10 is a photograph of the camera with an illustration indicating the different components that make up the gamma camera. The commercially available system is equipped with an HD³ (High Definition Digital Detector) mounted on a stand that can be manually adjusted and rotated. A collimator is fitted over the entire detector plane and can be removed for replacement. The collimator is protected by a placement template, which defines the area of the scintillation crystal for placement of the animals over the fixed field of view (FOV) of $54.4 \times 39.7 \text{ cm}^2$. The collimator is a medium energy low penetration (MELP) collimator with a resolution of 4–20 mm and sensitivity of 237 cpm/ μCi . The M.CAM instrumentation also includes a SNAC (Siemens Nuclear Acquisition Computer) for controlling the M.CAM detector functions, and an ICONTM computer for user interfacing and data processing. Static nuclear imaging was achieved at medium energy collimation settings (237 keV energy window) and by integrating the detector over a time interval of 15 minutes for which a single planar gamma image was acquired. The M.CAM system produces a total imaging matrix size of 1024×1024 pixels, and the image type was read as a 16-bit multi-pixel array providing intensity counts on the order of 2^{16} levels of gray.

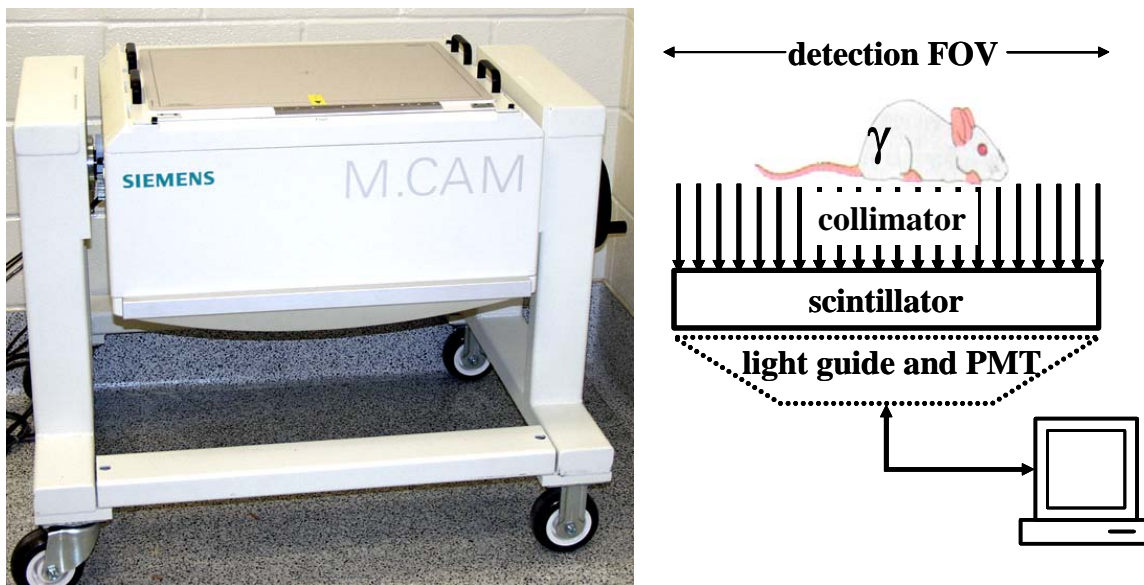


Figure 3.10 Small animal gamma camera (photograph on left) and illustration of the components of a conventional gamma camera (on right).

3.5 Fluorescence Point Detection Measurement System

This final instrumentation section lists the materials required for measuring dynamic fluorescence changes in the blood stream of a nude mouse injected with a fluorescent contrast agent. The instrumentation described below was developed to measure fluorescence from the blood vessels in the ear and in turn acts synergistically with dynamic ICCD measurements of fluorescence on the entire mouse body. The instrumentation for fluorescence detection from ear blood vessels is presented in this section and the proof of concept study for pharmacokinetic analysis of fluorophore blood clearance is described in Section 5.2.

Continuous wave optical imaging of fluorescent NIR photons is performed with a point source, and CW emission light is detected at a single point on the skin surface of a small animal. The measurement instrumentation is illustrated in Figure 3.11 and consists of (i) a silicon diode detector, (ii) DAQ instruments, (iii) a fiber optic probe, and (iv) optical accessories for fluorescence measurements.

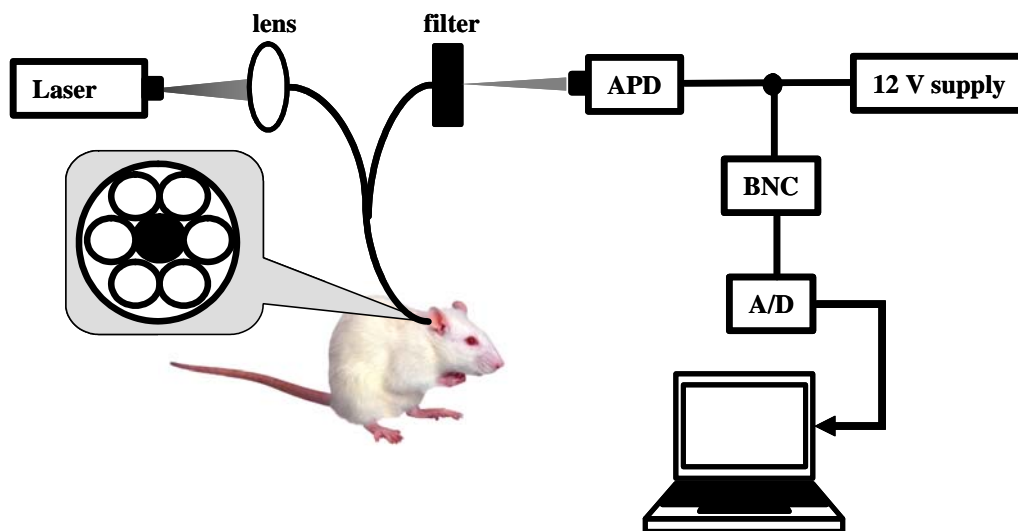


Figure 3.11 Illustration of fluorescence point detection measurement system for detecting dynamic fluorescence changes in the blood of a live nude mouse.

3.5.1 Avalanche Photodiode

A silicon avalanche photodiode (APD) module (model C5460-01, Hamamatsu, Bridgewater, NJ) was chosen for the point detection measurements because of the need for low level NIR light detection in a temperature-stable imaging environment. The APD module provides dc photo-detection at a high gain and includes a low-noise amplifier and a bias power supply. The module has a low-band cut-off frequency of dc to 100 kHz permitting sensitive cw measurements. The effective active diameter of the APD is 3 mm and the photoelectric sensitivity at 800 nm is maximized at 10^8 V/W. The APD module shown in Figure 3.12 is powered by a 12-V dc power supply (model 12EB20, Acopian, Easton, PA).



Figure 3.12 Hamamatsu APD module used for cw fluorescence detection *in vivo*.

3.5.2 DAQ Instruments

In order to collect the output APD voltage signal, an analog-to-digital conversion is required. The small animal ICCD system described in Section 3.4.3 includes a laptop computer for data acquisition therefore a DAQ system for the APD was designed to interface to the same computer. A connector block (model BNC-2110, National Instruments, Austin, TX) interfaces the analog output of the APD to an analog-to-digital data acquisition card (model 6036E National Instruments, Austin, TX). More specifically, a BNC-to-BNC cable carries the APD output signal to the noise rejecting, and shielded connector block. The connector block is then coupled to a shielded 1 m cable (model SHC68-68-EP, National Instruments, Austin, TX) which provides the connectivity to a DAQ card. The DAQ card provides the analog-to-digital conversion of the measured voltage signal from the APD and is interfaced to the laptop via a PCMCIA slot. The DAQ card is 16-bit and can be configured for up to eight analog inputs and operates at a maximum speed of 200 kS/s. Lastly, a LABVIEW software (National Instruments, Austin, TX) DAQ routine is used for measurement control, read, and write.

3.5.3 Fiber Optic Probe

Fluorescence imaging was performed first by delivering a 785-nm excitation source to the ear of the animal via a bifurcated fiber optic probe (RoMack Inc., Williamsburg, VA). The fiber probe illustrated in Figure 3.13 is used to deliver excitation to and emission light from the animal's ear. A single fiber delivers 785-nm excitation light from the laser source through one subminiature version A (SMA) 905,

bifurcated end to the animal's ear via a 1000- μm fiber with a numerical aperture equivalent to 0.37. At half the length of the fiber probe, the single source fiber is joined with six detector fibers of same type. At halfway, the six detector fibers are packed in a ring around the single source fiber and terminate by ferrule at a common end. Thus, the bundle provides both light collection and light delivery for fluorescence measurements in reflectance geometry. The bundle diameter is 0.25 inches and may be mounted directly over the surface of the animal's ear. The six detector fibers thereafter deliver emission light to the APD from the ferrule end to a second bifurcated ferrule leg.

3.5.4 Other Optic Accessories

In order to acquire fluorescence measurements, the SMA 905 emission end of the fiber probe was positioned normal to two stacked, round, 1-in fluorescence filters so that the collected light is filtered before being detected by the APD. An 830-nm band-pass filter (Image quality, Andover Corp., Salem, NH, model 830.0-1.0) and 785-nm holographic band rejection filter was used. The APD system described herein can be used for multiple wavelength measurements by implementing different optical filter sets.

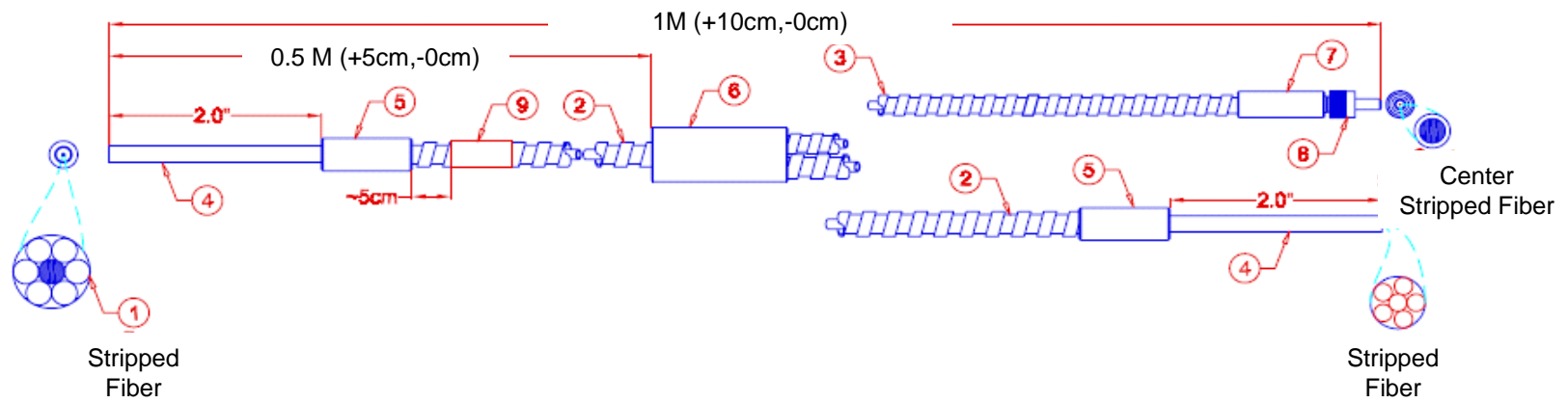


Figure 3.13 Drawing of the bifurcated fiber bundle used for fluorescence measurements on the mouse ear reproduced with permission from RoMack Inc.

4. PHASE 1: IMAGING PHANTOMS

Depth penetration phantom studies using the gain-modulated ICCD camera system, which is described in Section 3, are provided below. The measurable depth of photon penetration is important for accurate sentinel lymph node localization as well as for future use in tomographic reconstruction algorithms. The following section describes phantom measurements validated by photon diffusion models to verify the ability of the ICCD system to precisely measure photon migration at clinically relevant depths and over a range of optical property combinations. In addition, these studies explore certain phenomena such as the dependence of penetration depth on fluorescent lifetime, continuous wave measurements, and frequency-domain measurements.

4.1 Probabilistic Model of Penetration Depth

Probabilistic models of photon diffusion have been studied in several situations including for NIR light propagation in tissues,¹⁹² prediction of the volume of light probed in pharmaceutical powder blends,¹⁹³ and time-resolved fluorescence NIR light propagation.¹⁹⁴⁻¹⁹⁷ Additionally, models describing the penetration depth of photons have been investigated.^{194, 198-206} Yet these models are limited to non-fluorescing media, shallow propagation, pulsed light sources, or frequency domain simulations that lack experimental validation. Here, we use a frequency-domain fluorescence-enhanced probability model to investigate the depth of penetration for frequency-domain optical lymphography. The photon diffusion approximation to the radiative transport equation can be analytically solved leading to a function describing the distribution of modulated

fluorescence signals within tissues. Ultimately the solution, or probability density function (PDF) describes the probability that a photon contributing to a photon density wave is at depth, \mathbf{z} , in a simulated homogeneous scattering medium.

The derivation of the PDF is described in two parts with the first component describing the probability of a fluorescent or phosphorescent photon generated at time, t^* , and position, \mathbf{z} , following a pulse of excitation light incident at the tissue surface at time $t = 0$. The probability, P_S is provided by Equation 4.1.

$$P_S(\mathbf{z}, t^*) = \frac{\phi \mu_{ax}}{\tau} \int_0^{t^*} \exp\left(\frac{t' - t^*}{\tau}\right) \Phi_x(\mathbf{z}, t') dt' \quad (4.1)$$

The probability, P_S , depends on the generation of emission photons upon excitation at time, t' , from within the homogeneous and semi-infinite tissue, thus is expressed in terms of the excitation fluence, Φ_x [W/cm^2]. Additionally, the probability depends on ϕ , μ_{ax} , and τ , the quantum efficiency of the fluorophore, absorption coefficient at the excitation wavelength due to fluorophores, and the average lifetime of the fluorophore, respectively. The excitation fluence is approximated from an analytic Green's function solution²⁰⁷ to the time-domain diffusion equation and is shown in Equation 4.2. The excitation fluence is solved by defining a semi-infinite and homogeneous medium in which the source and detector are positioned on the same surface; Figure 4.1 illustrates the semi-infinite geometry. By employing the zero-fluence boundary condition in which the fluence is equal to zero at $z = 0$, the excitation solution can be defined.

$$\Phi_x(\mathbf{z}, t') = \frac{c}{(4\pi Dct')^{1/2}} \left[\exp\left(\frac{-(\mathbf{z} - z_o)}{4Dct'}\right) - \exp\left(\frac{-(\mathbf{z} + z_o)}{4Dct'}\right) \right] \exp[-(\mu_{ax})ct'] \quad (4.2)$$

In Equation 4.2, D is the diffusion coefficient at the excitation wavelength and is given

$$\text{by: } D = \frac{1}{3(\mu_{ax} + \mu_s')} \quad (4.3)$$

Additionally, μ_s' is the reduced scattering coefficient at the excitation wavelength and μ_{ax} is the total absorption at the excitation wavelength due to tissue chromophores and embedded fluorophores. The constants, c and z_0 , are the speed of light and the position of the photon source, respectively, and the vector \mathbf{z} , represents the depth location. Equation 4.2 is uni-directional to model the propagation of a planar wave within the semi-infinite tissue sample. Figure 4.1 is portrays the propagation of a planar photon density wave.

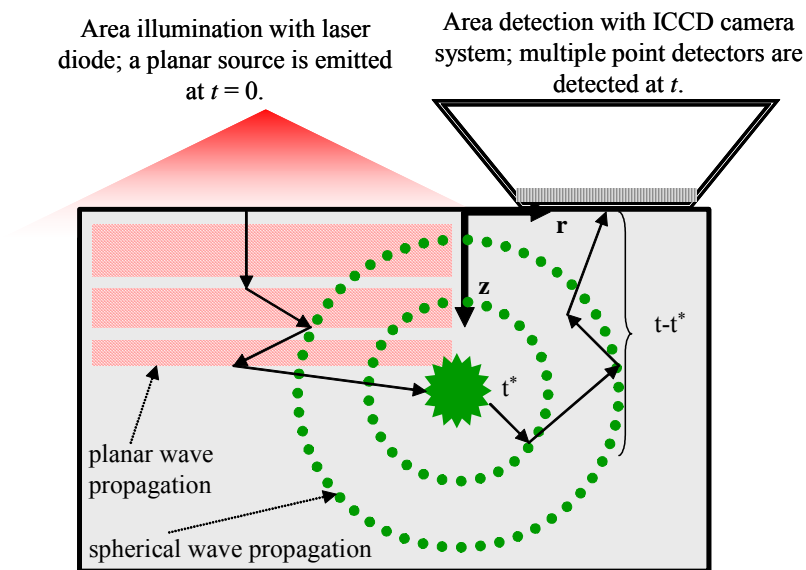


Figure 4.1 Illustration of photon propagation through a scattering solution. Illumination with an expanded beam at time $t=0$, creates the planar propagation of excitation light. The excitation light is absorbed by a fluorophore at time t' and spherical fluorescence emission is emitted at time t^* . The fluorescent or phosphorescent photon travels to the surface to be detected at time, t . The transit time from emission to the surface is described by time $t-t^*$.

Continuing to describe the fluorescence process in PDF form, a second expression is taken, which describes the probability, P_D , that a spherically emitted fluorescent or phosphorescent photon produced at position (\mathbf{r}, \mathbf{z}) and time $(t-t^*)$ is observed. The probability of an isotropically emitted photon, which is also illustrated in Figure 4.1, is equivalent to the emission fluence, Φ_m [W/cm²], given by:

$$\Phi_m(\mathbf{r}, \mathbf{z}, t-t^*) = \frac{c}{[4\pi Dc(t-t^*)]^{3/2}} \left[\exp \frac{-(\mathbf{z}-z_o)^2 - (\mathbf{r})^2}{4Dc(t-t^*)} - \exp \frac{-(\mathbf{z}+z_o)^2 - (\mathbf{r})^2}{4Dc(t-t^*)} \right] \exp[-(\mu_{am})c(t-t^*)] \quad (4.4)$$

where t^* is the time when photons are emitted from the excited fluorophore, and t is the time when emission photons reach the surface and are detected. The emission solution differs from the excitation solution because it represents the propagation of a spherical photon density wave, where $\mathbf{r}^2 = \mathbf{y}^2 + \mathbf{x}^2$.

The probability density function that describes photon fluence at position \mathbf{z} and any time from the start of the planar, pulsed light source to the time at which a lower energy photon is created, spherically emitted, and detected is the summation of the product of $P_S(\mathbf{r}, \mathbf{z}, t^*)$ and $P_D(\mathbf{z}, t-t^*)$ over a finite time. The product of P_S and P_D is based on the assumption that reciprocity is applicable for propagation of a planar excitation wave and subsequent emission of a spherical wave. The principle of reciprocity which assumes that a photon detected at depth z' , after being emitted from position z_o , has an equivalent detection probability as a photon detected at depth z_o after emission from position \mathbf{z}' was valid in previous work by Pan¹⁹³ and Sevic-Muraca.¹⁹⁵ However, for the case of a planar excitation wave propagation and spherical emission

wave propagation, reciprocity is assumed. Equation 4.4 provides the total probability, $P(\mathbf{z}, t)$, summed over all detection times, t :

$$\begin{aligned}
 P(\mathbf{z}, t) &= \int_0^t \left[P_S(\mathbf{z}, t^*) \cdot P_D(\mathbf{r}, \mathbf{z}, t - t^*) \right] dt^* \\
 &= \int_{t^*=0}^{t^*=t} \left[\Phi_m(\mathbf{r}, \mathbf{z}, t - t^*) \frac{\phi \mu_{ax}}{\tau} \int_{t'=0}^{t'=t^*} \Phi_x(\mathbf{z}, t') dt' \right] dt^*
 \end{aligned} \tag{4.5}$$

For the computations herein, the probability is represented as a normalized value by the following ratio:

$$P_{\text{normalized}} = \frac{P_i(\mathbf{z}, t)}{P_{\text{max}}(\mathbf{z}, t)} \tag{4.6}$$

where $P_i(\mathbf{z}, t)$ is the probability [W/cm²] at the depth, \mathbf{z}_i , and time t_i and P_{max} is the maximum probability [W/cm²] value over the generated probability data for all times, t , and depths, \mathbf{z} .

Sevick-Muraca and Burch¹⁹⁵ were the first to describe this process in the time domain and with a spherical point source, yet a frequency-domain representation is desired to predict the propagation of a planar and modulated light source. Therefore, the uni-directional PDF in the time-domain, $P(\mathbf{z}, t)$, is Fourier transformed to obtain the frequency-domain representation, $P(\mathbf{z}, \omega)$. A time-domain starting point provides ease of computation before conversion to the frequency domain by the following:

$$P(\mathbf{z}, \omega) = \mathfrak{F}[P(\mathbf{z}, t)] = \int_{-\infty}^{\infty} \exp(i\omega t^*) \left\{ \int_0^t \left[P_S(\mathbf{z}, t^*) \cdot P_D(\mathbf{r}, \mathbf{z}, t - t^*) \right] dt^* \right\} dt^* \tag{4.7}$$

The purpose of the probability function is to investigate which depth in the scattering domain contributes most to the detected photon signal, thus the mean depth of photon visitation is computed by the following equation:

$$\langle z \rangle = \frac{\int P(\mathbf{z}, \omega) \cdot z dz}{\int P(\mathbf{z}, \omega) dz} \quad (4.8)$$

where $\langle z \rangle$ is the mean depth of photon occurrence using the probability function, $P(\mathbf{z}, \omega)$.

4.2 Probability Distributions in the Frequency Domain for a Homogeneously Distributed Fluorophore Excited by a Planar Wave

Using Equation 4.7, the probability of detecting photons at any depth \mathbf{z} , for different frequencies ω , can be estimated using any familiar mathematical modeling software. The discrete FFT of Equation 4.5, which should resemble a Gaussian-like distribution, was computed using MatLab (The MathWorks, Inc.) and follows the steps below:

1. A discrete time array is first defined for a series of time points that range from $t = 0$ to $t = t_{final}$. The time array, which can also be depicted by $0 \leq t \leq t_{final}$, has a total number of time points that is equivalent to a factor of 2^n . The number of discrete time points, $N= 64$, is chosen to maximize the computational effort of the FFT and render an accurate solution. Two time arrays were created to observe fluorescent and phosphorescent signals at the tissue surface. First, $t_{final} = 6$ ns was used to calculate the PDF when fluorescent lifetimes were employed.

Similarly, an array with $t_{final} = 25$ ns was generated to compute the PDF when a phosphorescent lifetime was simulated.

2. Uni-directional time-domain probability data, $P(\mathbf{z}, t)$, are then generated using Equation 4.4, for the discrete range of times created in step 1. Calculation of $P(\mathbf{z}, t)$ is also dependent on the vector, \mathbf{z} , which represents the depth within the tissue. The resulting time domain probability solution therefore is a matrix with probability values computed for each combination of discrete depths and time points.
3. The simulated probability data, $P(\mathbf{z}, t)$, are then Fourier transformed by a discrete, or fast, Fourier transform.
4. A frequency spectrum, $\mathfrak{F}[P(\mathbf{z}, \omega)]$, is obtained by the transform of $P(\mathbf{z}, t)$.
5. $P(\mathbf{z}, \omega)$ is then computed by taking the modulus of the complex frequency spectrum.
6. Lastly, a frequency array is created to plot the resulting probability, $P(\mathbf{z}, \omega)$, versus ω . The discrete frequency array, $0 \leq \omega \leq \omega_{final}$, is calculated based on the previously described time array. More specifically, $0 < \omega < 1/\Delta t$,

where $\Delta t = \frac{t_{final} - t_{initial}}{N}$, N is the number of samples computed, $t_{initial} = 0$,

$$\text{and } \Delta \omega = \frac{2\pi}{N\Delta t}.$$

Ultimately, the frequency domain PDF provides the probability for the occurrence of a spherically emitted photon in a homogeneous, semi-infinite tissue medium following excitation by a planar and modulating photon density wave.

4.3 Analytical Predictions for Comparison to Phantom Experiments

A comparison of the probability solutions to experimental measurements requires a direct solution of I_{AC} and θ from Equation 4.7. Therefore an analytical solution to the frequency-domain diffusion equation is used. Employing an extrapolated boundary condition²⁰⁸ for a semi-infinite homogeneous medium, Li *et al.* defined the following:²⁰⁹

$$\Phi_m(\mathbf{r}, \mathbf{r}_s, \omega) = \frac{C(\omega)}{|\mathbf{r} - \mathbf{r}_s|} \left[\exp(ik_x |\mathbf{r} - \mathbf{r}_s|) - \exp(ik_m |\mathbf{r} - \mathbf{r}_s|) \right] - \frac{C(\omega)}{|\mathbf{r} - \mathbf{r}_s^*|} \left[\exp(ik_x |\mathbf{r} - \mathbf{r}_s^{\text{ebc}}|) - \exp(ik_m |\mathbf{r} - \mathbf{r}_s^{\text{ebc}}|) \right] \quad (4.9)$$

where: \mathbf{r}_s is the position of the real source and $\mathbf{r}_s^{\text{ebc}}$ is the position of the image source with respect to the extrapolated boundary condition. The variables C and k are defined by the equations below:

$$C(\omega) = \frac{\phi \mu_{\text{axf}} S}{4\pi D_x D_m} \left[\frac{1 + i\omega\tau}{1 + (\omega\tau)^2} \right] \left[\frac{1}{k_x^2 - k_m^2} \right] \quad (4.10)$$

$$k^2(\omega) = \frac{i\omega - c\mu_a}{cD} \quad (4.11)$$

where S is the source power; ϕ , is the quantum efficiency of the fluorophore; μ_{axf} is the absorption coefficient of the fluorophore at the excitation wavelength; D_x and D_m are the excitation and emission diffusion coefficients, respectively; and ω is the frequency. Li *et al.* found this solution to agree with finite difference methods to within 3% accuracy

in I_{AC} and 1.2° in θ .²⁰⁹ With the ICCD camera system, θ and I_{AC} can be measured directly and translate to the photon fluence by the following relationships:

$$\theta = \arctan\left(\frac{\text{IMAG}[\Phi_m]}{\text{REAL}[\Phi_m]}\right) \quad (4.12)$$

$$I_{AC} = \left(\text{IMAG}[\Phi_m]^2 + \text{REAL}[\Phi_m]^2\right)^{\frac{1}{2}} \quad (4.13)$$

Therefore, experimental data can be directly compared to the analytical solutions.

4.5 Experimental Design

To replicate experimentally the photon migration models presented in Sections 4.1 through 4.3 as well as mimic clinical optical lymphography conditions, tissue phantoms were constructed and an experimental design to measure the mean depth of photon occurrence was developed. The experiments involve two tissue-mimicking cases: (1) a homogeneous optical property distribution with a uniform concentration of fluorophore and (2) a single fluorescent target within a homogeneous optical property background that has either no fluorophore or a uniform concentration of fluorophore in the background. Only case (1) may be directly compared to the analytical solutions described previously since reciprocity is not applicable between a plane wave and a spherical wave solution for a heterogeneous optical properties distribution. Figure 4.2 illustrates this difference in heterogeneity for both phantoms constructed.

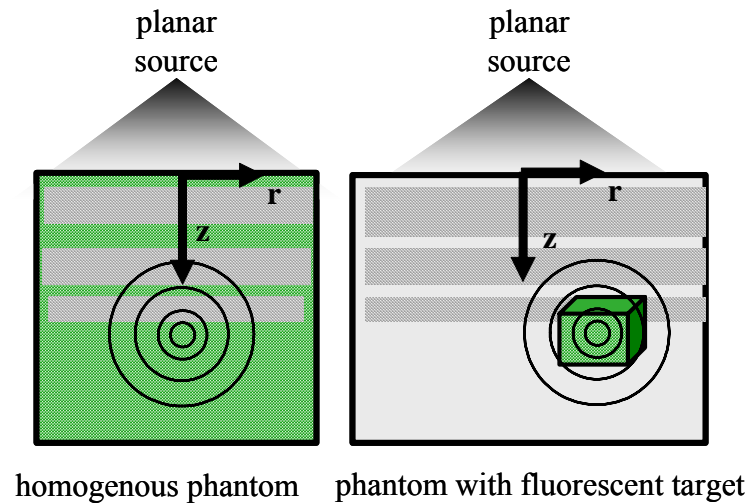


Figure 4.2 The phantom on the left contains a homogeneous distribution of optical properties having a uniform distribution of fluorophore, which is depicted by the green shaded area. The phantom on the right contains a cubic fluorescent target with optical properties different from its homogeneous surroundings, which is illustrated by the difference in color between the target and background. As depicted in the homogeneous phantom, a planar wave propagates through the medium and upon reaching a fluorophore at any location a spherical emission photon density wave is produced. Alternatively, with a phantom containing a fluorescent target, the propagating photon density wave reaches the target region, which is the only location where spherical emission waves are produced.

4.5.1 Homogeneous Experiment

Investigating depth of penetration with a geometry that houses no fluorescent targets and lacks heterogeneity in the fluorescence distribution involves construction of a simple phantom, which was described in Section 3.3. Using a homogeneous phantom, the optical properties (μ_a and μ_s') and fluorescent lifetime were altered by varying the concentration of scattering solution and absorbing dye, and by altering the fluorophore used to either a dilute solution of ICG or DTTCl. Additionally, to investigate the impact

of time-resolved measurements, namely modulated light detection, measurements at different modulation frequencies were obtained. Table 4.1 outlines the range of experiments performed for each fluorescent lifetime investigated.

Table 4.1 Matrix of experiments performed for homogeneous phantom measurements in which either ICG or DTTCI was used. The frequency was varied in increments of 30 MHz starting from 30 MHz to 130 MHz, and the scattering solution was either a 1% (vol/vol) solution of Liposyn® in water or a 0.5 % solution.

Frequency (MHz)		30	60	90	100	130
ICG	1%	Measured I_{AC} and θ : 10^{-6} M homogeneous concentration				
	0.5%					
DTTCI	1%					
	0.5%					

Owing to the same excitation and emission spectra and differing lifetimes, the two fluorescent dyes, ICG and DTTCI, were used to compare the ability of the ICCD camera system to resolve fluorescent lifetime changes at ranging penetration depths.

4.5.2 Heterogeneous Experiment

In addition to the homogeneous phantom measurements, phantom studies with a fluorescent target were acquired to simulate the presence of a fluorescent sentinel lymph node within tissue. Section 3.3 provides details on the target construction. Since the direct match of probability distributions and experimental measurements are not entirely correct owing to lack of reciprocity, only the experimental results are investigated for

the depth of experimental photon detection. Table 4.2 provides a matrix of the experiments performed with a fluorescent target.

Table 4.2 Matrix of experiments performed for heterogeneous phantom measurements in which either ICG or DTTCI was used. The frequency was varied in increments of 30 MHz starting from 30 MHz to 130 MHz, and the scattering solution was a 0.5 % (vol/vol) solution of Liposyn® in DIUF water.

Frequency (MHz)		30	60	90	100	130
ICG	0.5%	Measured I_{AC} and θ : 10^{-6} M in target to 10^{-8} M in background and 10^{-6} M in target to 0 M in background				
DTTCI	0.5%					

Similar to the homogeneous phantom studies, a range of frequency measurements were acquired. The background concentration of fluorescence was varied to either have no fluorophore or a concentration ratio of 100:1 target-to-background fluorescence. Lastly, for each case, measurements were acquired at three target depth locations: 1.5 cm, 3.5 cm, and 5 cm below the phantom surface.

4.6 Results and Discussion on Probability Analysis Predictions

The final and uni-directional probability models, $P(\mathbf{z}, \omega)$ and $P(\mathbf{z}, t)$, were first plotted to observe the change in photon occurrence from zero to 4 cm beneath the tissue surface. Figure 4.3 is an example of the time-domain PDF solution using Equation 4.4 and is plotted versus \mathbf{z} at different times, t . The plot represents the probability that a

spherically emitted wave occurs after being excited by a planar excitation pulse of light. Five different probability distributions are plotted in Figure 4.3 representing five arbitrarily chosen times at which the probability solution was observed. The times range from approximately 0.2 to 2.3 ns. Additionally, Figure 4.3 represents probabilities calculated based on a fluorophore with spontaneous re-emission in which the lifetime is zero.

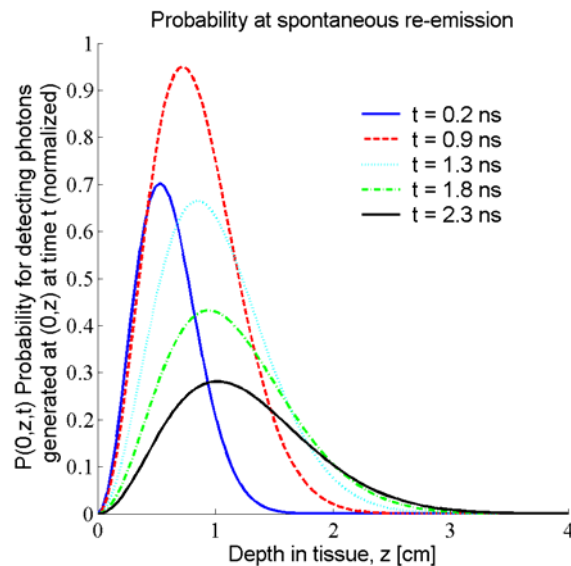


Figure 4.3 Normalized probability distribution of fluorescence spontaneously re-emitted over the depth, z , and for varying times, t . The reduced scattering and absorption coefficients are equivalent to $\mu_s' = 10 \text{ cm}^{-1}$ and $\mu_{\text{axf}} = 0.02 \text{ cm}^{-1}$, respectively.

Likewise, Figure 4.4 represents the time-domain probability calculated from Equation 4.5; however the solution was computed using a phosphorescent lifetime equal to 10 ns. The probabilities are observed at different time points than those sampled in

Figure 4.3 because longer sampling times were required for the observation of phosphorescent signals. The times chosen ranged from 2.7 to 16.7 ns. As in the spontaneous re-emission case, the phosphorescent photon probability solution describes the occurrence of a spherically emitted photon subsequent to excitation by a planar pulse of light.

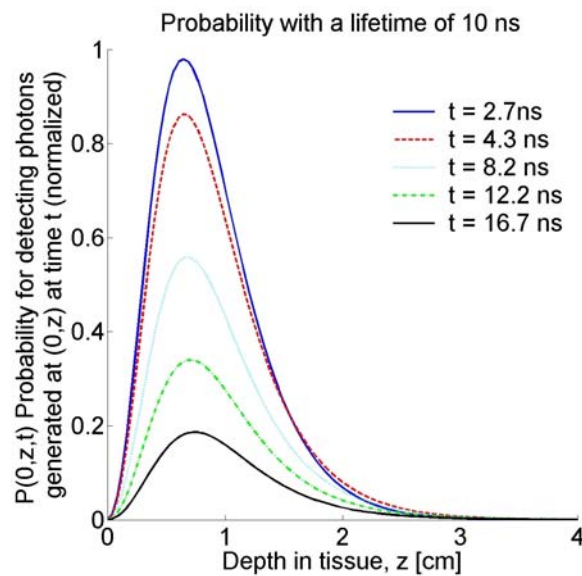


Figure 4.4 Normalized probability distribution of fluorescence from a fluorophore with a lifetime of 10 ns distributed over the dimensionless depth, z , and for varying times, t . The reduced scattering and absorption coefficients are equivalent to $\mu_s' = 10 \text{ cm}^{-1}$ and $\mu_{\text{axf}} = 0.02 \text{ cm}^{-1}$, respectively.

The time-domain probability distributions presented above show that there is a dependence of penetration depth on two factors: (1) the fluorophore lifetime and (2) the time at which the emitted signal is detected at the tissue surface. In Figure 4.3, which presents probability distributions simulated for a spontaneously emitting fluorophore, it

is shown that tissues contributing most to the detected signal are either closer to the surface or significantly deeper depending on the time of detection. This is in opposition to the probability simulation presented in Figure 4.4, in which a long-lived lifetime equal to 10 ns was studied. The tissue depths probed are consistently shallow for any time, t , when a phosphorescent signal is detected. The probability functions which provide planar wave excitation and spherical wave emission resulted in simulations that agree with previous results from Sevick-Muraca.¹⁹⁵

In addition to the time-domain results, the frequency-domain probability models are plotted below based on computations from Equation 4.7. The plotted data represent the probability that a modulated and spherical emission wave occurs after being excited by a modulated and planar excitation light source. Figure 4.5 provides the resulting probability distributions plotted versus z at different frequencies, ω , and for a spontaneous emission lifetime. The five probability distributions in Figure 4.5 were calculated at five arbitrarily chosen frequencies. The frequencies range from approximately 0 to 100 MHz.

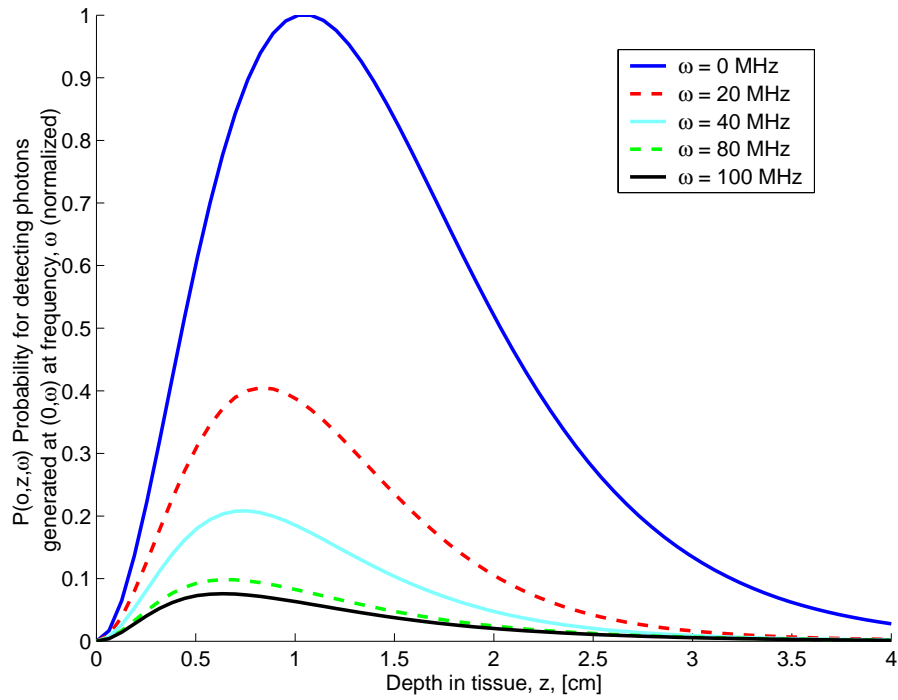


Figure 4.5 Normalized probability distribution of fluorescence spontaneously re-emitted over the depth, z and for varying frequencies, ω . The reduced scattering and absorption coefficients are equivalent to $\mu_s' = 10 \text{ cm}^{-1}$ and $\mu_{\text{axf}} = 0.02 \text{ cm}^{-1}$, respectively.

Figure 4.6 is an illustration of the frequency-domain probability results for a phosphorescent fluorophore with a lifetime equal to 10 ns. Like Figure 4.5, the plot below represents five probability distributions taken from five different frequency simulations. The frequencies sampled are 0, 20, 40, 80, and 100 MHz. As in the spontaneous re-emission case, the phosphorescent photon probability solutions describe the occurrence of a spherically emitted photon subsequent to excitation by a planar and modulated light source.

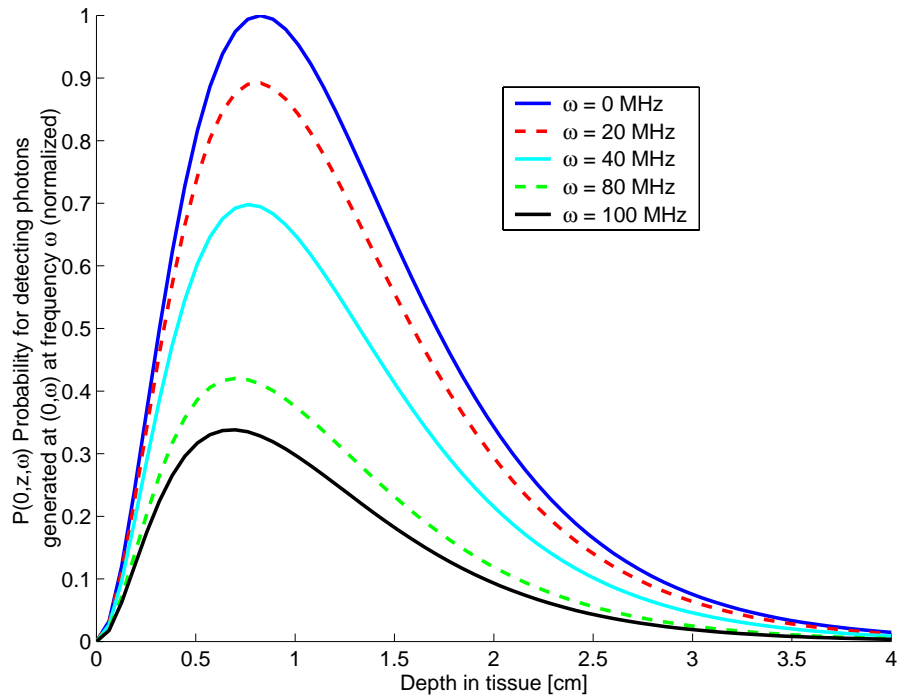


Figure 4.6 Normalized probability distribution of fluorescence from a fluorophore with a lifetime of 10 ns distributed over the depth, z and for varying frequencies, ω . The reduced scattering and absorption coefficients are: $\mu_s' = 10 \text{ cm}^{-1}$, $\mu_{\text{axf}} = 0.02 \text{ cm}^{-1}$.

The frequency-domain PDF plots show that tissues contributing to the detected signal depend on two factors: (1) the modulation frequency and (2) the fluorophore lifetime. Figures 4.5 and 4.6 both reveal maximum probabilities at modulation frequencies equal to zero. The probabilities obtained for the continuous wave case agree with the inherent trend of penetration depth decrease following modulation frequency increase. Also upon comparing Figure 4.5 to 4.6 it is apparent that the depth of tissue sampled changes with fluorophore lifetime. That is, the bulk of the detected signal is consistently shallow when a phosphorescent fluorophore is present compared to the

deeper and shifted detected signals resulting from spontaneous fluorophore emission. The frequency-domain results therefore agree with the time-domain solutions.

In addition to the probability distributions, the mean depth was plotted following Equation 4.8. The mean depth was evaluated for both the time-domain as well as frequency-domain case and was computed for three lifetimes: 0, 1, and 10 ns. Figure 4.7 provides the mean depth versus detection time and mean depth versus modulation frequency. The time-domain results clearly show that as lifetime increases, the mean depth becomes shallower, asymptotically reaching a smaller number than the spontaneously emitted mean depth value. The resulting mean depth computed in the frequency-domain result show a decrease in the depth of photon penetration with increasing modulation frequency. Additionally the mean depth is overall larger when a spontaneously emitted fluorophore is present as opposed to when 1 ns and 10 ns fluorescent and phosphorescent lifetimes are detected. Thus, the frequency domain results substantiate the fact that detected fluorescence signals originate from deeper in the tissue when emitted spontaneously by a fluorophore. Also revealed in Figure 4.7 is a small perturbation in the mean depth computed from a signal that is phosphorescently emitted. The perturbation occurs from ~ 10 to 50 MHz. A possible explanation for the mean depth perturbation may be due to the relationship⁷⁷ between modulation frequency and fluorophore lifetime, $\omega \cong \frac{1}{2\pi\tau}$. The relationship describes a modulation frequency, ω , that will maximally perturb a detected emission signal from a fluorophore with a lifetime equal to τ . Thus, the optimum frequency at which to measure a fluorophore

with a lifetime of 10 ns, is approximately 15 MHz. The mean depth perturbation revealed in Figure 4.7 may be a result of that phenomenon.

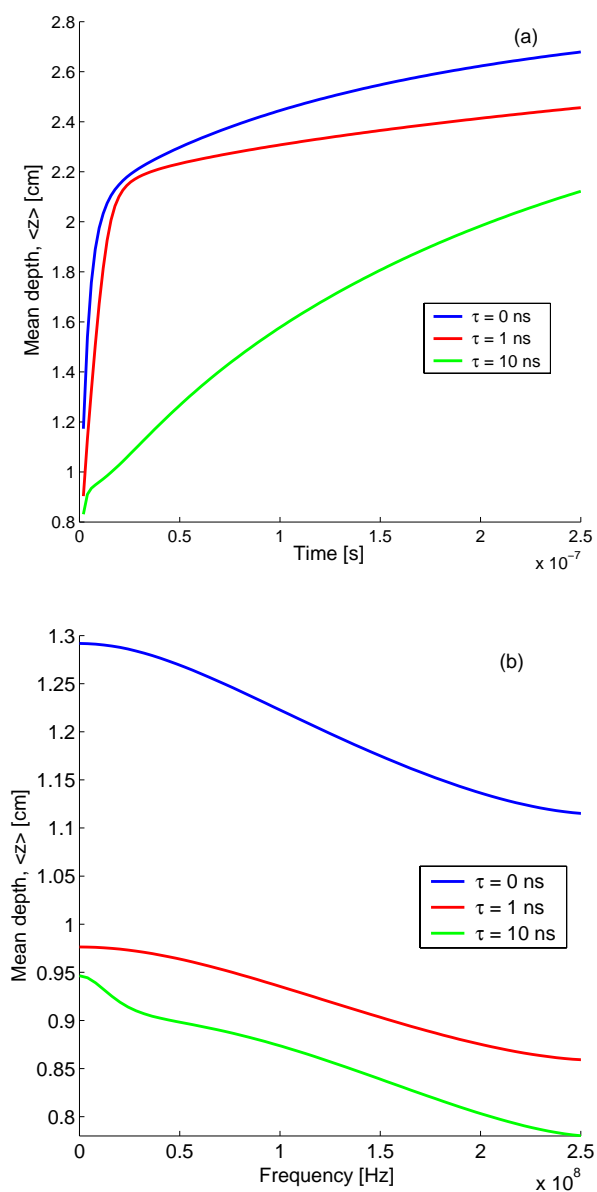


Figure 4.7 Mean depth, $\langle z \rangle$, versus detection time, t , (a), and mean depth, $\langle z \rangle$, versus modulation frequency, ω , (b) calculated from a PDF analysis on a fluorescent solution with uniform concentration of fluorophore at lifetimes of 0, 1, and 10 ns.

4.7 Results and Discussion on Homogeneous Phantom Experiments vs. Analytical Predictions

The simulated mean depth and probability values reveal important dependencies of penetration depth on frequency and fluorescence lifetime; therefore the phantom experiments were inspected closely for similar traits. The experimental data was processed and the results were compared to the analytical solution computed by Equation 4.9. Several homogeneous phantom studies were performed, as outlined in Table 4.1; however only limited results are presented below, all of which are indicative of the overall phantom study results. Figures 4.8 through 4.12 show the typical I_{AC} , θ , I_{AC} relative error, $\frac{I_{AC}^{\text{pred}} - I_{AC}^{\text{exp}}}{I_{AC}^{\text{pred}}} \times 100$, and absolute θ error, $\theta^{\text{pred}} - \theta^{\text{exp}}$, obtained from homogeneous phantoms measured at 30, 60, 90, 100, and 130 MHz. The normalized experimental data points measured at discrete 1 cm increments are plotted with predictions, indicated by the solid lines. The θ data error bars represent the standard deviation in the extracted multi-pixel regions of interest from the phase images.

Figure 4.8 is an example of I_{AC} and θ results measured at 30 MHz for a phantom with $\tau = 1.18$ ns, $\mu_a = 0.063$ cm⁻¹, and $\mu_s = 17$ cm⁻¹. As seen in the figure below, the normalized I_{AC} decreases with increasing depth whereas θ increases. The I_{AC} error becomes larger at depths above 4 cm. Also, the standard deviation in the θ value increases at depths above 4 cm, which is a result of the noisy and highly attenuated fluorescence signal obtained from deeper within the tissue phantom. All experimental data points with a modulation depth (I_{AC}/I_{DC}) greater than 0.05 were plotted. All other

data were regarded as instrument noise and thus was not considered relevant I_{AC} or θ measurements. For the overall results obtained, the I_{AC} relative error and absolute θ error were found to be equivalent to previously measured data²¹⁰ obtained by a similar ICCD system at the PML.

Similarly, Figure 4.9 provides the results of I_{AC} and θ measured at 60 MHz for a phantom with the following properties: $\tau = 1.18$ ns, $\mu_a = 0.063$ cm⁻¹, and $\mu_s = 17$ cm⁻¹. As in the 30 MHz measured data, 60 MHz results show an increase in noise at depths above 5 cm. However, despite the noise increase, the I_{AC} and phase measurements remain close to the predicted values and can be resolved to depths up to 9 cm. Figures 4.8 and 4.9 represent data obtained from DTTCl, a fluorophore with a lifetime equal to 1.18 ns. Alternatively, Figures 4.10 and 4.11 are representative I_{AC} and θ data obtained from a phantom with a homogeneous distribution of ICG, which has a lifetime equal to 0.56 ns. Figure 4.10 displays results measured at 90 MHz for a phantom with μ_a equal to 0.18 cm⁻¹, and μ_s equivalent to 10 cm⁻¹.

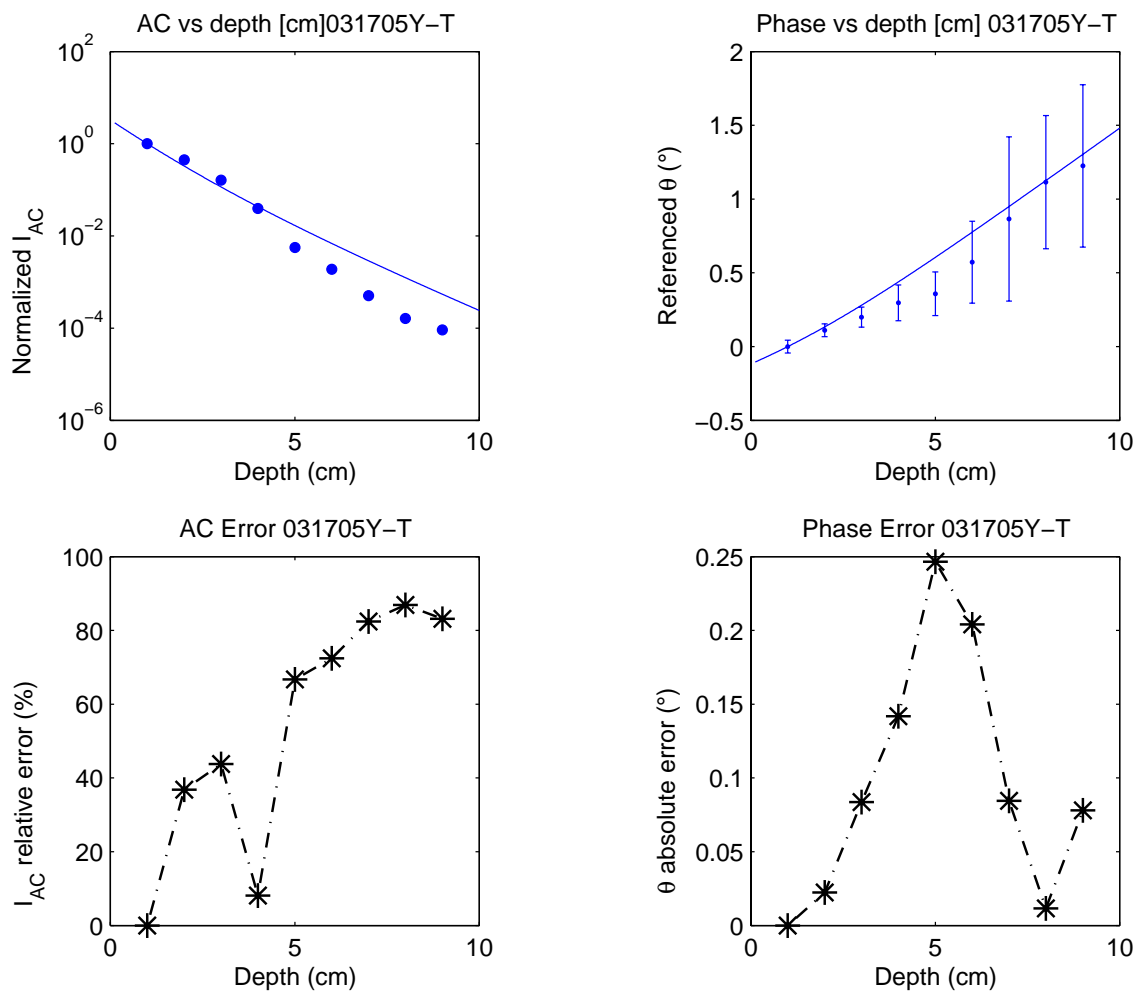


Figure 4.8 I_{AC} (top left), θ (top right), I_{AC} relative error (bottom left) and absolute θ error (bottom right) vs. depth measured at 30 MHz. Experimental data (dotted points) are plotted with predictions (solid line) for a phantom in which $\mu_a = 0.063 \text{ cm}^{-1}$, $\mu_s' = 17 \text{ cm}^{-1}$, and $\tau = 1.18 \text{ ns}$. The error bars on the phase plot represent the standard deviation in the pixel region of interest selected.

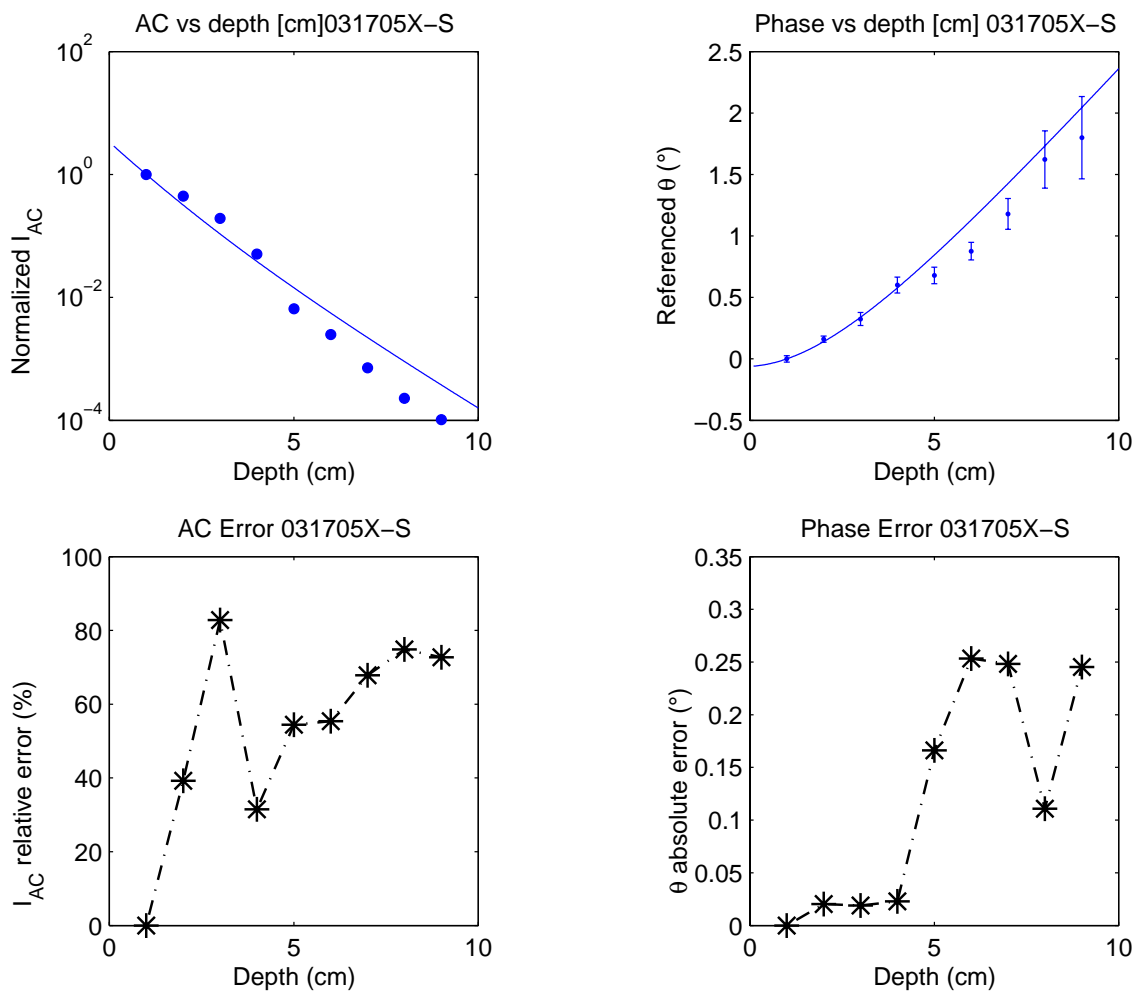


Figure 4.9 I_{AC} (top left), θ (top right), I_{AC} relative error (bottom left) and absolute θ error (bottom right) vs. depth measured at 60 MHz. Experimental data (dotted points) are plotted with predictions (solid line) for a phantom in which $\mu_a = 0.063 \text{ cm}^{-1}$, $\mu_s' = 17 \text{ cm}^{-1}$, and $\tau = 1.18 \text{ ns}$. The error bars on the phase plot represent the standard deviation in the pixel region of interest selected.

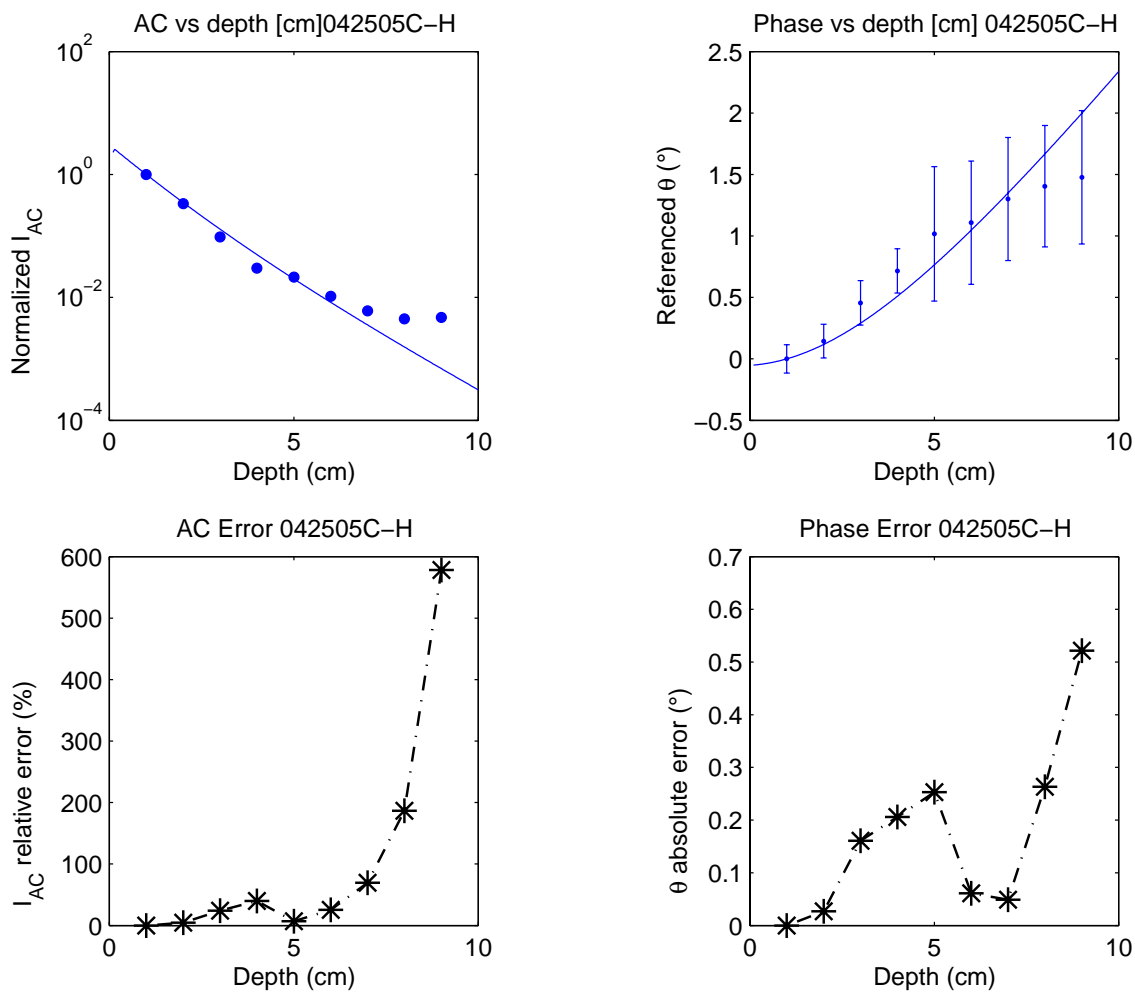


Figure 4.10 I_{AC} (top left), θ (top right), I_{AC} relative error (bottom left) and absolute θ error (bottom right) vs. depth measured at 90 MHz. Experimental data (dotted points) are plotted with predictions (solid line) for a phantom in which $\mu_a = 0.18 \text{ cm}^{-1}$, $\mu_s' = 10 \text{ cm}^{-1}$, and $\tau = 0.56 \text{ ns}$. The error bars on the phase plot represent the standard deviation in the pixel region of interest selected.

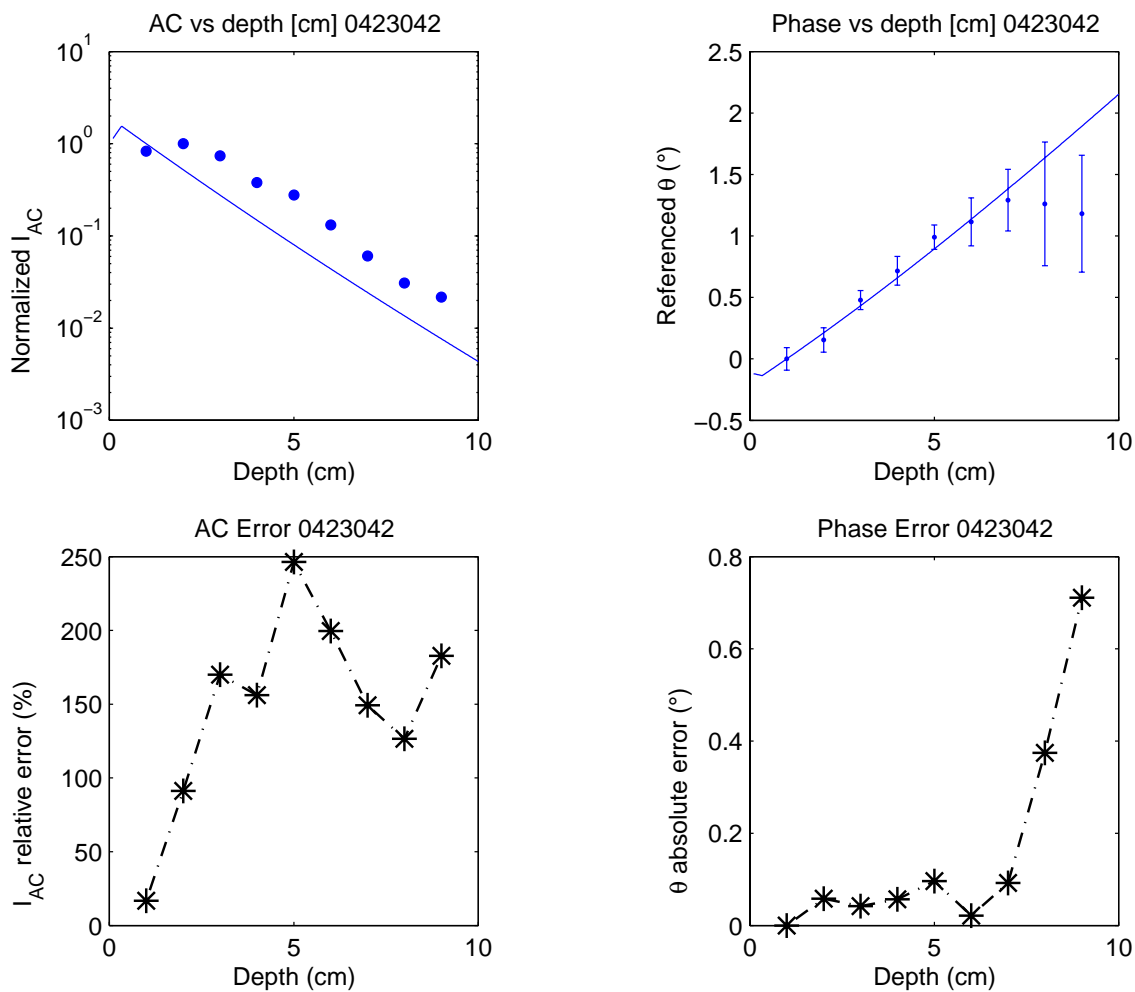


Figure 4.11 I_{AC} (top left), θ (top right), I_{AC} relative error (bottom left) and absolute θ error (bottom right) vs. depth measured at 100 MHz. Experimental data (dotted points) are plotted with predictions (solid line) for a phantom in which $\mu_a = 0.1 \text{ cm}^{-1}$, $\mu_s' = 5 \text{ cm}^{-1}$, and $\tau = 0.56 \text{ ns}$. The error bars on the phase plot represent the standard deviation in the pixel region of interest selected.

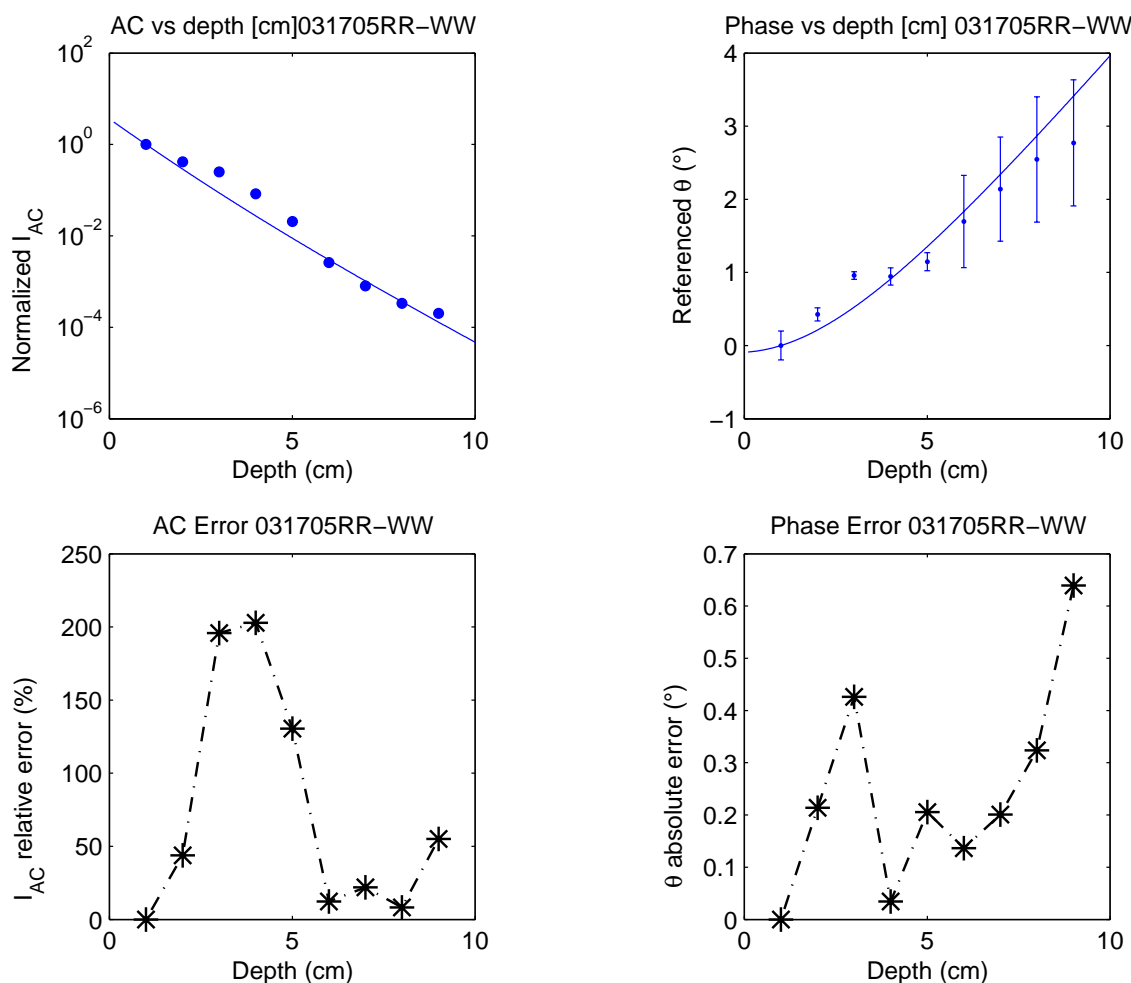


Figure 4.12 I_{AC} (top left), θ (top right), I_{AC} relative error (bottom left) and absolute θ error (bottom right) vs. depth measured at 130 MHz. Experimental data (dotted points) are plotted with predictions (solid line) for a phantom in which $\mu_a = 0.0063 \text{ cm}^{-1}$, $\mu_s' = 17 \text{ cm}^{-1}$, and $\tau = 1.18 \text{ ns}$. The error bars on the phase plot represent the standard deviation in the pixel region of interest selected.

Indocyanine green had a higher measured absorption coefficient than DTTCI at the same concentration; the value generally differed by an order of magnitude. Nonetheless, as shown in Figure 4.10, I_{AC} and θ data were fully resolvable at depths up to 9 cm. Additionally, the ICCD camera system measured I_{AC} and θ at an overall lower

modulation depth at 90 MHz which resulted in noisy measurements compared to all other modulation frequencies. Figure 4.11 displays results measured at 100 MHz for a phantom with $\tau = 0.56$ ns, $\mu_a = 0.1$ cm⁻¹, and $\mu_s = 5$ cm⁻¹.

In Figure 4.11, the phase measurements decrease at 7 cm, indicating the increase in measurement noise. Lastly, Figure 4.12 presents the I_{AC} and θ data measured at 130 MHz. The tissue phantom for the data in Figure 4.12 contained the following properties: $\tau = 1.18$ ns, $\mu_a = 0.063$ cm⁻¹, and $\mu_s = 17$ cm⁻¹.

The experimental data represent half of the total distance the photon density wave travels before detection on the tissue surface. Recall the probability density function computes the total signal as it propagates into the tissue and is re-emitted at the surface. Therefore, the measured I_{AC} and θ values can only compare to the first part of the simulated probability function, P_S . Nonetheless, based on the principle of reciprocity, the fluorescence photon density wave can be expected to behave similar to the probability results upon changes in ω and τ . Therefore in addition to simply examining experimental data accuracy relative to predictions, phantom results were compared to each other to inspect the dependence of penetration depth on μ_a , μ_s' , fluorescence lifetime, and modulation frequency. Figures 4.13 through 4.15 present typical results from experiments in which the values of μ_a , μ_s' , ω , or τ , were altered. Figure 4.13 provides the results from homogeneous phantom experiments in which the absorption coefficient, μ_a , was varied from 0.04 to 0.12 cm⁻¹. All other phantom optical properties were held constant so as to compare the maximum tissue depth probed and ability of the ICCD system to measure small changes in the absorption coefficient at

clinically relevant depths. From Figure 4.13, it is apparent that increasing the absorption coefficient decreases the tissue penetration depth, which is reflected in the I_{AC} measurement. The θ value also decreases with increasing μ_a but to a lesser extent than the I_{AC} values. Owing to the small change in θ , the ICCD measured data did not significantly detect changes μ_a by time-of-flight measurements. Additionally, the maximum penetration depth measured was 9 cm with the phantom having $\mu_a = 0.04 \text{ cm}^{-1}$ and 6 cm for the phantom having $\mu_a = 0.12 \text{ cm}^{-1}$.

Similarly, Figure 4.14 provides the results from homogeneous phantom experiments in which the reduced scattering coefficient, μ_s' , was varied from 3 cm^{-1} to 10 cm^{-1} . It is apparent that a change in the reduced scattering coefficient greatly affects both the measured I_{AC} and θ values. The I_{AC} value increases and the measured θ value decreases upon a reduction in scattering coefficient. The ICCD system was able to accurately measure the aforementioned changes owing to scattering up to depths of 7 cm for both I_{AC} and θ measurements. Accordingly, the phase value was measured at a greater accuracy up to 9 cm for the lower scattering phantom, whereas the maximum depth measurable by phase was 4 cm for the highly scattering phantom.

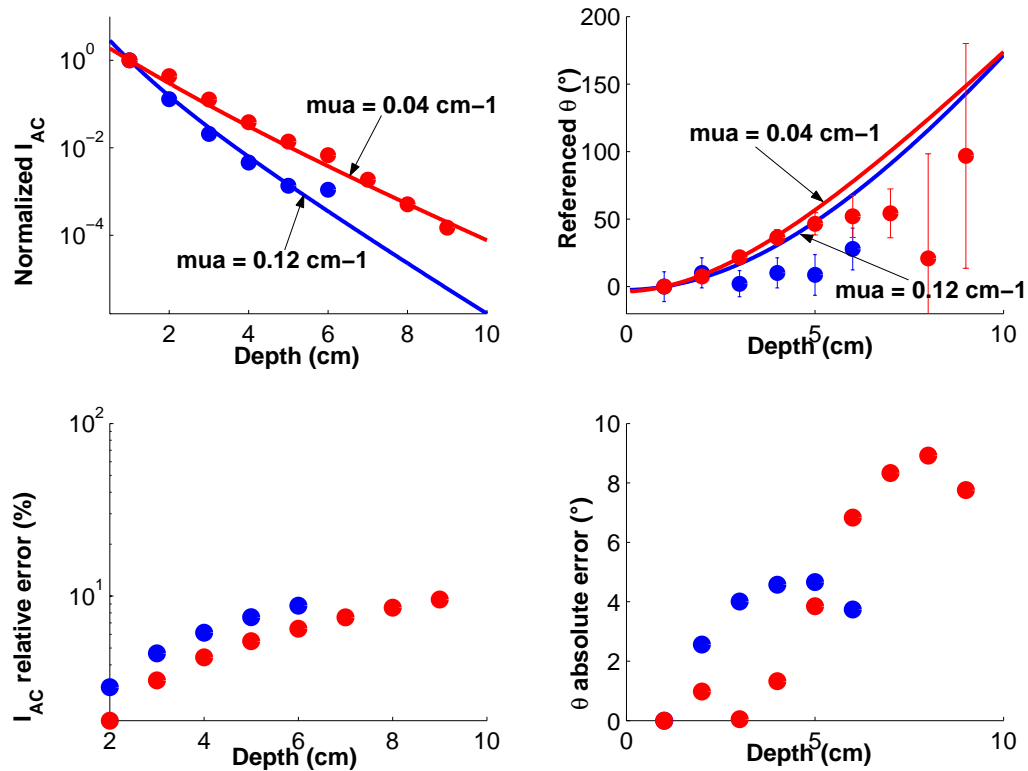


Figure 4.13 Experiments (dotted line) vs. predictions (solid line) for a highly absorbing (blue color, $\mu_a = 0.12 \text{ cm}^{-1}$) and low absorbing (red color, $\mu_a = 0.03 \text{ cm}^{-1}$) phantom ($\mu_s' = 10 \text{ cm}^{-1}$). The amplitude (top left), phase (top right), amplitude relative error (bottom left) and absolute phase error (bottom right) are plotted versus depth. The error bars on the phase plot represent the standard deviation in the pixel region of interest selected.

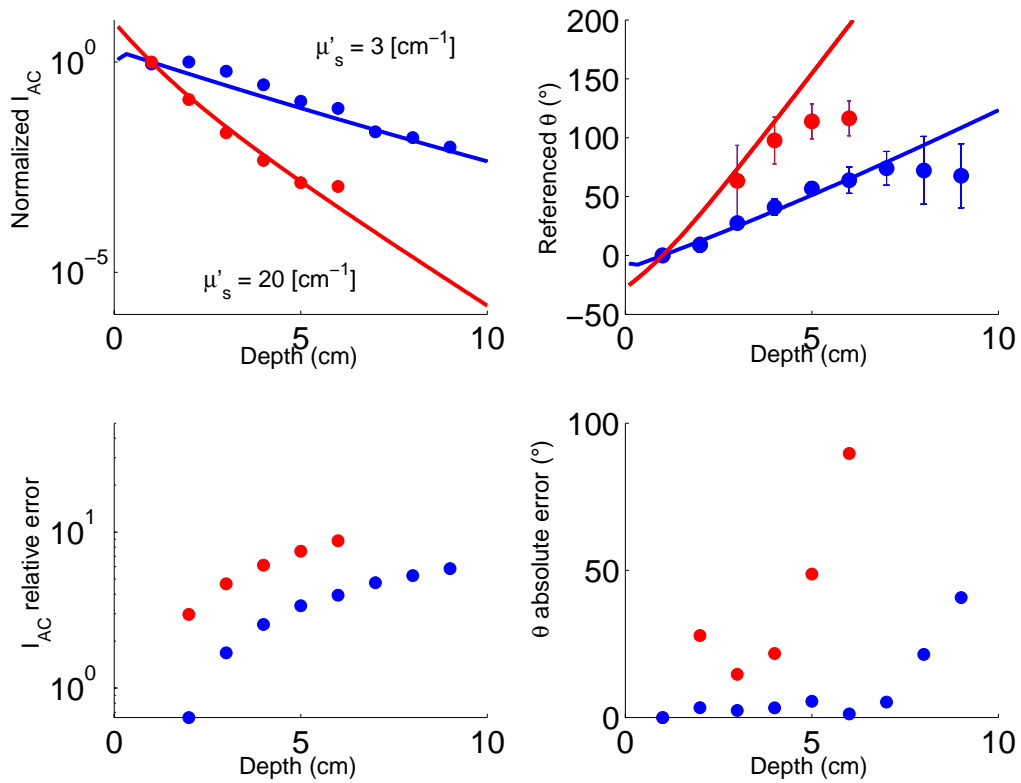


Figure 4.14 Experiments (dotted line) vs. predictions (solid line) for a highly scattering (red color, $\mu'_s = 10 \text{ cm}^{-1}$) and low scattering (blue color, $\mu'_s = 20 \text{ cm}^{-1}$) phantom ($\mu_a = 0.1 \text{ cm}^{-1}$). The amplitude (top left), phase (top right), amplitude relative error (bottom left) and absolute phase error (bottom right) are plotted versus depth. The error bars on the phase plot represent the standard deviation in the pixel region of interest selected.

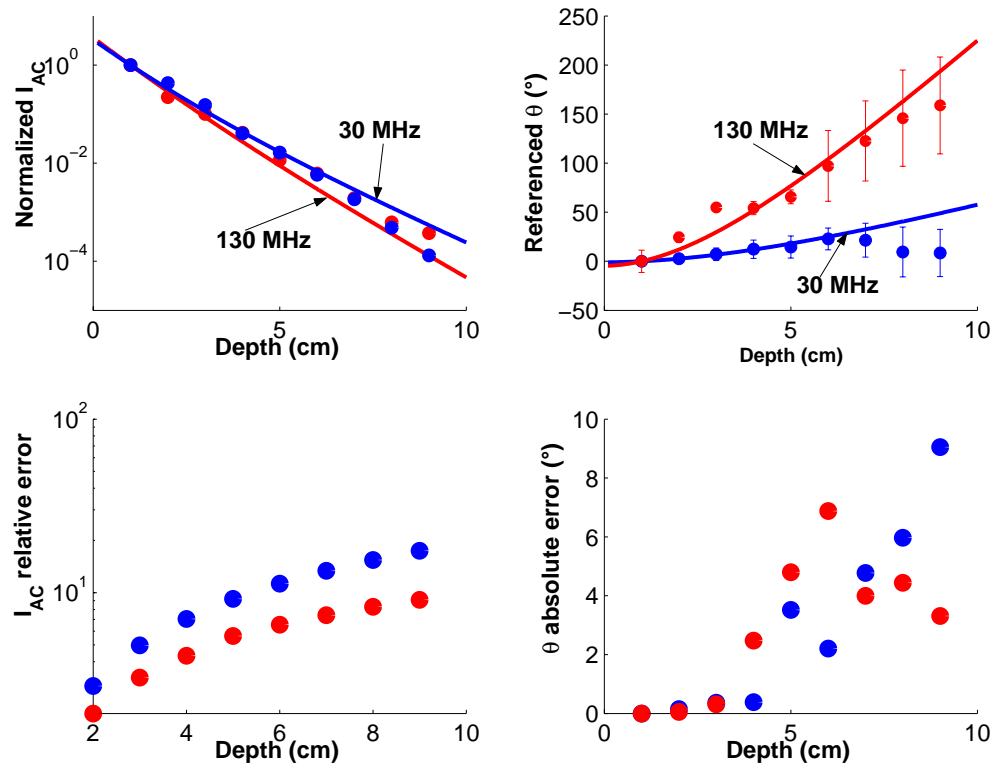


Figure 4.15 Experiments (dotted line) vs. predictions (solid line) for high frequency (red color) and low frequency (blue color) measurements on a homogeneous phantom with optical properties: $\mu_a = 0.04 \text{ cm}^{-1}$ and $\mu_s' = 10 \text{ cm}^{-1}$. The amplitude (top left), phase (top right), amplitude relative error (bottom left) and absolute phase error (bottom right) are plotted versus depth. The error bars on the phase plot represent the standard deviation in the pixel region of interest selected.

Alternatively, Figure 4.15 shows the dependence of measured I_{AC} and phase on modulation frequency. Figure 4.15 compares phantom measurements at 30 and 130 MHz and clearly demonstrates that the modulation frequency to a greater extent alters the measured phase value than the measured I_{AC} value. The ICCD system accurately detected a phase change in modulation frequency at a depth of 9 cm. However, the AC intensity measurement could not distinguish the same changes in the modulation frequency. An important factor therefore, in detecting maximum penetration depths is the use of time-resolved measurements.

Recalling from the previous sections that fluorophore lifetime also plays a large role on the origin of measured fluorescence signals, two phantoms were constructed having similar optical properties and differing fluorescent lifetimes. Two fluorophores having a lifetime difference of 0.62 ns were compared. Although the probability results compared a lifetime change of 10 ns, for the phantom experiments herein, a phosphorescent fluorophore was not used owing to dissimilar excitation and emission spectra.

It is apparent in Figure 4.16 that the measured and predicted I_{AC} and θ values change upon a difference in fluorescent lifetime. Moreover, as the lifetime increases, the measured I_{AC} decreases and measured θ value increases. The ICCD system could accurately detect changes in lifetime up to 9 cm for the phantom with the lifetime equal to 1.18 ns. Alternatively, the ICCD system measurements were resolved to a depth of 8 cm for the phantom with the shorter lifetime fluorescent medium. Although the greater penetration depth measurable was found for the longer lifetime, opposite to the PDF

results, the data are not indicative of the probability simulation owing to differences in absorption between the two phantoms. Moreover, small changes in lifetime may not impact the mean depth probed as do larger changes such as 10 ns. Nonetheless, the results are significant for the translation of the imaging system to a clinical situation because they demonstrate that the ICCD system provides robust measurements upon small changes in optical properties.

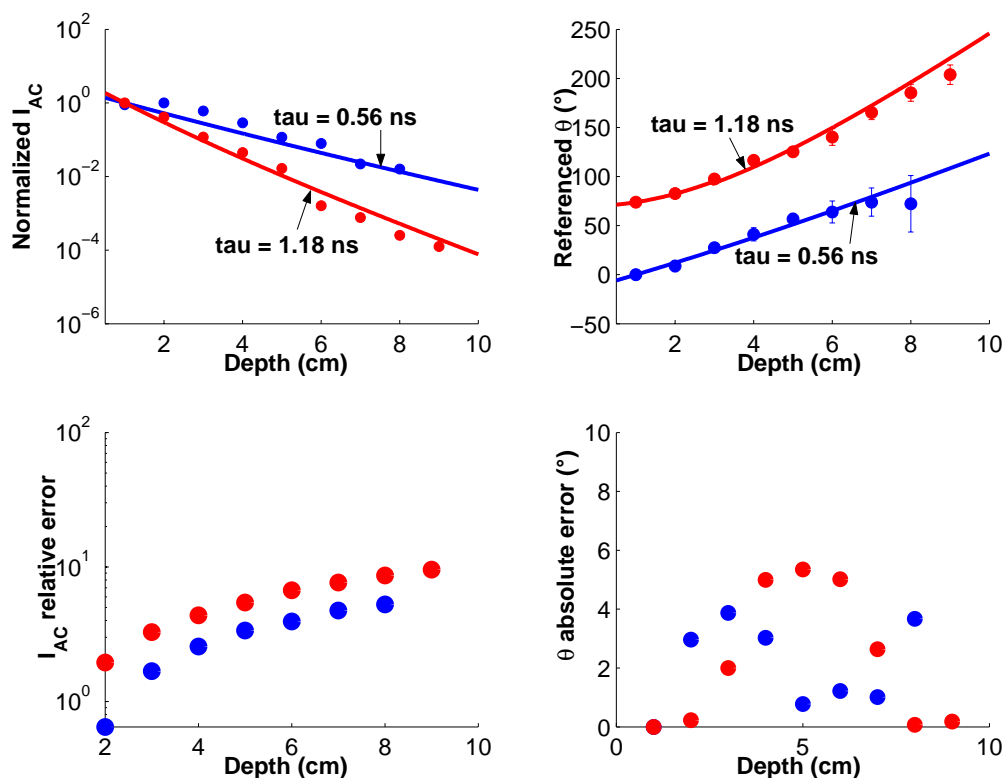


Figure 4.16 Experiments (dotted line) vs. predictions (solid line) for a large lifetime (red color, $\tau = 1.18$ ns) and small lifetime (red color, $\tau = 0.56$ ns) phantom ($\mu_a = 0.04$ cm $^{-1}$, $\mu_s' = 10$ cm $^{-1}$). The amplitude (top left), phase (top right), amplitude relative error (bottom left) and absolute phase error (bottom right) are plotted versus depth. The error bars on the phase plot represent the standard deviation in the pixel region of interest selected.

Similar to the calculated mean depth results from the PDF simulations, the mean depth was computed on all experimentally obtained I_{AC} values. The mean depth results provided a comprehensive outlook on penetration depths measurable by the ICCD system. Figure 4.17 is a bar plot of the mean depth values computed from all experiments; the results are displayed by either the 1.18 ns phantom results or the 0.56 ns phantom results so as to compare the overall mean penetration depth on fluorescent lifetime. From Figure 4.17 it is apparent that the overall maximum depth measurable is greater on the phantom having the longer lifetime fluorophore than with the phantom having the shorter lifetime fluorophore. Although this is opposite from the probability results, the maximum depth achieved is likely due to the lower absorption coefficient of DTTCI fluorophores relative to ICG fluorophores. Also revealed in the mean depth plots is the change in penetration depth owing to modulation frequency. The mean depth decreases with increasing frequency, which is most apparent in the measured data from the ICG phantoms. The DTTCI phantoms did not exhibit a similar trend, which may be attributed to the overall greater depth of penetration due to the lower absorption properties.

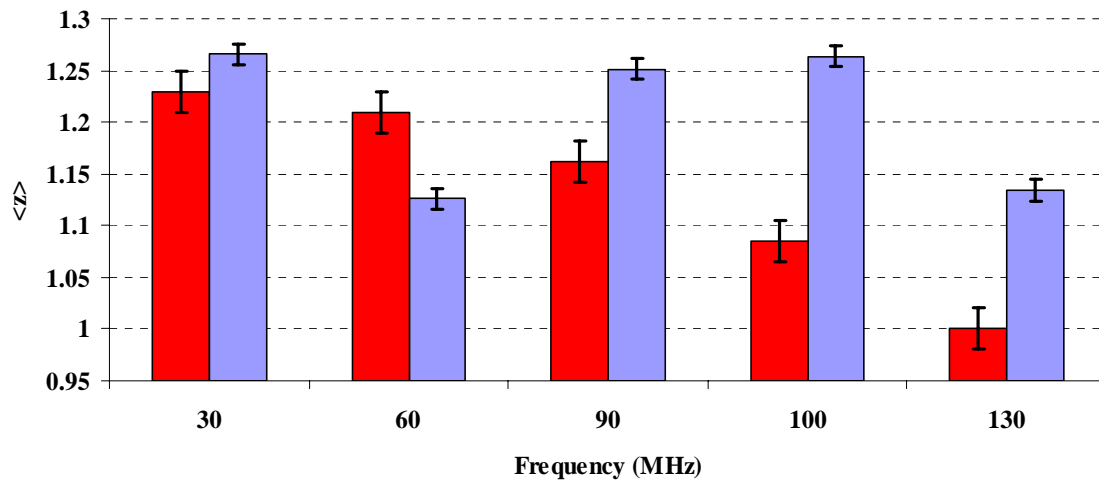


Figure 4.17 Mean depth experimental results for 30, 60, 90, 100, and 130 MHz. Data were acquired from a phantom with a fluorophore lifetime of 1.18 ns (blue) and a fluorophore lifetime equal to 0.56 ns (red). The error bars represent the standard deviation computed on the mean value.

In addition to the computed experimental mean depth values, predicted mean depth values were calculated and are plotted in Figure 4.18. The predictions were found to be statistically similar to the experimental results, demonstrating the accuracy of the ICCD system. The predictions also showed a similar trend of penetration depth decrease following modulation frequency increase. Again, the overall mean depth was larger for the 1.18 ns lifetime phantoms relative to the shorter lifetime phantoms.

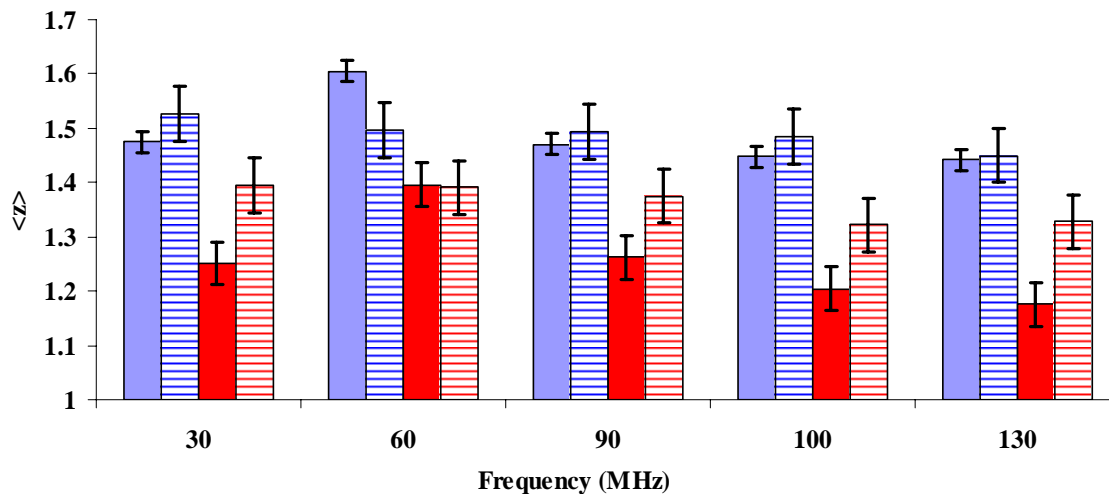


Figure 4.18 Mean depth experimental results (solid bars) as well as predictions (striped bars) for 30, 60, 90, 100, and 130 MHz. Data were acquired from a phantom with a fluorophore lifetime of 1.18 ns (blue) and a fluorophore lifetime equal to 0.56 ns (red). The error bars represent the standard deviation computed on the mean value.

Ultimately, the purpose of the mean depth measurements was to (1) determine the maximum depth measurable by the ICCD system for the application of sentinel lymph node mapping, (2) to observe changes in mean depth due to increases in fluorescent lifetime, and (3) examine how time-resolved measurements may impact the measured penetration depth. The homogeneous study resulted in I_{AC} and θ measurements which demonstrated that the ICCD system could accurately detect changes in lifetime and modulation frequency at depths up to 9 cm. Moreover, θ measurements are more sensitive to changes in fluorophore lifetime and modulation frequency than I_{AC} measurements. Since photon time-of-flight measurements may more precisely discriminate changes in fluorescence signals, and the ICCD system can

accurately detect θ at depths up to 9 cm, the time-resolved measurements may provide a better means for measuring signals originating from deep within scattering tissues.

4.8 Results and Discussion on Heterogeneous Phantom Experiments

Fluorescence-enhanced optical imaging for sentinel lymph node mapping relies not only on detecting signals at increasing tissue depths but also on detecting signals that originate from small volumes located at a individual depths within the tissue. Heterogeneous phantom studies provide a better surrogate for breast tissue containing fluorescent lymph nodes; fluorescent targets suspended within the homogeneous tissue phantom mimic the presence of lymph nodes. Section 4.5.2 provided a description on the heterogeneous phantoms measured for the experiments herein. Since the I_{AC} and θ measurements on phantoms containing a target are not comparable to Equation 4.9, the results are provided as I_{DC} , I_{AC} , θ , and modulation depth measurements only.

Figures 4.19, 4.20, and 4.21 provide the results from a phantom with a fluorescent target located 1.5, 3.5, and 5.5 cm below the tissue surface, respectively. The target contained a 1 μ M concentration of ICG and the background phantom solution contained no fluorophore. As revealed by each figure, the I_{DC} , I_{AC} , and θ values are maximally perturbed at the depth within the phantom where the target is located. Measurements on the phantom with the target located at 5.5 cm do in fact reveal perturbations, which indicate that the ICCD system may be sensitive to concentrated fluorescent signals originating from a sentinel lymph node located up to 5.5 cm below the tissues surface. The heterogeneous phantom measurements were also obtained at 30,

60, 90, 100, and 130 MHz. The data are plotted for each frequency to inspect the difference in maximum depth detectable with changing modulation frequency.

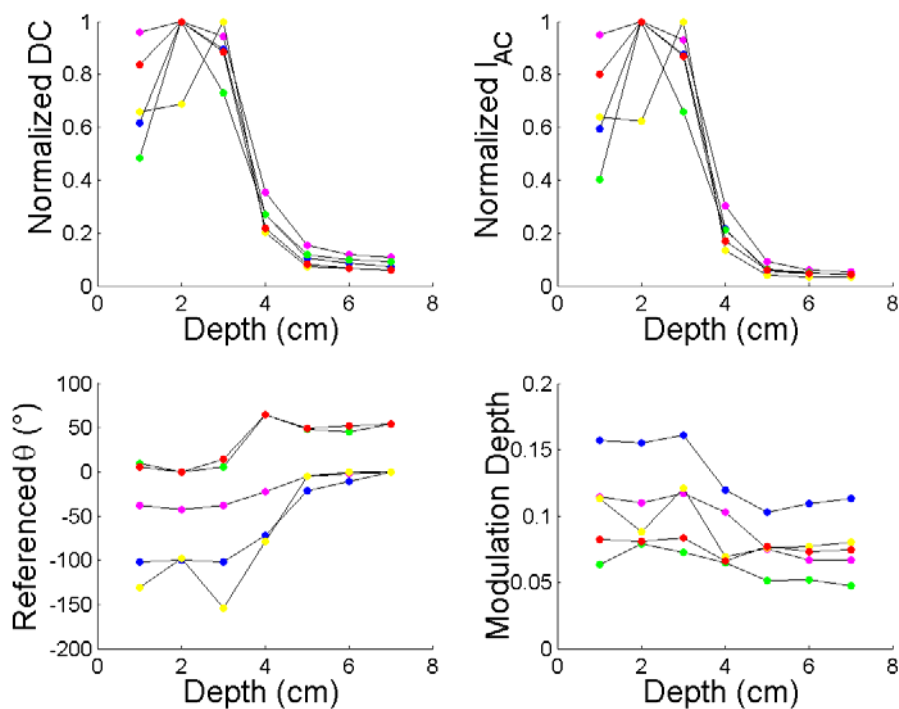


Figure 4.19 Normalized I_{DC} (top left), I_{AC} (top right), θ (bottom left), I_{AC}/I_{DC} (bottom right) versus tissue depth for a 1 μM fluorescent ICG target immersed 1.5 cm below the surface of a non-fluorescing phantom. The target optical properties were: $\mu_a = 0.12 \text{ cm}^{-1}$, and $\mu_s' = 10 \text{ cm}^{-1}$, and the background optical properties were: $\mu_a = 0.1 \text{ cm}^{-1}$ and $\mu_s' = 10 \text{ cm}^{-1}$. Measurements were acquired at 30 (red points), 60 (yellow points), 90 (green points), 100 (blue points), and 130 MHz (magenta points).

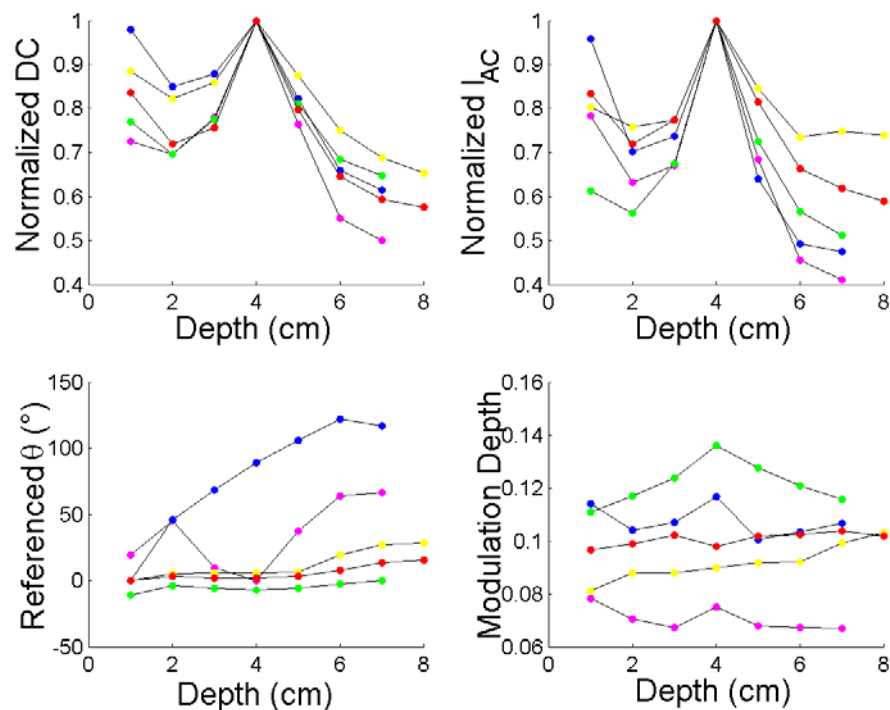


Figure 4.20 Normalized I_{DC} (top left), I_{AC} (top right), θ (bottom left), I_{AC}/I_{DC} (bottom right) versus tissue depth for a $1 \mu\text{M}$ fluorescent ICG target immersed 3.5 cm below the surface of a non-fluorescing phantom. The target optical properties were: $\mu_a = 0.12 \text{ cm}^{-1}$, and $\mu_s' = 10 \text{ cm}^{-1}$, and the background optical properties were: $\mu_a = 0.1 \text{ cm}^{-1}$ and $\mu_s' = 10 \text{ cm}^{-1}$. Measurements were acquired at 30 (red points), 60 (yellow points), 90 (green points), 100 (blue points), and 130 MHz (magenta points).

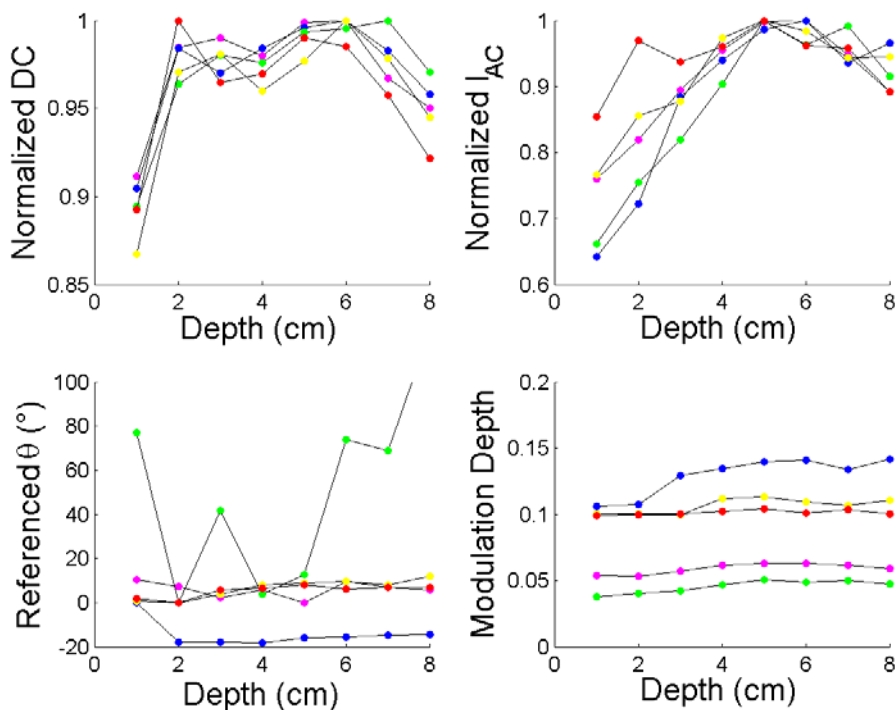


Figure 4.21 Normalized I_{DC} (top left), I_{AC} (top right), θ (bottom left), I_{AC}/I_{DC} (bottom right) versus tissue depth for a 1 μM fluorescent ICG target immersed 5.5 cm below the surface of a non-fluorescing phantom. The target optical properties were: $\mu_a = 0.12 \text{ cm}^{-1}$, and $\mu_s' = 10 \text{ cm}^{-1}$, and the background optical properties were: $\mu_a = 0.1 \text{ cm}^{-1}$ and $\mu_s' = 10 \text{ cm}^{-1}$. Measurements were acquired at 30 (red points), 60 (yellow points), 90 (green points), 100 (blue points), and 130 MHz (magenta points).

Similarly, Figures 4.22, 4.23, and 4.24 provide the results from a phantom with a fluorescent target located 1.5, 3.5, and 5.5 cm below the tissue surface, respectively. The target however contained a 1- μM concentration of DTTCI so as to compare the impact of fluorophore lifetime. Like the ICG target, the DTTCI target was immersed in a phantom in which there was no fluorophore in the background. The results from the DTTCI target are similar to the measurements obtained using ICG. At a 5.5 cm depth,

the target caused a distinct perturbation in the θ and I_{AC} measurements. There was however, no discernable difference in the maximum depth perturbed between the ICG target and DTTCI target measurements.

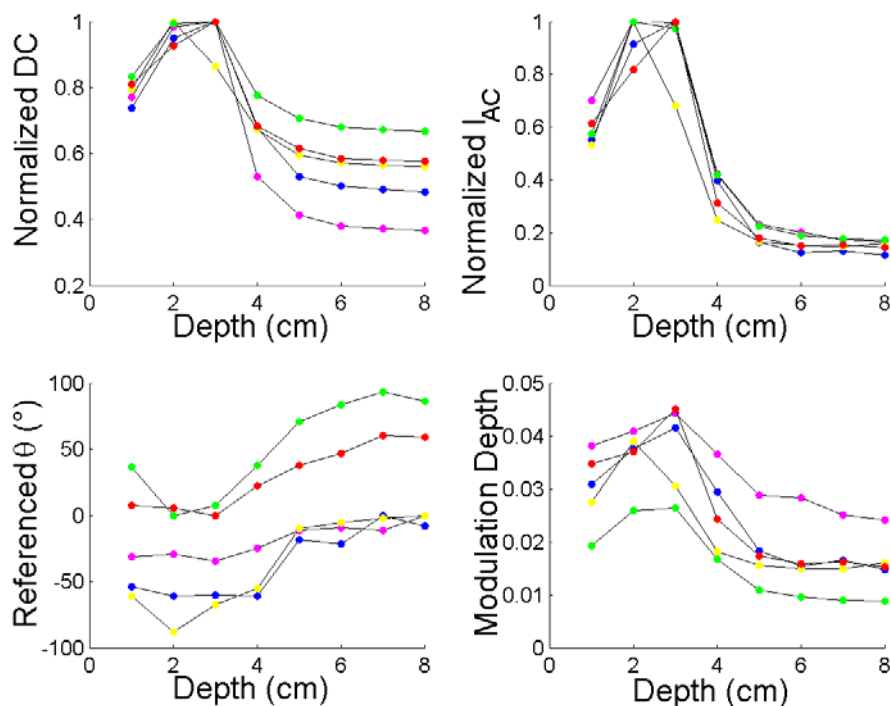


Figure 4.22 Normalized I_{DC} (top left), I_{AC} (top right), θ (bottom left), I_{AC}/I_{DC} (bottom right) versus tissue depth for a 1 μM fluorescent DTTCI target immersed 1.5 cm below the surface of a non-fluorescing phantom. The target optical properties were: $\mu_a = 0.063 \text{ cm}^{-1}$, and $\mu_s' = 10 \text{ cm}^{-1}$, and the background optical properties were: $\mu_a = 0.01 \text{ cm}^{-1}$ and $\mu_s' = 10 \text{ cm}^{-1}$. Measurements were acquired at 30 (red points), 60 (yellow points), 90 (green points), 100 (blue points), and 130 MHz (magenta points).

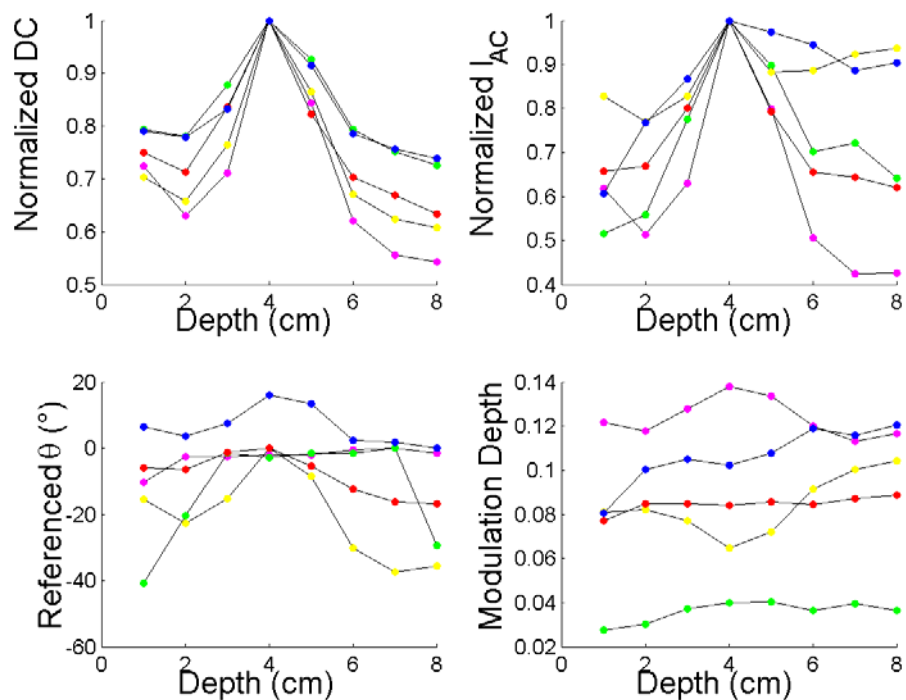


Figure 4.23 Normalized I_{DC} (top left), I_{AC} (top right), θ (bottom left), I_{AC}/I_{DC} (bottom right) versus tissue depth for a $1 \mu\text{M}$ fluorescent DTTCI target immersed 3.5 cm below the surface of a non-fluorescing phantom. The target optical properties were: $\mu_a = 0.063 \text{ cm}^{-1}$, and $\mu_s' = 10 \text{ cm}^{-1}$, and the background optical properties were: $\mu_a = 0.01 \text{ cm}^{-1}$ and $\mu_s' = 10 \text{ cm}^{-1}$. Measurements were acquired at 30 (red points), 60 (yellow points), 90 (green points), 100 (blue points), and 130 MHz (magenta points).

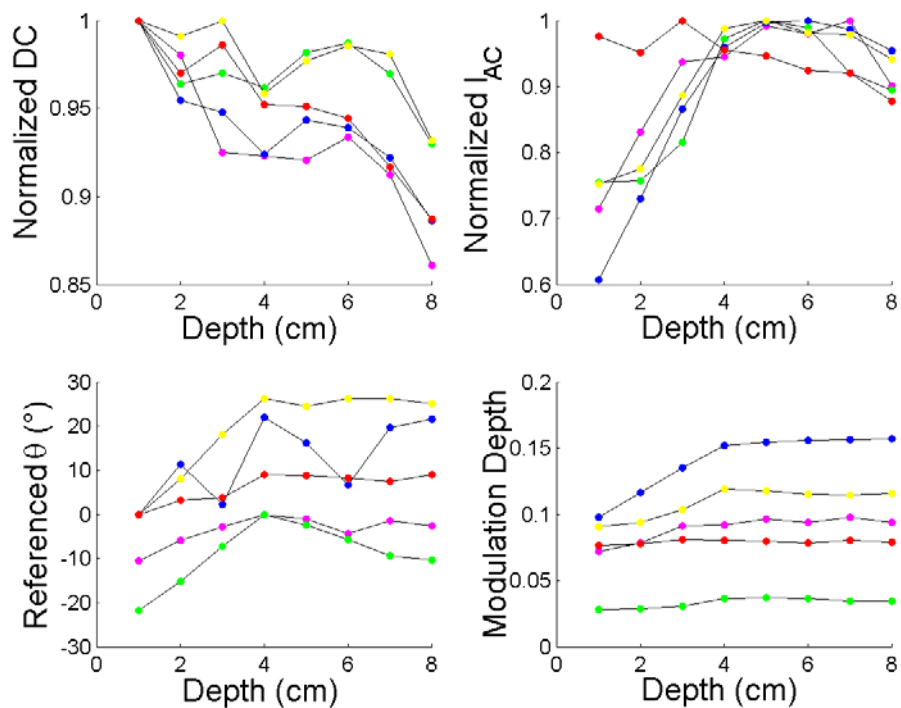


Figure 4.24 Normalized I_{DC} (top left), I_{AC} (top right), θ (bottom left), I_{AC}/I_{DC} (bottom right) versus tissue depth for a $1 \mu\text{M}$ fluorescent DTTCl target immersed 5.5 cm below the surface of a non-fluorescing phantom. The target optical properties were: $\mu_a = 0.063 \text{ cm}^{-1}$, and $\mu_s' = 10 \text{ cm}^{-1}$, and the background optical properties were: $\mu_a = 0.01 \text{ cm}^{-1}$ and $\mu_s' = 10 \text{ cm}^{-1}$. Measurements were acquired at 30 (red points), 60 (yellow points), 90 (green points), 100 (blue points), and 130 MHz (magenta points).

In addition to measuring the fluorescence signal from a target immersed in a non-fluorescing solution, phantoms were constructed to contain a 100:1 fluorophore concentration ratio between the target and background. The presence of fluorophore in the background is clinically relevant, particularly when a non-specific fluorophore is injected into the body and will accumulate throughout both diseased and normal tissues. Fluorescence may occur not only in the positive lymph nodes but in the surrounding tissues and extravascular regions. Thus, the measurable I_{DC} , I_{AC} , and θ were investigated for a phantom containing a target and fluorophore in the surrounding background. Figures 4.25, 4.26, and 4.27 provide the results from a phantom with a fluorescent target located 1.5, 3.5, and 5.5 cm below the tissue surface, respectively. The target contained a 1- μ M concentration of ICG and the background phantom solution contained a 10^{-8} -M concentration of ICG. The figures again show perturbations in the signal for measurements acquired at 30, 60, 90, 100, and 130 MHz. By visual inspection, the change in I_{DC} , I_{AC} , θ and modulation depth are greatest at the depth where target is located, however the change is less obvious than in the perfect uptake case.

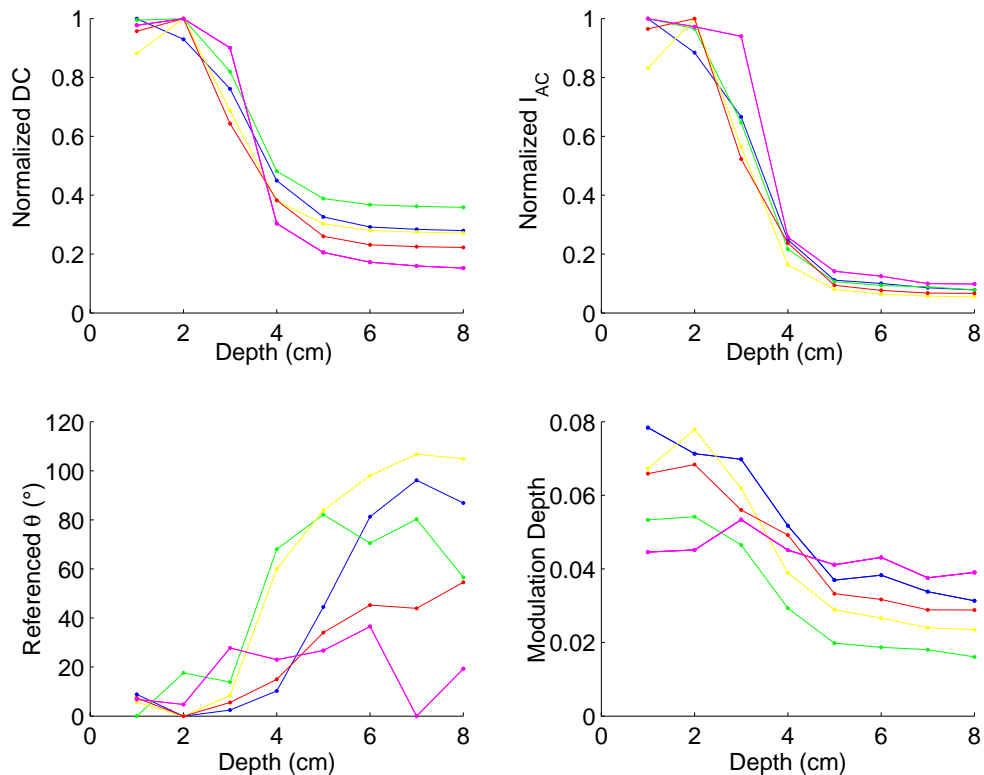


Figure 4.25 Normalized I_{DC} (top left), I_{AC} (top right), θ (bottom left), I_{AC}/I_{DC} (bottom right) versus tissue depth for a $1 \mu\text{M}$ fluorescent ICG target immersed 1.5 cm below the surface of a phantom with a 10^{-8} M uniform concentration of ICG. The target optical properties were: $\mu_a = 0.12 \text{ cm}^{-1}$, and $\mu_s' = 10 \text{ cm}^{-1}$, and the background optical properties were: $\mu_a = 0.1 \text{ cm}^{-1}$ and $\mu_s' = 10 \text{ cm}^{-1}$. Measurements were acquired at 30 (red points), 60 (yellow points), 90 (green points), 100 (blue points), and 130 MHz (magenta points).

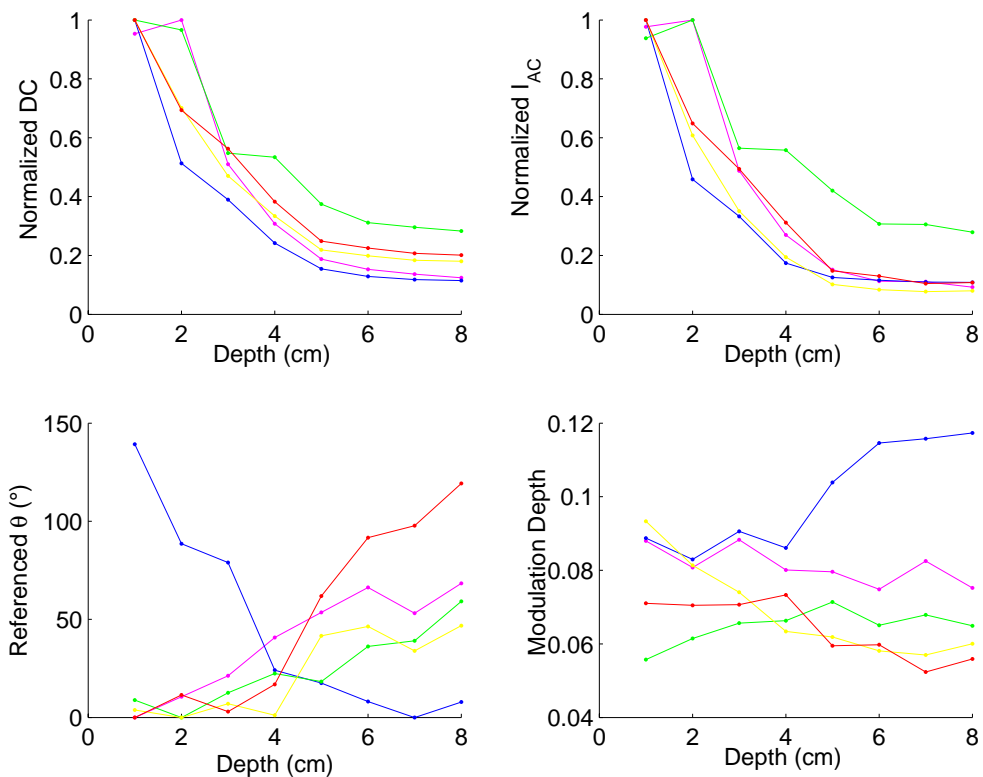


Figure 4.26 Normalized I_{DC} (top left), I_{AC} (top right), θ (bottom left), I_{AC}/I_{DC} (bottom right) versus tissue depth for a 1 μM fluorescent ICG target immersed 3.5 cm below the surface of a phantom with a 10^{-8} M uniform concentration of ICG. The target optical properties were: $\mu_a = 0.12 \text{ cm}^{-1}$, and $\mu_s' = 10 \text{ cm}^{-1}$, and the background optical properties were: $\mu_a = 0.1 \text{ cm}^{-1}$ and $\mu_s' = 10 \text{ cm}^{-1}$. Measurements were acquired at 30 (red points), 60 (yellow points), 90 (green points), 100 (blue points), and 130 MHz (magenta points).

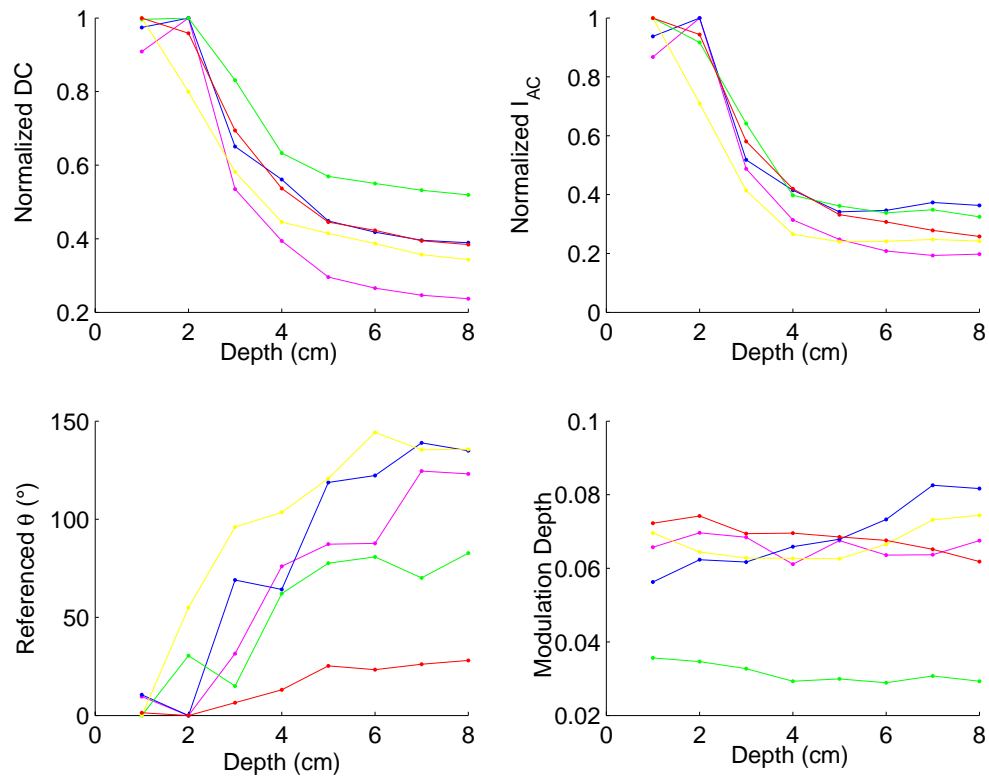


Figure 4.27 Normalized I_{DC} (top left), I_{AC} (top right), θ (bottom left), I_{AC}/I_{DC} (bottom right) versus tissue depth for a 1 μM fluorescent ICG target immersed 5.5 cm below the surface of a phantom with a 10^{-8} M uniform concentration of ICG. The target optical properties were: $\mu_a = 0.12 \text{ cm}^{-1}$, and $\mu_s' = 10 \text{ cm}^{-1}$, and the background optical properties were: $\mu_a = 0.1 \text{ cm}^{-1}$ and $\mu_s' = 10 \text{ cm}^{-1}$. Measurements were acquired at 30 (red points), 60 (yellow points), 90 (green points), 100 (blue points), and 130 MHz (magenta points).

Despite the reduced signal perturbation, the normalized I_{DC} , I_{AC} values measured when the target was immersed 3.5 and 5.5 cm deep, are larger than the I_{DC} and I_{AC} values measured for the 1.5 cm deep target. The difference in I_{DC} and I_{AC} at 1.5 cm versus 5.5 cm for example, is an indication that the ICCD system may be sensitive to fluorescence from deeply seated fluorescent lymph nodes when there is a significant concentration of fluorophore in the surrounding tissue. Moreover, there are obvious perturbations in θ which may indicate the need for time-of-flight measurements to sensitively obtain fluorescence measurements at locations up to 8 cm. The results are qualitatively promising, and comparison to diffusion equation predictions are necessary to determine the measurement sensitivity of the ICCD for changes in I_{DC} , I_{AC} , and θ due to a fluorescent target surrounded by a fluorescing background.

In addition to the heterogeneous studies with ICG in the target and background, DTTCI was used to examine the impact of a change in lifetime on target detectability when there is fluorophore in the background. Figures 4.28, 4.29, and 4.30 provide the results from a phantom with a fluorescent target located 1.5, 3.5, and 5.5 cm below the tissue surface, respectively. The target contained a 1- μ M concentration of DTTCI and the background phantom solution contained a 10^{-8} -M concentration of DTTCI.

Similar to the ICG target results, the DTTCI targets could be resolved when positioned up to 5.5 cm below the surface. However there was no obvious change in the depth of penetration due to the longer-lived lifetime. Overall, in order to quantify the true perturbations, a comparison to a forward model of the diffusion equation is required.

Nonetheless, the phantom measurement results are promising for the clinical application of sentinel lymph node mapping.

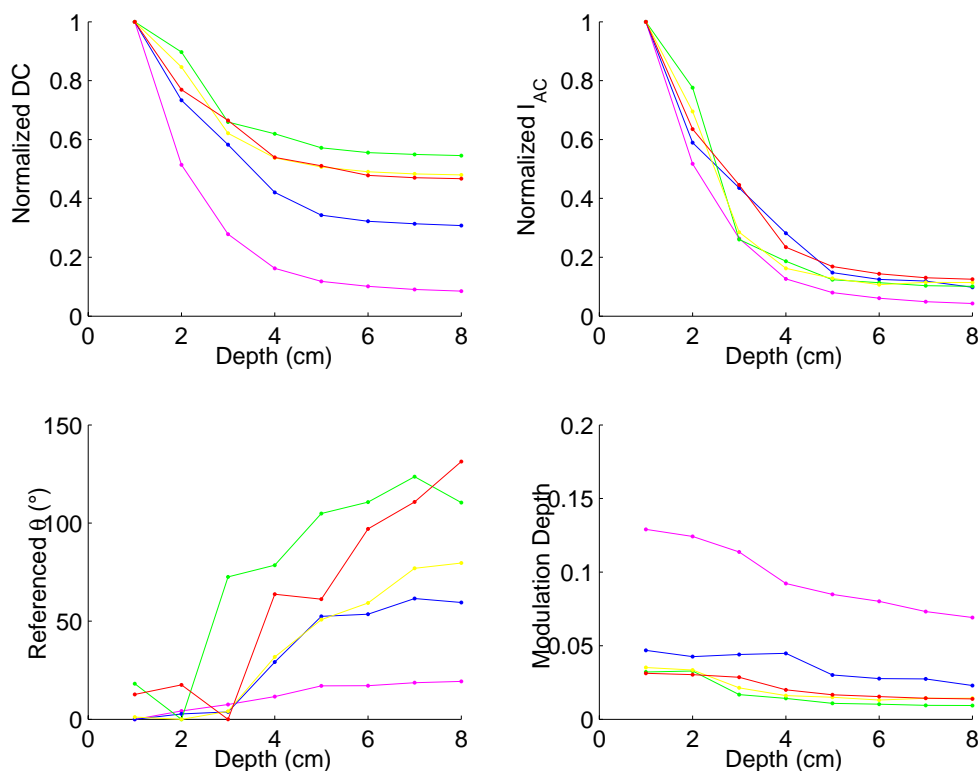


Figure 4.28 Normalized I_{DC} (top left), I_{AC} (top right), θ (bottom left), I_{AC}/I_{DC} (bottom right) versus tissue depth for a 1 μM fluorescent DTTCl target immersed 1.5 cm below the surface of a phantom with a 10^{-8} M uniform concentration of DTTCl. The target optical properties were: $\mu_a = 0.063 \text{ cm}^{-1}$, and $\mu_s' = 10 \text{ cm}^{-1}$, and the background optical properties were: $\mu_a = 0.01 \text{ cm}^{-1}$ and $\mu_s' = 10 \text{ cm}^{-1}$. Measurements were acquired at 30 (red points), 60 (yellow points), 90 (green points), 100 (blue points), and 130 MHz (magenta points).

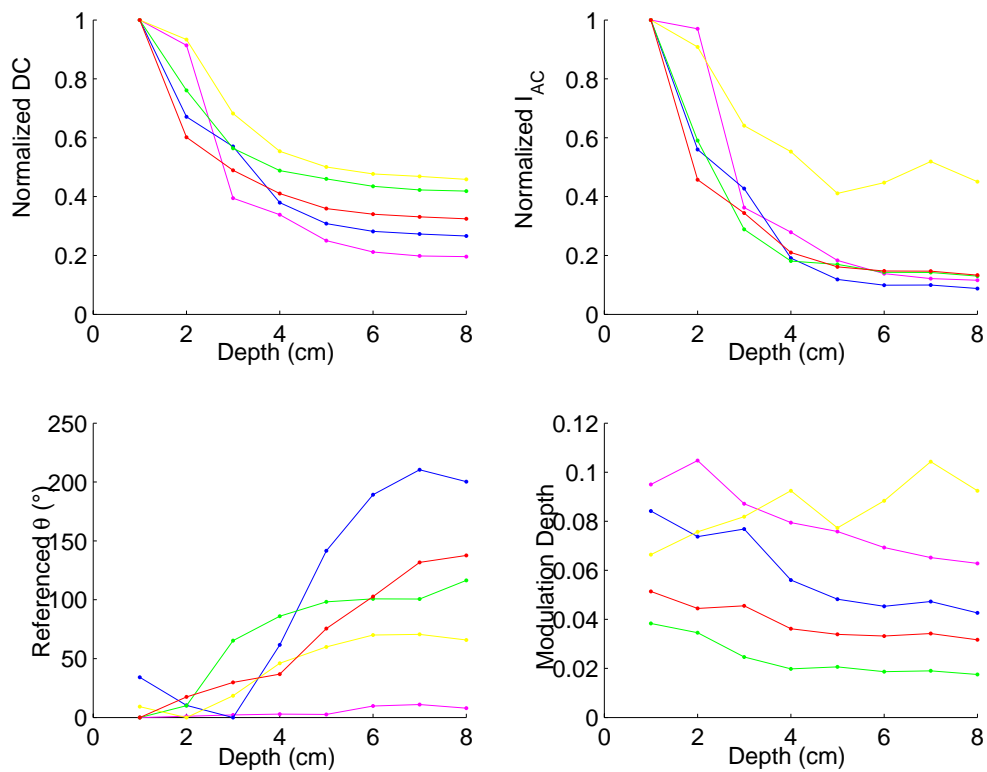


Figure 4.29 Normalized I_{DC} (top left), I_{AC} (top right), θ (bottom left), I_{AC}/I_{DC} (bottom right) versus tissue depth for a 1 μM fluorescent DTTCl target immersed 3.5 cm below the surface of a phantom with a 10^{-8} M uniform concentration of DTTCl. The target optical properties were: $\tau = 1.18$ ns, $\mu_a = 0.063$ cm^{-1} , and $\mu_s' = 10$ cm^{-1} , and the background optical properties were: $\mu_a = 0.1$ cm^{-1} and $\mu_s' = 10$ cm^{-1} . Measurements were acquired at 30 (red points), 60 (yellow points), 90 (green points), 100 (blue points), and 130 MHz (magenta points).

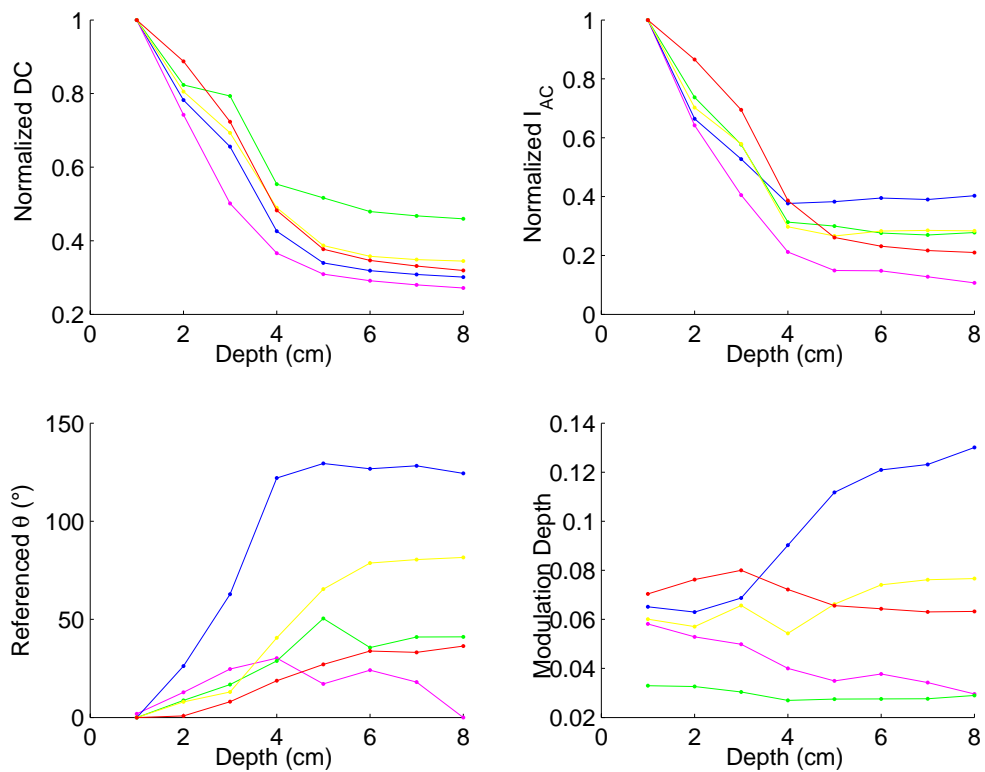


Figure 4.30 Normalized I_{DC} (top left), I_{AC} (top right), θ (bottom left), I_{AC}/I_{DC} (bottom right) versus tissue depth for a 1 μM fluorescent DTTCI target immersed 5.5 cm below the surface of a phantom with a 10^{-8} M uniform concentration of DTTCI. The target optical properties were: $\tau = 1.18$ ns, $\mu_a = 0.063$ cm^{-1} , and $\mu_s' = 10$ cm^{-1} , and the background optical properties were: $\mu_a = 0.1$ cm^{-1} and $\mu_s' = 10$ cm^{-1} . Measurements were acquired at 30 (red points), 60 (yellow points), 90 (green points), 100 (blue points), and 130 MHz (magenta points).

In addition to I_{DC} and I_{AC} measured at discrete points within the phantom, the I_{DC} and I_{AC} were measured at the surface of the phantom. Figures 4.31 and 4.32 are resulting I_{DC} and I_{AC} images of the phantom surface taken with a DTTCI target using a modulation frequency of 30 MHz. The surface measurements are indicative of the data obtained in a reflectance geometry, similar to clinically acquired data. Therefore the surface measurements detect fluorescence that has re-emitted from within the tissue. Figure 4.31 demonstrates the reduction in fluorescence DC intensity as the target is located deeper within the tissue. At 5.5 cm, the target is no longer resolvable by I_{DC} measurements. Although the I_{AC} measurements at 5.5 cm clearly show a circular region of high intensity suggesting the target is detectable, the I_{DC} value which represents the average intensity is in fact equivalent to zero. The data from the three target depths are plotted on different color scales to represent by an arbitrary intensity value if the target is detectable or not.

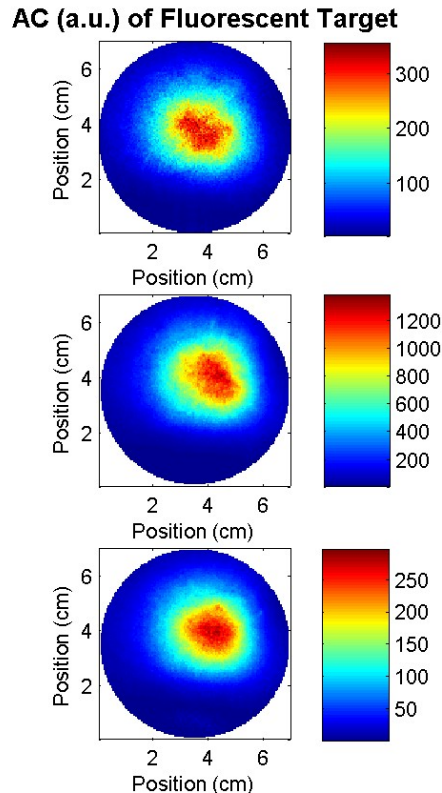


Figure 4.32 I_{AC} area measurement acquired at the surface of a phantom with a $1 \mu\text{M}$ fluorescent target ($\tau = 1.18 \text{ ns}$, $\mu_a = 0.063 \text{ cm}^{-1}$, $\mu_s' = 10 \text{ cm}^{-1}$) immersed 1.5 cm (top), 3.5 cm (middle), and 5.5 cm (bottom) below the surface of a non-fluorescing Liposyn® scattering solution ($\tau = 1.18 \text{ ns}$, $\mu_a = 0.01 \text{ cm}^{-1}$, $\mu_s' = 10 \text{ cm}^{-1}$). The color bars represent the arbitrary intensity levels of I_{AC} .

Similarly, when fluorescence was added to the background at a concentration ratio of 100:1, the phantom was imaged at the surface. The images of the phantom when fluorophore is uniformly mixed in the background are shown in Figures 4.33 and 4.34. They are similar in that there is a centralized region of high intensity within the detection area. However, the region has an intensity profile that is irregular. Due to the presence of fluorophore within the entire phantom, the I_{DC} and I_{AC} images reflect fluorescent

signals located over the area on which the laser is incident. Recall, the laser was expanded to an approximate diameter of 5 cm across the phantom. The non-uniformity in the laser beam output causes irregular regions of high intensity across the phantom surface. In spite of the non-uniformity in the laser output fluorescence was detected when the target was immersed at all depths. Again, a forward model is required to compare the accuracy of the I_{DC} and I_{AC} measurements.

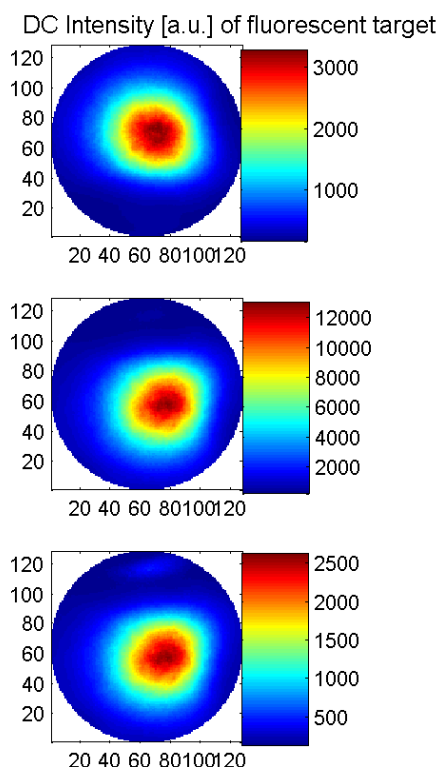


Figure 4.33 I_{DC} area measurement acquired at the surface of a phantom with a 1 μM fluorescent target ($\tau = 1.18 \text{ ns}$, $\mu_a = 0.063 \text{ cm}^{-1}$, $\mu_s' = 10 \text{ cm}^{-1}$) immersed 1.5 cm (top), 3.5 cm (middle), and 5.5 cm (bottom) below the surface of a fluorescing Liposyn® scattering solution ($\tau = 1.18 \text{ ns}$, $\mu_a = 0.01 \text{ cm}^{-1}$, $\mu_s' = 10 \text{ cm}^{-1}$). The color bars represent the arbitrary intensity levels of I_{AC} .

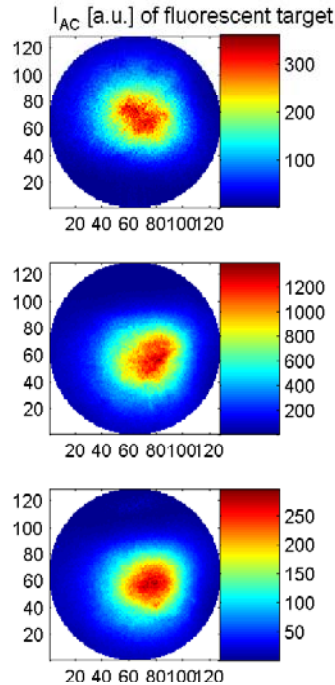


Figure 4.34 I_{AC} area measurement acquired at the surface of a phantom with a $1 \mu\text{M}$ fluorescent target ($\tau = 1.18 \text{ ns}$, $\mu_a = 0.063 \text{ cm}^{-1}$, $\mu_s' = 10 \text{ cm}^{-1}$) immersed 1.5 cm (top), 3.5 cm (middle), and 5.5 cm (bottom) below the surface of a fluorescing Liposyn® scattering solution ($\tau = 1.18 \text{ ns}$, $\mu_a = 0.01 \text{ cm}^{-1}$, $\mu_s' = 10 \text{ cm}^{-1}$). The color bars represent the arbitrary intensity levels of I_{AC} .

Overall, the heterogeneous study was performed to obtain fluorescence measurements that most likely reflect the clinical situation in which fluorescing lymph nodes are detected in breast tissue. From the phantom studies, it was found that the presence of a fluorescent target perturbs I_{DC} and I_{AC} and θ signals when the target is up to 5.5 cm deep. Additionally, a fluorescent target can be detected at the phantom surface up to 3.5 cm, which is promising for the application of sentinel lymph node mapping. Future work should include comparison of the experimental data to forward models that predict the fluence at the detection boundaries.

5. PHASE 2: IMAGING SMALL ANIMALS*

Section 5 of this thesis describes the small animal imaging studies undertaken at the University of Texas M. D. Anderson Cancer Center for the evaluation of tumor targeting with fluorescent contrast agents *in vivo*. More specifically, Section 5.1 provides work and excerpts from a manuscript by Houston *et al.* to be published in the *Journal of Biomedical Optics*, (2005), and Section 5.2 is a study to support work towards the development of fluorescence pharmacokinetic models.

5.1 Optical Imaging vs. Conventional Nuclear Imaging

Nuclear imaging is currently the most effective available medical imaging modality for measuring tracer uptake associated with disease markers as well as with tissue metabolism. Recall from Section 1 that nuclear medicine is prominent in cancer diagnosis, treatment, and prognosis and generally involves the injection of a radionuclide that is targeted for disease specificity. In contrast to nuclear imaging, optical imaging may become a significant molecular imaging tool since it provides digital photo-quality images with low noise and high photon signal emission that can be quantized for pharmacokinetic information as well as tomography. Optical imaging by intensified charge coupled device (ICCD) systems is comparable to conventional nuclear scintigraphy. As ICCDs collect fluorescent photons for image generation, gamma

* Part of the data reported in this chapter is reprinted with permission from Jessica P. Houston, Shi Ke, Wei Wang, Chun Li, and Eva M. Sevick-Muraca "Quality analysis of *in vivo* NIR fluorescence and conventional gamma images acquired using a dual-labeled tumor-targeting probe," ©*Journal of Biomedical Optics*, in press, 2005.

cameras detect gamma emissions and render images that are processed post-acquisition to identify diseased tissue sites.

In this section optical and nuclear imaging is directly compared using a single, targeting moiety containing both a fluorophore and a gamma emitter that is exogenously introduced in trace, diagnostic concentrations. In previous work, Frangioni and coworkers compared optical and nuclear imaging modalities by evaluating osteoblastic activity in a male nude mouse using a targeting radionuclide and a second targeting fluorophore to provide complementary optical and nuclear images for comparison.¹²⁴ Although other investigators have employed radionuclide and fluorescent agent combinations via gene vectors, recall Section 2, to date there have been no studies which employ a single, dual-labeled exogenous agent for direct comparison of optical and nuclear imaging modalities. Herein, a single contrast agent, dual labeled to provide direct comparison of optical and nuclear molecular imaging techniques using established figures of merit was used. The use of the nuclear-optical contrast agent enabled the detection of tumor receptors and targeting ligands in a mouse model by both conventional nuclear imaging and fluorescence-enhanced optical imaging techniques. The acquired nuclear scintigraphy and cw optical images enabled an analysis on the differences between optical and nuclear image qualities.

5.1.1 Dual-labeled Contrast-agent

For the dual-labeled contrast agent, a peptide containing the amino acid sequence arginine-glycine-aspartic acid, which is known to bind to $\alpha v \beta 3$ integrin was used. The synthesis was performed at UTMDACC by Dr. Wei Wang with the chemical structure

shown in Figure 5.1.^{211, 212} Specifically, Lys-c(KRGDf) was synthesized on linker-PL-DMA resin using Fmoc solid phase chemistry as previously described.^{160, 163} The radiometal chelator, P-succinamidobenzyl diethylenetriaminepenta-acetic acid, (DTPA) derivative, was first reacted with the α -amino group of the Lys unit in Lys-c(KRGDf). Subsequently IRdye800 was conjugated to the ω -amino group of the Lys unit in DTPA-Lys-c(KRGDf) to give DTPA-Lys(IRDye800)-c(KRGDf). Lastly, the DTPA-Lys(IRDye800)-c(KRGDf) was mixed with $^{111}\text{InCl}_3$ to form the final product, ^{111}In -DTPA-Lys(IRDye800)-c(KRGDf). The NIR dye (IRDye800) excitation/emission wavelengths were measured at 785/830 nm.

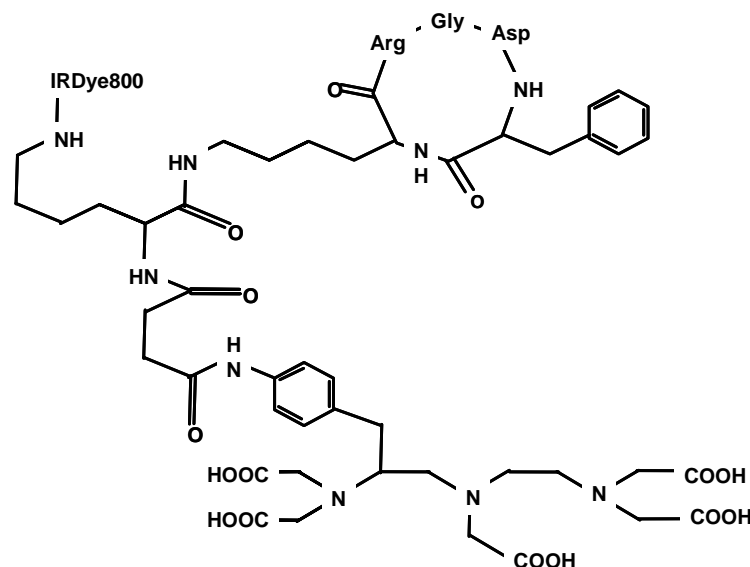


Figure 5.1 Chemical structure of cyclic RGD peptide (courtesy of Dr. Wei Wang) dual-labeled with IRDye800 and a derivative of diethylenetriaminepenta-acetic acid.

5.1.2 Animal Studies

For animal preparation, 4- to 6-week-old female athymic nude mice (nu/nu 13 - 21 g) were purchased from Harlan Sprague Dawley, Inc. (Indianapolis, IN). Well characterized human melanoma tumor cells positively expressing the $\alpha v\beta 3$ integrin receptors (M21) and human melanoma tumor cells not expressing the $\alpha v\beta 3$ integrin receptors (M21-L) were maintained at 37 °C in a humidified atmosphere containing 5% CO₂ in Dulbecco's modified Eagle's medium with F12 nutrient and 10% fetal bovine serum. Cells from the positive and negative integrin lines were implanted subcutaneously into the right and left hind region of the six nude mice, respectively. The M21 and M21-L tumor cell lines were kindly provided by Dr. Cheresh (The Scripps Research Institute, La Jolla, CA). The $\alpha v\beta 3$ integrin positive and integrin negative melanoma cell lines have been used in several studies to investigate integrin expression and activity in cell signaling, angiogenesis, and proliferation.²¹³⁻²¹⁷ Cheresh and Spiro originally explored the M21 variants by looking at receptor affinity to the RGD amino acid sequence. This investigation led to the isolation of the M21-L, or "M21 Lows," variant via FACS.²¹⁴ The M21-L was found to have low reactivity with the monoclonal antibody, LM142, and ultimately determined to have an altered α chain level. For the study herein, the six mice were injected with the dual-labeled contrast agent when the M21 and M21-L tumor sizes reached approximately 5 mm in diameter. The dual-labeled contrast agent was intravenously injected into the mouse tail vein at an equivalent dose of 5 nmol of IRDye800 and 90 μ Ci of ¹¹¹indium.

Imaging commenced 24 hours after administration of the dual-labeled conjugate. Before imaging, the mice were tagged for identification and anesthetized with Nembutal (50 mg/kg body weight). Animals were then imaged individually with the NIR optical imaging system. After optical imaging, the animals were transferred (approximately 15 min later) to the nuclear gamma camera system to acquire planar scintigraphy images. The nuclear imaging system and NIR optical imaging system were described in Section 3.

Animals were maintained in a specific pathogen-free mouse colony in the Department of Veterinary Medicine (The University of Texas M. D. Anderson Cancer Center, Houston, TX). The facility is accredited by the American Association for Laboratory Animal Care and all experiments were performed in accordance with the guidelines of the Institutional Animal Care and Use Committee.

5.1.3 Image Processing

Images acquired from the ICCD camera system and the nuclear M.CAM gamma camera were processed on a 2.6-GHz Windows PC using both the gratis imaging software, ImageJ, (National Institutes of Health, Washington, DC), and the Precision Digital Imaging System software, V++ (Digital Optics, Auckland, New Zealand). ImageJ is an image analysis and processing program in Java and supports both the optical and nuclear image file formats. The nuclear imaging file format, namely an Interfile (containing the file types, .HDR and .IMG) was opened with support from an ImageJ Java script, or “plugin” (<http://www.med.harvard.edu/JPNM/ij/plugins/NucMed.html>). V++ is the Roper Scientific CCD camera software interface with programmable modules

for ICCD operation. The processed nuclear images were opened and read as unsigned 16-bit intensity matrices. That is, each pixel was represented by a positive floating point integer up to a total of 2^{16} possible levels of gray. Likewise, the optical file formats (.TIF files) were imported into ImageJ or V++ for the intensity calculations described below. Similarly, the optical images were of unsigned data type with integer values ranging from 0 to 65,536.

5.1.4 Calculation of Nuclear vs. Optical

To assess relative performance of optical imaging and conventional gamma imaging, the mean and standard deviation of intensity counts associated with five primary regions of interest (ROI) were computed (see Figure on page 146). Of the five regions of interest evaluated, one region represented the image “target” and the remaining four regions represented the image “background” for various calculations presented herein.

First, the “hot” area selected for the “target” ROI was the positive tumor, M21. The M21 tumor was fixed as the “target” ROI for all calculations throughout this analysis. The second ROI selected encompassed the negative tumor, M21-L, and this region represented one of the “background” regions of interest in selected computations. The third region of interest surrounded non-tumor, or normal tissue (NT). The NT ROI encircled an area on the chest region of the mouse body, and similar to the M21-L ROI, the NT ROI represented a “background” in the computations presented herein. Fourthly, the mean and standard deviation of intensity counts were computed for a ROI that delimited the entire mouse body (WB). The last “background” ROI selected was of

the true image background (BK), an area located adjacent to the animal in the surrounding background and not over the body.

The same selected regions of interest corresponding to the M21, M21-L, NT, WB, and BK were used for analysis of optical and nuclear images. That is, the true area of each region remained constant between the nuclear and optical images.

The mean intensity, or mean projected signal, \bar{P} is defined below where the integers 'm' and 'n' represent the pixel values that make up the $[i \times j]$ image intensity matrix for the respective regions of interest selected.

$$\bar{P} = \frac{\sum_{i=1}^m \sum_{j=1}^n P_{(i,j)}}{mn} \quad (5.1)$$

The optical and nuclear images were evaluated by target to background (TBR) and signal to noise (SNR) ratios. TBR and SNR are image quality figures of merit used to evaluate signal detection and are often reported in medical imaging analyses. The TBR and SNR are computed by:

$$TBR = \frac{\bar{P}^t}{\bar{P}^b} \quad (5.2)$$

$$SNR = \frac{\bar{P}^t - \bar{P}^b}{\sqrt{\frac{\sum_{i=1}^m \sum_{j=1}^n [P_{(i,j)}^b - \bar{P}^b]^2}{mn}}} \quad (5.3)$$

where the superscript 't' represents the mean projected target signal and the superscript 'b' represents the mean projected background signal.

In addition to correlating the variability in emission signals obtained between optical and nuclear modalities, an analysis of image contrast was assessed. The contrast was calculated by the following relationship:

$$C = \frac{\bar{P}^t - \bar{P}^b}{\bar{P}^b} = TBR - 1 \quad (5.4)$$

Using these figures of merit described above, we compared: (i) the TBR for both nuclear and optical techniques; (ii) the SNR as a function of integrated area for optical and nuclear images and (iii) the contrast achievable from both the optical and nuclear images.

Table 5.1 Specifications of the parameters used to collect images using the intensified CCD camera system and the M.CAM small animal gamma imager. All images were obtained under the instrumentation parameters outlined, with the exception of one M.CAM image that was arbitrarily cropped to 648×900 pixels (resolution unchanged) and three animals that were imaged with a smaller field of view during the optical imaging study (values in parentheses).

Modality	Integration time [sec]	Total pixels		Field of view		True resolution size [$\mu\text{m}/\text{pixel}$]
		rows	columns	height [cm]	width [cm]	
MCAM	900	652	896	39.7	54.4	609
CCD	0.800	300	300	11.4 (8.1)	11.4 (8.1)	380 (303)

5.1.5 Results of Nuclear and Optical Image Comparison

The figure on page 142 shows a typical nuclear gamma scan and fluorescence-enhanced optical image of a nude mouse bearing the M21 and M21-L tumors 24 hours post-injection of the dual-labeled contrast agent. Both images are presented on equivalent pseudo-color schemes and were acquired with the imaging specifications listed in Table 5.1. The optical image resolution was 380 $\mu\text{m}/\text{pixel}$, or 303 $\mu\text{m}/\text{pixel}$, for three animals imaged with a slightly decreased field of view and the nuclear image resolution was 609 $\mu\text{m}/\text{pixel}$. Notably, the total integration time required for the acquisition of the optical image was 800 milliseconds while the projected gamma scintigram took a total of 15 minutes to acquire.

Despite an equivalent dynamic range, the conventional scintigram and optical image have obvious differences in appearance. The M21 tumor is clearly delineated in the optical image; the M21 ROI intensity is much higher in contrast to the background M21-L tumor. Note however, additional intensity rises in the optical image most apparent in the animal's neck and abdomen region. The raised signal at those regions can be attributed to elevated fluorescence signals owing to an irregularity in the expanded excitation beam as well as excitation light leakage from the reflected laser light through the optical filters. Alternatively, the nuclear scintigram of the same animal appears noisy and the tumor is hard to delineate. The scintigram displays low contrast between the M21 ROI and the rest of the body. This reduction in contrast, common in nuclear imaging, arises due to the scatter of gamma photons which are captured into the collimator wells and contribute to the high background signal.

In addition, in all of the images, which are displayed in both Figure 5.2 and Figure 5.3, the uptake of the dual-labeled peptide in the liver and kidneys is evident in the nuclear scan by a saturated intensity signal in the abdomen region. However, the high abdomen signal is not present in the optical image. Owing to the lower energetics and greater attenuation experienced by NIR photons in comparison to gamma emission, CW planar optical imaging is surface weighted. While tomographic approaches for 3-D interior imaging have been developed for diffusion based in large and small tissue volumes, diffusion-based approaches are invalid for small animal imaging and the length scales under consideration in this study. While radiative transport equation -based tomography is currently under development for small animal optical imaging for comparison with PET or SPECT, we use currently available non-tomographic, CW imaging and gamma scintigraphy to compare optical and nuclear imaging modalities.

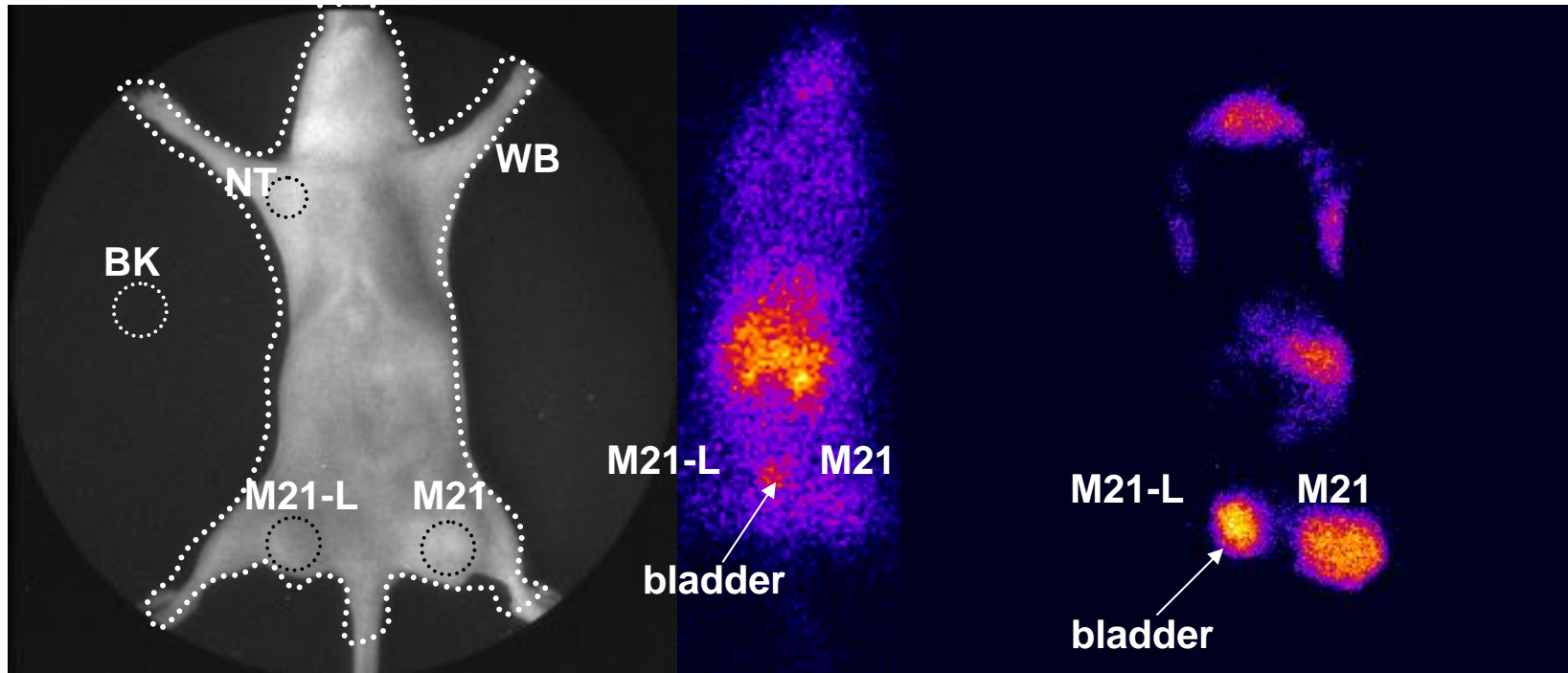


Figure 5.2 White light (left), nuclear scintigram (center), and fluorescence-enhanced optical image (right) of a typical nude mouse xenograph bearing an integrin-positive (M21) tumor in the left thigh (right side: anterior view is displayed by figure) and an integrin-negative (M21-L) tumor in the right thigh (left side: anterior view is displayed by figure). The digital photo of the animal depicts the regions of interest (ROIs) selected for the collection of intensity signals either in the positive tumor, negative tumor, or normal tissue regions. The nuclear and optical images show a low signal in the negative (M21-L) tumor (left side), a high signal in the bladder indicating wash-out of the dye, and a high signal in the integrin positive (M21) tumor (right side). The optical image was plotted in a pseudo-color format for enhancement of the intensity scale in the tumor and background. The nuclear image was also adjusted with the same color scale for better discrimination between the several levels of gray provided by the 16-bit image. The nuclear image was acquired after 15 minutes of integration whereas the optical image was acquired for a total exposure time of 800 ms.

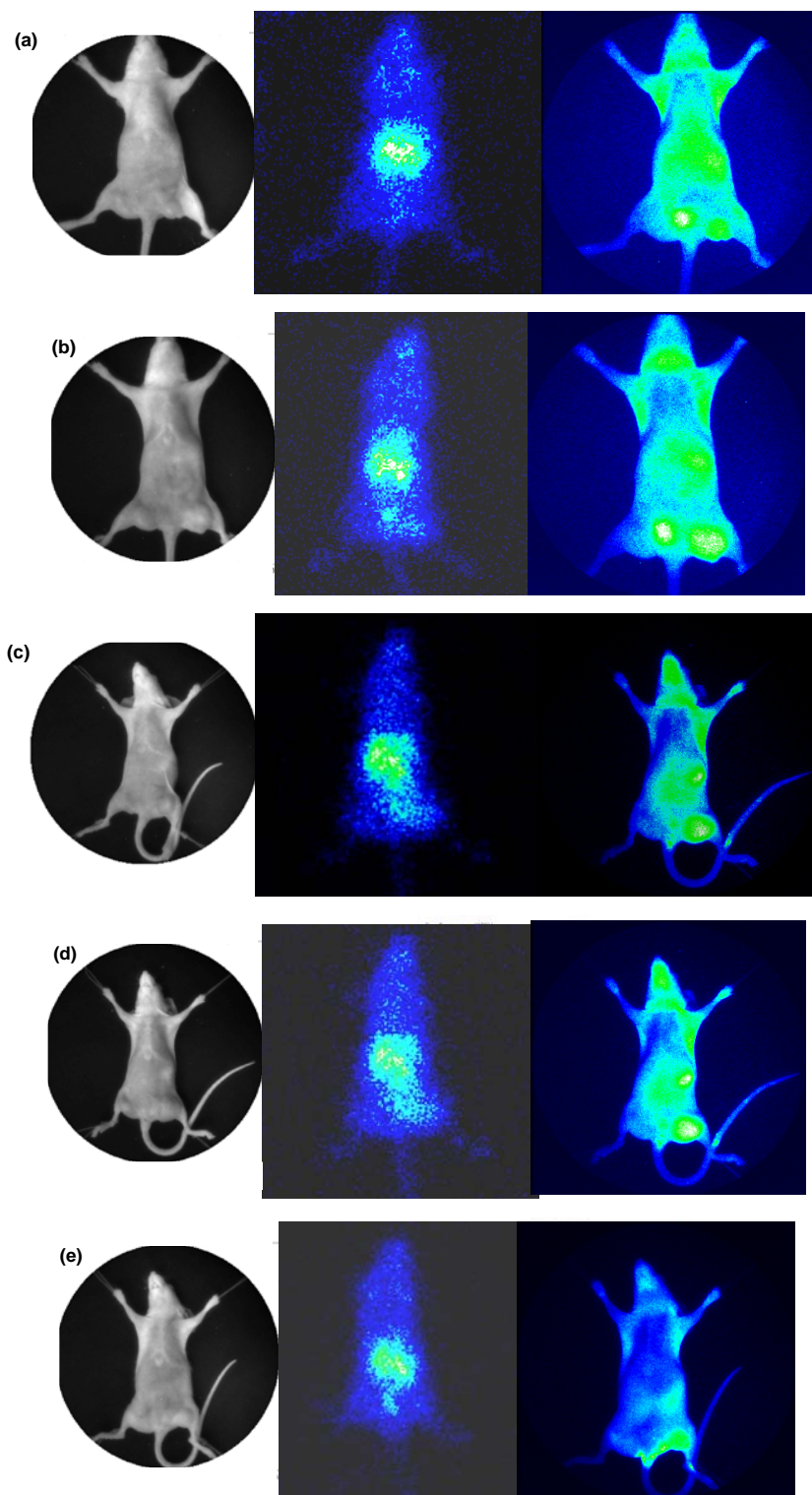


Figure 5.3 White light (left), nuclear scintigram (center), and fluorescence-enhanced optical image (right) of the remaining five nude mice xenografts (a - e).

Table 5.2 summarizes six image quality factors computed from the nuclear and optical images: (1) the WB ROI area [cm^2], (2) the M21, M21-L, and NT ROI areas [cm^2], (3) the mean projected signal from the M21 tumor ROI, (4) the mean projected signal from the WB ROI, (5) the mean projected signal from the M21-L tumor ROI, and (6) the mean projected signal from the NT ROI. The mean projected signals were computed from Equation 5.1, and the total tumor and whole body areas ranged from 0.8 to 1.2 cm^2 and 40 to 45 cm^2 , respectively. Owing to the successful targeting of the dual-labeled contrast agent, the mean intensity in the M21 ROI was higher than the M21-L ROI for both the gamma scintigram and optical image. The average intensity [a.u.] in the M21 ROI for the six optical images was 1138.4 (+/-529) and 1257.5 (+/-507), for the six scintigrams. In comparison, the average intensity [a.u.] in the M21-L ROI for the six optical images was 701.6 (+/-330) and 860.9 (+/-352), for the six scintigrams. The TBR figures of merit resulting from each imaged animal are summarized in Table 5.3. The TBR values, computed by Equation 5.2, are presented for the three background regions of interest: (1) M21 target to M21-L background, (2) M21 target to NT background, and (3) M21 target to WB background. The average M21 tumor to M21-L tumor ratios for optical (1.4 +/- 0.3) and nuclear (1.5 +/- 0.2) were similar based on a statistical significance analysis using a paired t-test ($\alpha = 0.05$). The average M21:NT ratios from the acquired optical and nuclear images were 1.3 (+/- 0.2) and 1.5 (+/-0.5), and the similar TBR ratios with the whole body as the “background” (M21:WB) for optical and nuclear resulted in 1.6 (+/- 0.3) and 1.6 (+/- 0.7), respectively.

Table 5.2 Summary of the mean projected signals for the M21 tumor ROI, the whole body (WB) ROI, the M21-L ROI and the normal tissue (NT) ROI. All mean intensity values listed in the table were computed following Equation 5.1. The resulting ROI data are from the ICCD imaging system and M.CAM system's measured 16-bit intensities [a.u.]. The error bar values are standard deviations computed on the mean projected signal.

Animal Number	Image modality	WB ROI area [cm ²]	WB ROI mean projected signal [a.u.]	M21, M21-L, and NT ROI area [cm ²]	M21 ROI mean projected signal [a.u.]	M21-L ROI mean projected signal [a.u.]	NT ROI mean projected signal [a.u.]
1	M.CAM	45	705.4 (+/-) 1116.5	1.2	1352.6 (+/-) 623.2	896.4 (+/-) 498.1	803.4 (+/-) 614
	ICCD		814.2 (+/-) 319.9		1539.5 (+/-) 294.7	924.4 (+/-) 141.5	955.0 (+/-) 139.3
2	M.CAM	45	579.2 (+/-) 904.6	1.2	1267.6 (+/-) 714.5	786.6 (+/-) 477.9	777.7 (+/-) 549.0
	ICCD		762.2 (+/-) 244.1		1290.2 (+/-) 158.9	883.2 (+/-) 84	893.4 (+/-) 80.9
3	M.CAM	45	742.3 (+/-) 1164.6	1.2	1138.3 (+/-) 578.3	987.7 (+/-) 547.1	936.3 (+/-) 682.8
	ICCD		824.8 (+/-) 288.3		1471.7 (+/-) 180.3	981.2 (+/-) 120.6	1029.3 (+/-) 107
4	M.CAM	40	924.6 (+/-) 1318.4	0.82	1117.3 (+/-) 582.6	684.9 (+/-) 453	1177.6 (+/-) 788.7
	ICCD		660.9 (+/-) 123.5		817.1 (+/-) 77.6	691.9 (+/-) 29.3	781.3 (+/-) 59.4
5	M.CAM	40	872.6 (+/-) 1312.9	0.82	1075.2 (+/-) 629.9	826.0 (+/-) 506.1	1085.4 (+/-) 749.7
	ICCD		652.6 (+/-) 113.1		789.5 (+/-) 90.1	710.7 (+/-) 38.7	773.1 (+/-) 53.5
6	M.CAM	40	923.8 (+/-) 1302.3	0.82	1594.0 (+/-) 816.3	850.0 (+/-) 583.1	708.8 (+/-) 529.9
	ICCD		662.8 (+/-) 124.9		922.6 (+/-) 889.1	713 (+/-) 42.4	762.6 (+/-) 44.6

Table 5.3 also lists the SNR computed by Equation 5.3 and contrast computed by Equation 5.4 from the optical and nuclear image data. The SNR using the M21 and M21-L tumor ROIs was greater from measurements acquired by the ICCD system than from measurements acquired by the M.CAM (statistically significant, $P_{\text{value}} = 1.3 \times 10^{-6}$).

In fact, the maximum SNR value among all six optical images was 7.7 dB. The SNR from the scintigram corresponding to the same optical SNR was 0.3 dB. The average SNR [a.u.] from the optical images was 4.7 (+/-0.7) and 0.78 (+/-0.5) from the nuclear images. The SNR and TBR for the six animals are presented by a bar plot in Figure 5.4. The contrast was determined by the mean projected signal in the M21 tumor and the mean projected signal in the M21-L tumor. The tumor was detected over the background at an elevated contrast by the M.CAM system with an average contrast of 0.5 (+/-0.3) as opposed to 0.4 (+/-0.2), the average contrast obtained from the ICCD system.

Table 5.3 Target to background ratios, signal to noise ratios, and contrast values computed following Equations 5.2, 5.3, and 5.4. The SNR value is from the M21 target and M21-L background. The resulting TBR values for the (i) M21 target with M21-L background, the (ii) M21 target with NT background, and the (iii) M21 target with WB background are outlined. The contrast results were computed using the target M21 tumor and the background M21-L tumor. The error bars are relative standard deviation values propagated for the computed ratios.

Animal Number	Image modality	SNR M21 & M21-L	TBR M21:M21-L	TBR M21:NT	TBR M21:WB	Contrast M21:M21-L
1	MCAM	0.9 (+/-) 1.8	1.5 (+/-) 0.7	1.7 (+/-) 0.9	1.9 (+/-) 2.3	0.51
	CCD	4.3 (+/-) 0.5	1.7 (+/-) 0.3	1.6 (+/-) 0.2	1.9 (+/-) 5.8	0.67
2	MCAM	1.0 (+/-) 1.9	1.6 (+/-) 0.8	1.6 (+/-) 0.9	2.2 (+/-) 1.9	0.61
	CCD	4.8 (+/-) 0.5	1.5 (+/-) 0.2	1.4 (+/-) 0.2	1.7 (+/-) 8.7	0.46
3	MCAM	0.28 (+/-) 5.3	1.2 (+/-) 0.7	1.2 (+/-) 0.9	1.5 (+/-) 2.1	0.02
	CCD	4.1 (+/-) 0.5	1.5 (+/-) 0.2	1.4 (+/-) 0.2	1.8 (+/-) 8.7	0.50
4	MCAM	1.0 (+/-) 1.8	1.6 (+/-) 0.8	1 (+/-) 0.9	1.2 (+/-) 2	0.63
	CCD	4.3 (+/-) 0.7	1.2 (+/-) 0.1	1.1 (+/-) 0.1	1.2 (+/-) 11.8	0.18
5	MCAM	0.5 (+/-) 3.3	1.3 (+/-) 0.9	1 (+/-) 0.9	1.2 (+/-) 1.8	0.30
	CCD	6.0 (+/-) 0.3	1.3 (+/-) 0.1	1.2 (+/-) 0.1	1.4 (+/-) 18.7	0.32
6	MCAM	1.3 (+/-) 1.5	1.9 (+/-) 0.9	2.3 (+/-) 0.9	1.7 (+/-) 2.1	0.88
	CCD	5.3 (+/-) 0.29	1.3 (+/-) 0.1	1.2 (+/-) 0.1	1.4 (+/-) 1.4	0.29

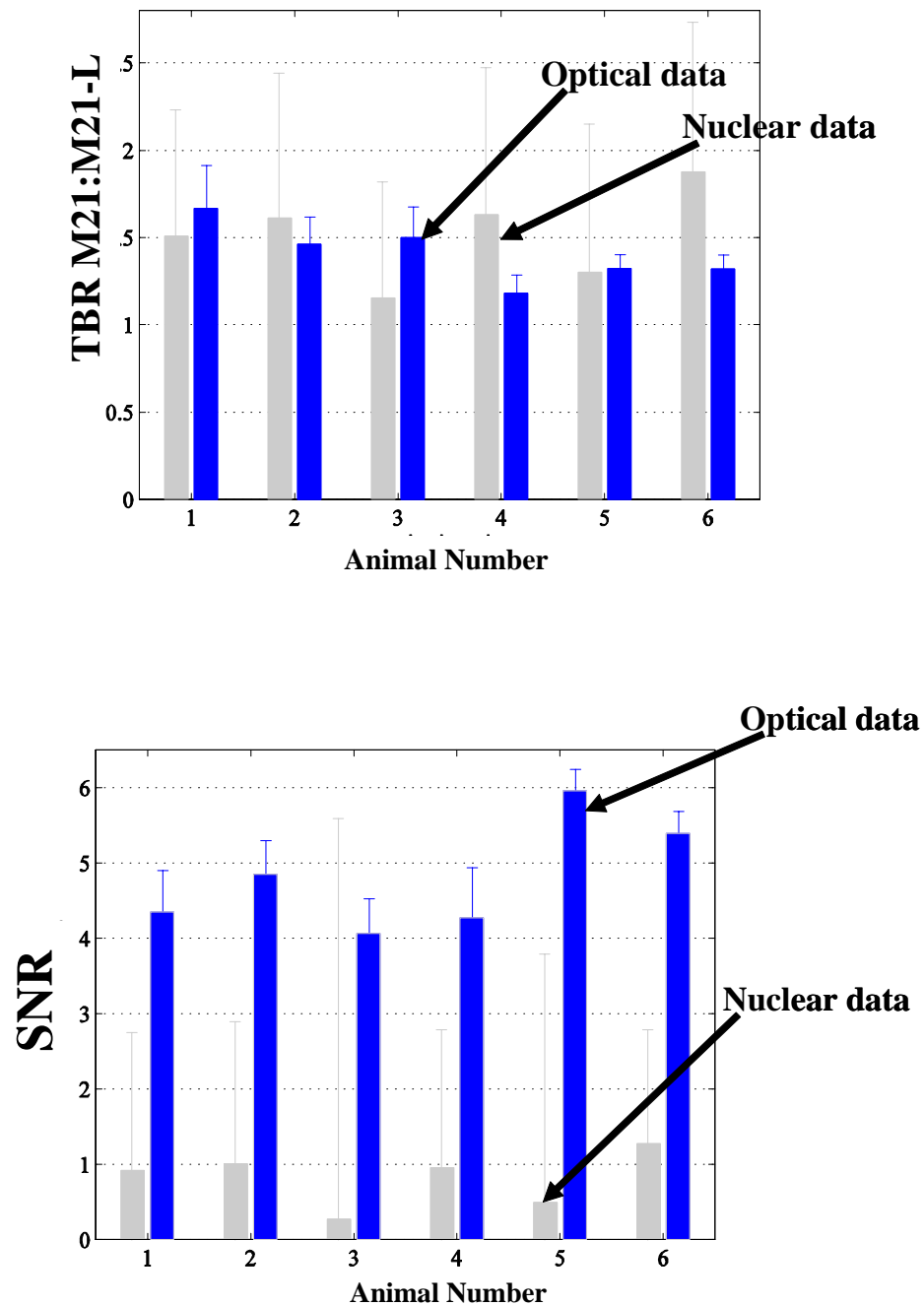


Figure 5.4 Bar plots of target to background ratios (top) and signal to noise ratios (bottom) of the M21 tumor region of interest to the M21-L tumor background region of interest computed from NIR (dark-shaded) and gamma (light-shaded) images for all six animals studied. Error bars represent the relative standard deviation.

Figure 5.5 is a plot of the SNR vs. contrast for selected contrast values arranged in increasing magnitude and computed from all six mice. The contrast and SNR displayed by Figure 5.5 were computed using the M21 tumor and BK ROIs. That is, the true background signal was compared to the highest signal present in the images, the tumor intensity. This analysis permits a comparison between nuclear and optical image noise floor. Because SNR and contrast are proportional, their linearity provides an outlook on the tumor “detectability” for various levels of image contrast. The SNR required to achieve a specified contrast was lower for the nuclear system than for the optical system. The ICCD camera system was estimated to have a 200+ fold greater sensitivity at the lower contrast values then the nuclear M.CAM imager.

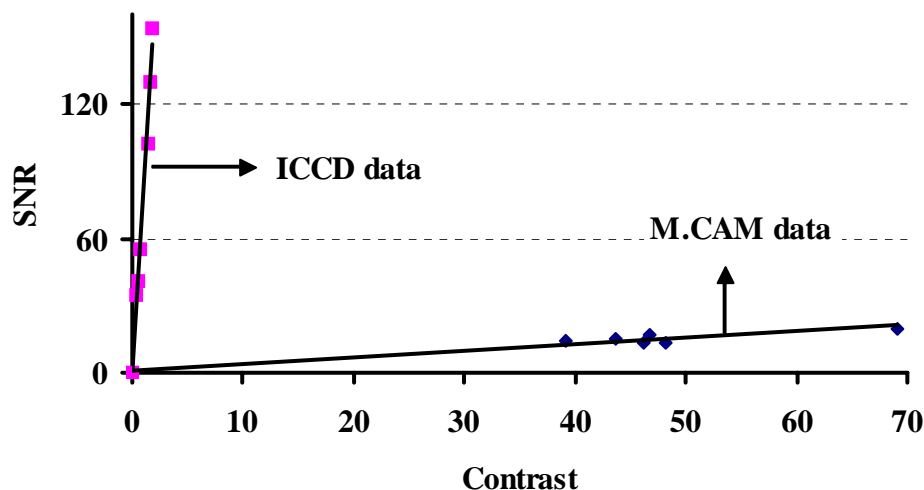


Figure 5.5 SNR vs. contrast calculated using Equations 5.3 and 5.4 using optical and nuclear image intensity data [a.u.]. The expected linear relationship between the SNR and contrast are different between optical and nuclear. That is, the optical imaging SNR vs. contrast slope is dramatically increased over the nuclear imaging SNR vs. contrast.

5.1.6 Discussion of Nuclear and Optical Imaging Comparison

To date, optical techniques have yet to demonstrate the robust detection of cancer in humans that nuclear systems can clinically provide. In this work, we identify the features of fluorescence optical imaging that give rise not only to improvements in optical image quality but also to sensitive acquisition of whole body fluorescent signals using a simple ICCD system. Herein, we have shown that surface melanoma tumors can be easily delineated in all six optical images, while the tumor boundary could not be identified on a qualitative level by the gamma images using a single, dual labeled targeting agent. Several factors that contribute to these differences in measured signal are discussed below.

First, although the functional imaging aims of optical and nuclear techniques are similar, it should be prefaced that the purpose of nuclear imaging modalities used in clinical practice is not strictly to define superficial tumor margins. Rather, nuclear systems play dominant roles for bone scans, lymphoscintigraphy, immunoscintigraphy, and the tracing of diseases (e.g., cancers, Alzheimer's, Parkinson's, AIDS dementia, etc.). Positron emission tomography and single photon emission computed tomography are employed over conventional gamma imaging and provide improved image quality and sensitivity. In this study we compare conventional gamma imaging to NIR optical imaging for superficially localized tumors in small animals; both are non-tomographic methods with instrumentation designed for small animal imaging.

Secondly, in order to provide an impartial comparison of nuclear and optical signals, a well documented and equally detectable contrast agent dose must be

established. The dual-labeled peptide, ^{111}In -DTPA-Lys(IRDye800)-c(KRGDf), used in this study was synthesized for a 1:1 molar ratio of DTPA to conjugated IRDye800. After addition of the radiolabel, ^{111}In , a final product equivalent to 20 μCi of radioisotope per nmol of fluorophore was obtained. Indeed the specific activity can be altered by varying the amount of ^{111}In to be chelated to DTPA-Lys(IRDye800)-c(KRGDf). The total specific activity however, should be balanced for adequate detection of both radio- and fluorescent signals. When applied to the clinical setting, radionuclide dosimetry is calculated based on realistic integration times (for patient comfort), radiation exposure (for patient safety), half-life and energy of the isotope, and the minimum detectable signal. Typical clinical intravenous injection doses of Octreoscan (^{111}In -D-Phe-DTPA-octreotide) change depending on imaging circumstances (3 mCi to 6.0 mCi), and as clinical doses vary so do experimental doses in small animals. Despite a $>10^3$ lower bodyweight, mice may be administered 100 times lower doses than humans in order to obtain an adequate signal at realistic integration times. It is noteworthy that the tracer dose does not linearly scale with body mass. Our small animal study required 3.3MBq ^{111}In in order to detect ligand receptor interaction. Similar doses ranging from 1.8MBq to 7.2MBq have been used in small animals with ^{111}In , ^{18}F , and ^{99}Tc , for studies involving targeting of a radiolabel to the $\alpha v\beta 3$ integrin via an RGD peptide conjugate.

Despite controlled fluorophore and isotope specific activities, the high fluorescent photon sensitivity of the ICCD system may be due to the theoretically larger number of fluorescent photons available for imaging over the available gamma rays

emitted from the animal. Indeed, the number of radiative events per second emitted by a fluorescent dye can be several orders of magnitude greater than the total emitted by a radionuclide of the same quantity. For example, ^{111}In has a specific activity of 4.2×10^6 [Ci/g]. To quantify this in terms of emitted disintegrations, the rationale is:

$$\frac{4.2 \times 10^6 \text{ Ci}}{\text{g}} \times \frac{3.7 \times 10^{10} \text{ Bq}}{\text{Ci}} \times \frac{1 \text{ event} \cdot \text{s}^{-1}}{\text{Bq}} = 1.5 \times 10^{19} \text{ event} \cdot \text{s}^{-1} \cdot \text{g}^{-1}$$

A direct comparison of this activity to the fluorescent dye, IRDye800 which has a molecular weight of 1166 g/mole and a fluorescent lifetime estimated at 0.5 nanoseconds, produces:

$$\frac{1 \text{ mole}}{1166 \text{ g}} \times \frac{6.02 \times 10^{23} \text{ molecule}}{\text{mole}} \times \frac{0.5 \times 10^9 \text{ event} \cdot \text{molecule}}{\text{s}} = 2.6 \times 10^{29} \text{ event} \cdot \text{s}^{-1} \cdot \text{g}^{-1}$$

Thus, an equivalent “specific activity” for the fluorophore and radionuclide in theory provide significantly different amounts of photons emitted per second (10^{10}). Owing to this low sensitivity, nuclear scans require several minutes for data collection. Optical techniques are favorable for the clinic because they require only a fraction of a second to resolve a fluorescent image.

The discrepancy between the theoretical difference in sensitivity and the actual observed image sensitivity can be explained by the comparative attenuation of NIR and gamma rays during tissue propagation. In tissue, gamma rays attenuate to a much lesser extent than NIR photons. For example, with a linear attenuation coefficient of $\mu=0.16 \text{ cm}^{-1}$ for a gamma ray, and a reduced scattering and absorption coefficient of $\mu'_s=10 \text{ cm}^{-1}$ and $\mu'_a=0.1 \text{ cm}^{-1}$ for NIR photons in thick tissue, a rough estimate of the attenuation

of gamma and NIR intensity across 5 cm of tissue can be made: showing that almost 50% of gamma rays are transmitted and much less than 0.01% of optical NIR photons are transmitted through an equivalent tissue depth.

$$I_{\text{gamma}} = I_o e^{-\mu L} = 1 \cdot e^{-0.16 \cdot 5} = 0.45$$

$$I_{\text{optical}} = I_o e^{-\mu L} = 1 \cdot e^{-10.1 \cdot 5} = 1 \cdot 10^{-22}$$

Attenuation unquestionably depends on the radiation energy; for example $\mu \cong 0.16 - 0.35 \text{ cm}^{-1}$ for photon energies of 30 to 100 keV and $\mu_s \cong 100 - 300 \text{ cm}^{-1}$ for NIR photons, where scattering dominates. Additionally, photons and gamma rays experience different types of scattering (i.e., Rayleigh vs. Compton) in soft tissue.

A large part of NIR attenuation for fluorescence-enhanced imaging is due to scattering and absorption as well as the decay kinetics of the fluorophore. Excitation light attenuates before reaching the embedded fluorophore and the quantum efficiency, ϕ , of the fluorophore reduces the amount of fluorescent light that is re-emitted. Upon traveling back to the tissue surface, fluorescent photon attenuation occurs. Ultimately the photon fluence measured at the tissue surface is reduced and for the small animal imaging described herein, its attenuation must be predicted by the full radiative transport equation.

A last and important preface to nuclear and optical imager differences that may impact equal comparison is camera resolution. The CCD chip has fixed, 24 μm -size wells, thus the image resolution, or actual pixel size, may vary depending on the field of view chosen and achieved using any typical camera focusing lens. For the ICCD system,

the resolution on an optical image is ultimately limited by the image intensifier; the CCD images a constant FOV at the phosphor screen, which likewise can be controlled by a simple zoom lens. Unlike the optical system however, the M.CAM has a fixed field of view, therefore the resolution is fixed for a given collimator size.

The comparative target to background ratios that are presented reflect some distinguishing qualities between the planar optical and nuclear image display. The M21:M21-L TBR values were analyzed and found to be similar; this similarity was anticipated because the contrast agent was dual-labeled causing the radionuclide and fluorophore to have an equal relative accumulation between the M21 and M21-L tumor. Yet upon viewing the ROI intensities in the actual optical and nuclear images (Figure 5.2) this TBR similarity is less apparent. There is little signal delineating the gamma image M21 ROI over the M21-L ROI, which indicates a high variance in pixel intensity resulting from a raised background signal. The large background signal in the nuclear scinitogram reflects the fact that gamma cameras detect scattered gamma rays that are emitted from deep tissue sections. Thus, any annihilated photons that emit from the liver, kidneys, and deeper tissue (>5 mm) are imaged and contribute to the total mean projected signal. Moreover, gamma rays that scatter into a single collimating well and emit from locations not adjacent to that well, are weighted the same as those photons that travel in a straight trajectory from the tumor to the collimator. Thus, the deviation in pixel intensity values is much greater for the M.CAM than for the ICCD system.

Additionally, the similarities between the optical and nuclear M21:NT ratios and optical and nuclear M21:WB ratios further demonstrate that the dual-labeled agent was

target-specific to the $\alpha v\beta 3$ integrin positive melanoma tumor. The nuclear and optical detectors equally discriminated between targeted signals and non-targeted signals from the background of the entire animal body and normal tissue regions. Yet, the optical and nuclear imaging systems appear to detect different background signals because (i) optical ICCD sensitivity is weighted towards shallow, sub-surface photons; (ii) attenuated optical signals are often reported at suppressed intensities relative to non-attenuated signals owing to excessive excitation light leakage; (iii) conventional gamma camera systems detect gamma rays from any depth or location in the body with equal sensitivity; and (iv) gamma systems detect photons that travel in a mostly linear fashion through the body with little attenuation. Therefore the background signals from the optical M21:WB and M21:NT ratios are from fluorescence emitted by tissues and blood located a few millimeters below the skin's surface as well as excitation light leakage through the optical filters. Alternatively, the gamma camera TBRs are indicative of the total radionuclide emissions from within the whole body relative to the gamma ray emission from the entire tumor volume.

Unlike the target to background ratios, the statistically different signal to noise ratios may be an indication of the reduced noise floor that an ICCD system provides. ICCDs are typically operated under shot-noise limited conditions, where photon noise is the limiting noise factor. Therefore, when high photon signals emitting from the tumor are detected, the Poisson distributed shot-noise becomes relatively much smaller and this is reflected in the image output SNR. The SNR computed from the conventional gamma images is much lower than the optical owing also to the imaging system's intrinsic

signal to noise characteristics. The radioactive decay and gamma detection variance is closer to the gain, or sensitivity of the detector; this is reflected in the scintigram pixel values. However the favorable SNR of optical over nuclear may dramatically decrease when comparing deeply seated tumors as in the case of human imaging. Consider two targets 0.5 and 2 cm deep to be imaged using planar optical and nuclear imaging. The noise associated with each of the imaging modalities remains constant as the depth of the target increases. Assuming that the gamma emitting targets are of equal energy, the signal from the two centimeter depth ($e^{-(0.16 \times 2)} = 0.7$) will be attenuated by a difference of 0.2 in comparison to that emitted from the target 0.5 cm in depth ($e^{-(0.16 \times 0.5)} = 0.9$). For optical imaging, greater attenuation occurs with typical tissue scattering and absorption coefficients like $\mu_s' = 10 \text{ cm}^{-1}$ and $\mu_a = 0.1 \text{ cm}^{-1}$. Using these optical properties for a total attenuation coefficient of $\mu_t = 10.1$, the comparative attenuation of photons from 0.5 cm to 2 cm is 0.006 and 2×10^{-9} , respectively, a magnitude difference of 10^6 . Of course, these calculations do not consider the half-life of the radiotracer, wherein the SNR of fluorescent targets at all depths may be significantly greater than that of a spent tracer at any depth.

Yet for detection of surface signals, plotting the SNR vs. contrast further demonstrates improved sensitivity by the ICCD system. A high photon signal detected by the ICCD system yields a large SNR value despite the low contrast between the tumor and background. For the SNR contrast plots, the background value used was a true background ROI; a selected area outside of the animal body was used as the baseline noise signal. The change in optical SNR relative to the change in optical image

contrast is more than 200 fold greater than the conventional gamma camera SNR-contrast gradient. Moreover, fluorescence-enhanced optical imaging has potential for improved SNR with better reduction in the excitation light noise. With the increase in intensified CCD sensitivity, excitation light is hard to eliminate from the total detected signal because of the fraction of excitation light (19%) passed through standard band rejection and optical band pass filters.

Although this work demarcates favorable optical image quality relative to a conventional gamma camera, multi-modality imaging combinations are truly complementary with neither imaging method providing completely autonomous diagnostic information. In this work however, the combined imaging methods provided a comparative tool for optical ICCD camera image quality assessment, which is essential for clinical translation of functional planar NIR imaging. Upon comparison to conventional nuclear imaging, it is evident that optical imaging with ICCD cameras is highly sensitive to photons emanating from superficial depths. Additionally, as optical tomography is developed for multi-pixel techniques on larger volumes, assessment of the target detection for small target sizes and greater target depths is increasingly important for locating the tumor position through a three dimensional map in thick (> 1 cm) human tissues.

5.2 Single-point Fluorescence Detection in the Mouse Ear

In addition to the previously described nuclear and optical imaging work, dynamic fluorescence measurements were acquired on nude mice using a point source-point detection measurement system. The system was designed and constructed for

pharmacokinetic (PK) mapping of tracer uptake into and out of the bloodstream of small animals and is presented in this thesis as an initial proof of concept. Accordingly, this section (i) introduces dynamic imaging, pharmacokinetic measurements, and the PK model used to predict the uptake of a fluorophore into and out of the bloodstream; (ii) describes the *in vivo* study undertaken with a review of the dynamic fluorescence measurement instrumentation, which was described in Section 3; (iii) presents feasibility results based on fluorescence intensity measurements taken from the tail vein of nude mice simultaneous to a bolus injection of fluorophore into the tail vein, and (iv) provides a brief discussion on the implications of this measurement system.

5.2.1 Pharmacokinetic Model of Contrast Agent Uptake in Small Animals

Pharmacokinetic models which describe the kinetics of fluorescent contrast agent uptake into the blood, extra-cellular and intra-cellular space, and into the renal system organs have been described previously.^{53, 132, 158, 162} Specific studies include analyses on hepatic and renal function through ICG injection, uptake into tissues by non-specific HPPH-car as well as analyses of the binding rates of ligands to subcutaneously implanted tumors using cancer-specific fluorophores.^{53, 158, 162, 218} The latter studies, performed by Gurfinkel *et al.*¹⁶² and Kwon *et al.*¹⁵⁸ employed ICCD data in which a time series of CW fluorescence images were acquired continuously after a bolus injection of a targeting fluorophore.

The pharmacokinetic models for targeted-dye uptake reported by Gurfinkel and Kwon involve either two-compartment or three-compartment kinetic models that describe the uptake of a specific or non-specific contrast agent. The two compartment

models developed by Gurfinkel *et al.* describe (i) the partitioning of a non-specific agent from the blood to a generalized tissue compartment; or (ii) the uptake of a specific agent from the blood to the tissue compartment irreversibly. In contrast, more recent pharmacokinetic studies rely on three compartment kinetic models which may describe (i) the partitioning of a specific agent from the blood to the extravascular extracellular space (EES) and finally to the cell where the agent is bound; (ii) the uptake of a specific agent from the EES, to the vascular endothelium, and finally to the cell; or (iii) the uptake of a specific agent from the vascular endothelium, to the EES, and finally to the cell.¹⁵⁸ All three-compartment models include the irreversible rate of uptake into the bound cell compartment, which is denoted in previous works as k_c . The three-compartment kinetic models also include an irreversible step which represents the removal of the specific agent from the blood by the renal system, which is denoted here as k_1 . Figure 5.6 is an illustration of the generic two- and three-compartment models. A detailed description of the three compartment models is provided elsewhere; moreover, PK measurements of fluorophore blood concentration herein involve injection of a non-specific fluorophore. Therefore, the focus of Section 5.2 is on a two compartment reversible PK model.

The two compartment model is based on accumulation of the fluorophore into either the bloodstream (Compartment 1) or the tissue (Compartment 2). From Compartment 1, the dye will be irreversibly removed via the renal system at a rate represented by k_1 or reversibly removed from the bloodstream into the tissue with rates represented by k_2 and k_3 . Irreversibility occurs when the fluorophore is tumor-specific

and when in a tumor-bound state, it will not return to the bloodstream within the total dynamic imaging time. The reversible model is used for non-specific fluorophores, which enter the tissue then may partition back into the blood for removal from the body. The results presented here include injection of the non-specific dye, ICG, therefore the pharmacokinetic description below considers the reversible step between Compartments 1 and 2.

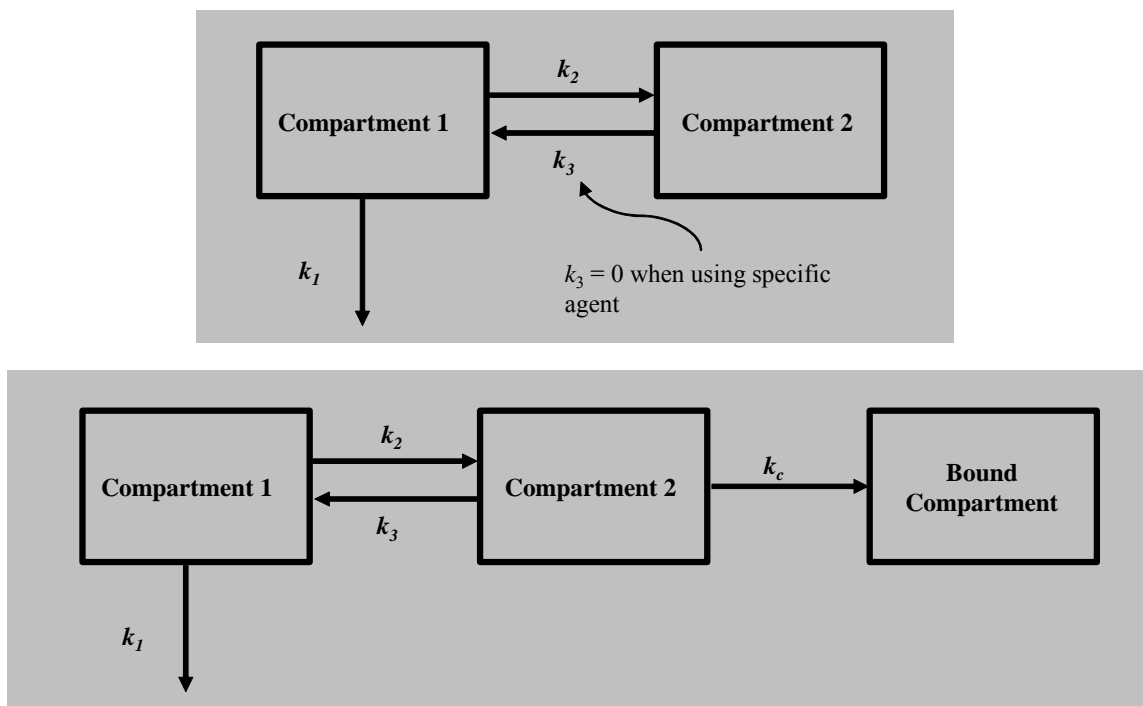


Figure 5.6 Two (top) and three (bottom) compartment generic pharmacokinetic models used to describe the uptake of a fluorescent contrast agent by either (i) the blood and tissue; (ii) the blood, extravascular, extracellular space and the cell membrane; (iii) the extravascular endothelium, vascular endothelium and cell membrane; or (iv) the vascular endothelium, extravascular endothelium and the cell membrane.

The rates of change of concentration of the fluorophore in the blood and in the tissue are described by the two differential equations below:

$$\frac{dC_B}{dt} = -k_1 C_B + k_3 C_T \quad (5.5)$$

$$\frac{dC_T}{dt} = -k_3 C_T + k_2 C_B \quad (5.6)$$

where C_B is the concentration of fluorophore in the blood and C_T is the concentration of fluorophore in the tissue. The solution to these equations can be found by assuming the initial condition: at $t = 0$, $C_B = C_{B_0}$ and $C_T = 0$. As described by Gurfinkel *et al.*,⁵³ Equations 5.5 and 5.6 are solved and the solutions to C_B and C_T may be correlated with experimentally measured fluorescence intensity by the equation below:

$$I(t) \cong w_1 C_T(t) + w_2 C_B(t) \quad (5.7)$$

where $I(t)$ is the fluorescence intensity [a.u.] measured as a function of time; C_T and C_B , are the concentration in the corresponding compartments at time t ; and w_1 and w_2 are constant weighting factors. Equation 5.7 is based on an assumption that the fluorescence intensity measured at a point on the body such as the ear is proportional to the sum of fluorophore molecules at that location in the body at a given time, t , after injection. Since the fluorophore molecules will reside in any of the two compartments, incorporating the solutions into each compartmental concentration produces the following four-parameter double exponential expression:

$$I(t) = I_o + A[\exp(-\alpha t)] + B[\exp(-\beta t)] \quad (5.8)$$

where $I_0 = w_1 C_1(0)$ is the intensity before injection, A and B are pre-exponential parameters that depend on the magnitude of fluorescence intensity, and α and β are parameters that depend on the rate of change of fluorescence intensity as defined by:

$$\alpha + \beta = k_1 + k_2 + k_3 \quad (5.9)$$

Gurfinkel *et al.* and Kwon *et al.* used this summation to compare the kinetics of dye uptake using different tumor models and under different conditions (i.e. specific binding, competitive inhibition, non-specific binding, and with vascular tumors) to assess the binding kinetics.

By acquiring $C_B(t)$ with the APD system, the time-dependent concentration of dye in the blood can be obtained and incorporated into Equations 5.5 and 5.6.

5.2.2 Animal Studies

The single-point measurement system described in Section 3.5 was tested on normal nude mice at the University of Texas M. D. Anderson Cancer Center. A catheter was inserted into the tail vein of three mice for preparation of a bolus injection of indocyanine green. ICG was dissolved in sterile saline to a concentration of 1 μM .

The SMA connector, detector bundle, and ferrule bundle ends of the bifurcated optical fiber described in Section 3.5.3 were individually positioned at the laser diode source output, the APD detector input, and ~ 2 mm from the surface of the tail vein, respectively. The three locations permitted excitation light delivery from the laser to the mouse tail vein and emission light delivery from the tail vein to the APD detector. During fluorescence detection and for each animal studied, the tail was not compressed and the

bundle was placed at a close distance without touching the skin surface. The light source used was a 785 nm and 80 mW laser diode (model Sanyo DL7140-201, ThorLabs, Newton, NJ), and was connected to the fiber bundle via SMA attachment. The bundle detector end was positioned normal to a holographic notch-plus band rejection filter (Kaiser Optical Systems Inc., Ann Arbor, MI, model HNPF-785.0-2.0) to block excitation light. The APD detector was mounted directly behind the band rejection filter. Fluorescence measurements were rapidly acquired for 20 minutes during which the ICCD system continuously captured a series of CW fluorescence images for comparison. The measurements followed the procedure below:

1. Phenobarbital anesthesia was administered to the mouse.
2. A catheter was inserted into the tail vein of the animal and the mouse was restrained on a flat surface.
3. The fiber bundle was mounted directly normal to the skin at an approximate distance of 2 mm from the skin surface. The bundle was positioned to measure fluorescence from the tail vein upon fluorophore injection; therefore the bundle was placed at the base of the animal's tail directly over the vein.
4. Image acquisition with the ICCD camera began by acquiring a 200-ms CW fluorescence image every 2 seconds. The ICCD camera continued to capture dynamic images throughout the entire fluorescence measurement sequence.
5. DC measurements of light intensity at a rate of 1 sample every 0.02 second were acquired from the surface of the mouse's tail using the APD detector. Background intensity measurements were first obtained by integrating the detector for approximately 10 seconds before the ICG was injected.
6. A bolus injection of the ICG-saline solution was next administered to the animal.
7. Fluorescence intensity measurements were acquired at a constant rate of one data point every 0.02 second.

8. After 20 minutes, data acquisition was stopped and the data were processed for PK analyses.

The procedure above was repeated on three animals to significantly measure the uptake of fluorophore into the blood stream and the slow partition of the fluorophore out of the blood of a healthy animal. Prior to the study, the animals were maintained in a pathogen-free mouse colony in the Department of Veterinary Medicine (The University of Texas M. D. Anderson Cancer Center, Houston, TX). The facility is accredited by the American Association for Laboratory Animal Care and all experiments were performed in accordance with the guidelines of the Institutional Animal Care and Use Committee.

5.2.3 Results of Pharmacokinetic Mapping using the Fiber Optic Fluorescence

Measurement System

Figure 5.7 is a plot of the fluorescence intensity as a function of time for three normal nude mice injected with 1 μM of indocyanine green. The intensity data are plotted over an approximate time period of 15 min. The fluorescence signal detected from all three animals follows a similar trend in which there are approximately 10–30 seconds of data representing the intensity acquired pre-bolus injection. Then upon injection, a rapid wash-in of the fluorophore occurs and is indicated by the sharp rise in intensity. The bolus injection peak rises to a maximum and is followed by a rapid decline in the arbitrary fluorescence intensity value. The decrease in signal can be attributed to the fluorophore partitioning from the blood to the surrounding tissues and into the renal system. After 15 min, the fluorescence intensities asymptotically reach the value of the measured background signal. The rapid decrease in intensity is consistent

with previously reported results.²¹⁸ Figure 5.8 shows the resulting ICCD images of the normal nude mice before bolus injection of 1 μM ICG, immediately upon injection, and 15 min after injection. It is apparent that before injection, there is little or no fluorescence signal in the animal's body, and after 15 min the signal has increased, indicated by the rise in intensity over the entire mouse body.

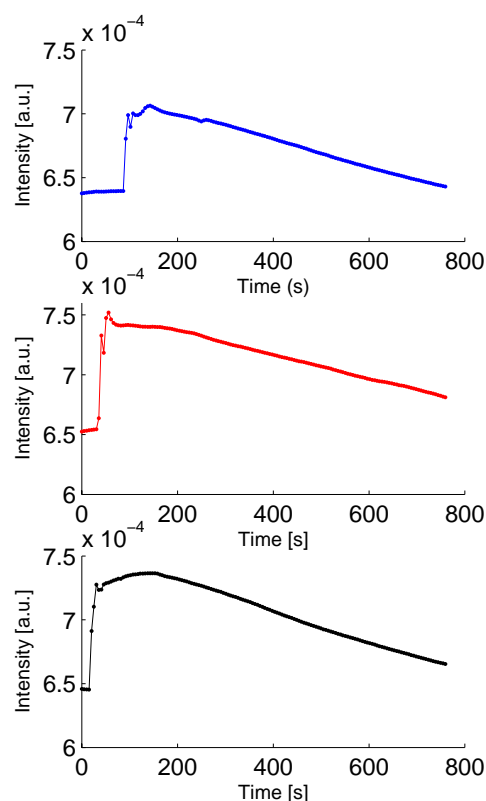


Figure 5.7 APD fluorescence intensity [a.u.] data acquired from the tail veins of three normal nude mice. Data from animal #1 are plotted in blue, data from animal #2 are plotted in red and data from animal #3 are plotted in black. The intensity measurements are plotted versus data acquisition time [s] and were acquired upon a bolus intravenous injection of 1 μM of indocyanine green.

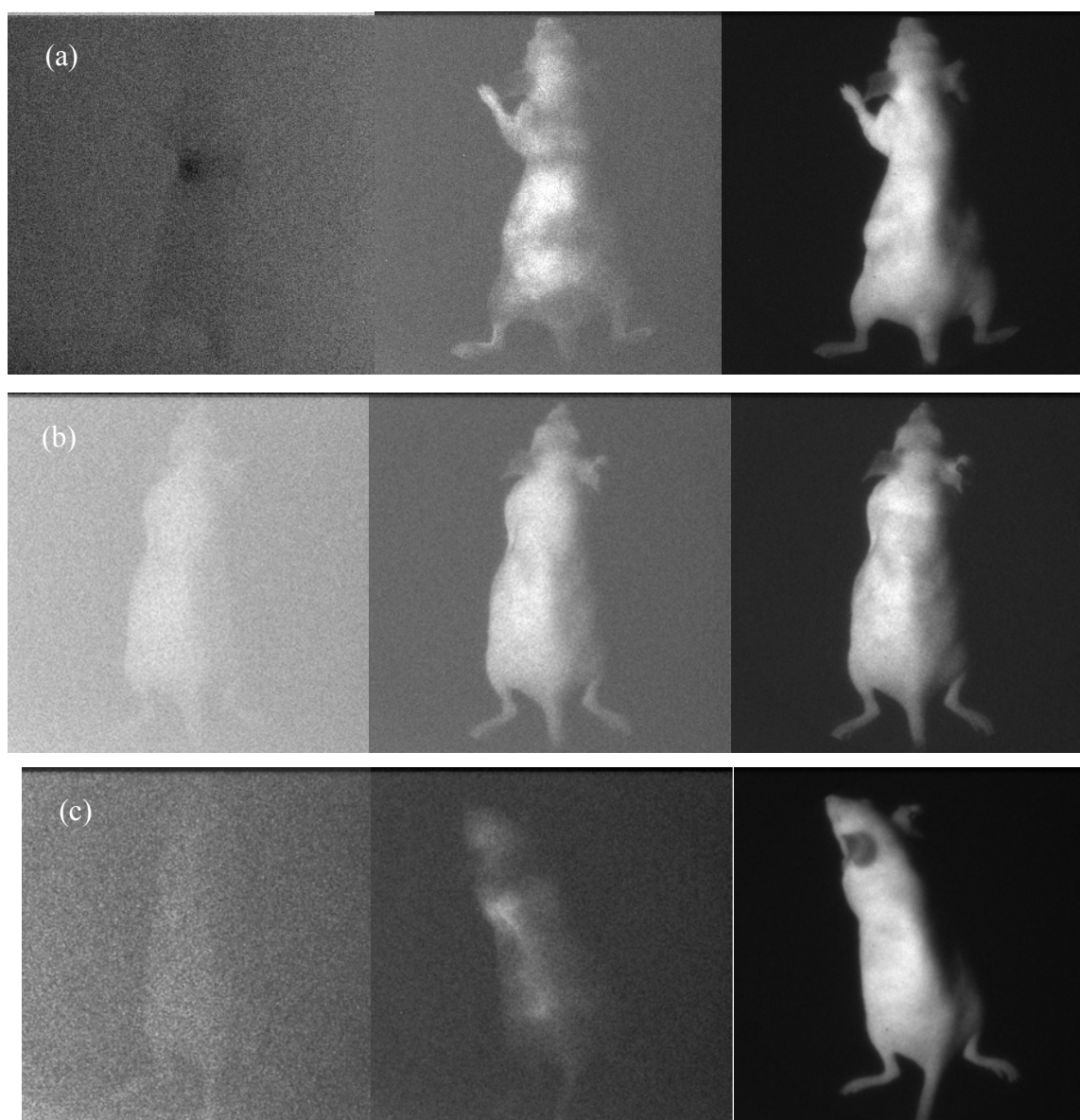


Figure 5.8 ICCD images of three nude mice before indocyanine green injection (left), upon injection (middle) and 15 min after injection (right). Data from animal #1 are plotted in figure 5.7 (a), data from animal #2 are plotted in figure 5.7 (b) and data from animal #3 are plotted in figure 5.7 (c). The images are plotted in a monochrome pseudocolor scheme.

Regions of interest on the right flank of each nude mouse were selected and extracted from the dynamic ICCD fluorescence intensity data. To demonstrate the wash-in of fluorescence into the tissue of a normal nude mouse, the ROI intensity data are plotted in Figure 5.9. The ICCD camera system detected a continuous rise in intensity as ICG accumulated in the entire body, whereas the APD detected a continuous drop in intensity as ICG partitioned from the blood in the tail vein into the surrounding tissue and EES.

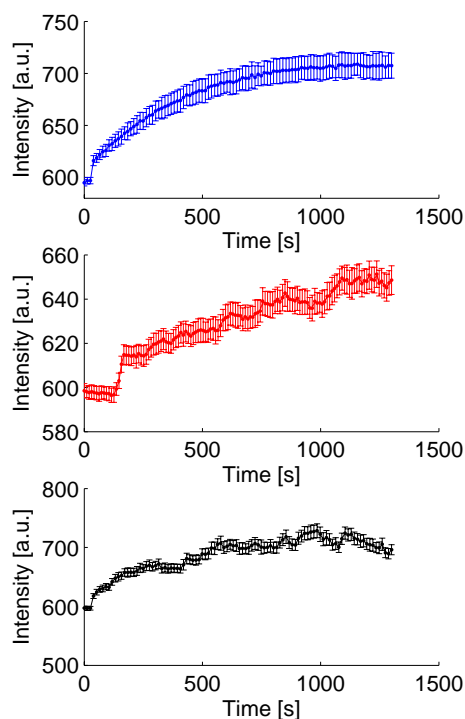


Figure 5.9 Fluorescence ROI ICCD intensity [a.u.] data acquired from the right flanks of three normal nude mice. Data from animal #1 are plotted in blue, data from animal #2 are plotted in red and data from animal #3 are plotted in black. The intensity measurements are plotted versus data acquisition time [sec] and were acquired upon a bolus intravenous injection of $1 \mu\text{M}$ of indocyanine green. Error bars represent the standard deviation in the pixel intensity values for each ROI drawn.

The APD fluorescence intensity data for each animal were fit with the two-exponential, four parameter pharmacokinetic model described previously. The least squares regression was performed with Sigma Plot 8.02. The data and corresponding regressions are plotted in Figure 5.10. The r-squared values resulting from each non-linear regression were 0.86, 0.98, and 0.99 for Animals 1–3, respectively.

5.2.4 Discussion on Single Point Fluorescence Measurements in vivo

Gurfinkel *et al.* related the parameters, α and β , to ICG uptake rate in canines by observing that the summation of α and β is equivalent to $k_1 + k_2 + k_3$. The comparison of $\alpha + \beta$ allowed Gurfinkel *et al.* to compare uptake rates between normal and diseased tissue. Although ICG uptake in normal and diseased tissue was not compared in the nude mice studies herein, the values of $\alpha + \beta$ nonetheless were examined for similarity between all three animals. The values of $\alpha + \beta$ [s^{-1}] for Animals 1–3 were found to be 0.0015 [s^{-1}], 0.07 [s^{-1}], and 0.02 [s^{-1}], respectively. The $\alpha + \beta$ value for Animal 1 is an order of magnitude lower than that of Animals 2 and 3, which may be a result of the poor fit by the two-compartment model. The APD intensity data presented herein is nonetheless promising, as it demonstrates that fluorescence intensity data can be rapidly acquired simultaneous to a bolus injection of ICG. Future work is necessary to improve the sensitivity of the imaging system so that fluorescence from the ear of the mouse can be detected upon injection of nanomole quantities of ICG.

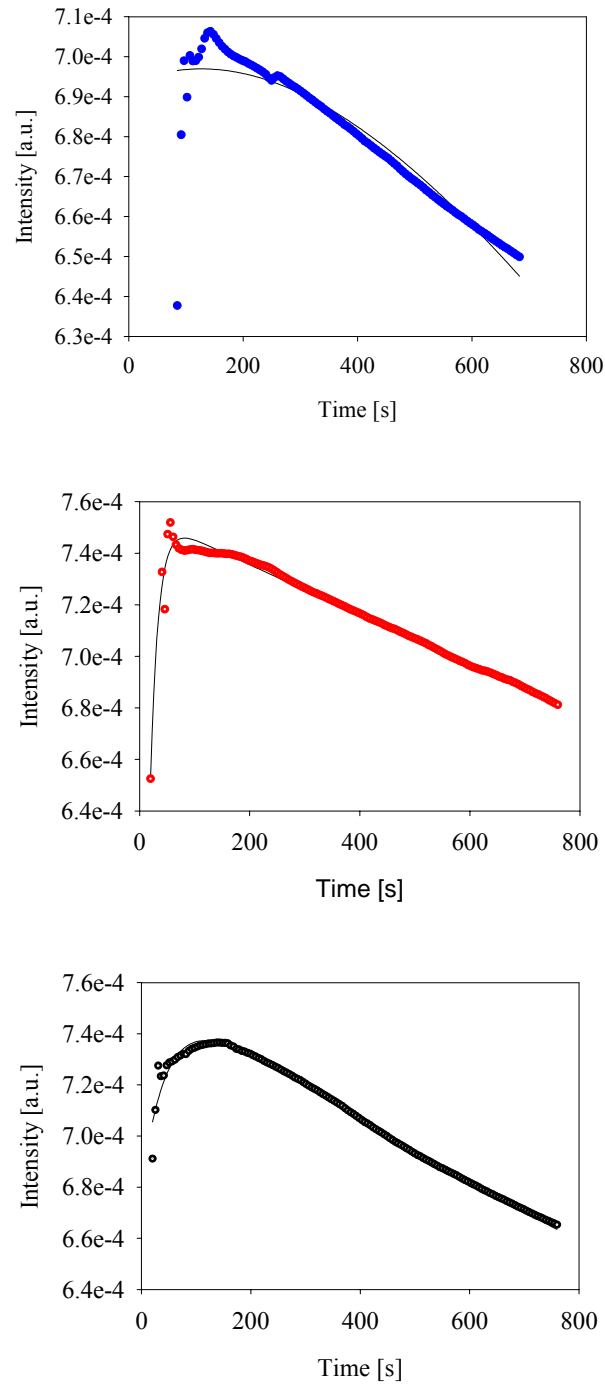


Figure 5.10 APD fluorescence intensity [a.u.] vs. time and with a corresponding non-linear regression. Data from animal #1 are plotted in blue, data from animal #2 are plotted in red and data from animal #3 are plotted in black. The intensity measurements were acquired upon a bolus intravenous injection of 1 μM of indocyanine green.

6. PHASE 3: IMAGING PATIENTS

At the date of this thesis a twelve patient study was pending and scheduled to be completed at the University of Texas M. D. Anderson Cancer Center using the ICCD camera system described in Section 3. As a collaborative effort, the Photon Migration Laboratories at Texas A&M University and UT MDACC have designed a study in which breast cancer patients are subject to fluorescence-enhanced optical imaging. Several steps leading to this study include approval of the protocol by the UTMDACC Institutional Review Board (IRB) and approval of a combined Investigational New Drug (IND) and Investigational Device Exemption (IDE) by the Food and Drug Administration. Therefore in light of the several steps achieved towards this goal, the last section of this thesis includes work on the development of “optical lymphography” including: (i) fluorescence data supporting the stability of ICG as an investigational new drug for intravenous administration in combination with technetium 99m sulfur colloids, (ii) the fluorescence enhanced optical imaging clinical trial protocol, (iii) the standard operating procedure written for employment of the ICCD imaging system in a clinical setting, and (iv) statistical considerations and handling of the acquired optical images.

6.1 Stability of ICG and Sulfur Colloid

Before describing the clinical protocol, preliminary data is presented in this section which supports the use of indocyanine green dye in combination with the technetium 99m filtered sulfur colloid. In previous work, the fluorescence spectra of ICG with the isosulfan blue dye used in SLNM was acquired to evaluate any spectral

overlap between the two molecules. It was found that ICG excitation and emission spectra was not hindered upon mixing with the intra-operative blue dye.²¹⁹ Likewise, the combination of ICG with the sulfur colloid must be assessed to evaluate the impact of a colloid suspension on ICG fluorescence and visa versa. Therefore, this section describes results from two studies: (1) a fluorescence measurement study to assess the ability of ICG to retain its photochemical properties upon mixing with sulfur colloid and (2) a particle sizing study to measure the longevity and stability of the colloid suspension upon mixing with ICG.

6.1.1 Fluorescence Spectra

The fluorescence measurement study was performed by taking the fluorescence spectra of five samples using a fluorimeter (Jobin Yvon Ltd., Middlesex, UK). The five samples are listed below.

1. Deionized ultrafiltered (DIUF) water
2. ICG diluted in DIUF water at a concentration of 0.5 μM
3. ICG diluted in DIUF water at a concentration of 1 μM
4. ICG diluted in saline and filtered sulfur colloid at a concentration of 1 μM
5. Filtered sulfur colloid in saline

The colloid sample (CIS-SULFUR COLLOID™, CIS-US, Inc., Bedford, MA) was kindly provided by Professor Ron Fisher from the Department of Radiology at Baylor College of Medicine, Houston, TX. Each sample was prepared, added at a volume of 3 mL to a crystal cuvette, and placed in a fluorimeter to obtain both excitation spectra

(from 660 nm to 810 nm) and emission spectra (from 790 nm to 900 nm). The following describes the procedure undertaken to obtain the excitation and emission spectra for each sample.

An excitation scan was first performed in which the emission monochromator was set at 830 nm and in increments of 5 nm, the absorbance of light at each wavelength was measured. The integration time of the detector was 1 second for each measured wavelength. Upon obtaining the excitation spectra, an excitation peak was identified. The peak was 763 nm for all samples that contained ICG, and there was no peak for the DIUF water-only and colloid-only samples.

The emission spectra were then collected by setting the excitation monochromator at the identified absorbance peak wavelength (763 nm). The emission spectrum was read at wavelength intervals of 5 nm for which the intensity of the emitted light was detected at an integration time of 1 second for each measured emission wavelength.

The resulting spectra of the 1- μM and 0.5- μM ICG solutions in DIUF water are provided in Figure 6.1. The excitation spectra for both concentrations were normalized to the maximum absorbance value [a.u] of the 1 μM ICG solution. Both the 1- μM and 0.5- μM ICG solutions produced the same absorbance properties; the similarity is apparent by the unchanging excitation peaks and excitation valleys revealed in the plotted spectrum. Additionally a single ICG excitation peak maximum was readily visible at the same wavelength for both concentrations. The total excitation spectrum corresponding to the 1- μM ICG solution is approximately two times higher in intensity

[a.u.] than the spectrum for the 0.5- μM ICG solution, which reflects the proportionality of absorbance to the concentration of fluorescing species. Likewise, the emission spectra for both concentrations were normalized to the maximum intensity value of the 1- μM ICG solution and are plotted in Figure 6.1. Again, two emission peaks at the same wavelength are revealed for both concentrations. The emission spectrum intensity [a.u.] of the 1 μM solution was two times that of the 0.5- μM solution. Figure 6.1 reveals the results of a positive control study by presenting the excitation and emission properties of a typical and unperturbed solution of indocyanine green. The ICG-only excitation and emission peaks are equivalent to well-known values previously reported in the literature. The absorbance of DIUF water-only was measured for background intensity counts [a.u.] and is also indicated on Figure 6.1.

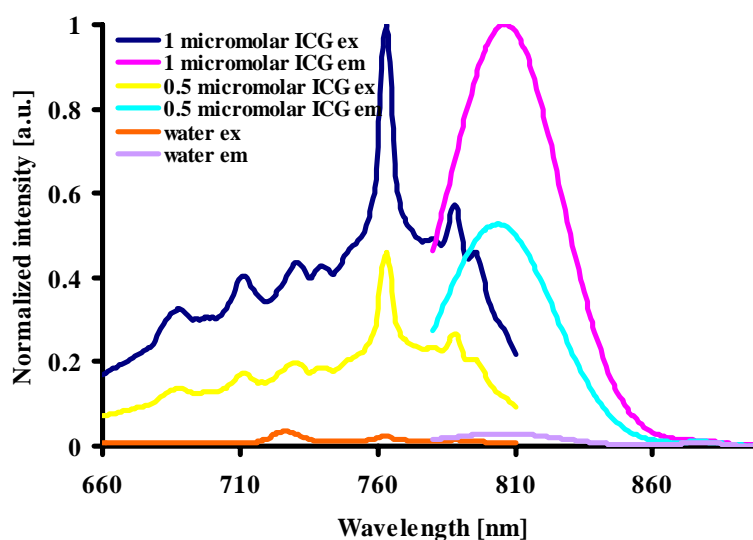


Figure 6.1 Normalized excitation and emission spectral data of a 1- μM concentration of ICG in DIUF water (blue excitation and pink emission lines), a 0.5- μM concentration of ICG in DIUF water (yellow excitation and cyan emission lines), and DIUF water (orange excitation and purple emission lines).

Figure 6.2 is a plot of the excitation and emission spectrum of both the sulfur colloid suspension in saline and 1 μM of ICG in DIUF water without addition of the sulfur colloid. The excitation and emission spectra of the colloid suspension alone is a negative control with results that reveal the non-fluorescent properties of the colloid. That is, the colloid sample was found to have no apparent peak absorbance or emission. The excitation and emission spectra for the colloid alone resulted in near-constant intensity [a.u.] across all measured wavelengths. The non-fluorescent properties of the sulfur colloid are most apparent when plotted with the 1- μM ICG excitation and emission scan, as shown in Figure 6.2.

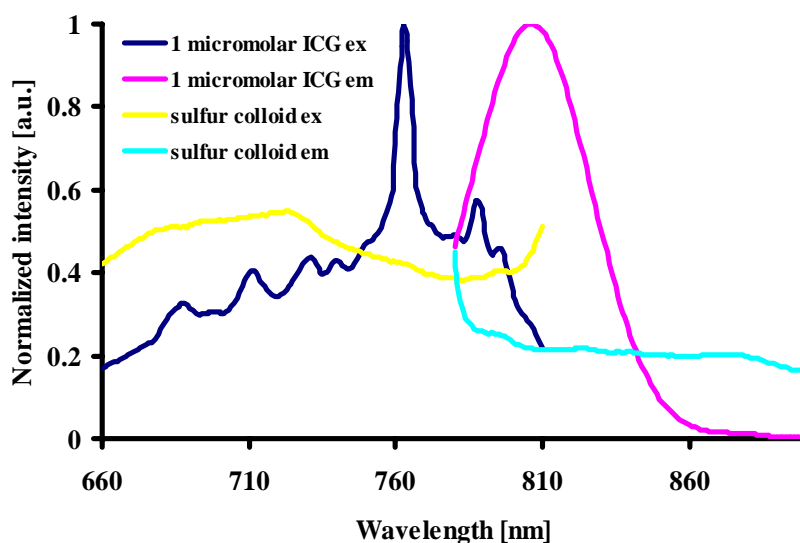


Figure 6.2 Normalized excitation and emission spectral data of a 1- μM concentration of ICG in DIUF water (blue excitation and pink emission lines) and sulfur colloid suspension (yellow excitation and cyan emission lines).

Figure 6.3 is the excitation and emission spectrum of both 1- μ M ICG in DIUF water and 1 μ M ICG mixed with sulfur colloid. The excitation and emission spectra for both samples are normalized by the maximum excitation and emission intensity [a.u.] values of 1- μ M ICG in DIUF water. The addition of the sulfur colloid to ICG dampened the ICG excitation peak, however no shift or change in the peak excitation occurred. In other words, the excitation peak for the ICG + colloid mixture was at the same wavelength as the ICG in DIUF water mixture. The emission spectra results were similar in that the addition of sulfur colloid to ICG lowered the ICG emission peak intensity [a.u] but did not create an emission spectrum shift or total emission peak loss.

Ultimately the spectra results indicate that before addition of a sulfur colloid suspension, ICG excites and fluoresces at distinct wavelengths in the NIR, and upon dissolving with a sulfur colloid suspension, retains the abovementioned photochemical properties. Additionally the sulfur colloid was found to have no radiative absorption or relaxation properties; the addition of the colloid to ICG only dampens the peak ICG absorption and emission rather than creating a total loss of fluorescence. Because ICG was found to retain its photochemical properties when mixed with sulfur colloid, it can be concluded as acceptable as a mixed species for fluorescence measurements on human subjects undergoing lymphoscintigraphy.

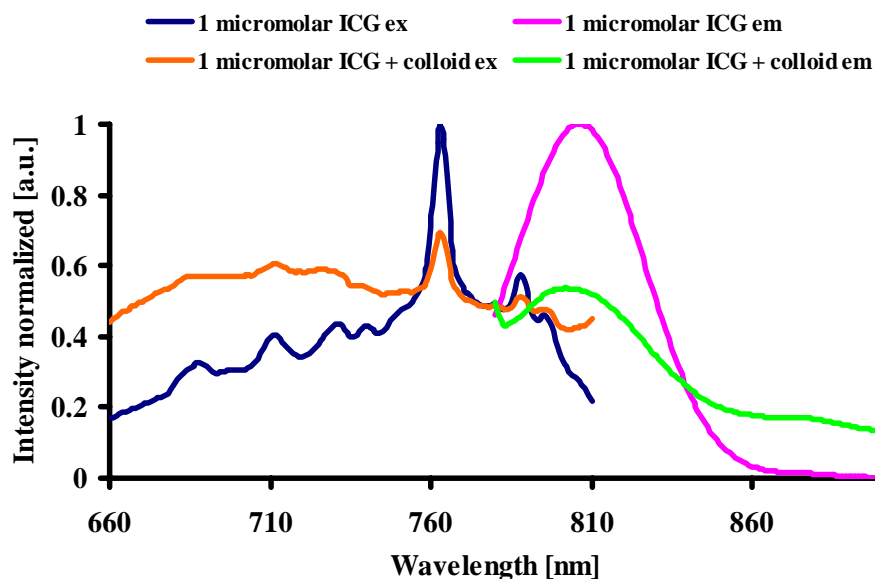


Figure 6.3 Normalized excitation and emission spectra of a 1- μ M concentration of ICG in DIUF water (blue excitation and pink emission lines), and a 1- μ M concentration of ICG in a sulfur colloid suspension (orange excitation and green emission lines).

6.1.2 Particle Sizing

In addition to the excitation and emission measurements, a particle sizing measurement was performed to assess the stability of the sulfur colloid mixed with ICG. Dynamic light scattering (DLS) was the technique used to determine the particle size of the colloid with and without ICG. DLS measures the Brownian motion of particles and through visible light scattering and relates the measurement to particle size. The criteria for evaluating the colloid stability was simply assessing if the size of the colloid remained the same when measured with and without ICG. If it is measured accurately under both conditions, the physical composition of the sample is believed to not be

compromised (i.e., no coagulation, precipitation, or change in suspension resulting from addition of ICG). It is imperative that the colloid integrity is steadfast or else the biokinetics of the inert colloid transport throughout the lymphatics may be hindered.²²⁰

The particle sizing was accomplished with a DLS machine developed by Malvern Instruments Ltd. (Zetasizer 3000HS, Malvern, UK). The results provide a quality factor reading (pass/fail) as well as an average diameter reading. Each sample was read three times for statistical significance. Figures 6.4(a and b), 6.5(a and b), and 6.6(a and b), are the size reports for the colloid, colloid + ICG, and ICG, respectively. The colloid alone had an average measured diameter of ~450 nm. This value is consistent with the size of sulfur colloids reported in literature for sentinel lymph node mapping.²²¹ The colloid when mixed with ICG was found to have an average diameter of ~450 nm. Both readings passed the instrument's internal quality control assessment. Therefore, the colloid's integrity was not compromised upon the addition of ICG. As a negative control, DLS was performed on a solution of ICG in DIUF water. This sample failed the quality assessment, giving erroneous particle size measurements. In light of these favorable results on the mixture of ICG with the sulfur colloid, the protocol for imaging patients is provided below.

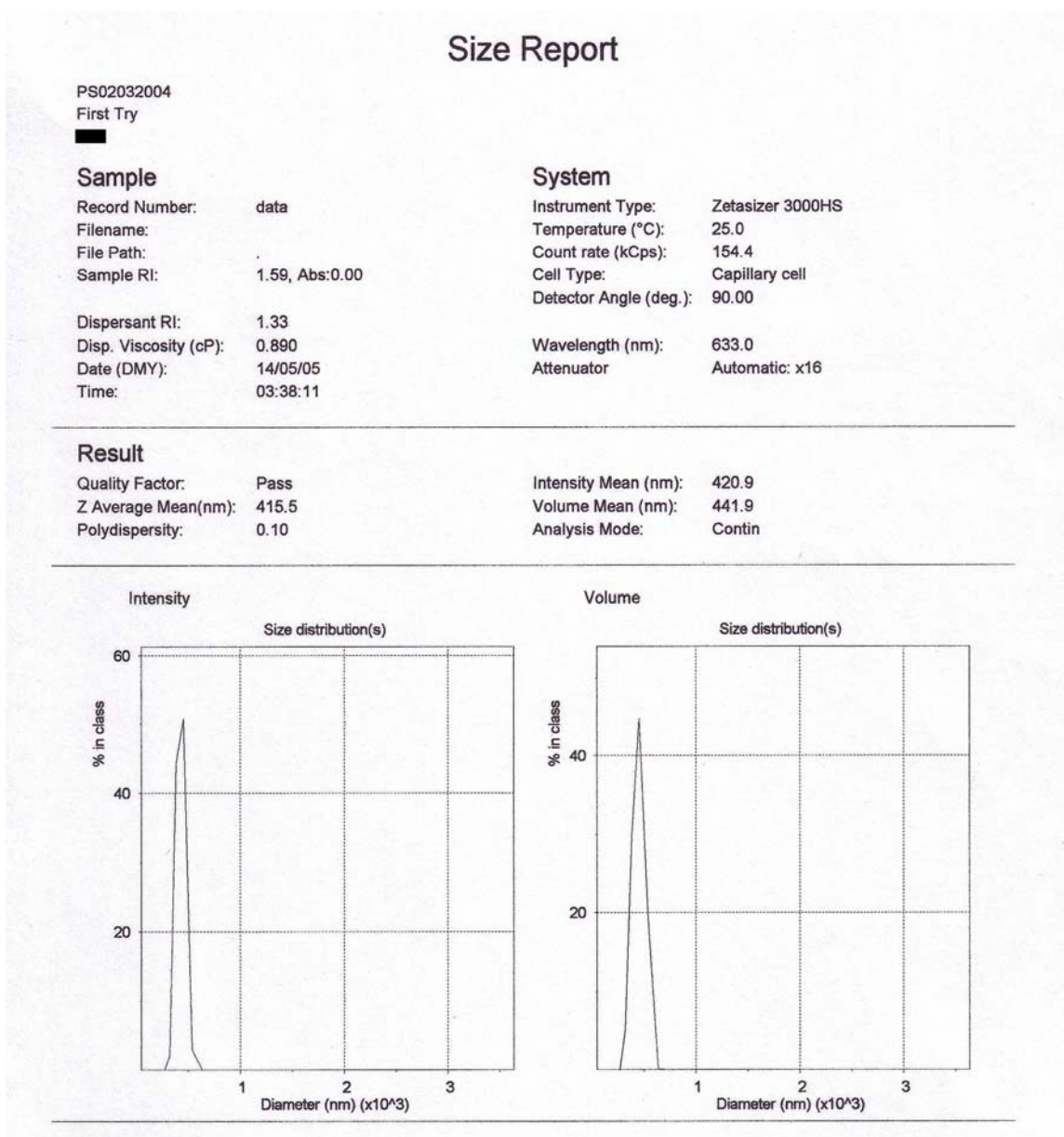


Figure 6.4(a) Dynamic light scattering size report of the filtered sulfur colloid used for SLNM. The average diameter of the particle was measured using a Zetasizer (Malvern Instruments Ltd, Malvern UK).

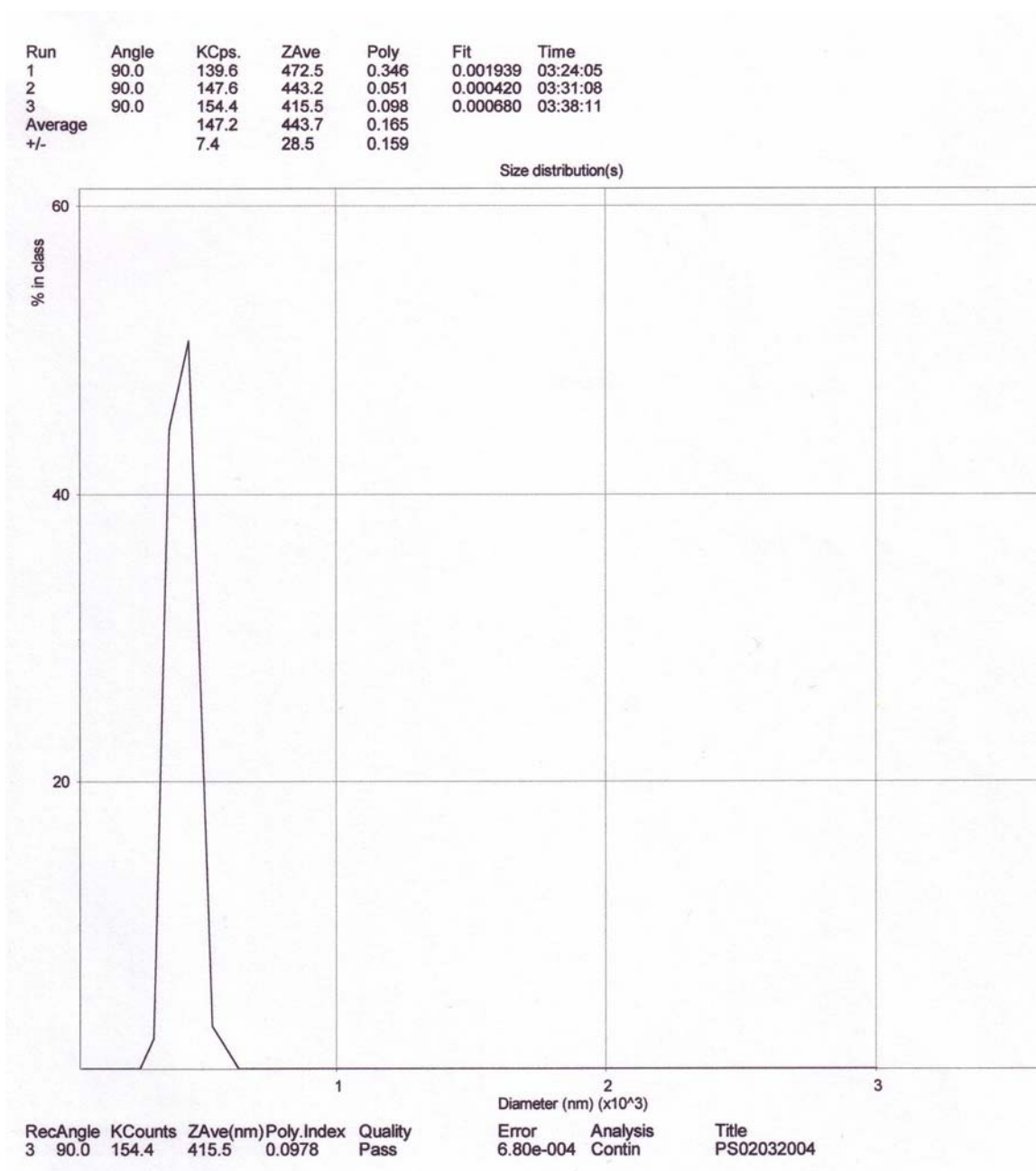


Figure 6.4(b) Second page of the dynamic light scattering size report of the filtered sulfur colloid used for SLNM.

Size Report

PS02032004

First Try

Sample

Record Number: data
 Filename:
 File Path:
 Sample RI: 1.59, Abs:0.00

Dispersant RI: 1.33
 Disp. Viscosity (cP): 0.890
 Date (DMY): 14/05/05
 Time: 04:08:34

System

Instrument Type: Zetasizer 3000HS
 Temperature (°C): 25.0
 Count rate (kCps): 123.7
 Cell Type: Capillary cell
 Detector Angle (deg.): 90.00

Wavelength (nm): 633.0
 Attenuator: Automatic: x 8

Result

Quality Factor: Pass
 Z Average Mean(nm): 415.5
 Polydispersity: 0.29

Intensity Mean (nm): 997.7
 Volume Mean (nm): 5086.5
 Analysis Mode: Contin

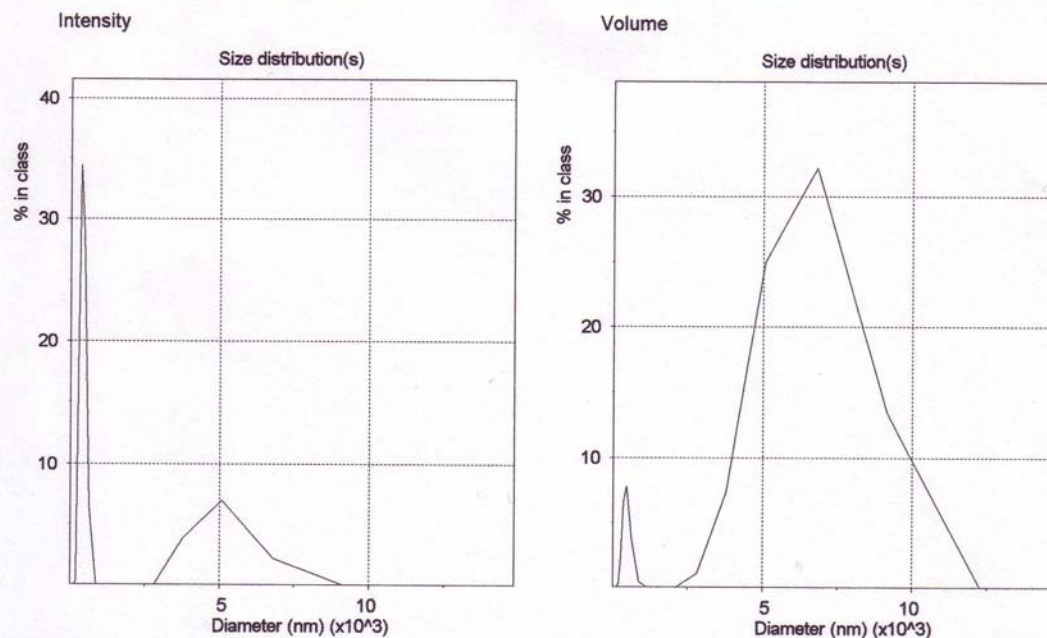


Figure 6.5(a) Dynamic light scattering size report of a mixture of 1- μM of indocyanine green and filtered sulfur colloid used for SLNM. The average diameter of the particle was measured using a Zetasizer (Malvern Instruments Ltd, Malvern UK).

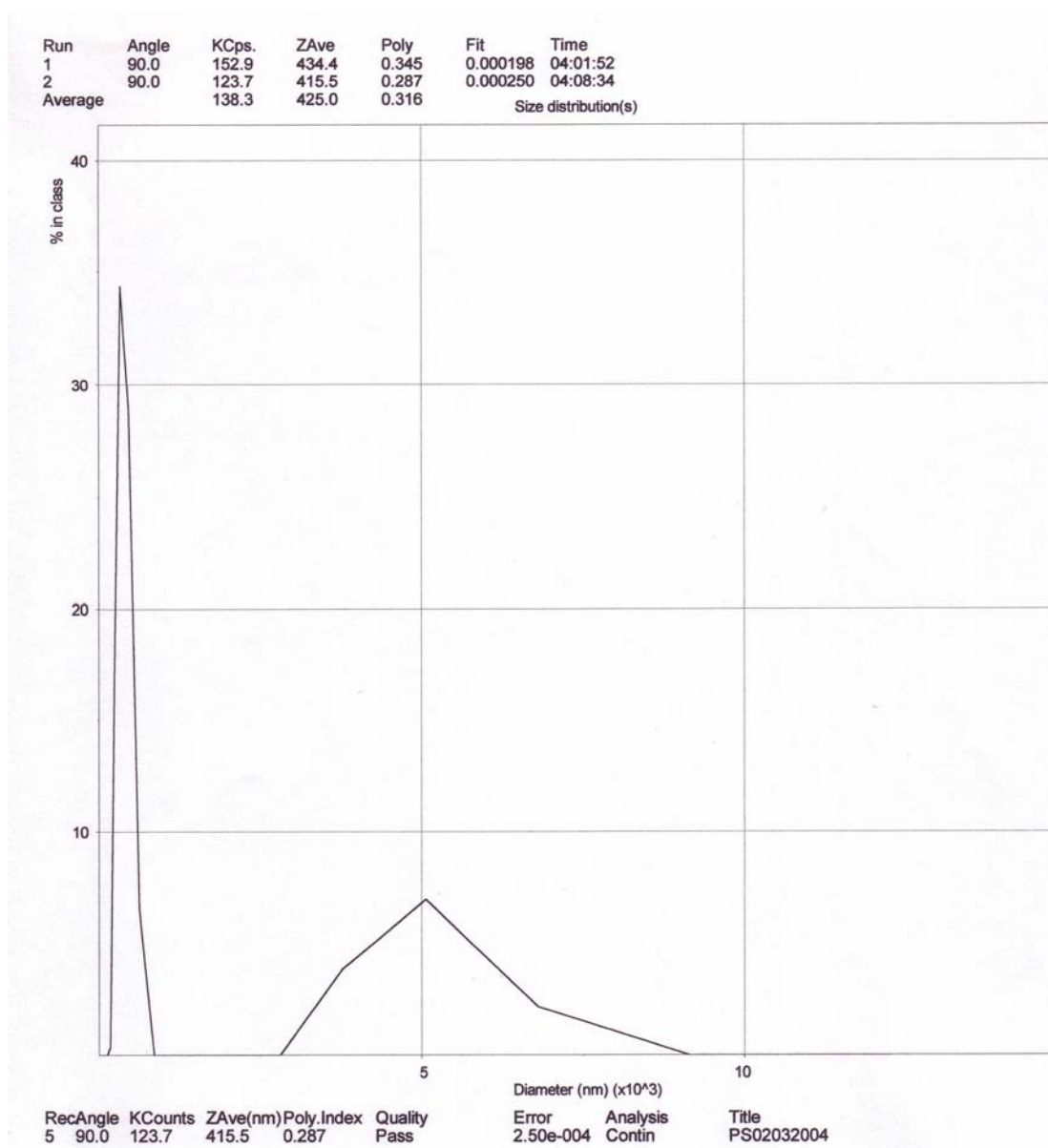


Figure 6.5(b) Second page of the dynamic light scattering size report of a mixture of 1- μ M indocyanine green and filtered sulfur colloid used for SLNM.

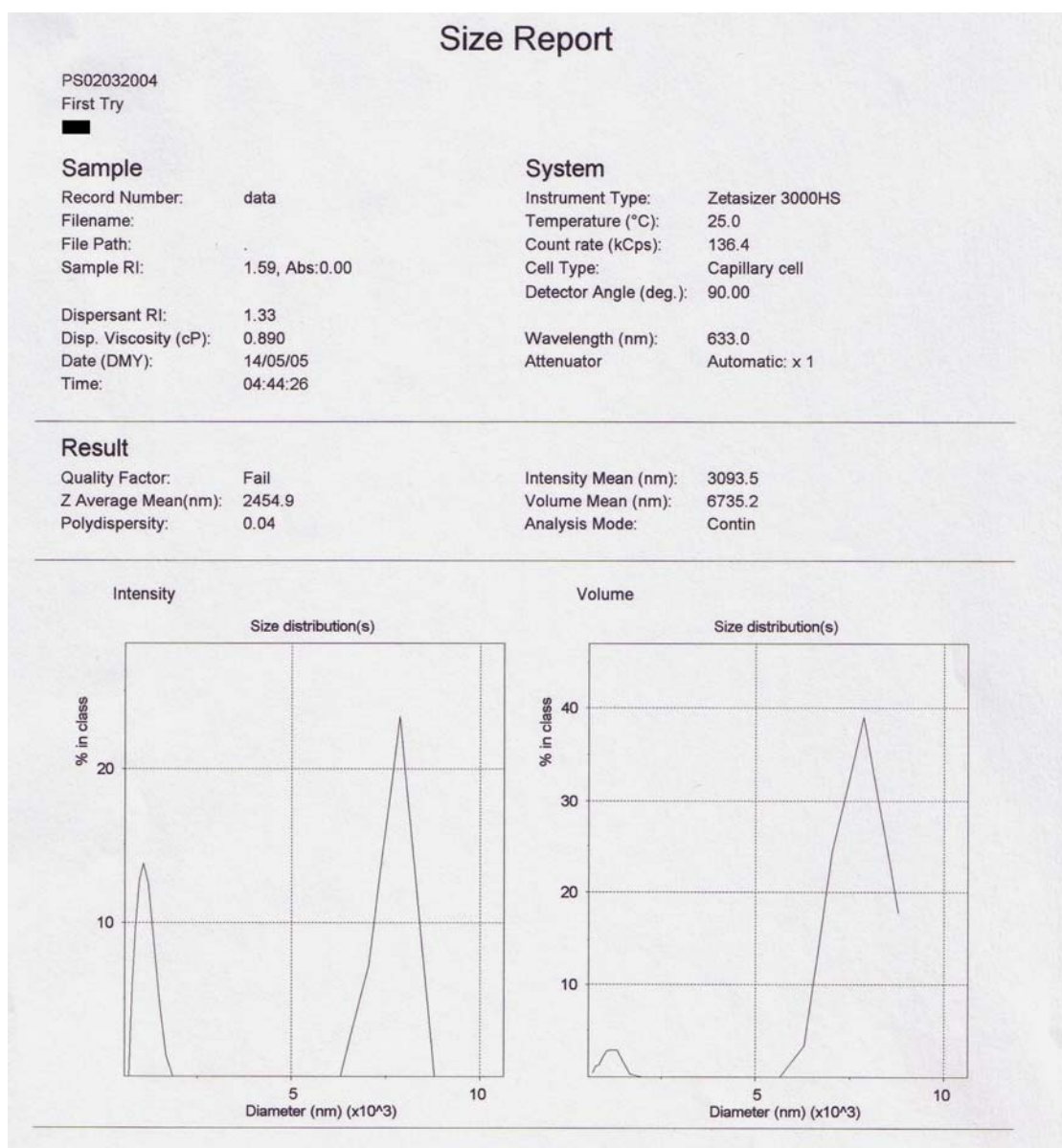


Figure 6.6(a) Dynamic light scattering size report of 1- μ M of indocyanine green in DIUF water. The size report was obtained from a Zetasizer (Malvern Instruments Ltd, Malvern UK).

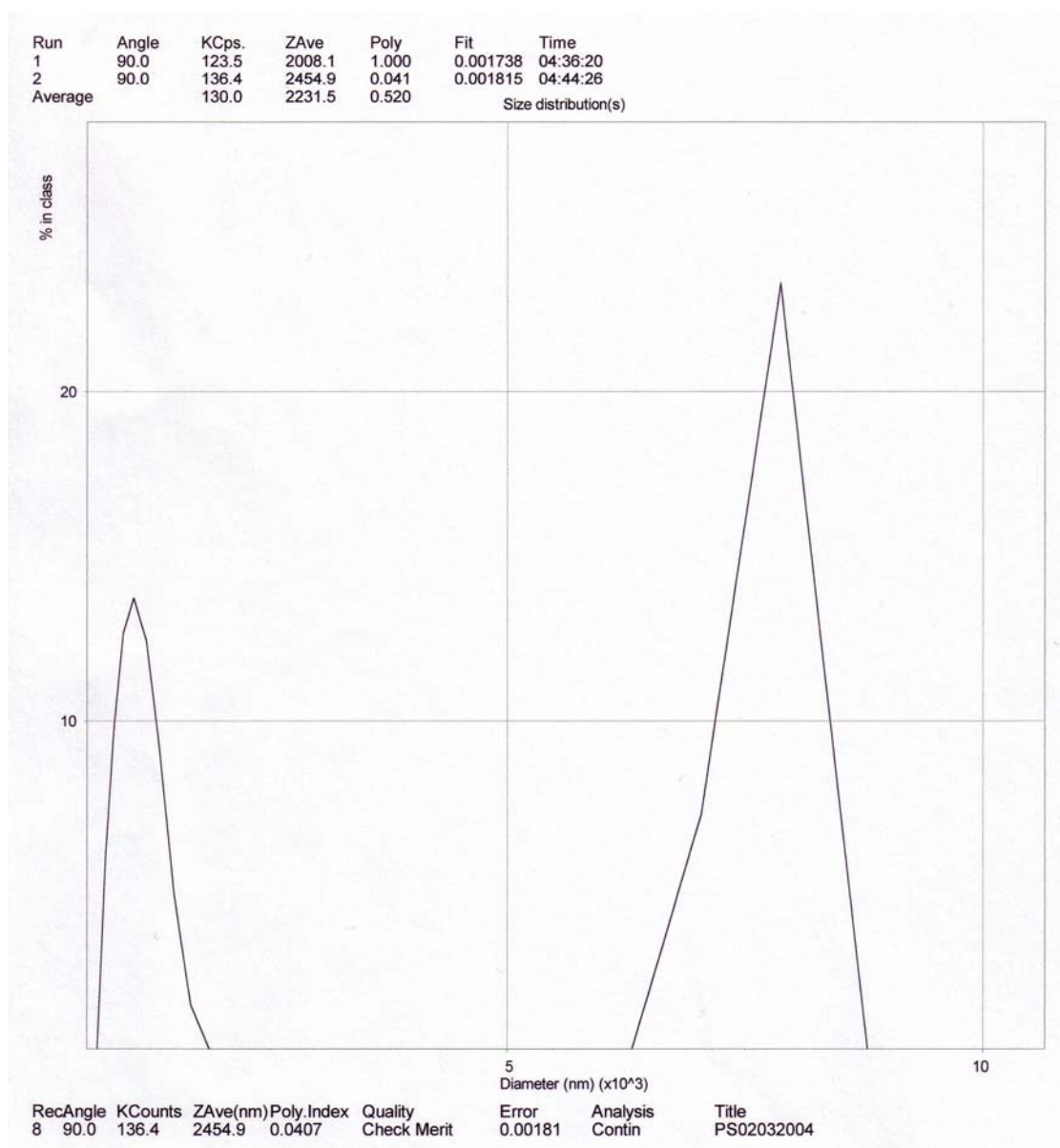


Figure 6.6(b) Second page of the dynamic light scattering size report of 1- μ M indocyanine green in DIUF water.

6.2 Protocol

The formal clinical protocol document (ID01-512) entitled, "Sentinel Lymph Node Mapping Using Fluorescent Contrast Agents and NIR Optical Imaging," is authored by the candidate under the UTMDACC Protocol Document On-Line System (PDOL), managed by the UTMDACC Office of Protocol Research, and is approved by the UTMDACC IRB. Patient consent forms are also controlled by UTMDACC PDOL. A general description of what is lightly based on the IRB approved document is provided below.

6.2.1 Objectives

The two-fold objective of the optical lymphography study is: (1) to construct an optical ICCD system capable of frequency-domain measurements of fluorescence on breast cancer patients in the nuclear imaging suite of UTMDACC, and (2) to demonstrate the ability of the said system to dynamically or statically obtain fluorescent images of sentinel lymph nodes, non-invasively on patients undergoing lymphoscintigraphy using the non-specific fluorescent dye, ICG.

6.2.2 Background

Sentinel lymph node mapping is fast becoming a routine clinical practice in assessing breast cancer metastasis. SLNM is accomplished (recall Section 1) by employing nuclear imaging systems, which may aid surgeons in the identification of the sentinel lymph node, or the first node which harbors metastatic drainage from the primary tumor. This node, which is resected by the surgeon for histological analysis for

the presence of breast carcinoma metastases, may be irregularly visualized (false-negative) by gamma cameras, which function by imaging radiopharmaceuticals that have been injected for localization within lymphatic system and lymph nodes. Although the surgeon can visualize the sentinel node during surgery with the help of a blue dye, fluorescence-enhanced optical imaging may become one methodology for imaging the node non-invasively, and if proven, in the identification of positive nodes (with a cancer-targeting fluorophore). Optical imaging may aid with node localization.

Despite being the gold standard, nuclear imaging requires radiopharmaceuticals that are ionizing and bulky making them slow to drain through the lymph to the sentinel node. The drainage of the isotope can be disrupted due to the presence of scar tissue, hyperplasia, fatty degeneration and gross metastasis. Moreover it is unclear whether or not nuclear imaging performed before surgery is beneficial or not.^{31, 35, 222} Because there is no standardized procedure for the facets of SLNM, particularly the choice of radioisotope, the size of isotope colloid used, the injection site, injection volume, and the timing of the imaging scans, optical imaging has potential to become the methodology of choice for imaging the sentinel lymph node.

6.2.3 Procedural Steps

The protocol includes twelve human subject volunteers to be imaged using the ICCD camera system in the nuclear imaging suites located in the 3rd floor of the main hospital within the Division of Diagnostic Imaging and the Department of Nuclear Medicine. The optical imaging will be in conjunction with each patient's regularly scheduled nuclear lymphoscintigraphy procedure, which is the hospital's standard

protocol for determining metastasis of cancer in the breast. Table 6.1 outlines generally the steps for the optical lymphography study as they will coincide with the M.D. Anderson SLNM protocol.

Table 6.1 The University of Texas M. D. Anderson Cancer Center Nuclear Medicine sentinel lymph node mapping general procedure combined with fluorescence-enhanced optical imaging as described in the ID01-512 protocol

Nuclear Lymphoscintigraphy Procedure	Optical Imaging Procedure
<ol style="list-style-type: none"> 1. Local anesthesia is injected into the breast using lidocaine mixed with sodium bicarbonate. 2. Peritumoral injection of filtered technetium 99m sulfur colloid at a dose of 0.5 mCi. 4. Breast area is gently massaged. 6. Diagnostic lymphoscintigraphy is performed (either static or dynamic to visualize lymph flow) with a gamma camera. 7. The skin is marked with ink to delineate the position of the sentinel lymph node 8. Intraoperative localization and excision of the sentinel lymph node is performed on the same day or the day after lymphoscintigraphy. 	<ol style="list-style-type: none"> 3. Peritumoral injection of indocyanine green in saline at a dose of 1 μM. 5. Fluorescence enhanced FDPM imaging is performed

Briefly, the optical/nuclear SLNM procedure involves the peritumoral injection of a mixture of the filtered Technetium 99m sulfur colloid (0.50 mL ~ 2.0 mCi of activity, Mallinckrodt, Houston, TX) and indocyanine green at a concentration of 1 μ M

or less. The ICG will be provided by AKORN Pharmaceuticals, Inc. (Ophthalmic and Parenteral Health Care, Buffalo Grove, IL), who sponsors of the FDA IND. Fluorescence imaging will then be initiated immediately following injection over the tissue region of injection. The maneuverable, articulating arm, which holds the ICCD camera and lens will be scanned over the site of injection, across the breast, to the axilla, and on the sternum for imaging. The NIR laser beam will be expanded over this same area for excitation of ICG into the lymphatics. Imaging and frequency-domain data collection will be conducted in the nuclear medicine suite immediately after injection up until the time for the first lymphoscintigraphy, which is estimated to be approximately 20 minutes following both technetium 99m sulfur colloid and ICG injections. During the period of dynamic imaging, the patient will lie on her side or back to enable imaging of the axillary and the internal mammary nodes. Dynamic and static FDPM images will be conducted during the hours between injections and the final lymphoscintigrams. After injection of the agent, the patient will wait in the nuclear imaging suite while the breast area is massaged to expedite the flow of the sulfur colloid into the lymph. FDPM images of fluorescent emission will be captured in the suite after the injection and consent of the physician. Patients with palpable lesions only will be recruited. The ICCD camera system will be focused onto the subject to collect a series of frequency-domain data. The standard operating procedure for controlling the ICCD camera system in the clinic will follow the steps listed in Table 6.2. The time frame for the entire optical lymphography procedure is also estimated in Table 6.2. The total time required of the patient to participate in the optical imaging component of the protocol is

approximately 16.5 minutes. The total time for the outlined steps (involving start-up, shut-down and removal of the instrument from the nuclear imaging suite) is ~33 minutes.

6.3 Standard Operating Procedure for Clinical ICCD Imager

The steps for operation of the FDPM ICCD system are described in a numerical outline below. The procedure, initially developed as a reference for doctors and clinicians who are to participate in the study and who require awareness of laser safety, is provided here to demonstrate the actual clinical trial process.

Table 6.2 The step-by-step operation of frequency-domain optical imaging to be undertaken on human subjects undergoing sentinel lymph node mapping in the nuclear imaging suite. The steps are part of the optical lymphography protocol.

	Step-by-Step Operation	Time for Completion	Other Information
1.	Check safety placards and room security		
2.	Power on CCD Cooler		
3.	Power on CCD Controller		
4.	Open V ++ Imaging Software, open Camera 1	10 min	Performed by research graduate student
5.	Allow CCD to cool to set point temperature: -35 °C and monitor		
6.	Patient arrives and is made comfortable on nuclear imaging bed and dons laser safety eyewear	5 min	Health care personnel may perform this step
7.	Adjust camera height and positioning to patient		Count-down procedure prior to verification of eye protection
8.	Power laser controller and temperature regulator to lase 78-nm diode	30 seconds	
9.	Set laser diode current (50 mA) and temperature (15 °C)		
10.	Power on Marconi; set to 13 dB and 100 MHz		
11.	Dim room lights (if possible)	30 seconds	Laser to be incident on patient
12.	Turn on white light lamp to uniformly illuminate patient in area of interest		

Table 6.2 Continued.

	Step-by-Step Operation	Time for Completion	Other Information	
13.	Adjust laser to uniformly illuminate patient in area of interest (use NIR card if necessary)			
14.	Turn on power supplies to image intensifier (gain should be zero)	30 seconds	Start-up procedure	
15.	Power on PTS frequency synthesizer (RF should be zero)			
16.	Power on ENI Amplifier			
17.	Slowly turn up RF on PTS to 13 dB			
18.	Adjust image intensifier gain via power supplies to desired signal			
19.	Focus camera onto patient with grid for patient to hold on area of interest.			
20.	Allow patient to remove focusing grid.			
21.	Collect five white light images of patient area of interest with lamp on	15 min		Data acquisition steps
22.	Turn off white light lamp			
23.	Attach band-pass and band rejection filters to the lens for fluorescence imaging			
24.	Run FDPM imaging program via V++ and GPIB interface to synthesizers			
25.	Power off Marconi synthesizer	10 seconds	Laser is removed from patient at this step	
26.	Power off laser diode controller and temperature regulator			
27.	Slowly turn down RF power on PTS to zero			
28.	Power off ENI amplifier			
29.	Power off PTS frequency synthesizer	30 seconds	Shut-down procedure	
30.	Power off image intensifier			
31.	Turn on room lights			
32.	Close Camera1 using V++ imaging software			
33.	Power off CCD controller and cooler			

6.4 Statistical Considerations and Data Management

The images acquired from the optical lymphography study will be processed identical to the FFT method described in Section 3. Images of I_{AC} , I_{DC} , and θ will be obtained and evaluated to determine the fluorescing lymph regions. The main factors to be addressed are: (i) the overall ability of the ICCD camera system to track lymphatic

flow to the axillary as well as the internal mammary nodes, (ii) the overall comparison of optical ICCD imaging to the success of nuclear lymphoscintigraphy during SLNM, (iii) the performance of optical fluorescence detection of the sentinel lymph node as a function of depth, the location, and size, and (iv) possible pharmacokinetic analysis of the transit of technetium 99m sulfur colloid in the lymphatics through dynamic optical ICCD images of indocyanine green.

A total of 12 patients will provide a significant population for determining first the ability to detect a fluorescent signal from ICG injected into the breast of a woman. Upon realizing a true fluorescent signal, sentinel lymph node identification rates will be performed by comparing the fluorescent signal (x,y) location to the marked region on the body which identifies the sentinel node location and drainage patterns following lymphoscintigraphy. Additionally, negative predictive values [true negative/ (true negative + false negative)], and positive predictive values [true positive/(true positive + false positive)] from the lymphoscintigraphy and optical images will be assessed following surgery. Lastly, TBR and SNR values (similar to that described in Section 5) will be calculated and compared to the nuclear lymphoscintigraphy values using a paired t-test with $\alpha=0.05$. The images of I_{AC} , I_{DC} , and θ may also be collected for tomographic studies at the Photon Migration Laboratories. 3-D tomographic reconstructions may be conceived for this proposal because reconstructions from data collected using plane-wave area illumination and area detection have been accomplished. At the time of writing this dissertation, the SLNM clinical trial has been terminated at UTMDACC and is scheduled to be completed at Baylor College of Medicine in Houston, TX.

7. SUMMARY AND CONCLUSIONS

A molecular imaging modality which relies on the detection of near-infrared fluorescence emission was designed and studied for clinical translation. The optical imaging system was developed to compliment and compare to the gold-standard molecular imaging modality, namely nuclear imaging. Nuclear medicine dominates clinical imaging of cancer relying on the injection of ionizing radiation into the body for external detection and localization of disease. Nuclear imaging is widely used to identify the spread of breast cancer cells throughout the axillary and sentinel lymph nodes which surround the primary tumor. Lymphoscintigraphy has provided oncologists with a method of mapping lymphatic flow so that surgical resection of positive lymph nodes is possible. Optical imaging with a frequency-domain fluorescence-enhanced ICCD camera system may provide adjuvant detection and become an optimal method for detecting lymph nodes in the breast if it is shown to (1) accurately detect fluorescence signals at clinically relevant depths, (2) optimally compare to nuclear imaging *in vivo* through image quality comparisons, (3) sensitively measure dynamic changes in fluorescence due to blood flow, and (4) safely provide a mobile, maneuverable, and clinically adaptable device for combination with a federally approved drug that remains stable during lymphoscintigraphy procedures on breast cancer patients. Hence, the following conclusions were found as a result of the hypotheses enumerated above.

1. The clinical ICCD camera system sensitively detected I_{AC} and θ , using several different tissue phantoms that were constructed with ranging optical and fluorescent properties. A probability theory was developed to inspect the mean

depth of photon propagation upon a 10-ns change in fluorescent lifetime and 100-MHz change in modulation frequency. The probability was simulated to mimic a clinical situation in which area detection and area illumination in a reflectance geometry is employed. Accordingly, the excitation diffusion equation was modeled in 1-D to simulate propagation of a planar wave. Likewise, a three dimensional model was developed to simulate emission from a spherically emitted fluorescent wave. The probability function was compared to experiments in which the ICCD system accurately detected fluorescent signals up to 9 cm in depth. Significant changes in the mean depth of photon density owing to modulation frequency and fluorescent lifetime were also measured. Upon addition of a target into the phantom to represent the presence of a sentinel lymph node, the ICCD system sensitively detected perturbations in I_{AC} , I_{DC} and θ up to 9 cm for a target located 1.5, 3.5, and 5.5 cm below the detection surface.

2. Upon comparing optical image quality to nuclear image quality *in vivo*, a molecular imaging study found that the ICCD system measures at a significantly greater signal-to-noise than conventional gamma imaging when detecting the binding of a ligand to the membrane receptors of superficial melanoma tumor cells grown in nude mice. Also, the improved image resolution and high photon count enabled optical imaging to clearly delineate the melanoma tumor boundaries relative to the nuclear image, which weakly delineated the tumor boundaries and alternatively detected higher intensity signals from the kidneys and liver. The dual-modality study demonstrated for the first time a direct

nuclear and optical imaging comparison and emphasized the synergy between the two molecular imaging modalities.

3. A continuous wave, point source-point dynamic fluorescence detection measurement system was designed, constructed, and tested for the use in small animal imaging studies. The system includes an avalanche photodiode detector and bifurcated fiber bundle to non-invasively measure fluorescence at a point on the animal's body upon injection of a fluorescent contrast agent. The dynamic measurements more specifically provide a measure of the amount of fluorophore in the blood when fluorescence is detected directly from the vein of a small animal. The system was tested using three healthy nude mice and the results showed that upon injection of a large concentration of indocyanine green, fluorescence can be detected and that the contrast agent accumulation in the blood follows a 2 compartment kinetic model, which describes the clearance of the fluorophore from the blood by the renal system and the tissues.
4. Lastly, the ICCD system was constructed for clinical use on breast cancer patients undergoing lymphoscintigraphy. Appropriate mounting and support structures were designed for ICCD use within a nuclear imaging suite. A clinical protocol was devised, a step-by-step optical imaging procedure was outlined for combining with lymphoscintigraphy, and federal approval was achieved. Moreover, indocyanine green, which is to be injected into patients for the optical lymphography study, was combined with technetium 99m sulfur colloid solutions and found to retain its photochemical properties. Additionally, the

colloid suspension remained stable upon particle sizing with dynamic light scattering measurements, thus supporting the feasibility of combining optical contrast with nuclear contrast for imaging studies.

Overall, the abovementioned studies proved that optical imaging in the clinic can be successful and may provide additional diagnostic imaging information for doctors and clinicians if translated to the bed-side. Based on the favorable results, it is recommended that the optical lymphography study be activated and proceed on breast cancer patients. Future work should also include a statistical analysis on the ability of optical imaging to detect the sentinel lymph node relative to the ability of nuclear imaging.

REFERENCES

1. S. H. Britz-Cunningham and S. J. Adelstein, "Molecular targeting with radionuclides: state of the science," *J. Nucl. Med.* **44**, 1945-1961 (2003).
2. J. P. Houston, A. B. Thompson, M. Gurfinkel and E. M. Sevick-Muraca, "Sensitivity and depth penetration of continuous wave versus frequency-domain photon migration near-infrared fluorescence contrast-enhanced imaging," *Photochem. Photobiol.* **77**, 420-430 (2003).
3. A. Godavarty, A. B. Thompson, R. Roy, M. Gurfinkel, M. J. Eppstein, C. Zhang and E. M. Sevick-Muraca, "Diagnostic imaging of breast cancer using fluorescence-enhanced optical tomography: phantom studies," *J. Biomed. Opt.* **9**, 488-496 (2004).
4. S. Ke, X. Wen, M. Gurfinkel, C. Charnsangavej, S. Wallace, E. M. Sevick-Muraca and C. Li, "Near-infrared optical imaging of epidermal growth factor receptor in breast cancer xenografts," *Cancer Res.* **63**, 7870-7875 (2003).
5. M. Fraile, M. Rull, F. J. Julian, F. Fuste, A. Barnadas, M. Llatjos, E. Castella, J. Gonzales, V. Vallejos, A. Alastreu and M. Broggi, "Sentinel node biopsy as a practical alternative to axillary lymph node dissection in breast cancer patients: an approach to its validity," *Ann. Oncol.* **11**, 701-705 (2000).
6. E. J. Donahue, "Sentinel node imaging and biopsy in breast cancer patients," *Am. J. Surg.* **182**, 426-428 (2001).
7. G. d'Eredita, G. Serio, M. Mele, C. Giardina, M. Martellotta and F. Ferrarese, "Effect of the use of vital dye, lymphoscintigraphy or a combination for axillary lymphatic mapping and sentinel node biopsy in breast cancer," *World J. Surg.* **26**, 588-590 (2002).
8. P. J. Tanis, O. E. Nieweg, R. A. Valdes Olmos and B. B. Kroon, "Anatomy and physiology of lymphatic drainage of the breast from the perspective of sentinel node biopsy," *J. Am. Coll. Surg.* **192**, 399-409 (2001).
9. H. S. Cody, "Clinical aspects of sentinel node biopsy," *Breast Cancer Res.* **3**, 104-108 (2001).
10. H. S. Cody and P. I. Borgen, "State-of-the-art approaches to sentinel node biopsy for breast cancer: study design, patient selection technique, and quality control at Memorial Sloan-Kettering Cancer Center," *Surg. Oncol.* **8**, 85-91 (1999).

11. K. Sugi, Y. Kaneda, M. Sudoh, H. Sakano and K. Hamano, "Effect of radioisotope sentinel node mapping in patients with cT1 N0 M0 lung cancer," *J. Thoracic Cardiovascular Surg.* **126**, 568-573 (2003).
12. T. Nakagawa, Y. Minamiya, Y. Katayose, H. Saito, K. Taguchi, H. Imano, H. Watanabe, K. Enomoto, M. Sageshima, T. Ueda and J. Ogawa, "A novel method for sentinel lymph node mapping using magnetite in patients with non-small cell lung cancer," *J. Thoracic Cardiovascular Surg.* **126**, 563-567 (2003).
13. H. Kato, T. Miyazaki, M. Nakajima, J. Takita, M. Sohda, Y. Fukai, N. Masuda, M. Fukuchi, R. Manda, H. Ojima, K. Tsukada, T. Asao, H. Kuwano, N. Oriuchi and K. Endo, "Sentinel lymph nodes with technetium-99m colloidal rhenium sulfide in patients with esophageal carcinoma," *Cancer Res.* **98**, 932-939 (2003).
14. T. Belhocine, G. Pierard, M. DeLabrassinne, T. Layaye and P. Rigo, "Staging of regional nodes in AJCC stage I and II melanoma: 18FDG PET imaging versus sentinel node detection," *Oncologist* **7**, 271-278 (2002).
15. J. Mulsow, D. C. Winter, J. C. O'Keane and P. R. O'Connell, "Sentinel lymph node mapping in colorectal cancer," *Br. J. Surg.* **90**, 659-667 (2003).
16. E. Pelosi, V. Arena, B. Baudino, M. Bello, M. Giusti, T. Gargiulo, D. Palladin and G. Bisi, "Pre-operative lymphatic mapping and intra-operative sentinel lymph node detection in early stage endometrial cancer," *Nucl. Med. Commun.* **24**, 971-975 (2003).
17. S. Stoeckli, M. Pfaltz, H. Steinert and S. Schmid, "Sentinel lymph node biopsy in thyroid tumors: a pilot study," *Eur. Arch. Otorhinolaryngol.* **260**, 364-368 (2003).
18. G. Y. Meyer-Rochow, R. C. Martin and C. R. Harman, "Sentinel node biopsy in breast cancer: validation study and comparison of blue dye alone with triple modality localization," *ANZ J. Surg.* **73**, 815-818 (2003).
19. F. D. Rahusen, R. Pijpers, P. J. Van Diest, R. P. Bleichrodt, H. Torrenge and S. Meijer, "The implementation of the sentinel node biopsy as a routine procedure for patients with breast cancer," *Surgery* **128**, 6-12 (2000).
20. A. Goyal, R. G. Newcombe, R. E. Mansel, U. Chetty, P. Ell, L. Fallowfield, M. Kissin and M. Sibbering, "Role of routine preoperative lymphoscintigraphy in sentinel node biopsy for breast cancer," *Eur. J. Cancer* **41**, 238-243 (2005).
21. R. L. Birdwell, K. L. Smith, B. J. Betts, D. M. Ikeda, H. W. Strauss and S. S. Jeffrey, "Breast cancer: variables affecting sentinel lymph node visualization at preoperative lymphoscintigraphy," *Radiology* **220**, 47-53 (2001).

22. W. E. Burak, Jr., M. J. Walker, L. D. Yee, J. A. Kim, S. Saha, G. Hinkle, J. O. Olsen, R. Pozderac and W. B. Farrar, "Routine preoperative lymphoscintigraphy is not necessary prior to sentinel node biopsy for breast cancer," *Am. J. Surg.* **177**, 445-449 (1999).
23. C. T. Wu, E. T. Morita, P. A. Treseler, L. J. Esserman, E. S. Hwang, H. M. Kuerer, C. L. Santos and S. P. Leong, "Failure to harvest sentinel lymph nodes identified by preoperative lymphoscintigraphy in breast cancer patients," *Breast J.* **9**, 86-90 (2003).
24. M. S. Zinmeister, "Lymphoscintigraphy: current techniques and indications," *Appl. Radiol.* **26**, 32-39 (1997).
25. S. Saha, W. B. Farrar, M. J. Walker, L. D. Yee, J. A. Kim, J. Masic, J. Olsen, G. Hinkle, R. V. Pozderac, and W. E. Burak, "Utility of lymphoscintigraphy for lymphatic mapping in breast cancer: a prospective study," *Curr. Surg.* **56**, 62-66 (1999).
26. P. J. Borgstein, R. Pijpers, E. F. Comans, P. J. van Diest, R. P. Boom, and S. Meijer, "Sentinel lymph node biopsy in breast cancer: guidelines and pitfalls of lymphoscintigraphy and gama probe detection," *J. Am. Coll. Surg.* **186**, 275-282 (1998).
27. P. I. Haigh, N. M. Hansen, A. E. Giuliano, G. K. Edwards, W. Ye and E. C. Glass, "Factors affecting sentinel node localization during preoperative breast lymphoscintigraphy," *J. Nucl. Med.* **41**, 1682-1688 (2000).
28. K. A. Kern and R. J. Rosenberg, "Preoperative lymphoscintigraphy during lymphatic mapping for breast cancer: improved sentinel node imaging using subareolar injection of technetium 99m sulfur colloid," *J. Am. College Surg.* **191**, 479-489 (2000).
29. K. M. McMasters, S. L. Wong, T. M. Tuttle, D. J. Carlson, C. M. Brown, R. Dirk Noyes, R. L. Glaser, D. J. Vennekotter, P. S. Turk, P. S. Tate, A. Sardi and M. J. Edwards, "Preoperative lymphoscintigraphy for breast cancer does not improve the ability to identify axillary sentinel lymph nodes," *Ann. Surg.* **231**, 724-731 (2000).
30. A. Mudun, I. Aslay, M. Aygen, M. Muslumanoglu, Y. Bozfakioglu and S. Cantez, "Can preoperative lymphoscintigraphy be used as a guide in treatment planning of breast cancer?," *Clin. Nucl. Med.* **26**, 405-411 (2001).

31. M. Pandey, S. V. Deo and R. Maharajan, "Fallacies of preoperative lymphoscintigraphy in detecting sentinel node in breast cancer," *World J. Surg. Oncol.* **3**, 31-45 (2005).
32. E. Pelosi, A. Ala, M. Bello, A. Douroukas, G. Migliaretti, E. Berardengo, T. Varetto, R. Bussone and G. Bisi, "Impact of axillary nodal metastases on lymphatic mapping and sentinel lymph node identification rate in patients with early stage breast cancer," *Eur. J. Nucl. Med. Mol. Imaging* **32**, 937-942 (2005).
33. D. C. Lineham, A. D. K. Hill, K. N. Tran, H. Yeung, S. D. J. Yeh, P. I. Borgen, and H. S. Cody III, "Sentinel lymph node biopsy in breast cancer: unfiltered radioisotope is superior to filtered," *J. Am. Coll. Surg.* **188**, 377-381 (1999).
34. S. Mirzaei, M. Rodrigues, B. Hoffmann, P. Knoll, M. Riegler-Keil, W. Kreuzer, H. Salzer, H. Kohn, A. Polyak and G. A. Janoki, "Sentinel lymph node detection with large human serum albumin colloid particles in breast cancer," *Eur. J. Nucl. Med. Mol. Imaging* **30**, 874-878 (2003).
35. L. L. Lawson, M. Sandler, W. Martin, R. D. Beauchamp and M. C. Kelley, "Preoperative lymphoscintigraphy and internal mammary sentinel lymph node biopsy do not enhance the accuracy of lymphatic mapping for breast cancer," *Am. Surg.* **70**, 1050-1055; discussion 1055-1056 (2004).
36. K. Suga, Y. Yuan, N. Ogasawara, M. Okada and N. Matsunaga, "Visualization of normal and interrupted lymphatic drainage in dog legs with interstitial MR lymphography using an extracellular MR contrast agent, gadopentetate dimeglumine," *Invest. Radiol.* **38**, 349-357 (2003).
37. H. Kobayashi, S. Kawamoto, R. A. Star, T. A. Waldmann, Y. Tagaya and M. W. Brechbiel, "Micro-magnetic resonance lymphangiography in mice using a novel dendrimer-based magnetic resonance imaging contrast agent," *Cancer Res.* **63**, 271-276 (2003).
38. A. Dietrich, M. Wuttke, F. Walter, I. DeLeon, R. Kloeppe and M. Schoenfelder, "Indirect lymph node lymphangiography using an iodine-based contrast medium and projection radiography following submucosal injection in a rabbit model," *Langenbecks Arch. Surg.* **387**, 315-319 (2002).
39. K. Suga, N. Ogasawara, M. Okada and N. Matsunaga, "Interstitial CT lymphography-guided localization of breast sentinel lymph node: preliminary results," *Surgery* **133**, 170-179 (2002).

40. D. Patel, P. Dayton, J. Gut, E. Wisner and K. W. Ferrara, "Optical and acoustical interrogation of submicron contrast agents," *IEEE Trans. Ultrason. Ferroelectr. Freq. Control* **49**, 1641-1651 (2002).
41. S. Gretschel, K. T. Moesta, M. Hunerbein, T. Lange, B. Gebauer, C. Stroszczinski, A. Bembenek and P. M. Schlag, "New concepts of staging in gastrointestinal tumors as a basis of diagnosis and multimodal therapy," *Onkologie* **27**, 23-30 (2004).
42. M. Moreto, "Diagnosis of esophagogastric tumors," *Endoscopy* **37**, 26-32 (2005).
43. H. Nimura, N. Narimiya, N. Mitsumori, Y. Yamazaki, K. Yanaga and M. Urashima, "Infrared ray electronic endoscopy combined with indocyanine green injection for detection of sentinel nodes of patients with gastric cancer," *Br. J. Surg.* **91**, 575-579 (2004).
44. T. Ikeda, H. Jinno, H. Fujii and M. Kitajima, "Recent development of sentinel lymph node biopsy for breast cancer in Japan," *Asian J. Surg.* **27**, 275-278 (2004).
45. N. Ito, M. Fukuta, T. Tokushima, K. Nakai and S. Ohgi, "Sentinel node navigation surgery using indocyanine green in patients with lung cancer," *Surg. Today* **34**, 581-585 (2004).
46. A. J. Leu, S. B. Gretener, S. Enderlin, P. Bruhlmann, B. A. Michel, O. Kowal-Bielecka, U. Hoffmann and U. K. Franzeck, "Lymphatic microangiopathy of the skin in systemic sclerosis," *Rheumatology (Oxford)*. **38**, 221-227 (1999).
47. A. Bollinger, K. Jager, F. Sgier and J. Seglias, "Fluorescence microlymphography," *Circulation* **64**, 1195-1200 (1981).
48. T. P. Padera, A. Kadambi, E. di Tomaso, C. M. Carreira, E. B. Brown, Y. Boucher, N. C. Choi, D. Mathisen, J. Wain, E. J. Mark, L. L. Munn and R. K. Jain, "Lymphatic metastasis in the absence of functional intratumor lymphatics," *Science* **296**, 1883-1886 (2002).
49. M. Jeltsch, A. Kaipainen, V. Joukov, X. Meng, M. Lakso, H. Rauvala, M. Swartz, D. Fukumura, R. K. Jain and K. Alitalo, "Hyperplasia of lymphatic vessels in VEGF-C transgenic mice," *Science* **276**, 1423-1425 (1997).
50. A. J. Leu, D. A. Berk, A. Lymboussaki, K. Alitalo and R. K. Jain, "Absence of functional lymphatics within a murine sarcoma: a molecular and functional evaluation," *Cancer Res.* **60**, 4324-4327 (2000).

51. K. T. Moesta, B. Ebert, T. Handke, H. Rinneberg and P. M. Schlag, "Fluorescence as a concept in colorectal lymph node diagnosis," *Recent Results Cancer Res.* **157**, 293-304 (2000).
52. J. S. Reynolds, T. L. Troy, R. H. Mayer, A. B. Thompson, D. J. Waters, K. K. Cornell, P. W. Snyder and E. M. Sevick-Muraca, "Imaging of spontaneous canine mammary tumors using fluorescent contrast agents," *Photochem. Photobiol.* **70**, 87-94 (1999).
53. M. Gurfinkel, A. B. Thompson, W. Ralston, T. L. Troy, A. L. Moore, T. A. Moore, J. D. Gust, D. Tatman, J. S. Reynolds, B. Muggenburg, K. Nikula, R. Pandey, R. H. Mayer, D. J. Hawrysz and E. M. Sevick-Muraca, "Pharmacokinetics of ICG and HPPH-car for the detection of normal and tumor tissue using fluorescence, near-infrared reflectance imaging: a case study," *Photochem. Photobiol.* **72**, 94-102 (2000).
54. E. G. Soltesz, S. Kim, R. G. Laurence, A. M. DeGrand, C. P. Parungo, D. M. Dor, L. H. Cohn, M. G. Bawendi, J. V. Frangioni and T. Mihaljevic, "Intraoperative sentinel lymph node mapping of the lung using near-infrared fluorescent quantum dots," *Ann. Thorac. Surg.* **79**, 269-277; discussion 269-277 (2005).
55. C. P. Parungo, Y. L. Colson, S. W. Kim, S. Kim, L. H. Cohn, M. G. Bawendi and J. V. Frangioni, "Sentinel lymph node mapping of the pleural space," *Chest* **127**, 1799-1804 (2005).
56. C. P. Parungo, S. Ohnishi, A. M. De Grand, R. G. Laurence, E. G. Soltesz, Y. L. Colson, P. M. Kang, T. Mihaljevic, L. H. Cohn and J. V. Frangioni, "In vivo optical imaging of pleural space drainage to lymph nodes of prognostic significance," *Ann. Surg. Oncol.* **11**, 1085-1092 (2004).
57. S. Kim, Y. T. Lim, E. G. Soltesz, A. M. D. Grand, J. Lee, A. Nakayama, J. A. Parker, T. Mihaljevic, R. G. Laurence, D. M. Dor, L. H. Cohn, M. G. Bawendi and J. V. Frangioni, "Near-infrared fluorescent type II quantum dots for sentinel lymph node mapping," *Nat. Biotechnol.* **22**, 93- (2004).
58. A. M. De Grand and J. V. Frangioni, "An operational near-infrared fluorescence imaging system prototype for large animal surgery," *Technol. Cancer Res. Treat.* **2**, 553-562 (2003).
59. L. Josephson, U. Mahmood, P. Wunderbaldinger, Y. Tang and R. Weissleder, "Pan and sentinel lymph node visualization using a near-infrared fluorescent probe," *Mol. Imaging* **2**, 18-23 (2003).

60. H. W. Lim and N. A. Soter, *Clinical Photomedicine*, Marcel Dekker, New York (1993).
61. M. A. Franceschini, K. T. Moesta, S. Fantini, G. Gaida, E. Gratoon, H. Jess, W. W. Mantulin, M. Seeber, P. M. Schlag and M. Kaschke, "Frequency-domain techniques enhance optical mammography: initial clinical results," *Proc. Natl. Acad. Sci. U. S. A.* **94**, 6468-6473 (1997).
62. D. Groesnick, H. Wabnitz, H. H. Rinneberg, K. T. Moesta and P. M. Schlag, "Development of a time-domain optical mammography and first *in vivo* applications," *Appl. Opt.* **38**, 2927-2943 (1999).
63. K. T. Moesta, S. Fantini, H. Jess, S. Totkas, M. A. Franceschini, M. Kaschke and P. M. Schlag, "Contrast features of breast cancer in frequency-domain laser scanning mammography," *J. Biomed. Opt.* **3**, 129-136 (1998).
64. B. J. Tromberg, N. Shah, R. Lanning, A. Cerussi, J. Espinoza, T. Pham, L. Svaasand and J. Butler, "Non-invasive *in vivo* characterization of breast tumors using photon migration spectroscopy," *Neoplasia* **2**, 26-40 (2000).
65. N. Shah, A. Cerussi, C. Eker, J. Espinoza, J. Butler, J. Fishkin, R. Hornung and B. Tromberg, "Noninvasive functional optical spectroscopy of human breast tissue," *Proc. Natl. Acad. Sci. U. S. A.* **98**, 4420-4425 (2001).
66. R. L. van Veen, H. J. Sterenborg, A. W. Marinelli and M. Menke-Pluymers, "Intraoperatively assessed optical properties of malignant and healthy breast tissue used to determine the optimum wavelength of contrast for optical mammography," *J. Biomed. Opt.* **9**, 1129-1136 (2004).
67. E. Heffer, V. Pera, O. Schutz, H. Siebold and S. Fantini, "Near-infrared imaging of the human breast: complementing hemoglobin concentration maps with oxygenation images," *J. Biomed. Opt.* **9**, 1152-1160 (2004).
68. L. Spinelli, A. Torricelli, A. Pifferi, P. Taroni, G. M. Danesini and R. Cubeddu, "Bulk optical properties and tissue components in the female breast from multiwavelength time-resolved optical mammography," *J. Biomed. Opt.* **9**, 1137-1142 (2004).
69. A. Pifferi, J. Swartling, E. Chikoidze, A. Torricelli, P. Taroni, A. Bassi, S. Andersson-Engels and R. Cubeddu, "Spectroscopic time-resolved diffuse reflectance and transmittance measurements of the female breast at different interfiber distances," *J. Biomed. Opt.* **9**, 1143-1151 (2004).

70. B. W. Pogue, S. P. Poplack, T. O. McBride, W. A. Wells, S. O. K, U. L. Osterberg and K. D. Paulsen, "Quantitative hemoglobin tomography with diffuse near-infrared spectroscopy: pilot results in the breast," *Radiology* **218**, 261-266 (2001).
71. S. Fantini, S. A. Walker, M. A. Franceschini, M. Kaschke, P. M. Schlag and K. T. Moesta, "Assessment of the size, position, and optical properties of breast tumors *in vivo* by noninvasive optical methods," *Appl. Opt.* **37**, 1982-1989 (1998).
72. J. B. Fishkin, O. Coquoz, E. R. Anderson, M. Brenner and B. J. Tromberg, "Frequency-domain photon migration measurements of normal and malignant tissue optical properties in a human subject," *Appl. Opt.* **36**, 10-20 (1997).
73. T. O. McBride, Brian Pogue, Steven Poplack, Sandra Soho, Wendy A. Wells, Shudong Jiang, Ulf L. Osterberg, Keith D. Paulsen, "Multispectral near-infrared tomography: a case study in compensating for water and lipid content in hemoglobin imaging of the breast," *J. Biomed. Opt.* **7**, 72-79 (2002).
74. V. Ntziachristos, A. G. Yodh, M. Schnall and B. Chance, "Concurrent MRI and diffuse optical tomography of breast after indocyanine green enhancement," *Proc. Natl. Acad. Sci. U. S. A.* **97**, 2767-2772 (2000).
75. S. Srinivasan, B. W. Pogue, H. Dehghani, S. Jiang, X. Song and K. D. Paulsen, "Improved quantification of small objects in near-infrared diffuse optical tomography," *J. Biomed. Opt.* **9**, 1161-1171 (2004).
76. E. M. Sevick-Muraca, G. Lopez, J. S. Reynolds, T. L. Troy and C. L. Hutchinson, "Fluorescence and absorption contrast mechanisms for biomedical optical imaging using frequency-domain techniques," *Photochem. Photobiol.* **66**, 55-64 (1997).
77. X. D. Li, B. Chance and A. G. Yodh, "Fluorescence heterogeneities in turbid media, limits for detection, characterization, and comparison with absorption," *Appl. Opt.* **37**, 6833-6843 (1998).
78. A. Godavarty, E. M. Sevick-Muraca and M. J. Eppstein, "Three-dimensional fluorescence lifetime tomography," *Med. Phys.* in press (2005).
79. J. R. Lakowicz, *Principles of Fluorescence Spectroscopy*, Kluwer Academic/Plenum Publishers, New York (1999).
80. D. J. Hawyrasz, M. J. Eppstein, J. Lee and E. M. Sevick-Muraca, "Error consideration in contrast-enhanced three-dimensional optical tomography," *Opt. Lett.* **26**, 704-706 (2001).

81. R. Roy, A. B. Thompson, A. Godavarty and E. M. Sevick-Muraca, "Tomographic fluorescence imaging in tissue phantoms: a novel reconstruction algorithm and imaging geometry," *IEEE Trans. Med. Imag.* Submitted (2004).
82. A. B. Thompson, D. J. Hawrysz and E. M. Sevick-Muraca, "Near-infrared fluorescence contrast-enhanced imaging with area illumination and area detection: the forward imaging problem," *Appl. Opt.* **42**, 4125-4136 (2003).
83. J. P. Culver, R. Choe, M. J. Holboke, L. Zubkov, T. Durduran, A. Slemp, V. Ntziachristos, B. Chance and A. G. Yodh, "Three-dimensional diffuse optical tomography in the parallel plane transmission geometry: evaluation of a hybrid frequency domain/ continuous wave clinical system for breast imaging," *Med. Phys.* **30**, 235-247 (2003).
84. R. Biolo, G. Jori, J. C. Kennedy, P. Nadeau, R. Potteir, E. Reddi and G. Weagle, "A comparison of fluorescence methods used in the pharmacokinetic studies of Zn(II) phthalocyanine in mice," *Photochem. Photobiol.* **53**, 113-118 (1991).
85. A. Pelegrin, S. Folli, F. Buchegger, J.-P. Mach, G. Wagnieres and H. v. d. Bergh, "Antibody-fluorescein conjugates for photoimmunodiagnosis of human colon carcinoma in nude mice," *Cancer* **67**, 2529-2537 (1991).
86. R. C. Straight, R. E. Benner, R. W. McClane, P. M. N. Y. Go, G. Yoon and J. A. Dixon, "Application of charge-coupled device technology for measurement of laser light and fluorescence distribution in tumors for photodynamic therapy," *Photochem. Photobiol.* **53**, 787-796 (1991).
87. S. Folli, G. Wagnieres, A. Pelegrin, J.-M. Calmes, D. Braichotte, F. Buchegger, Y. Chalandon, N. Hardman, C. Heusser, J.-C. Givel, G. Chapuis, A. Chatelain, H. V. d. Bergh and J.-P. Mach, "Immunophotodiagnosis of colon carcinomas in patients injected with fluoresceinated chimeric antibodies against carcinoembryonic antigen," *Proc. Natl. Acad. Sci. U. S. A.* **89**, 7973-7977 (1992).
88. R. Cubeddu, G. Canti, P. Taroni and G. Valentini, "Time-gated fluorescence imaging for the diagnosis of tumors in a murine model," *Photochem. Photobiol.* **57**, 480-485 (1993).
89. R. Cubeddu, G. Canti, A. Pifferi, P. Taroni and G. Valentini, "Fluorescence lifetime imaging of experimental tumors in hematoporphyrin derivative-sensitized mice," *Photochem. Photobiol.* **66**, 229-236 (1997).

90. M. Kohl, U. Sukowski, B. Ebert and J. Neukammer, "Imaging of superficially growing tumors by delayed observation of laser-induced fluorescence," *Proc. SPIE* **1881**, 206-221 (1993).
91. S. Folli, P. Westermann, D. Braichotte, A. Pelegrin, G. Wagnieres, H. v. d. Bergh and J. P. Mach, "Antibody-indocyanin conjugates for immunophotodetection of human squamous cell carcinoma in nude mice," *Cancer Res.* **54**, 2643-2649 (1994).
92. M. M. Haglund, D. W. Hochman, A. M. Spence and M. S. Berger, "Enhanced optical imaging of rat gliomas and tumor margins," *Neurosurgery* **35**, 930-939 (1994).
93. S. Mordon, J. M. Devoisselle and V. Maunoury, "In vivo pH measurement and imaging of tumor tissue using a pH-sensitive fluorescent probe (5,6-carboxyfluorescein): instrumental and experimental studies," *Photochem. Photobiol.* **60**, 274-279 (1994).
94. B. Ballou, G. W. Fisher, A. S. Waggoner, D. L. Farkas, J. M. Reiland, R. Jaffe, R. B. Mujumdar, S. R. Mujumdar and T. R. Hakala, "Tumor labeling *in vivo* using cyanine-conjugated monoclonal antibodies," *Cancer Immunol. Immunother.* **41**, 257-263 (1995).
95. J. M. Devoisselle, S. Soulie, S. R. Mordon, G. Mestres, T. M. D. Desmettre and H. Maillols, "Effect of indocyanine green formulation on blood clearance and *in vivo* fluorescence kinetic profile of skin.," *Proc. SPIE* **2627**, 100-108 (1995).
96. I. Rokahr, S. Andersson-Engels, S. Svanberg, M.-A. D'Hallewin, L. Baert, I. Wang and K. Svangerg, "Optical detection of human urinary bladder carcinoma utilising tissue autofluorescence and protoporphyrin IX-induced fluorescence following low-dose ALA instillation," *Proc. SPIE* **2627**, 2-12 (1995).
97. M. M. Haglund, M. S. Berger and D. W. Hochman, "Enhanced optical imaging of human gliomas and tumor margins," *Neurosurgery* **38**, 308-316 (1996).
98. K. Sakatani, M. Kashiwasake-Jibu, Y. Taka, S. Wang, H. Zuo, K. Yamamoto and K. Shimizu, "Noninvasive optical imaging of the subarachnoid space and cerebrospinal fluid pathways based on near-infrared fluorescence," *J. Neurosurg.* **87**, 738-745 (1997).
99. D. Neri, B. Carnemolla, A. Nissim, A. Leprini, G. Querze, E. Balza, A. Pini, L. Tarli, C. Halin, P. Neri, L. Zardi and G. Winter, "Targeting by affinity-matured recombinant antibody fragments of an angiogenesis-associated fibronectin isoform," *Nature Biotechnology* **15**, 1271-1275 (1997).

100. B. Ballou, G. Fisher, J.-S. Deng, T. R. Hakala, M. Srivastava and D. L. Farkas, "Fluorochrome-labeled antibodies *in vivo*: assessment of tumor imaging using Cy3, Cy5, Cy5.5, and Cy7," *Cancer Detect. Prev.* **22**, 251-257 (1998).
101. C. Eker, S. Montan., E. Jaramillo, K. Koizumi, C. Rubio, S. Andersson-Engels, K. Svanberg, S. Svanberg and P. Slezak, "Clinical spectral characterization of colonic mucosal lesions using autofluorescence and d aminolevulinic acid sensitizations," *Gut* **44**, 511-518 (1999).
102. A. Becker, K. Licha, M. Kresse, B. Riefke, U. Sukowski, B. Ebert, H. Rinneberg and W. Semmler, "Transferrin-mediated tumor delivery of contrast media for optical imaging and magnetic resonance imaging," *Proc. SPIE* **3600**, 142-150 (1999).
103. R. Weissleder, C.-H. Tung, U. Mahmood and A. Bogdanov, " *In vivo* imaging of tumors with protease-activated near-infrared fluorescent probes," *Nat. Biotechnol.* **17**, 375-378 (1999).
104. U. Mahmood, C.-H. Tung, A. Bogdanov and R. Weissleder, "Near-infrared optical imaging of protease activity for tumor detection," *Radiology* **21**, 866-870 (1999).
105. C.-H. Tung, S. Bredow, U. Mahmood and R. Weissleder, "Preparation of a cathepsin D sensitive near-infrared fluorescence probe for imaging," *Bioconjug. Chem.* **10**, 892-896 (1999).
106. A. Becker, "Macromolecular contrast agents for optical imaging of tumors: comparison of indotricarboyanine-labeled human serum albumin and transferrin," *Photochem. Photobiol.* **72**, 234-241 (2000).
107. K. Licha, B. Riefke, V. Ntziachristos, A. Becker, B. Chance and W. Semmler, "Hydrophilic cyanine dyes as contrast agents for near-infrared tumor imaging: synthesis, photophysical properties and spectroscopic *in vivo* characterization," *Photochem. Photobiol.* **72**, 392-398 (2000).
108. M. Yang, E. Baranov, F. Sun, X. Li, L. Li, S. Hasegawa, M. Bouvet, M. Al-Tuwaijri, T. Chishima, H. Shimada, A. Moossa, S. Penman and R. Hoffman, " Whole-body optical imaging of green fluorescent protein-expressing tumors and metastases," *Proc. Natl. Acad. Sci. U. S. A.* **97**, 1206-1211 (2000).
109. R. Cubeddu, A. Pifferi, P. Taroni, A. Torricelli, G. Valentini, D. Comelli, C. D'Andrea, V. Angelini and G. Canti, "Fluorescence imaging during photodynamic therapy of experimental tumors in mice sensitized with

- disulfonated aluminum phthalocyanine," *Photochem. Photobiol.* **72**, 690-695 (2000).
110. J. E. Bugaj, S. Achilefu, R. B. Dorshow and R. Rajagopalan, "Novel fluorescent contrast agents for optical imaging of *in vivo* tumors based on a receptor-targeted dye-peptide conjugate platform," *J. Biomed. Opt.* **6**, 122-133 (2001).
 111. S. Achilefu, R. B. Dorshow, J. E. Bugaj and R. Rajagopalan, "Novel receptor-targeted fluorescent contrast agents for *in vivo* tumor imaging," *Invest. Radiol.* **35**, 479-485 (2000).
 112. S. Achilefu, J. E. Bugaj, R. B. Dorshow, H. N. Jimenez, R. Rajagopalan, R. R. Wilhelm, E. G. Webb, J. L. Erion and P. Brouwer, "Site-specific tumor targeted fluorescent contrast agents," *Proc. SPIE* **4156**, 69-78 (2001).
 113. A. Becker, C. Hessenius, S. Bhargava, C. Grotzinger, K. Licha, J. Schneider-Mergener, B. Wiedenmann and W. Semmler, "Cyanine dye labeled vasoactive intestinal peptide and somatostatin analog for optical detection of gastroenteropancreatic tumors," *Ann. N. Y. Acad. Sci.* **921**, 275-278 (2000).
 114. A. Becker, C. Hessenius, K. Licha, B. Ebert, U. Sukowski, W. Semmler, B. Wiedenmann and C. Grotzinger, "Receptor-targeted optical imaging of tumors with near-infrared fluorescent ligands," *Nat. Biotechnol.* **19**, 327-331 (2001).
 115. K. Licha, C. Hessenius, A. Becker, P. Henklein, M. Bauer, S. Wisniewski, B. Wiedenmann and W. Semmler, "Synthesis, characterization, and biological properties of cyanine-labeled somatostatin analogues as receptor-targeted fluorescent probes," *Bioconjug. Chem.* **12**, 44-50 (2001).
 116. C. Balas, "A novel optical imaging method for the early detection, quantitative grading, and mapping of cancerous and precancerous lesions of cervix," *IEEE Trans. Biomed. Eng.* **48**, 96-104 (2001).
 117. C. Bremer, C. Tung and R. Weissleder, "*In vivo* molecular target assessment of matrix metalloproteinase inhibition," *Nature Medicine* **7**, 743-748 (2001).
 118. B. Ebert, U. Sukowski, D. Grosenick, H. Wabnitz, K. T. Moesta, K. Licha, A. Becker, W. Semmler, P. M. Schlag and H. Rinneberg, "Near-infrared fluorescent dyes for enhanced contrast in optical mammography: phantom experiments," *J. Biomed. Opt.* **6**, 134-140 (2001).
 119. J. Finlay, D. L. Conover, E. L. Hull and T. H. Foster, "Porphyrin bleaching and PDT-induced spectral changes are irradiance dependent in ALA-sensitized normal rat skin *in vivo*," *Photochem. Photobiol.* **73**, 54-63 (2001).

120. B. W. Rice, M. D. Cable and M. B. Nelson, "*In vivo* imaging of light-emitting probes," *J. Biomed. Opt.* **6**, 432-440 (2001).
121. N. Soukos, M. R. Hamblin, S. Keel, R. L. Fabian, T. F. Deutsch and T. Hasan, "Epidermal growth factor receptor-targeted immunophotodiagnosis and photoimmunotherapy of oral precancer *in vivo*," *Cancer Res.* **91**, 4490-4496 (2001).
122. M. Yang, E. Baranov, X. M. Li, J. W. Wang, P. Jiang, L. Li, A. R. Moossa, S. Penman and R. M. Hoffman, "Whole-body and intravital optical imaging of angiogenesis in orthotopically implanted tumors," *Proc. Natl. Acad. Sci. U. S. A.* **98**, 2616-2621 (2001).
123. T. Boehm, A. Hochmuth, A. Malich, J. R. Reichenbach, M. Fleck and W. A. Kaiser, "Contrast-enhanced near-infrared laser mammography with a prototype breast scanner: feasibility study with tissue phantoms and preliminary results of imaging experimental tumors," *Invest. Radiol.* **36**, 573-581 (2001).
124. A. Zaheer, R. E. Lenkinski, A. Mahmood, A. G. Jones, L. C. Cantley and J. V. Frangioni, "*In vivo* near-infrared fluorescence imaging of osteoblastic activity," *Nat. Biotechnol.* **19**, 1148-1154 (2001).
125. J. Chen, C. H. Tung, U. Mahmood, V. Ntziachristos, R. Gyurko, M. C. Fishman, P. L. Huang and R. Weissleder, "*In vivo* imaging of proteolytic activity in atherosclerosis," *Circulation* **105**, 2766-2771 (2002).
126. A. Nakayama, F. del Monte, R. J. Hajjar and J. V. Frangioni, "Functional near-infrared fluorescence imaging for cardiac surgery and targeted gene therapy," *Mol. Imaging* **1**, 365-377 (2002).
127. V. Ntziachristos, C. Bremer, E. Graves, J. Ripoll and R. Weissleder, "*In vivo* tomographic imaging of near-infrared fluorescent probes," *Mol. Imaging* **1**, 82-88 (2002).
128. C. Bremer, C. H. Tung, A. Bogdanov, Jr. and R. Weissleder, "Imaging of differential protease expression in breast cancers for detection of aggressive tumor phenotypes," *Radiology* **222**, 814-818 (2002).
129. M. Solonenko, R. Cheung, T. M. Busch, A. Kachur, G. M. Griffin, T. Vulcan, T. C. Zhu, H. W. Wang, S. M. Hahn and A. G. Yodh, "*In vivo* reflectance measurement of optical properties, blood oxygenation and motexafin lutetium uptake in canine large bowels, kidneys and prostates," *Phys. Med. Biol.* **47**, 857-873 (2002).

130. S. Ke, X. Wen, M. Gurfinkel, C. Charnsangavej, Z. Fan, S. Wallace, E. M. Sevick-Muraca and C. Li, "Near infrared optical imaging of epidermal growth factor receptor in breast cancer xenografts," *Cancer Research* **63**, (2003).
131. M. Gurfinkel, S. Ke, X. Wen, C. Li and E. M. Sevick-Muraca, "Near-infrared fluorescence optical imaging and tomography," *Dis. Markers* **19**, 107-121 (2003).
132. D. J. Cuccia, F. Bevilacqua, A. J. Durkin, S. Merritt, B. J. Tromberg, G. Gulsen, H. Yu, J. Wang and O. Nalcioglu, "In vivo quantification of optical contrast agent dynamics in rat tumors by use of diffuse optical spectroscopy with magnetic resonance imaging coregistration," *Appl. Opt.* **42**, 2940-2950 (2003).
133. A. Petrovsky, E. Schellenberger, L. Josephson, R. Weissleder and J. Alexei Bogdanov, "Near-infrared fluorescent imaging of tumor apoptosis," *Cancer Res.* **63**, 1936-1942 (2003).
134. E. A. Schellenberger, A. Bogdanov, Jr., A. Petrovsky, V. Ntziachristos, R. Weissleder and L. Josephson, "Optical imaging of apoptosis as a biomarker of tumor response to chemotherapy," *Neoplasia* **5**, 187-192 (2003).
135. I. Gannot, A. Garashi, G. Gannot, V. Chernomordik and A. Gandjbakhche, "In vivo quantitative three-dimensional localization of tumor labeled with exogenous specific fluorescence markers," *Appl. Opt.* **42**, 3073-3080 (2003).
136. K. Sokolov, M. Follen, J. Aaron, I. Pavlova, A. Malpica, R. Lotan and R. Richards-Kortum, "Real-time vital optical imaging of precancer using anti-epidermal growth factor receptor antibodies conjugated to gold nanoparticles," *Cancer Res.* **63**, 1999-2004 (2003).
137. E. E. Graves, J. Ripoll, R. Weissleder and V. Ntziachristos, "A submillimeter resolution fluorescence molecular imaging system for small animal imaging," *Med. Phys.* **30**, 901-911 (2003).
138. X. Intes, J. Ripoll, Y. Chen, S. Nioka, A. G. Yodh and B. Chance, "In vivo continuous-wave optical breast imaging enhanced with Indocyanine Green," *Med. Phys.* **30**, 1039-1047 (2003).
139. J. M. McGreevy, M. J. Cannon and C. B. Grissom, "Minimally invasive lymphatic mapping using fluorescently labeled Vitamin B12," *J. Surg. Res.* **111**, 38-44 (2003).

140. M. D. Kennedy, K. N. Jallad, D. H. Thompson, D. Ben-Amotz and P. S. Low, "Optical imaging of metastatic tumors using a folate-targeted fluorescent probe," *J. Biomed. Opt.* **8**, 636-641 (2003).
141. R. E. Lenkinski, M. Ahmed, A. Zaheer, J. V. Frangioni and S. N. Goldberg, "Near-infrared fluorescence imaging of microcalcification in an animal model of breast cancer," *Acad. Radiol.* **10**, 1159-1164 (2003).
142. W. K. Moon, Y. Lin, T. O'Loughlin, Y. Tang, D. E. Kim, R. Weissleder and C. H. Tung, "Enhanced tumor detection using a folate receptor-targeted near-infrared fluorochrome conjugate," *Bioconjug. Chem.* **14**, 539-545 (2003).
143. W. T. Chen, U. Mahmood, R. Weissleder and C. H. Tung, "Arthritis imaging using a near-infrared fluorescence folate-targeted probe," *Arthritis Res. Ther.* **7**, R310-317 (2005).
144. A. Nakayama, A. C. Bianco, C. Y. Zhang, B. B. Lowell and J. V. Frangioni, "Quantitation of brown adipose tissue perfusion in transgenic mice using near-infrared fluorescence imaging," *Mol. Imaging* **2**, 37-49 (2003).
145. Y. Chen, G. Zheng, Z. H. Zhang, D. Blessington, M. Zhang, H. Li, Q. Liu, L. Zhou, X. Intes, S. Achilefu and B. Chance, "Metabolism-enhanced tumor localization by fluorescence imaging: *in vivo* animal studies," *Opt. Lett.* **28**, 2070-2072 (2003).
146. D. Citrin, A. K. Lee, T. Scott, M. Sproull, C. Menard, P. J. Tofilon and K. Camphausen, "*In vivo* tumor imaging in mice with near-infrared labeled endostatin," *Mol. Cancer Ther.* **3**, 481-488 (2004).
147. D. Citrin, T. Scott, M. Sproull, C. Menard, P. J. Tofilon and K. Camphausen, "*In vivo* tumor imaging using a near-infrared-labeled endostatin molecule," *Int. J. Radiat. Oncol. Biol. Phys.* **58**, 536-541 (2004).
148. C. S. Gondi, S. S. Lakka, N. Yanamandra, W. C. Olivero, D. H. Dinh, M. Gujrati, C. H. Tung, R. Weissleder and J. S. Rao, "Adenovirus-mediated expression of antisense urokinase plasminogen activator receptor and antisense cathepsin B inhibits tumor growth, invasion, and angiogenesis in gliomas," *Cancer Res.* **64**, 4069-4077 (2004).
149. M. F. Kircher, R. Weissleder and L. Josephson, "A dual fluorochrome probe for imaging proteases," *Bioconjug. Chem.* **15**, 242-248 (2004).

150. K. Kelly, H. Alencar, M. Funovics, U. Mahmood and R. Weissleder, "Detection of invasive colon cancer using a novel, targeted, library-derived fluorescent peptide," *Cancer Res.* **64**, 6247-6251 (2004).
151. A. Moore, Z. Medarova, A. Potthast and G. Dai, "*In vivo* targeting of underglycosylated MUC-1 tumor antigen using a multimodal imaging probe," *Cancer Res.* **64**, 1821-1827 (2004).
152. K. Shah, C. H. Tung, C. H. Chang, E. Sloatweg, T. O'Loughlin, X. O. Breakefield and R. Weissleder, "*In vivo* imaging of HIV protease activity in amplicon vector-transduced gliomas," *Cancer Res.* **64**, 273-278 (2004).
153. B. Ballou, B. C. Lagerholm, L. A. Ernst, M. P. Bruchez and A. S. Waggoner, "Noninvasive imaging of quantum dots in mice," *Bioconjug. Chem.* **15**, 79-86 (2004).
154. B. Tigani, H. U. Gremlich, C. Cagnet, S. Zurbruegg, H. K. Quintana and N. Beckmann, "Near-infrared fluorescence imaging and histology confirm anomalous edematous signal distribution detected in the rat lung by MRI after allergen challenge," *J. Magn. Reson. Imaging* **20**, 967-974 (2004).
155. H. Li, Z. Zhang, D. Blessington, D. S. Nelson, R. Zhou, S. Lund-Katz, B. Chance, J. D. Glickson and G. Zheng, "Carbocyanine labeled LDL for optical imaging of tumors," *Acad. Radiol.* **11**, 669-677 (2004).
156. X. Chen, P. S. Conti and R. A. Moats, "*In vivo* near-infrared fluorescence imaging of integrin $\alpha v \beta 3$ in brain tumor xenografts," *Cancer Res.* **64**, 8009-8014 (2004).
157. P. P. Ghoroghchian, P. R. Frail, K. Susumu, D. Blessington, A. K. Brannan, F. S. Bates, B. Chance, D. A. Hammer and M. J. Therien, "Near-infrared-emissive polymersomes: self-assembled soft matter for *in vivo* optical imaging," *Proc. Natl. Acad. Sci. U. S. A.* **102**, 2922-2927 (2005).
158. S. Kwon, S. Ke, J. P. Houston, W. Wang, Q. Wu, C. Li and E. M. Sevick-Muraca, "Imaging dose-dependent pharmacokinetics of an RGD-fluorescent dye conjugate targeted to $\alpha v \beta 3$ receptor expressed in Kaposi's sarcoma," *Mol. Imaging* in press (2005).
159. K. Hwang, J. P. Houston, J. Rassmussen, S. Ke, C. Li and E. M. Sevick-Muraca, "Enhanced fluorescent optical imaging with improved excitation light rejection," *Mol. Imaging* in press (2004).

160. S. Ke, W. Wang, Q. Wu, C. Charnsangavej, J. Houston, D. Chow, E. M. Sevick-Muraca and C. Li, "Dual Optical and Nuclear Imaging of Integrin $\alpha\beta 3$ in Human Melanoma Xenografts Using a Single Imaging Probe," *Eur. J. Nucl. Med. Mol. Imaging* Submitted (2005).
161. S. J. Goldsmith, "Receptor imaging: competitive or complementary to antibody imaging?," *Semin. Nucl. Med.* **27**, 85-93 (1997).
162. M. Gurfinkel, S. Ke, W. Wang, C. Li and E. M. Sevick-Muraca, "Quantifying molecular specificity of $\alpha\beta 3$ integrin-targeted optical contrast agents with dynamic optical imaging," *J. Biomed. Opt.* in press (2005).
163. W. Wang, S. Ke, Q. Wu, C. Charnsangavej, M. Gurfinkel, J. Gelovani, J. L. Abbruzzese, E. M. Sevick-Muraca and C. Li, "Near-Infrared Optical Imaging of Integrin $\alpha v \beta 3$ in Human Tumor Xenografts," *Mol. Imaging* **3**, 1-9 (2004).
164. J. E. Bugaj, S. Achilefu, R. B. Dorshow and R. Rajagopalan, "Bioactive peptide-fluorescent dye conjugates for *in vivo* tumor imaging," *OSA Proc. Series* (2000).
165. S. Achilefu, H. N. Jimenez, R. B. Dorshow, J. E. Bugaj, E. G. Webb, R. R. Wilhelm, R. Rajagopalan, J. Johler and J. L. Erion, "Synthesis, *in vitro* receptor binding, and *in vivo* evaluation of fluorescein and carbocyanine peptide-based optical contrast agents," *J. Med. Chem* **45**, 2003-2015 (2002).
166. H. C. Manning, T. Goebel, R. C. Thompson, R. R. Price, H. Lee and D. J. Bornhop, "Targeted molecular imaging agents for cellular-scale bimodal imaging," *Bioconjug. Chem.* **15**, 1488-1495 (2004).
167. N. Y. Morgan, S. English, W. Chen, V. Chernomordik, A. Russo, P. D. Smith and A. Gandjbakhche, "Real time *in vivo* non-invasive optical imaging using near-infrared fluorescent quantum dots," *Acad. Radiol.* **12**, 313-323 (2005).
168. X. Gao, Y. Cui, R. M. Levenson, L. W. Chung and S. Nie, "*In vivo* cancer targeting and imaging with semiconductor quantum dots," *Nat. Biotechnol.* **22**, 969-976 (2004).
169. M. F. Kircher, U. Mahmood, R. S. King, R. Weissleder and L. Josephson, "A multimodal nanoparticle for preoperative magnetic resonance imaging and intraoperative optical brain tumor delineation," *Cancer Res.* **63**, 8122-8125 (2003).
170. R. Richards-Kortum and E. M. Sevick-Muraca, "Quantitative optical spectroscopy for tissue diagnosis," *Ann. Rev. Phys. Chem.* **47**, 555-606 (1996).

171. A. Gillenwater, R. Jacob and R. Richards-Kortum, "Fluorescence spectroscopy: a technique with potential to improve the early detection of aerodigestive tract neoplasia," *Head Neck* **20**, 556-562 (1998).
172. S. G. Demos, R. Gandour-Edwards, R. Ramsamooj and R. deVere White, "Spectroscopic detection of bladder cancer using near-infrared imaging techniques," *J. Biomed. Opt.* **9**, 767-771 (2004).
173. S. G. Demos, R. Gandour-Edwards, R. Ramsamooj and R. White, "Near-infrared autofluorescence imaging for detection of cancer," *J. Biomed. Opt.* **9**, 587-592 (2004).
174. C. M. John, H. Leffler, B. Kahl-Knutsson, I. Svensson and G. A. Jarvis, "Truncated galectin-3 inhibits tumor growth and metastasis in orthotopic nude mouse model of human breast cancer," *Clin. Cancer Res.* **9**, 2374-2383 (2003).
175. C. S. Mitsiades, N. S. Mitsiades, R. T. Bronson, D. Chauhan, N. Munshi, S. P. Treon, C. A. Maxwell, L. Pilarski, T. Hideshima, R. M. Hoffman and K. C. Anderson, "Fluorescence imaging of multiple myeloma cells in a clinically relevant SCID/NOD *in vivo* model: biologic and clinical implications," *Cancer Res.* **63**, 6689-6696 (2003).
176. M. Bouvet, J. Wang, S. R. Nardin, R. Nassirpour, M. Yang, E. Baranov, P. Jiang, A. R. Moossa and R. M. Hoffman, "Real-time optical imaging of primary tumor growth and multiple metastatic events in a pancreatic cancer orthotopic model," *Cancer Res.* **62**, 1534-1540 (2002).
177. D. W. Burton, J. Geller, M. Yang, P. Jiang, I. Barken, R. H. Hastings, R. M. Hoffman and L. J. Deftos, "Monitoring of skeletal progression of prostate cancer by GFP imaging, X-ray, and serum OPG and PTHrP," *Prostate* **62**, 275-281 (2005).
178. R. G. Blasberg, "In vivo molecular-genetic imaging: multi-modality nuclear and optical combinations," *Nucl. Med. Biol.* **30**, 879-888 (2003).
179. J. C. Wu, I. Y. Chen, G. Sundaresan, J. J. Min, A. De, J. H. Qiao, M. C. Fishbein and S. S. Gambhir, "Molecular imaging of cardiac cell transplantation in living animals using optical bioluminescence and positron emission tomography," *Circulation* **108**, 1302-1305 (2003).
180. P. Ray, A. De, J. J. Min, R. Y. Tsien and S. S. Gambhir, "Imaging tri-fusion multimodality reporter gene expression in living subjects," *Cancer Res.* **64**, 1323-1330 (2004).

181. A. Jacobs, M. Dubrovin, J. Hewett, M. Sena-Esteves, C. W. Tan, M. Slack, M. Sadelain, X. O. Breakefield and J. G. Tjuvajev, "Functional coexpression of HSV-1 thymidine kinase and green fluorescent protein: implications for noninvasive imaging of transgene expression," *Neoplasia* **1**, 154-161 (1999).
182. V. Ponomarev, M. Dubrovin, I. Serganova, T. Beresten, J. Vider, A. Shavrin, L. Ageyeva, J. Balatoni, R. Blasberg and J. G. Tjuvajev, "Cytoplasmically retargeted HSV1-tk/GFP reporter gene mutants for optimization of noninvasive molecular-genetic imaging," *Neoplasia* **5**, 245-254 (2003).
183. J. P. Houston, S. Ke, W. Wang, C. Li and E. M. Sevick, "Quality analysis of *in vivo* NIR fluorescence and conventional gamma images acquired using a dual-labeled tumor targeting probe," *J. Biomed. Opt.* in press (2005).
184. A. Godavarty, M. Eppstein, C. Zhang and E. M. Sevick-Muraca, "Detection of single and multiple targets in tissue phantoms using fluorescence-enhanced optical imaging," *Radiology* in press (2005).
185. J. Reynolds, T. L. Troy, and E. M. Sevick-Muraca, "Multipixel techniques for frequency-domain photon migration imaging," *Biotech. Progress* **13**, 669-680 (1997).
186. A. Joshi and E. M. Sevick-Muraca, "Data acquisition of multi-pixel frequency domain data," *Opt. Lett.* under submission (2003).
187. A. Godavarty, M. J. Eppstein, C. Zhang, S. Theru, A. B. Thompson, M. Gurfinkel and E. M. Sevick-Muraca, "Fluorescence-enhanced optical imaging in large tissue volumes using a gain-modulated ICCD camera," *Phys. Med. Biol.* **48**, 1701-1720 (2003).
188. R. Rajagopalan, P. Uetrecht, J. E. Bugaj, S. A. Achilefu and R. B. Dorshow, "Stabilization of the optical tracer agent indocyanine green using noncovalent interactions," *Photochem. Photobiol.* **71**, 347-350 (2000).
189. S. M. Richter, R. R. Shinde, G. V. Balgi and E. M. Sevick-Muraca, "Particle sizing using frequency domain photon migration," *Part. Part. Syst. Charact.* **15**, 9-5 (1998).
190. Z. Sun, Y. Huang and E. M. Sevick-Muraca, "Precise analysis of frequency domain photon migration measurement for characterization of concentrated colloidal suspensions," *Rev. Sci. Instrum.* **73**, 383-393 (2002).

191. T. Pan, "Application and modeling of near-infrared frequency domain photon migration for monitoring pharmaceutical powder blending operations," *Chemical Engineering* (2005). Texas A&M University, College Station
192. A. H. Gandjbakhche, R. F. Bonner, R. Nossal and G. H. Weiss, "Effects of multiple-passage probabilities on fluorescent signals from biological media," *Appl. Opt.* **36**, 4613-4619 (1997).
193. T. Pan and E. M. Sevick-Muraca, "Volume of pharmaceutical powders probed by frequency-domain photon migration measurements of multiply scattered light," *Anal. Chem.* **74**, 4228-4234 (2002).
194. D. T. Delpy and M. Cope, "Quantification in tissue near-infrared spectroscopy," *Phil. Trans. R. Soc. Lond. B* **352**, 649-659 (1997).
195. E. M. Sevick-Muraca and C. Burch, "Origin of phosphorescence signals reemitted from tissues," *Opt. Lett.* **19**, 1928-1930 (1994).
196. E. M. Sevick, J. K. Frisoli, C. L. Burch and J. R. Lakowicz, "Localization of absorbers in scattering media by use of frequency-domain measurements of time-dependent photon migration," *Appl. Opt.* **33**, 3562-3570 (1994).
197. D. Hattery, V. Chernomordik, M. Loew, I. Gannot and A. Gandjbakhche, "Analytical solutions for time-resolved fluorescence lifetime imaging in a turbid medium such as tissue," *J. Opt. Soc. Am. A.* **18**, 1523-1530 (2001).
198. D. A. Boas, J. P. Culver, J. J. Stott, A. K. Dunn, "Three dimensional Monte Carlo code for photon migration through complex heterogeneous media including the adult human head," *Opt. Exp.* **10**, 159-170 (2002).
199. G. Weiss, H. and J. E. Kiefer, "A numerical study of the statistics of penetration depth of photons re-emitted from irradiated media," *J. Mod. Opt.* **45**, 2327-2337 (1998).
200. G. H. Weiss, R. Nossal and R. F. Bonner, "Statistics of penetration depth of photons re-emitted from irradiated tissue," *J. Mod. Opt.* **36**, 349-359 (1989).
201. J. Wu, Y. Wang, L. Perelman, I. Itzkan, R. R. Dasari and M. S. Feld, "Three-dimensional imaging of objects embedded in turbid media with fluorescence and Raman spectroscopy," *Appl. Opt.* **34**, 3425-3430 (1995).
202. S. T. Flock, M. S. Patterson, B. C. Wildson and D. R. Wyman, "Monte Carlo modeling of light propagation in highly scattering tissues--I: model predictions

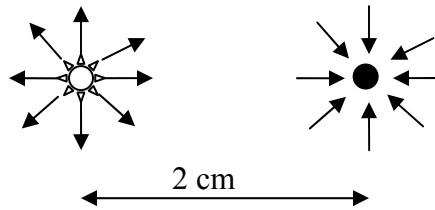
- and comparison with diffusion theory," *IEEE Trans. Biomed. Eng.* **36**, 1162-1168 (1989).
203. S. T. Flock, B. C. Wilson and M. S. Patterson, "Monte Carlo modeling of light propagation in highly scattering tissues--II: comparison with measurements in phantoms," *IEEE Transactions in Biomedical Engineering* **36**, 1169-1173 (1989).
204. A. A. Cox and D. J. Durian, "Spatial sampling by diffuse photons," *Appl. Opt.* **40**, 4228-4235 (2001).
205. A. E. Profio and D. R. Doiron, "Transport of light in tissue in photodynamic therapy," *Photochem. Photobiol.* **46**, 591-599 (1987).
206. D. J. Bicut and G. H. Weiss, "A measure of photon penetration into tissue in diffusion models," *Opt. Commun.* **158**, 213-220 (1998).
207. J. B. Fishkin and E. Gratton, "Propagation of photon-density waves in strongly scattering media containing and absorbing semi-infinite plane bounded by a straight edge," *J. Opt. Soc. Am. A.* **10**, 127-140 (1993).
208. R. C. Haskell, L. O. Svaasand, T.-T. Tsay, T.-C. Feng, M. S. McAdams and B. J. Tromberg, "Boundary conditions for the diffusion equation in radiative transfer," *J. Opt. Soc. Am. A.* **11**, 2727-2741 (1994).
209. X. D. Li, M. A. O'Leary, D. A. Boas, B. Chance and A. G. Yodh, "Fluorescent diffuse photon density waves in homogenous and heterogeneous turbid media: analytical solutions and applications," *Appl. Opt.* **35**, 3746-3758 (1996).
210. A. B. Thompson, "Development of a new optical imaging modality for detection of fluorescence-enhanced disease," *Chemical Engineering* 180 (2002). Texas A&M University, College Station
211. R. Pasqualini, E. Koivunen and E. Ruoslahti, "A peptide isolated from phage display libraries is a structural and functional mimic of an RGD-binding site on integrins," *J. Cell Biol.* **130**, 1189-1196 (1995).
212. R. Pasqualini, E. Koivunen and E. Ruoslahti, "Alpha v integrins as receptors for tumor targeting by circulating ligands," *Nat. Biotechnol.* **15**, 542-546 (1997).
213. E. Petitemerc, S. Stromblad, T. L. von Schalscha, F. Mitjans, J. Piulats, A. M. Montgomery, D. A. Cheresh and P. C. Brooks, "Integrin alpha(v)beta3 promotes M21 melanoma growth in human skin by regulating tumor cell survival," *Cancer Res.* **59**, 2724-2730 (1999).

214. D. A. Cheresh and R. C. Spiro, "Biosynthetic and functional properties of an Arg-Gly-Asp-directed receptor involved in human melanoma cell attachment to vitronectin, fibrinogen, and von Willebrand factor," *J. Biol. Chem.* **262**, 17703-17711 (1987).
215. R. Haubner, F. Bruchertseifer, M. Bock, H. Kessler, M. Schwaiger and H. J. Wester, "Synthesis and biological evaluation of a (99m)Tc-labelled cyclic RGD peptide for imaging the alphavbeta3 expression," *Nuklearmedizin* **43**, 26-32 (2004).
216. R. Haubner, H. J. Wester, W. A. Weber, C. Mang, S. I. Ziegler, S. L. Goodman, R. Senekowitsch-Schmidtke, H. Kessler and M. Schwaiger, "Noninvasive imaging of alpha(v)beta3 integrin expression using 18F-labeled RGD-containing glycopeptide and positron emission tomography," *Cancer Res.* **61**, 1781-1785 (2001).
217. P. C. Brooks, A. M. Montgomery, M. Rosenfeld, R. A. Reisfeld, T. Hu, G. Klier and D. A. Cheresh, "Integrin alpha v beta 3 antagonists promote tumor regression by inducing apoptosis of angiogenic blood vessels," *Cell* **79**, 1157-1164 (1994).
218. R. B. Dorshow, J. E. Bugaj, B. D. Burleigh, J. R. Duncan, M. A. Johnson and W. B. Jones, "Noninvasive fluorescence detection of hepatic and renal function," *J. Biomed. Opt.* **3**, 341-345 (1998).
219. M. Gurfinkel, "Cancer diagnostics using dynamic near-infrared optical imaging and fluorescent contrast agents," *Chemical Engineering* 250 (2003). Texas A&M University, College Station, TX
220. L. Bergqvist, S. E. Strand and B. R. Persson, "Particle sizing and biokinetics of interstitial lymphoscintigraphic agents," *Semin. Nucl. Med.* **13**, 9-19 (1983).
221. C. Tsopelas, "Particle size analysis of (99m)Tc-labeled and unlabeled antimony trisulfide and rhenium sulfide colloids intended for lymphoscintigraphic application," *J. Nucl. Med.* **42**, 460-466 (2001).
222. S. H. Kim, J. Shim, C. K. Kim, J. Machac and B. R. Krynyckyi, "Reverse echelon node and a lymphatic ectasia in the same patient during breast lymphoscintigraphy: the importance of injection and imaging technique," *Br. J. Radiol.* **77**, 1053-1056 (2004).

APPENDIX I

CALCULATION OF ATTENUATED EXCITATION AND EMISSION WAVE

A simple calculation for approximating the fluence at a distance of 2 cm away from an isotropic and modulated point source is based on a homogeneous and infinite solution to the diffusion equation described previously.²⁰⁷



The figure above illustrates the isotropic source (left) and the observation point (right) 2 cm away at which point the fluence, or attenuated modulated excitation light, is detected.

The equations below provide the magnitude of modulated photon density waves for the excitation source, attenuated excitation light and attenuated emission light:

$$S(t) = S_{DC} * (1 + S_{AC} \sin(\omega t))$$

$$F_x(r, t) = S_{DC} \frac{\exp\left(\frac{-r}{\delta}\right)}{4\pi D r} [1 + S_{AC} M \sin(\omega t + P)]$$

$$F_m(r, t) = S_{DC} \frac{\phi}{1 - \omega\tau} \frac{\exp\left(\frac{-r}{\delta}\right)}{4\pi D r} [1 + S_{AC} M \sin(\omega t + P)]$$

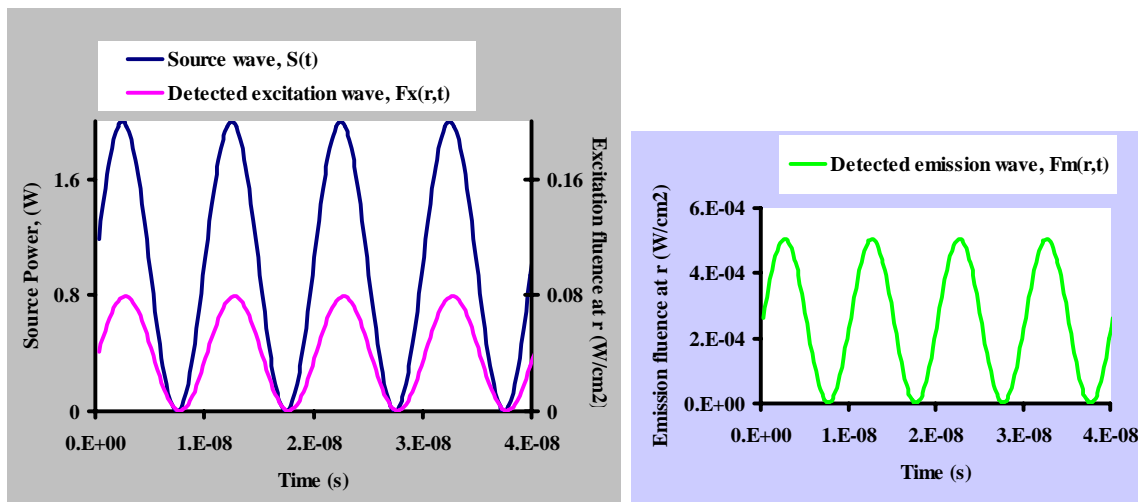
where $S(t)$ [W] is the source wave; $F_x(r, t)$ [W/cm²] is the fluence rate of the attenuated source wave; $F_m(r, t)$ [W/cm²] is the fluence rate of the attenuated fluorescent wave; δ is the diffusion penetration depth [cm]; D [cm] is the diffusion coefficient; r [2 cm] is the distance between the source and observation point; S_{DC} [W] is the steady state isotropic source power; S_{AC} is the modulation source power; P [radians] is the phase lag; M is a

temporary variable representing the modulation; ϕ is the fluorescence quantum yield; and τ is the fluorescence average lifetime.

By creating a time array, t , source array, $S(t)$, and fluence arrays, $F_x(t)$ and $F_m(t)$, one can observe the difference in magnitude between the source wave and detected emission and excitation waves. The emission wave is based on the decay kinetics of indocyanine green previously reported in the literature. The plots below provide the results for S , F_x , and F_m .

The following parameter values were used in the calculation to produce the photon density waves which are plotted in the figures below,

$$\begin{aligned}\mu_a &= 0.1 \text{ cm}^{-1} \\ \mu_s' &= 10 \text{ cm}^{-1} \\ \omega &= 200\pi \text{ MHz} \\ \tau &= 0.56 \text{ ns} \\ r &= 2 \text{ cm}\end{aligned}$$



In the plotted photon density waves above, it is apparent that the source wave, having a total amplitude of 1.0 W, is two orders of magnitude higher than the dampened excitation fluence amplitude, which is equivalent to approximately 0.02 W/cm^2 . The dampened emission fluence amplitude is two orders of magnitude less than the excitation fluence and is equivalent to approximately 0.0002 W/cm^2 .

VITA

JESSICA PEREA HOUSTON

1884 Brillante Lane
Santa Fe, New Mexico 87505

EDUCATION

Texas A&M University, College Station, TX
Ph.D., Chemical Engineering, December 2005

Texas A&M University, College Station, TX
M.S., Chemical Engineering, May 2002

New Mexico State University, Las Cruces, NM
B.S., Chemical Engineering, May 2000

PEER-REVIEWED PUBLICATIONS

J. P. Houston, A. B. Thompson, M. Gurfinkel and E. M. Sevick-Muraca, "Sensitivity and depth penetration of continuous wave versus frequency-domain photon migration near-infrared fluorescence contrast-enhanced imaging," *Photochem. Photobiol.* 77, 420-430 (2003).

J. P. Houston, S. Ke., W. Wang, C. Li, and E. M. Sevick-Muraca, "Quality analysis of *in vivo* NIR fluorescence and conventional gamma images acquired using a dual-labeled tumor-targeting probe," *J. Biomed. Opt.* in press (2005).

K. Hwang, J. P. Houston, J. Rasmussen, S. Ke, C. Li, and E. M. Sevick-Muraca, "Enhanced fluorescent optical imaging with improved excitation light rejection," 2004, *Molecular Imaging* in press (2005).

S. Kwon, S. Ke, J. P. Houston, W. Wang, Q. Wu, C. Li, and E. M. Sevick-Muraca, "Imaging dose-dependent pharmacokinetics of an RGD-fluorescent dye conjugate targeted to $\alpha V\beta 3$ receptor expressed in Kaposi's sarcoma," *Molecular Imaging* in press (2005).

S. Ke, W. Wang, Q. Wu, C. Charnsangavej, J. P. Houston, D. Chow, E. M. Sevick-Muraca and C. Li, "Dual optical and nuclear imaging of integrin $\alpha V\beta 3$ in human melanoma xenografts using a single imaging probe," submitted to *Eur. J. Nuc. Med.* (2005).